Aerodynamic effects of accelerating objects in air

Hamed Roohani

A thesis submitted to the Faculty of Engineering and the Built Environment, University of the Witwatersrand, Johannesburg, in fulfilment of the requirements for the degree of Doctor of Philosophy.

Johannesburg, September 2010

Declaration

I declare that this thesis is my own unaided work, except where otherwise acknowledged. It is being submitted for the degree of doctor of philosophy to the University of the Witwatersrand, Johannesburg. It has not been submitted before for any degree or examination to any other university.

Signed this ……. day of …………………………… 20…..

……………………………………………………..

Hamed Roohani

To my beloved wife, Ladan, my parents, Giti and Manuchehr, my brother, Vafa and my sister Mona.

Acknowledgements

I would like to thank the following people:

Professor Beric Skews for his brilliant supervision and for the opportunity to present aspects of this work in two Journal articles and five conferences.

Fluent for the support they provided throughout the course of this research.

My colleagues, Randall Paton for his assistance with software related issues and Craig Law for providing help with the use of the Wits University in-house code, which was originally written by Luke Felthun.

I would also like to thank Professor Edward Moss, our Head of School, for his support and encouragement.

Abstract

This is an investigation into the unsteady aerodynamics of accelerating bodies. The main objective of the study is to compare the unsteady flow fields and the aerodynamic forces and moments resulting from acceleration or retardation of various objects with the corresponding steady state results at specific Mach numbers. It is to focus on transonic and subsonic Mach numbers using two-dimensional numerical models of airfoils and axisymmetric bodies. Fluent is used as the computational fluid dynamic (CFD) software with a special technique for handling the unsteady conditions during acceleration. In most cases constant velocity (steady state) simulations were conducted at Mach numbers ranging from 0.1 to 1.6. The objects were then accelerated at 1041 m/s^2 (106 g) and 86.77 m/s^2 (8.845 g), starting at Mach 0.1, and decelerated at -1041 m/s^2 and -86.77 m/s^2, starting at Mach 1.6, through the same range of Mach numbers using time-dependent (unsteady) simulations. Airfoils were used at different angles of attack and occasionally smaller accelerations at lower Mach numbers were used to confirm generality of results. It was found that during acceleration subsonic lift was lower and subsonic drag was higher than the corresponding steady state values at the same Mach number, with the opposite effect identified during retardation. In the transonic regime differences between the steady and unsteady position for the shock waves on the surfaces of the airfoils and axisymmetric bodies were observed. These were used to explain the large differences between the steady and the unsteady aerodynamic forces in the transonic range of Mach numbers. Acceleration dependent behavior for the bow shock, the tail shock and the trailing compression wave were also observed. In conclusion, all differences between steady and unsteady transonic shock wave behavior were found to be predominantly a function of flow history. In the subsonic regime the differences between steady and unsteady lift were attributed to flow history but for unsteady drag these differences were mainly attributed to fluid inertia.

Scope and contribution

This work entails an investigation into the transient aerodynamic effects brought about by accelerating objects in air. The study focuses on transonic and subsonic Mach numbers with two-dimensional numerical models of airfoils and axisymmetric bodies. It is a known fact that the unsteady flow field at a given instantaneous Mach number, resulting from the acceleration or deceleration of an object, is different to the steady state flow field at that same Mach number, because unsteady flow fields are time dependent and are influenced by their history. This research quantifies some of these differences by conducting a study of the flow field and the aerodynamic forces. A summary of the main contributions made is as follows:

- In the subsonic region, flow history brings about a reduction in lift during acceleration and an increase in lift during deceleration, in comparison with the steady state values at the same Mach number.
- The unsteady flow fields had the opposite effect on subsonic drag, which was higher than the steady state during acceleration and lower during retardation. This was attributed to the inertia of the fluid, which based on the numerical results, dominated all other effects in determining unsteady subsonic drag.
- The differences between the steady and unsteady aerodynamic forces in the transonic region are mainly due to the variations in the position and strength of the shock waves on the surfaces of the object, which is brought about by the unsteady flow fields and is strongly influenced by flow history.
- In the transonic range of Mach numbers flow history also influences the unsteady positions of the bow shock in front of airfoils and the trailing compression wave in the wake of the airfoils. During high deceleration from supersonic Mach numbers, the position of the tail shock is also affected such that it reaches the front and detaches and moves ahead of the aerofoil at subsonic Mach numbers.

Published work

Aspects of this thesis have been published in the following references:

Accredited journal articles:

1. H Roohani and B W Skews. The influence of acceleration and deceleration on shock wave movement on and around aerofoils in transonic flight. *Shock waves,* 19, 4: 297-305, 2009.

2. H Roohani and B W Skews. Unsteady aerodynamic effects experienced by aerofoils during acceleration and retardation. *Proc. IMechE, Part G: J. Aerospace Engineering,* 222(G5): 631-636, 2008.

Conferences:

1. H Roohani and B W Skews. Shock wave profiles on a transonic wing during acceleration, *ISSW27 - 27th International Symposium on Shock waves,* St. Petersburg, Russia, 19– 24 July 2009.

2. H Roohani and B W Skews. The Aerodynamic effects of acceleration and Retardation on Axisymmetric Bodies, SACAM 08 -*Sixth South African Conference on Computational and Applied Mechanics,* Cape Town, South Africa, 26-28 March 2008, ISBN 978-0-620-43166-8.

3. H Roohani and B W Skews. Effect of Acceleration on Shock-wave Dynamics of Aerofoils During Transonic Flight, *ISSW26 - 26th International Symposium on Shock waves,* Göttingen, Germany, 15– 20 July 2007, ISBN 978-3-540-85180-6.

4. H Roohani and B W Skews. Transient aerodynamic forces experienced by aerofoils in accelerated motion, *ISSW26 - 26th International Symposium on Shock waves*, Göttingen, Germany, 15– 20 July 2007, ISBN 978-3-540-85180-6.

5. H Roohani and B W Skews. Investigation of the effects of acceleration on aerofoil aerodynamics, SACAM 06 -*Fifth South African Conference on Computational and Applied Mechanics*, Cape Town, South Africa, 16-18 January 2006, ISBN 1- 919966-01-3.

Contents

List of Figures

List of Symbols

$\boldsymbol{m}$	Mass in kg
ρ	Density in kg/m^3
$\boldsymbol{v}$	Velocity in m/s
$\boldsymbol{t}$	Time in seconds
$\boldsymbol{Vol}$	Volume in m^3
$\boldsymbol{C_p}$	Specific heat capacity in J/kgK
μ	Viscosity in kg/m-s
$\boldsymbol{T}$	Static temperature in K
μ_0	Reference value in kg/m-s
$\boldsymbol{T_0}$	Reference temperature in K
$\boldsymbol{S}$	an effective temperature in Kelvin (Sutherland constant)
$\boldsymbol{m_s}$	Mass source term
$\boldsymbol{M_s}$	Momentum source term

$\boldsymbol{E_s}$	Energy source term
$\boldsymbol{C_D}$	Drag coefficient
$\boldsymbol{C_L}$	Lift coefficient
P	Static pressure
y^+	Wall Yplus
u_τ	Friction velocity
y_P	Distance from the centre of the wall adjacent cell to the wall

1 Introduction and literature review

In the past, when studying objects moving through compressible fluids, nearly all the work was conducted on movement at constant speed through the fluid [2]. This was seldom extended to accelerating bodies, even though in many practical applications objects experience acceleration and retardation. For example when graphs of the variation of lift or drag versus Mach number were plotted for an aerofoil, these were based on steady state flight [4, 5, 6]. In other words sufficient time was allowed to lapse at each specific Mach number for aerodynamic equilibrium to be reached, before the lift or drag forces were determined. However, in accelerated motion there is no time for equilibrium to be reached at each Mach number. Therefore the graph of lift or drag versus Mach number for an accelerating body should differ from the steady state case.

The main reason for this expected difference is that the unsteady flow field generated during acceleration or retardation differs from the steady state flow field at the same instantaneous Mach number. An example of this for the simple case of a particle moving through a compressible medium is given in Lilley [1].

In figures 1.1 the steady state disturbances generated by particles moving at constant subsonic and supersonic velocities are shown. Figure 1.2 shows an unsteady supersonic scenario, where the particle is accelerated from subsonic to supersonic velocities. The distinct difference between the steady and unsteady supersonic cases is evident. In figure 1.3 the particle is moving at a subsonic Mach number after having been accelerated to supersonic Mach numbers followed by retardation to subsonic velocities. The unsteady disturbance generated is very different to the steady subsonic case of figure 1.1.

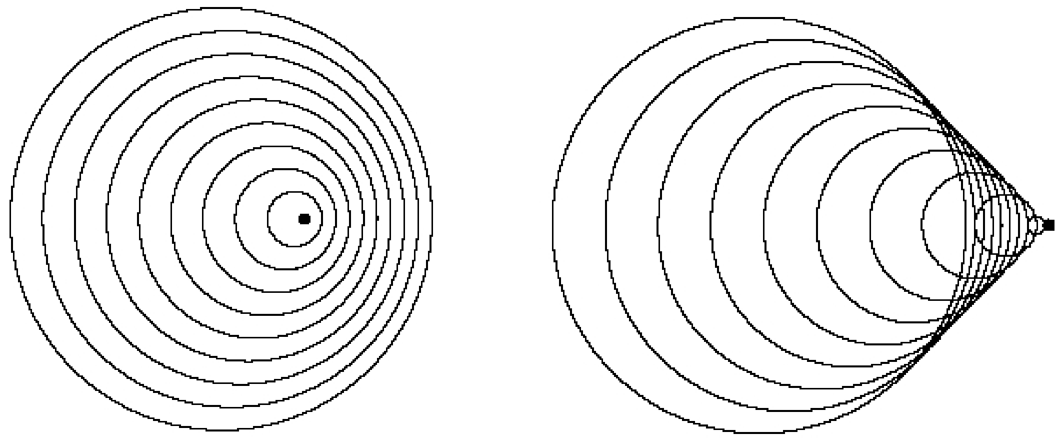

Figure 1.1: The steady state flow field generated by a particle moving at constant velocity. On the left the subsonic case and on the right the supersonic case is shown

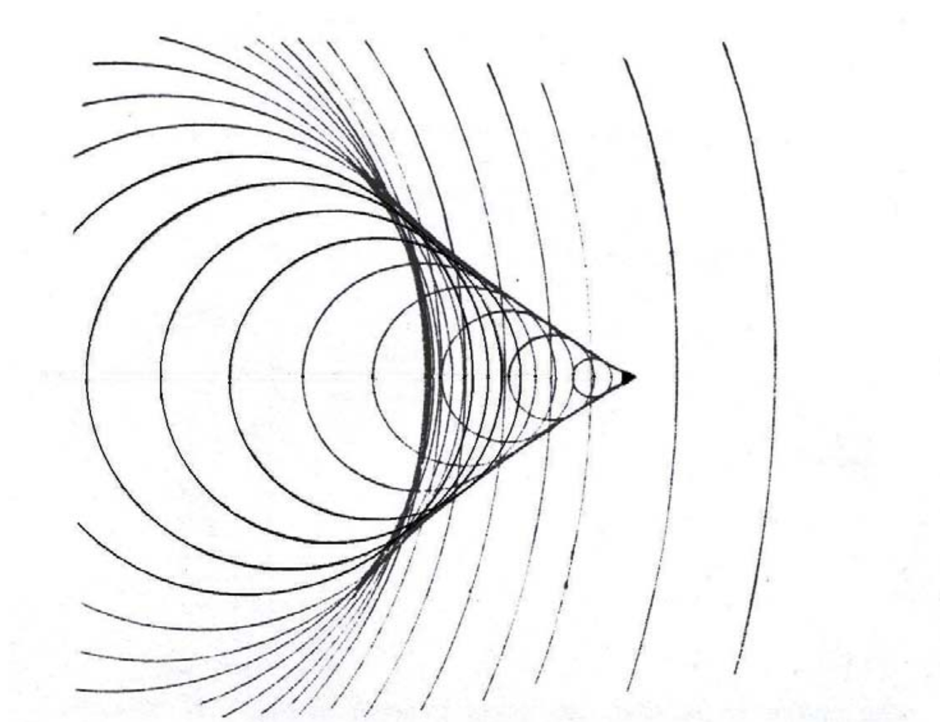

Figure 1.2: The unsteady flow field generated by a particle accelerated from subsonic to supersonic velocities.

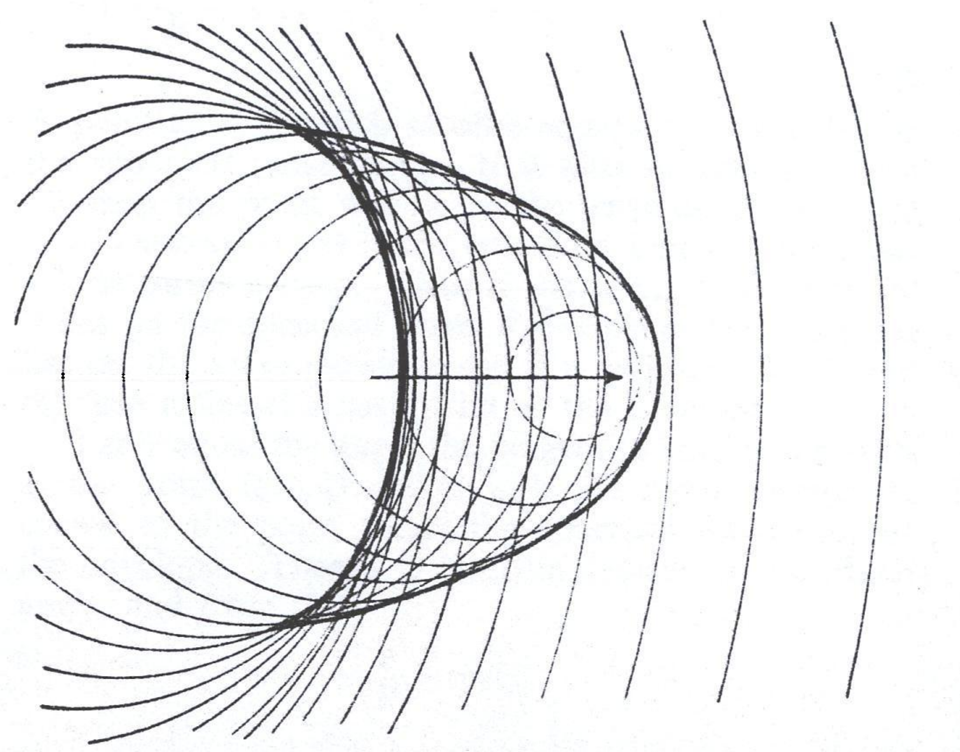

Figure 1.3: The unsteady flow field generated by a particle moving at a subsonic velocity after having been accelerated to supersonic velocities followed by retardation to subsonic velocities.

It can be concluded that, if for a moving particle such significant differences exist between the steady and the unsteady flow fields at similar Mach numbers, for a more complex object the differences could even be greater. This would in turn result in differences in the pressure distribution on the surfaces of the object, which would thus affect the aerodynamic forces.

Such studies of unsteady aerodynamics have many practical applications. For example, the study of forces on aircraft during takeoff and landing, the forces acting on fighter planes during acceleration and retardation and the aerodynamics around Formula 1 and other racing cars, which are designed to make use of aerodynamic forces to achieve stability around high speed bends [25]. Also, when designing missiles, the very high accelerations make it necessary to model the unsteady aerodynamic effects [31].

From the above discussion it is clear that the study of accelerated motion in compressible fluids is important. However, in the past research in this field has been limited for the following reasons:

a) It is difficult to mathematically model fluid behaviour when an object is accelerated in compressible fluids.
b) Experimental techniques cannot easily be used to measure transient effects caused by accelerating bodies, especially at high velocities.
c) Computation techniques were not sufficiently developed in the past.

Although the first two limitations still apply recent developments in Computational Fluid Dynamic (CFD) techniques have facilitated the study of unsteady effects caused by the acceleration and retardation of moving bodies in compressible fluids. However, this is best achieved by a comparative study of the steady and unsteady cases, which necessitates the use of both steady and unsteady computational models.

1.1 Review of numerical techniques

1.1.1 Steady state models

Numerous steady state numerical techniques have been developed over the last twenty years for the purpose of modelling objects moving at constant velocity through compressible fluids. These can be broadly classified as viscous and inviscid models. The use of inviscid models is based on the assumption that viscosity plays a negligible role in the determination of the flow field and the aerodynamic forces. These models are usually based on the Euler equations, which only calculate the pressure related effects in a flow field. A good example is the numerical model developed by Jiang and Forsyth [9], which was used for predicting transonic flow. However, inviscid codes show better correlation with experiment under subsonic rather than transonic conditions. When objects such as aerofoils move at transonic Mach numbers, shock waves are developed on their surfaces and the position of the shock wave is influenced by its interaction with the boundary layer on the surface of the aerofoil. It can be shown that, even under steady state conditions, the shock wave position predicted by inviscid codes do not match experimental results. This will be discussed in greater detail in the forthcoming chapters.

It is for reasons such as the ones given above that viscous turbulence models have become more popular in recent years. These are usually based on the Navier-Stokes equations. Some examples of these are the v^2-f turbulence model, the κ-ε and κ-ω [3] and the Spalart-Allmaras [3, 16]. Literature shows that such models are able to produce results that match experimental data. For example Lien and Kalitzin [11] have shown good correlation between experiment and transonic data produced by the v^2-f model. Fluent© has validated transonic data produced by the κ-ε, κ-ω and the Spalart-Allmaras turbulence models against experiment as reproduced in appendix C. These validations show that these models predict the position of the steady state transonic shock fairly accurately.

Hafez, Shatalov and Wahba [12, 13, 24] use viscous and invscid modelling to predict the flow field around a NACA0012 aerofoil at various steady state velocities. These range from Mach 0.1 to Mach 1.5 with the main focus on transonic Mach numbers. The study is a good example of the effectiveness of viscous and invscid models in predicting transonic flow behaviour.

1.1.2 Unsteady modelling techniques

In recent years the latest developments in unsteady aerodynamics have led to some progress in the design of numerical models for predicting accelerating flow. For example Gottfried and Fleeter [14] developed an unsteady incompressible model for predicting the aerodynamic forces on aerofoils during impulsive acceleration and arbitrary aerofoil motion. This is useful for modelling unsteady aerodynamics for a bladed disc environment. Prananta, Hounjet and Zwaan [15] developed a time-marching algorithm for the two-dimensional unsteady viscous transonic flow. Apart from analysis of the flow around an aerofoil the method is capable of handling forced vibration and shock induced separation. Becker, Reyer and Swoboda [17] have presented an application of the Spalart-Almaras turbulence model to the unsteady transitional shock-boundary-layer-interactions on a fan blade.

Lee, Raghunathan, Kim and Setoguchi [47] implemented another unsteady application of the Spalart-Almaras turbulence model using Fluent, which is a commercial CFD code, to model gradual acceleration or deceleration of an aerofoil at subsonic and transonic velocities. The far-field boundary condition was applied to the external boundaries of the computational domain and the fluid velocity at infinity was changed using constant acceleration and deceleration. The unsteady aerodynamic characteristics obtained from the simulations were then analysed. As discussed in more detail in section 2.2 of chapter 2, although this technique may be adequate for modelling low aerofoil accelerations at subsonic velocities, it does not yield good results for high aerofoil accelerations. Strictly speaking, accelerating the fluid at the boundaries of the computational domain does not adequately model the acceleration of an object in a stationary compressible fluid. This can only be achieved by accelerating the fluid inside the domain and the fluid at the boundaries simultaneously with equal acceleration. Alternatively, the reference frame of the object must be accelerated while the fluid at infinity is kept stationary.

1.1.3 Modelling techniques used in this investigation

In this study two CFD codes were utilised. Initially an in-house code, which was developed by L. T. Felthun [10] for The University of the Witwatersrand, was used. This code was experimentally validated for low velocities and has been used successfully to model acceleration related unsteady behaviour in some lower velocity applications. However, its major drawback is that it is an inviscid code, based on the Euler equations, and can therefore only be used in applications where the effects of viscosity are negligible. For example, as already explained, even under steady state conditions the position of the transonic shock predicted by Luke Felthun's and some other inviscid codes do not match experimental results. Therefore, in such applications, the unsteady results that such codes produce would also be unreliable.

As a result of the limitations in Luke Feltun's code it was decided to use Fluent as the main CFD software for this research. Fluent is a highly developed code capable of using both viscous and inviscid models. For the viscous case three of the turbulent models available in Fluent were used in this investigation. These were Spalart-Allmaras [3, 16], κ-ε and κ-ω [3]. Results obtained from one turbulent model, was sometimes checked against the others as a form of validation.

A technique, recommended by Fluent, was used in conjunction with these turbulent models in order to model acceleration and retardation of objects in compressible fluids. This will be discussed in more detail in chapter 2. Acceleration was also modelled using the same technique in conjunction with Fluent's invscid model. This was mainly done in order to validate Fluent's acceleration model against the University's in-house code. However, in certain cases inviscid modelling proved to be a useful tool for isolating purely pressure related effects in flow fields.

1.2 Subsonic and transonic steady state aerodynamics

An important area of research in this investigation was the study of unsteady aerodynamics around aerofoils during transonic acceleration and deceleration. However, in order to develop a good appreciation of the unsteady transonic effects, the steady transonic aerodynamics needed to be reviewed and used as a benchmark.

Information about the lift, drag and pitching moment of various wing sections at different angles of attack can be found in literature [4, 5, 6], which includes transonic data. In Van Dyke [7] shadowgraph pictures of flow fields generated by various objects moving at transonic Mach numbers give a good basis for comparison with numerical data obtained from Fluent. Becker's wind tunnel experiments of aerofoils in transonic flow [8] give evidence of the λ-foot on the surface of the aerofoil and trailing wave behind the aerofoil, which confirm some of the numerical data obtained in this investigation.

Also of interest is the work of Mavriplis and Levy [20] who conducted a numerical study of transonic drag, which is validated against experimental data. This study demonstrates the steep drag rise at transonic Mach numbers. Sekar and Laschka [18] presented a numerical procedure for the calculation of the transonic dip of aerofoils, which is the lowest flutter speed at transonic regimes. This work, among other things, shows the observed reduction in lift coefficient at a certain range of transonic Mach numbers. More discussion on transonic dip can be found in the work of Ballmann, Boucke and Braun [19], which also compares numerical results regarding aerodynamic parameters of an aerofoil in transonic flow with experimental results obtained from transonic wind tunnels.

The study of steady state shock boundary-layer interaction [21] and flow separation on the surface of aerofoils is of significance, since an important aspect of this thesis is about the effect of acceleration on the shockwave dynamics of arofoils in transonic flight. Swoboda and Nitsche [22] have conducted an experimental study of shock boundary-layer interaction on aerofoils in a transonic wind tunnel for laminar and turbulent flow. Both steady and unsteady measuring techniques were used. The unsteady measuring techniques were used to detect details in the separation regions and to determine the position of transition in the case of laminar flow. Ericsson's work [23] involves an analysis of existing theoretical and experimental results of flow separation and reattachment caused by a pitching down aerofoil.

The differences between the subsonic steady and unsteady flow fields are usually less significant than the observed differences in the transonic regime. Therefore, it is often necessary to compare aerodynamic forces or coefficients at a given Mach number. As will be demonstrated in later chapters, the unsteady lift, drag and pitching moment differ from those under steady state condition at the same Mach number, even at subsonic velocities. It will be established that even for low accelerations such as those experienced in formula racing cars the aerodynamic forces are affected significantly when compared to the steady state conditions [25]. However, it is also important to note that a proper study of the aerodynamics around racing cars must take into account the ground effect [48]. Ahmed and Sharma [26] have conducted an experimental study of the NACA 0015 aerofoil in ground effect at various angles of attack, which shows that ground clearance can affect the aerodynamic coefficients.

1.3 Unsteady aerodynamics

When studying accelerating flow, most of the developments deal with the acceleration of the actual fluid. For example Tahir, Molder and Timofeev [27] have presented a CFD study of hypersonic inlet starting, where air is accelerated at the inlet to geometries suitable for air intakes into engines operating at high supersonic velocities. It is generally easier to model such cases numerically or experimentally as the fluid itself is accelerated. However, this research is about accelerating different objects in stationary compressible fluids. In other words a numerical or experimental model must be developed which is equivalent to accelerating the object and keeping the fluid at infinity stationary.

As a review of such numerical techniques has already been given in section 1.1 the discussion below will be mostly focused on experimental models. However, it must be noted that experiments, which adequately model objects undergoing constant acceleration at high subsonic and transonic velocities were not found in the literature. Therefore, experimental validation of such numerical data is only possible if a new facility is developed for this purpose. As this proved too costly some recommendations for establishing such a facility is made in the forthcoming chapters.

1.3.1 Review of work done on acceleration of spherical objects

Ikushima, Kuroda and Ohji [28] have conducted an experimental study of acceleration of a sphere in free fall. The acceleration data obtained during the tests is used for determining the aerodynamic forces on the sphere. Lai and Fan [29] performed an analytical study of acceleration of a sphere moving along a rectilinear path and developed an exact solution for the drag on the sphere. As an example, the solution for the drag on a sphere suddenly brought to uniform motion is presented.

Of particular interest is the experimental work done by Tsuji, Kato and Tanaka [30] on the drag and wake of a sphere in a periodically pulsating flow. The experiments were conducted in a wind tunnel and pulsating flow was blown at a spherical test specimen. It was found that, in comparison with steady state conditions, the drag coefficient increased in accelerating flow and reduced when the flow was decelerated. Although wind tunnel models are not a true representation of objects being accelerated in stationary compressible fluids, the data obtained confirms in principle the numerical data on acceleration of spheres obtained by using Fluent in the present study.

1.3.2 Unsteady aerodynamics around aerofoils

Many of the recent developments regarding accelerating flow around aerofoils is focused on flow oscillations or periodic flow. Selerowicz and Szumowski [32] presented an experimental study on the effect of background flow oscillation on a NACA 0012 aerofoil in a transonic wind tunnel. Pressure history at selected points on the surface of the airfoil as well as interferometric photographs of oscillating aerofoil flow was shown for two different angles of attack. The influence of the unsteady loading on flow separation and reattachment at the higher angle of attack highlight the significant effect of flow oscillation on transonic aerofoil aerodynamics.

Fernie and Babinsky [33] performed another experiment on a NACA 0012 aerofoil using a non-circular rotating cam placed in the diffuser section of a transonic wind tunnel to bring about relatively smooth free stream velocity oscillations at low frequencies, typical for helicopter blades in forward flight. At the relatively low frequencies used in this study, little difference was observed in shock position between the steady and unsteady cases at the same instantaneous Mach number. However, the authors do point out that departures from this behaviour could be expected at higher frequencies. On the other hand, the unsteady flow did affect the shock strength even at low frequencies.

As this investigation focuses on the aerodynamic effects resulting from constant acceleration of various objects in air, publications in this specific area were of particular interest. Some of the earliest work in this field was conducted by Freymuth, Palmer, Bank and Finaish [34, 35, 36, 37, 38], who used flow visualization techniques to study accelerating flow around aerofoils starting from rest. The test specimen was placed in a wind tunnel where the flow was accelerated at 2.4 m/s^2 (approximately g/4) for about five seconds. The vortical patterns formed at various Reynolds numbers under different angles of attack were documented in photographic sequence and analysed. Although these results are of interest, they involve very low velocities and accelerations and it is at higher velocities and accelerations that the greatest unsteady effects are expected. Moreover, it is only at low accelerations that a wind tunnel is useful in approximating the acceleration of an object in a stationary compressible fluid. As will be explained in future chapters, at higher accelerations a pressure gradient is formed along the wind tunnel, rendering it completely non-representative of the flow field being modelled. Therefore the technique described in these experiments is not directly applicable to the present investigation.

Other experimental work using liquids, such as oil mixtures and water with solid tracers used for flow visualization [39], or a piston driven water tunnel with particle image velocimetry (PIV) techniques [41], have been effective in reducing the pressure gradient problem encountered in wind tunnel models during acceleration. These experimental models have been used to improve numerical techniques developed for low Reynolds number applications. However, as liquids are almost incompressible they are not suitable for modelling compressible fluid behaviour at high Reynolds numbers.

Ellsworth and Mueller [40] used hot wire anemometry to determine the effect of an accelerating free stream, from a non-zero velocity, on transitional separation bubble characteristics formed on a Wortmann FX 63-137 aerofoil at 7° angle of attack. This was compared to the characteristics resulting from a quasi-steady velocity change. A wind tunnel was used with the means to generate short-term flow acceleration or deceleration. Although the study was conducted for Reynolds numbers well below the critical value, it is a good example of how the position of the separation bubble is affected by acceleration or deceleration.

A number of experiments have been performed in order to determine the effect of acceleration on the lift coefficient of aerofoils. Minkkinen, Wilson and Beavers [42] mounted a stationary aerofoil in the driver section of a shock tube and utilizing the high fluid accelerations, which occur in an expansion fan, were able to obtain lift data resulting from rapidly accelerating flow. These were compared with steady state lift data obtained by opening both ends of the shock tube and installing a small blower at one end. The results showed that acceleration brought about an increase in lift coefficient when compared to the steady state values. Sawyer and Sullivan arranged experimental setups where an aerofoil was accelerated from rest, either by a step change [43] or by moving a few feet under constant acceleration [44]. After the step change the lift curve approached its steady state value from lower lift values. Under constant acceleration the lift coefficients were also lower than the steady state values for a given angle of attack. Clearly these contradict the results obtained from the shock tube [42]. This could be because different types of acceleration affect the aerodynamic coefficients differently.

It must be noted however, that the accelerating aerofoil offers a closer representation of the moving object in stationary fluid, which is the focus of this study. Through numerical simulations, it will be shown in future chapters that for subsonic velocities, the lift forces on an aerofoil during constant acceleration show a reduction in comparison with the steady state values. This is a confirmation of the results obtained by Sawyer and Sullivan [44]. On the other hand, Sawyer and Sullivan's experimental model, which involves the acceleration of an aerofoil from rest over a distance of a few feet, is not suitable for validating numerical data at high subsonic and transonic velocities.

Certain numerical techniques have been developed in order to model the effects of acceleration on the aerodynamic coefficients of aerofoils. Marquart and Eastep [45] presented a method for computing unsteady aerodynamic effects on an aerofoil undergoing linear acceleration. However, the acceleration was applied in a sudden stepped manner in order to save computational time, which is different to what would occur in the real world where it would be applied more gradually. Nevertheless, the results showed that acceleration affects the lift and drag coefficients significantly in comparison with the quasi-steady scenario. Hamdani and Sun [46] have performed a numerical study to demonstrate the reasons for the unusually high aerodynamic coefficients generated by insects during flight. They have shown that the main reason for this is the unsteady aerodynamics generated due to rapid acceleration and deceleration of the insect wing. The numerical model uses a two dimensional aerofoil, which is subjected to high acceleration and deceleration at low Reynolds numbers (Re = 100), showing that the maximum unsteady values of lift and drag are substantially greater than the steady state values. These numerical results confirm the experimental results obtained by Wilson and Beavers [42], who generated the rapid acceleration and deceleration in a shock tube.

At this point it is worth noting that, as a direct result of the work done for this dissertation, two journal papers have been published and a number of papers have been presented at conferences. These have not been included in the reference section but have instead been listed at the beginning of this document.

1.4 Objectives of this study

The aim of this research is to investigate the aerodynamics of accelerating bodies. This can be broken down to the following objectives:

- The study is focused on bodies moving at subsonic and transonic Mach numbers.
- It is restricted to two-dimensional numerical models of aerofoils and axisymmetric bodies.
- It is to quantify the differences in aerodynamic forces between the steady and unsteady (accelerating) cases at specific Mach numbers.
- It must compare the flow fields of the steady and unsteady cases, with special focus on flow fields at transonic Mach numbers in order to identify unsteady shock wave related flow behaviour.

2. Modelling techniques

This chapter describes the various computational models used in this investigation. Fluent, which is a well-established commercial code, was chosen and the techniques described below either make direct use of the facilities within Fluent or combine these with user defined functions.

2.1 Procedure for steady state computation

In order to simulate an object moving with constant velocity through a compressible fluid two techniques can be used in Fluent.

2.1.1 Moving reference frame technique

The first is to move the reference frame of the object at the desired velocity. This technique moves the object and the meshed domain simultaneously at the required velocity while the fluid at infinity remains stationary. The fluid velocity at far field is specified as zero and the magnitude and direction of the translational velocity of the reference frame of the object is given by specifying its components.

Figures 2.1 and 2.2 show the velocity flood plots for a NACA0012 aerofoil moving at Mach 0.85, modelled using the moving reference frame technique. The angle of attack of the aerofoil is 4 degrees and the ambient temperature at far field is 300 K. The diagrams clearly show that the fluid near the boundaries of the domain is stationary and the fluid near the aerofoil experiences the maximum velocity, as would be expected from this technique.

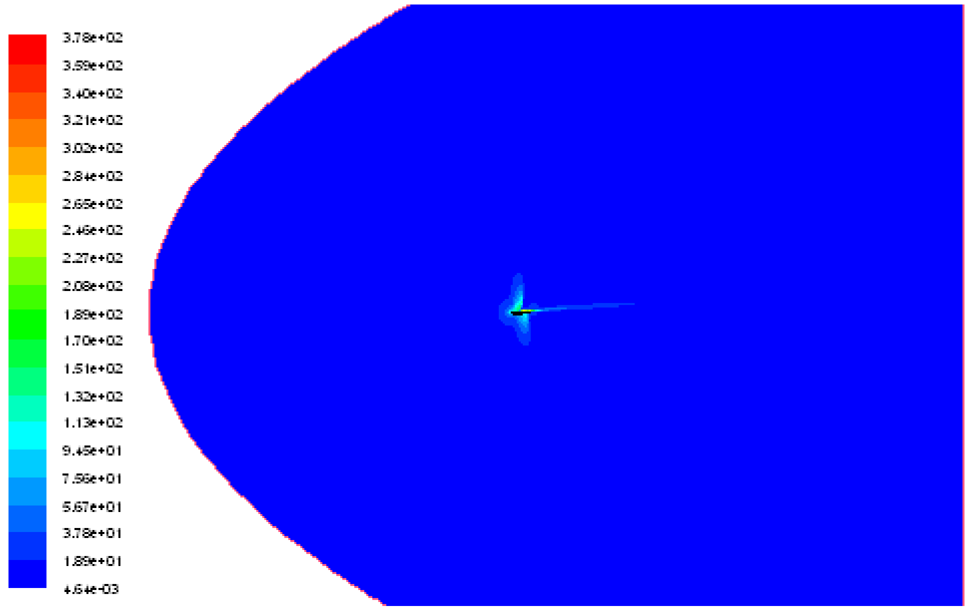

Figure 2.1: Velocity flood plot, representing the moving reference frame technique, with aerofoil moving at Mach 0.85 and the fluid at far field being kept stationary.

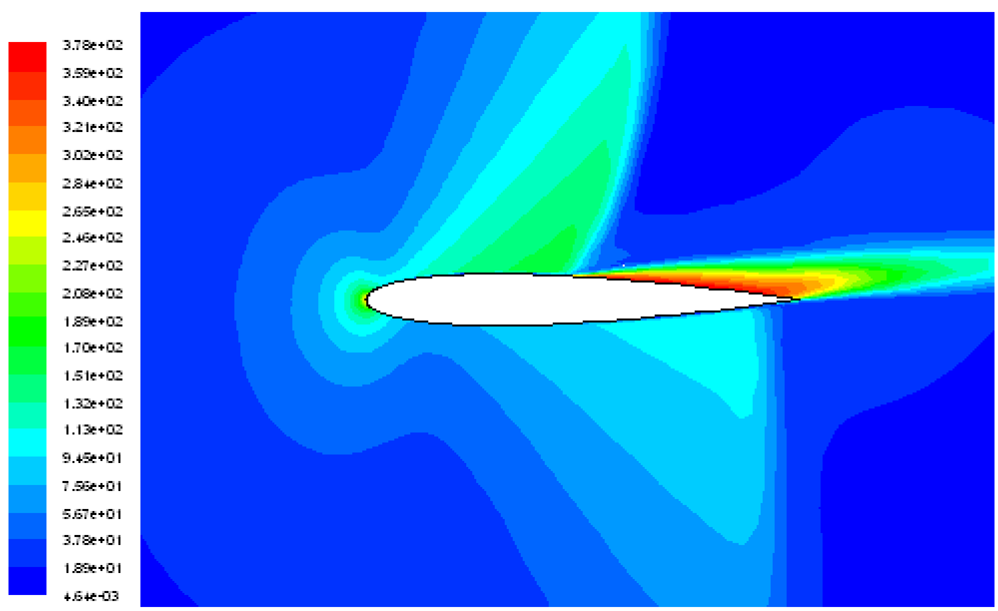

Figure 2.2: The moving reference frame velocity flood plot of figure 2.1, enlarged to show flow details near the aerofoil.

2.1.2 Pressure-far-field boundary conditions

The second technique requires the use of pressure-far-field boundary conditions [3]. These are used in Fluent to model free stream conditions at infinity, with free stream Mach number and static conditions being specified. In Fluent the pressure far-field boundary condition is a non-reflecting boundary condition, which handles both inflow and outflow. Pressure far-field boundary conditions are used for modeling objects moving with constant velocity through compressible fluids. Although this technique only specifies the velocity at the far-field, sufficient time is allowed in steady state simulations for the system to reach equilibrium. This will result in the entire flow field to be moved at the required velocity and the reference frame of the object to be kept stationary, hence producing results identical to the case of the moving reference frame described above.

Figures 2.3 and 2.4 show the case of the NACA0012 aerofoil from the previous section modelled using pressure-far-field boundary conditions. At the fluid boundary the fluid velocity is approximately Mach 0.85 (295 m/s) showing the distinction between this technique and the moving reference frame technique.

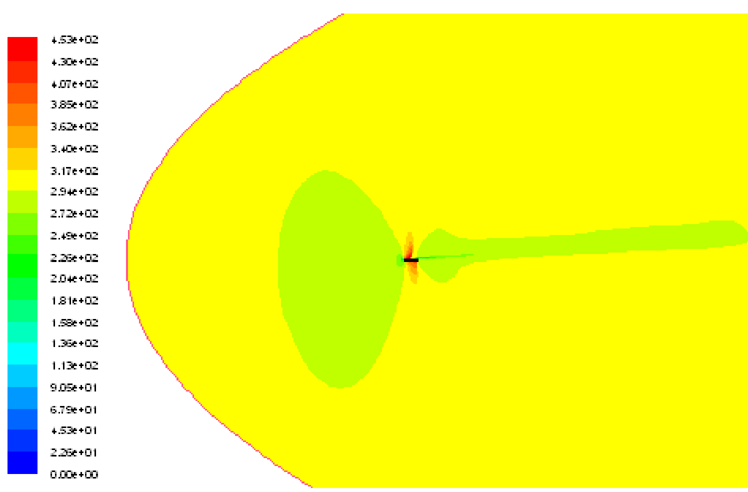

Figure 2.3: Velocity flood plot, representing the pressure-far-field boundary condition technique, with the aerofoil kept stationary and the fluid at far field moving at Mach 0.85.

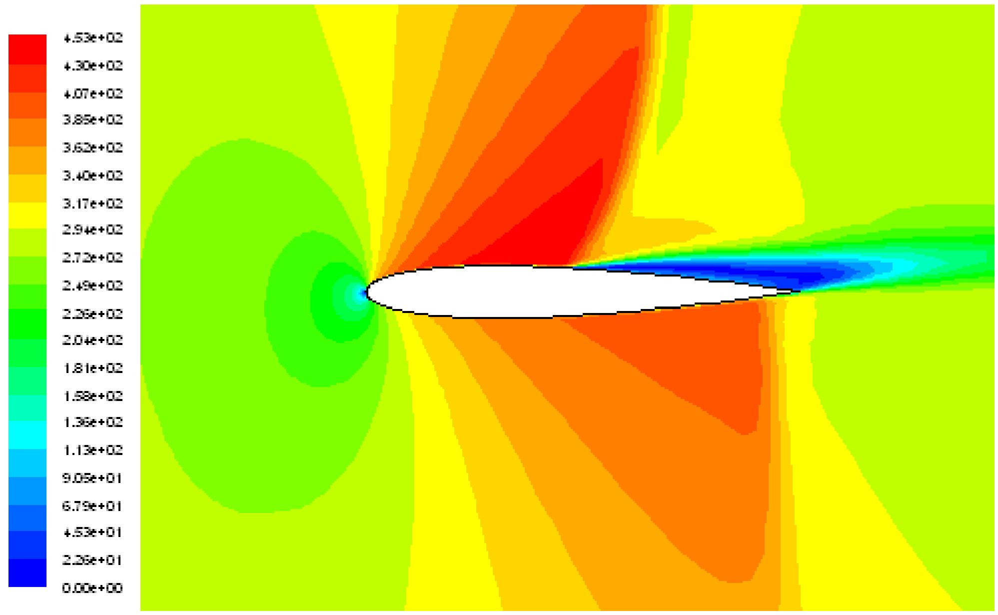

Figure 2.4: The velocity flood plot of figure 2.3, enlarged to show flow details near the aerofoil

As the same case is modelled by two different techniques, this could be used as a preliminary validation exercise for the steady state techniques. Figures 2.5 and 2.6 show the pressure flood plots for the two techniques and figures 2.7 and 2.8 show graphs of pressure versus position on the surfaces of the aerofoil. In each case these appear to be identical showing that the two techniques yield the same results. Note that the areas where the pressure in the flow field changes abruptly, representing the position of the shock waves, match closely when the results from the two techniques are compared. Although not shown here, the aerodynamic forces in each case were also found to be within 1% of each other. As these fairly different methods essentially yield the same results, this serves as a preliminary step towards the validation of such techniques.

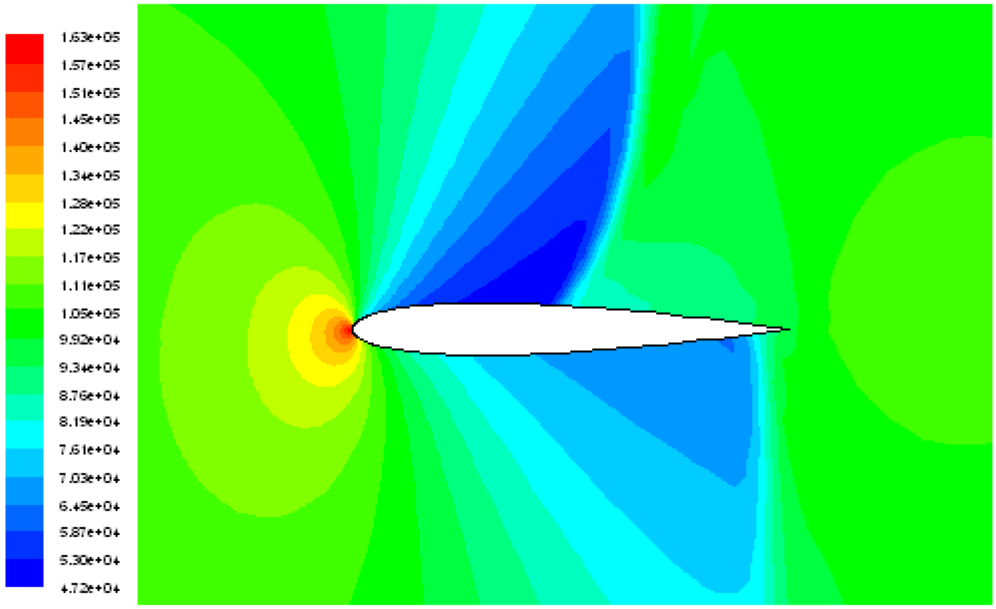

Figure 2.5: Pressure flood plot at Mach 0.85 for the pressure-far-field case

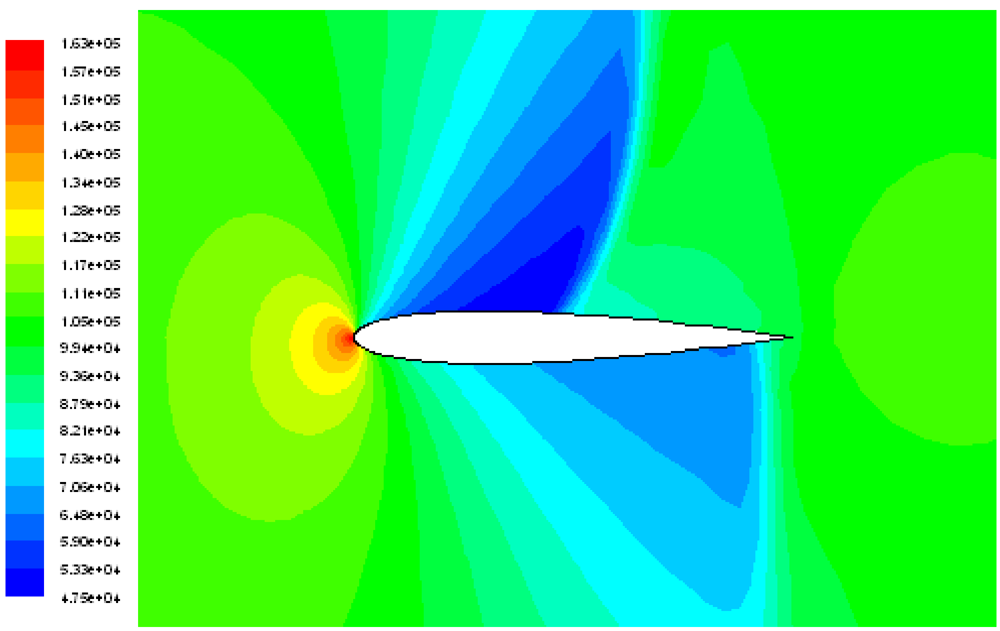

Figure 2.6: Pressure flood plot at Mach 0.85 for the moving reference frame case

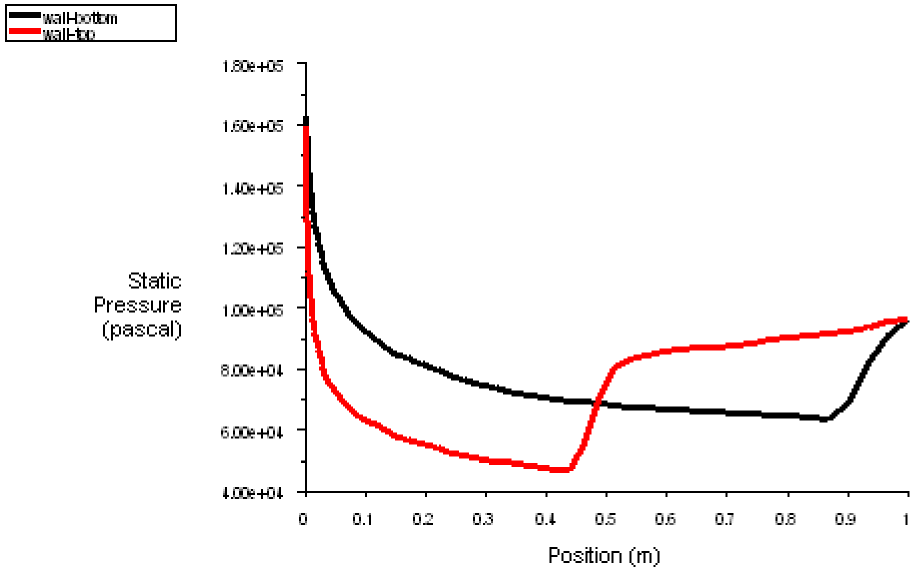

Figure 2.7: Pressure versus position on the upper and lower surfaces of the aerofoil at Mach 0.85 for the pressure-far-field case.

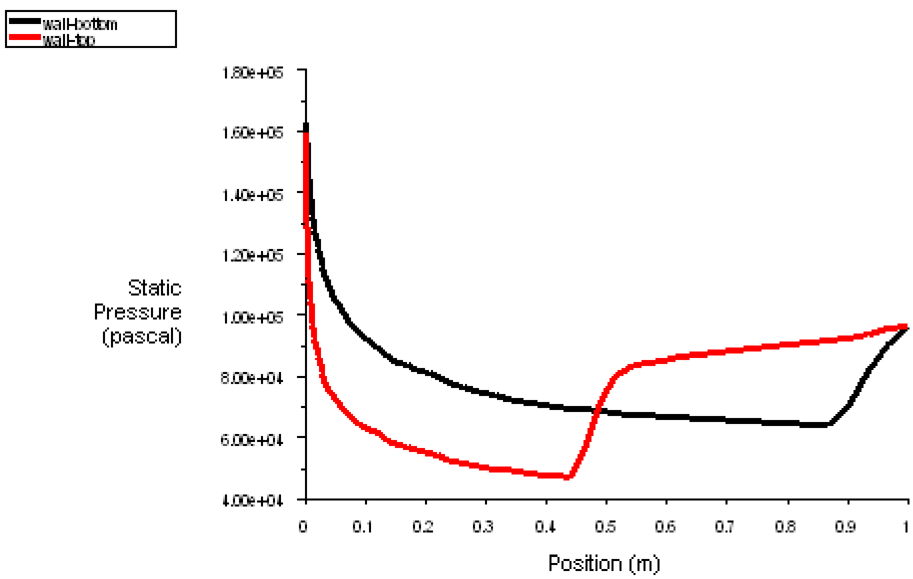

Figure 2.8: Pressure versus position on the upper and lower surfaces of the aerofoil at Mach 0.85 for the moving reference frame case.

However, it should be noted that Fluent has validated the pressure-far-field boundary condition technique against experimental data for steady state external aerodynamic problems. The validation case is given in appendix C.

2.2 Procedure for accelerating objects in compressible fluids

Fluent does not have the facility for translational acceleration of the reference frame of an object. The moving reference frame technique in Fluent can only solve problems with constant translational velocity as described above. An in-house code, for accelerating objects in compressible fluids, was developed by L. T. Felthun [10] for The University of the Witwatersrand, which uses a technique similar to the moving reference frame technique. However, as the code is based on an inviscid model, it does not yield good results for flow fields, which are influenced by boundary layer interaction. It will be used to confirm results in cases where the flow field away from the surface of an accelerating object is being investigated.

In order to deal with acceleration when using Fluent, the reference frame of an object must be kept stationary and the flow field must be accelerated. This will of course require a time dependent simulation. It is, however, important to note that accelerating a flow field cannot be achieved merely by accelerating the fluid at the far field boundary. Any change at the far field will propagate through the medium at the speed of sound and will be experienced by an object and by the fluid surrounding the object only some time after the change has taken place. In contrast, when an object is physically accelerated through a particular fluid, the changes in its velocity are experienced instantaneously by the fluid immediately surrounding the object and are propagated outwards.

In figures 2.9 and 2.10, the fluid at the boundaries of a meshed domain is accelerated by making use of pressure-far-field boundary conditions, together with an unsteady time dependant solver in Fluent. A user-defined function, which accelerates the fluid at far field at approximately 100 m/s^2, is used (see Appendix A for user defined functions). It can be observed from figure 2.9 that after 0.01 seconds the object has

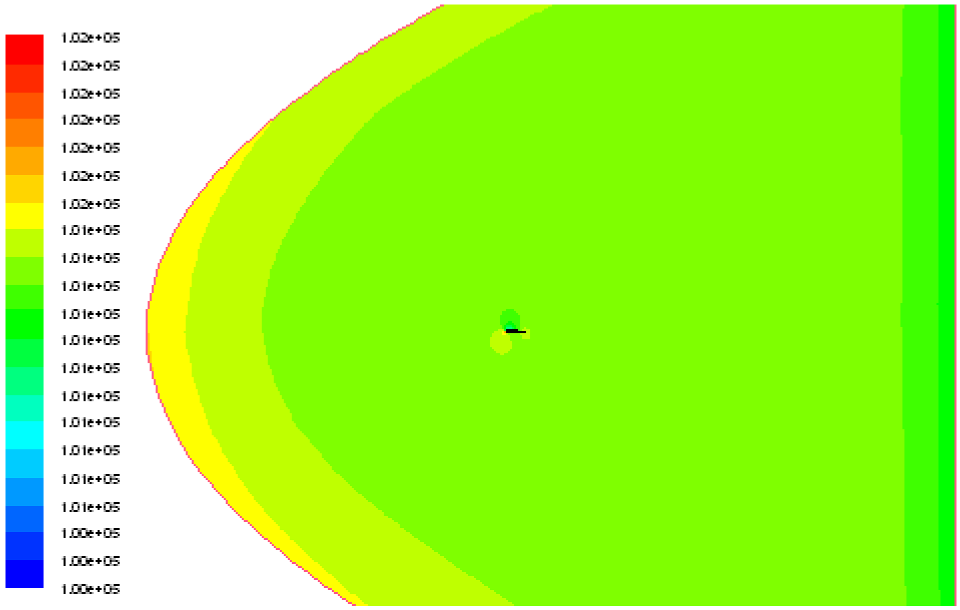

Figure 2.9: Pressure flood plot generated after 0.01 seconds by accelerating the fluid at far field at 100 m/s^2. Note the discrepancy with expected flow field in figure 2.11.

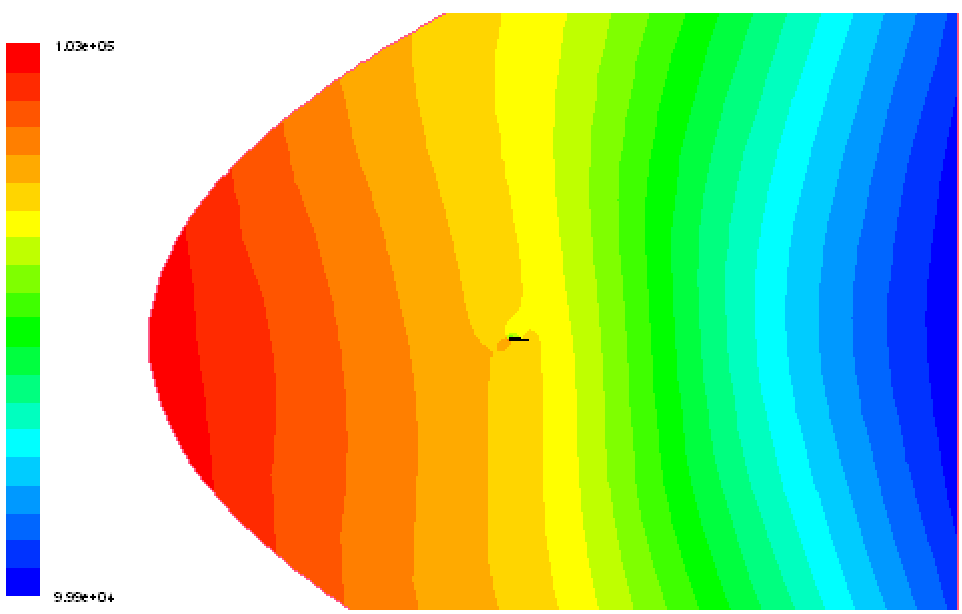

Figure 2.10: Pressure flood plot generated after 0.07 seconds by accelerating the fluid at far field at 100 m/s^2. Note the discrepancy with expected flow field in figure 2.11.

still not experienced any acceleration related disturbance. Changes in pressure resulting from acceleration are only present in areas close to the far field boundary. After more time lapses, say at 0.07 seconds as shown in figure 2.10, although the initial disturbance has reached the object the flow field generated by this technique is not at all representative of what would happen in the physical case. The pressure gradient generated along the domain is clearly not the result of accelerating an object in a stationary fluid.

In fact the above is a far closer representation of the flow field observed in a wind tunnel where the air is accelerated and the object is kept stationary. This is because, in a wind tunnel, either the speed of the fan or the system resistance would have to be changed gradually in order to model flow acceleration, which would create a similar pressure gradient along the wind tunnel. This is the main reason against the use of wind tunnels in modelling the acceleration of objects in stationary fluids.

The above numerical and experimental cases demonstrate the discrepancies, which are encountered when the fluid at far field is accelerated in an attempt to model the acceleration of objects in stationary compressible fluids.

2.2.1 Technique recommended by Fluent

In order to successfully model the case of an accelerating object in a stationary fluid, the object is kept stationary and every fluid particle is accelerated simultaneously with equal acceleration. In other words, at every time step, the fluid at the boundary of the domain and the fluid in every cell inside the boundary undergo the same incremental change in velocity. The resulting flow field is then computed by Fluent after a suitable number of iterations between time steps. The far field is accelerated by a user-defined function (see Appendix A), which determines the changing value of the input velocity at a given time. The fluid inside the boundaries is accelerated using momentum and energy source terms, which can form part of the same user defined function, if necessary. These are derived from the momentum and energy equations, which are built into the Fluent source code [3]. The source terms generally required are:

Mass Source (m_s) $= (dm/dt)/Vol$

$= d\rho/dt$ **[kg/m^3/s]**

Momentum Source (M_s) $= (d(mv)/dt)/Vol$

$= (d(\rho.Vol.v)/dt)/Vol$

$= d(\rho v)/dt$

$= \rho dv/dt + v d\rho/dt$ **[N/m^3]**

Energy Source (E_s) $= (d(energy)/dt)/Vol$

$= (d(mC_pT + mv^2/2)/dt)/Vol$

$= d(\rho C_p T + \rho v^2/2)/dt$

$= \rho C_p dT/dt + TC_p d\rho/dt + (v^2/2)d\rho/dt + \rho v dv/dt$ **[W/m^3]**

However, in this case, we need to correct for the unphysical acceleration of the fluid, and must therefore include just the acceleration terms of the above equations, namely those in dv/dt, the other terms must convect through the domain.

M_s $= \rho dv/dt$ **[N/m3]**

E_s $= \rho v dv/dt$ **[W/m3]**

The above technique was recommended by Fluent for acceleration of an object in compressible fluids in external aerodynamic problems. Accelerating the entire flow field and keeping an object stationary is equivalent to accelerating the object in the opposite direction and keeping the fluid at infinity stationary. In other words, this technique achieves identical results to the moving reference frame technique, for acceleration.

In figure 2.11 the source term technique is applied to the case in figure 2.10. The pressure flood plot shows the flow field after 0.07 seconds. The same pressure range is used in both figures to facilitate comparison. It is clear from figure 2.11 that the flow field throughout the domain is uniform and the only disturbance occurs at the accelerating object. This flow field is more representative of the physical case of an object accelerating through a compressible fluid.

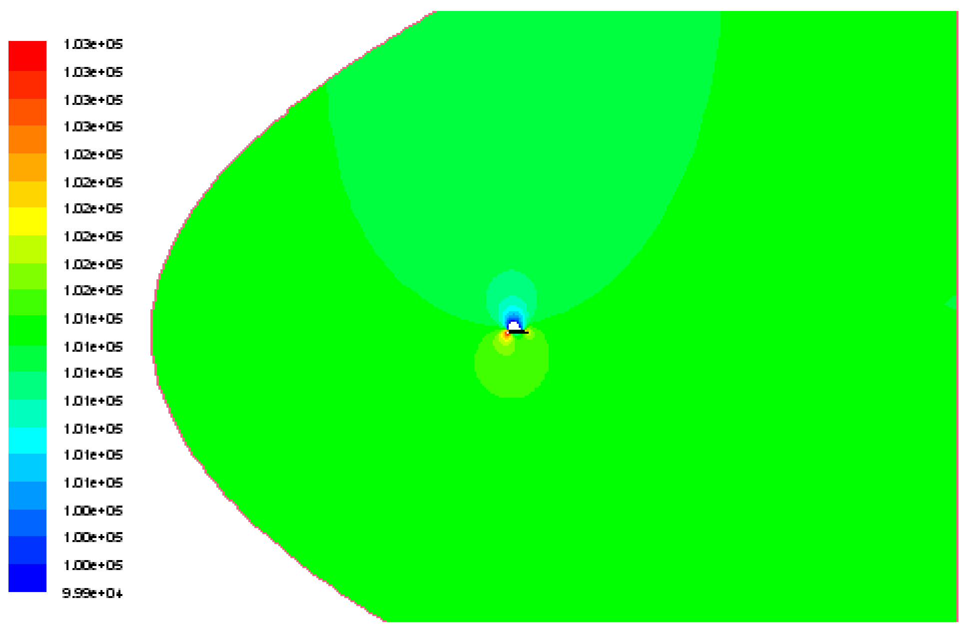

Figure 2.11: The case in figure 2.10 modified by accelerating the fluid at far field and using momentum and energy source terms to accelerate the fluid inside the meshed domain simultaneously with equal acceleration.

As a verification of the source term technique an empty meshed domain is subjected to an acceleration of 1041 m/s^2 (106g) using time steps of 0.001 seconds. As the acceleration is extremely high and the time steps are quite large for unsteady calculations, a type of worst-case scenario is created, which tests the reliability of the source term technique. Figure 2.12 shows the pressure flood plot for the empty domain after being subjected to the above conditions for 0.07 seconds (70 time steps). The uniform green colour represents a very narrow pressure range of 1.7 Pascal, which shows that despite the extreme conditions the flow field has remained at uniform pressure. A similar result was achieved with the same acceleration at transonic and supersonic velocities. This goes a long way to offer a numerical verification of the source term technique, as the flow field is accelerated by two very different mechanisms operating simultaneously and any discrepancy between the two would have resulted in an uneven pressure distribution.

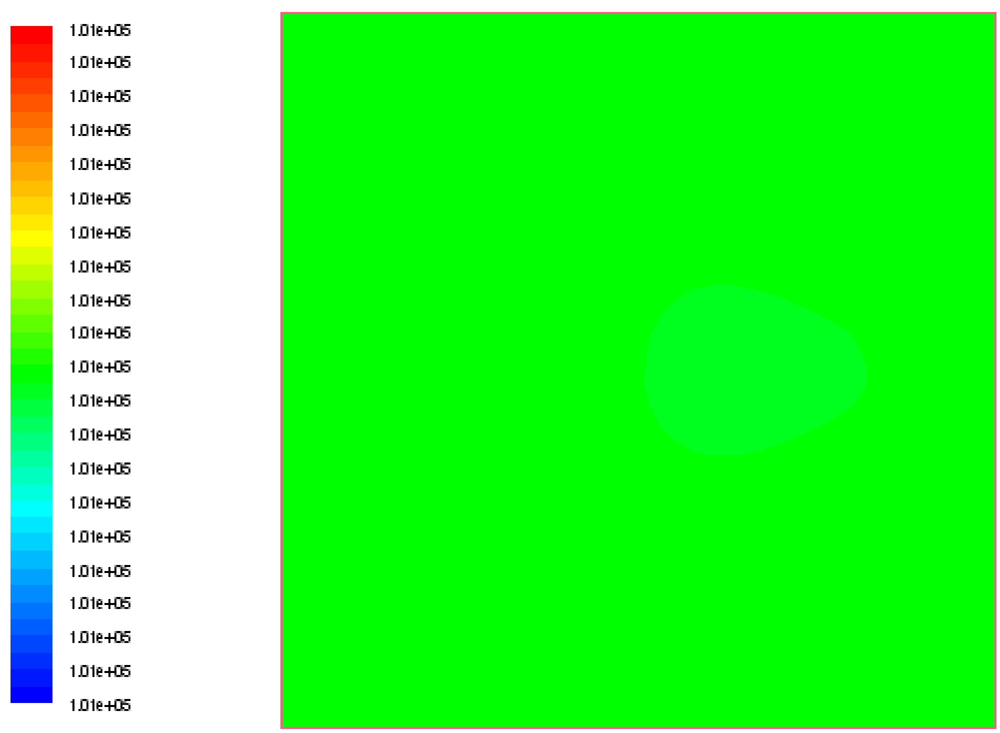

Figure 2.12: Verification of source term technique by showing uniform pressure distribution in an empty domain after 70 time steps. Acceleration = 1041 m/s^2.

It was also found that smaller time steps yield better results. For example the above cases were run with time steps of 0.0001 seconds. This reduced the pressure range across the domain to less than 0.1 Pascal. This case was also tested with different turbulence models and with Fluent's inviscid model with similar results.

2.3 Turbulence Models used in this research

The governing equations for this work are the Navier-Stokes equations, which are built into the Fluent source code (see Appendix B). Time-dependent solutions of the Navier-Stokes equations for high Reynolds-number turbulent flows, which set out to resolve all the way down to the smallest scales of the motions are unlikely to be attainable in the near future. Other techniques could be used so that the small-scale turbulent fluctuations do not have to be directly simulated. Reynolds-averaging is used here, which introduces additional terms in the governing equations that need to be modelled in order to achieve a "closure" for the unknowns. The Reynolds-averaged Navier-Stokes (RANS) equations govern the transport of the averaged flow quantities, with the whole range of the scales of turbulence being modelled. The RANS-based modelling approach therefore greatly reduces the required computational effort and resources. An entire hierarchy of closure models are available in Fluent [3], including Spalart-Allmaras, κ-ε and κ-ω, which are used in this investigation. The RANS equations are often used to compute time-dependent flows whose unsteadiness may be externally imposed, such as time-dependent boundary conditions or sources, which is applicable to this research.

The Spalart-Allmaras [3, 16] turbulence model is used most frequently in this investigation. It is a one-equation model that solves a modeled transport equation for the kinematic eddy (turbulent) viscosity. This embodies a relatively new class of one-equation models in which it is not necessary to calculate a length scale related to the local shear layer thickness. In Fluent, when the mesh is fine enough to resolve the laminar sub-layer, the wall shear stress is obtained from a laminar stress-strain relationship built into the Fluent source code. If the mesh is too coarse to resolve the laminar sub-layer, it is assumed that the centroid of the wall adjacent cell falls within the logarithmic region of the boundary layer, and the law-of-the-wall is employed [3]. The Spalart-Allmaras model was designed specifically for aerospace applications involving wall-bounded flows and has been shown to give good results for boundary layers subjected to adverse pressure gradients. The results obtained from the Spalart-Allmaras Model are compared with results from κ-ε and κ-ω as a form of numerical validation. In the subsonic range of Mach numbers, where the viscosity effects are insignificant in comparison with pressure effects, Fluent's invicid model is also used.

An attempt was also made to use large eddy simulations (LES) for this research. However this was abandoned, as a single simulation of an accelerating object was estimated to take years even on the most powerful computers available.

2.4 Defining viscosity as a function of temperature

When modelling problems that involve heat transfer, viscosity can be defined as a function of temperature by using the Sutherland law. In Fluent the formula is specified using two or three coefficients [3]. The Sutherland law with three coefficients is used here and has the form:

$$\mu = \mu_0 \, (T / T_0)^{3/2} \, (T_0 + S) / (T + S)$$

μ = Viscosity in kg/m-s

T = Static temperature in K

μ_0 = Reference value in kg/m-s

T_0 = Reference temperature in K

S = an effective temperature in Kelvin (Sutherland constant)

For air at moderate temperatures and pressures, $\mu_0 = 1.176*10^{-5}$ kg/ms, T_0 = 273.11 K and S = 110.56 K.

3. Validation of computational models

In order to validate the numerical modelling techniques used in this investigation, initially the steady state data is validated against experimental results. This confirms the integrity of the numerical code. As no reference to any suitable experimental facility for validating the unsteady results of this investigation was found in literature, these are validated numerically. However, as part of an on going research, efforts have been made to develop such a facility at the University of the Witwatersrand. A brief description of one such project is given at the end of this chapter.

3.1 Steady state validations against experimental results

In this section a steady state validation supplied by Fluent© is discussed briefly. Then in a number of additional cases, steady state numerical data produced by the author is compared to experimental results from literature.

3.1.1 Validation from Fluent

In appendix C a comprehensive validation from Fluent© is included, which tests various aspects of the code against experimental data. This remains the cornerstone of any validation of the code regarding external aerodynamic problems.

Steady state simulations using two different meshes and three turbulence models were conducted on a RAE 2822 transonic aerofoil. The meshes were a quadrilateral mesh with 126000 cells and a hybrid mesh of 35000 cells. The turbulence models were the Spalart-Allmaras the Realizable κ-ε and SST κ-ω. The pressure distribution on both surfaces of the aerofoil, the shock position and the lift and drag were compared with experimental data in all cases. The Spalart-Allmaras and Realizable κ-ε turbulence models gave the exact position for the shockwave and the Spalart-Allmaras turbulence model gave the best overall results. The results were found to be mesh-independent.

Based on this experimental validation supplied by Fluent© it was decided to choose the Spalart-Allmaras as the main turbulence model for this investigation. It must be noted that as the main focus of this research is transonic shockwave dynamics and the Spalart-Allmaras turbulence model is suited to the prediction of transonic shockwave position it becomes especially suitable for this research. The results obtained were, however, often confirmed against Realizable κ-ε and κ-ω.

3.1.2 Aerofoil lift validation at various angles of attack

Another aspect of this research was the study of the subsonic effects of acceleration in comparison with the steady state condition. Of particular interest was the effect of acceleration on lift and drag. Although Validation 11 in appendix C is sufficient for confirming the lift and drag prediction capabilities of Fluent, there was a need to ascertain Fluent's ability to predict the angle of separation.

Figure 3.1 compares values of lift coefficient versus angle of attack, for the NACA0012 aerofoil obtained through Fluent, with experimental results from Abbot [6]. The mesh from Fluent tutorial 3 is used for obtaining the numerical values. The top right hand portion of the experimental curve is matched with results from Fluent.

Fluent matches closely the points on the experimental curve and predicts the angle at which separation takes place to the nearest degree. It even gives the correct lift value at 20^0, which is an angle at which separation has already taken place.

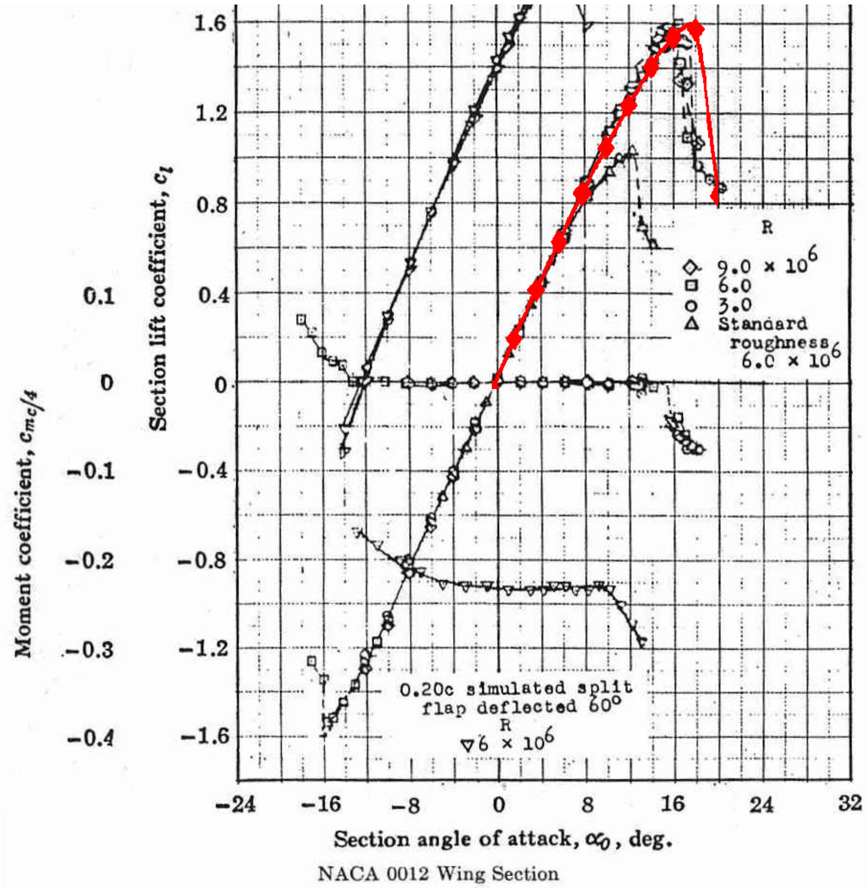

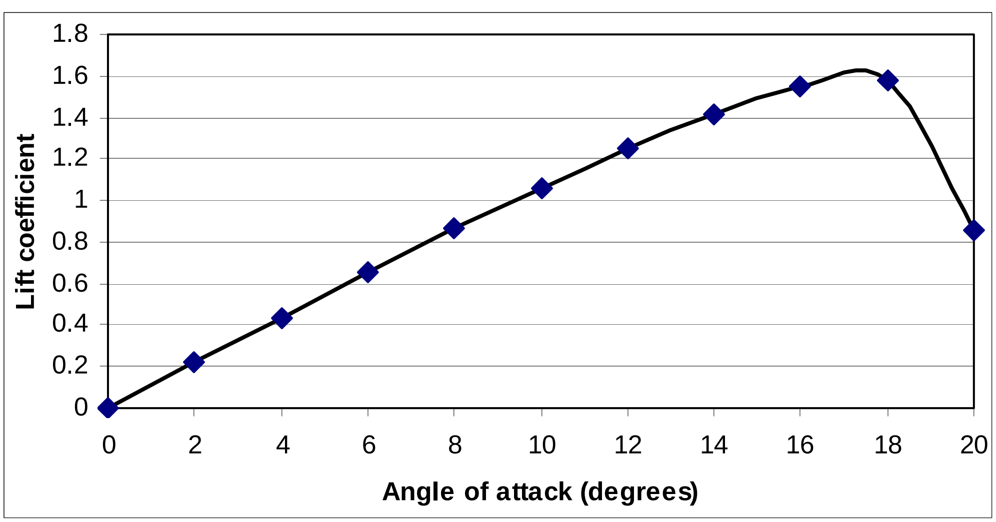

Figure 3.1: Lift coefficient versus angle of attack for NACA0012 aerofoil. The numerical results from Fluent are plotted at the bottom. At the top they are plotted in red, on the same set of axes as experimental results from Abbot [6].

3.1.3 Validation for some of the cases used in this investigation

In this section certain cases examined in this investigation are validated. This is done by comparing steady state simulations, performed on the meshed models from those cases, with experimental data. As a result two important things are achieved. The first is a confirmation of the integrity of the results produced by the specific model in question. The second is a further validation of Fluent as a code and its ability to model those specific cases.

In figure 3.2 the values of lift coefficient versus angle of attack for the NACA2412 aerofoil, obtained through Fluent at Mach 0.3, is compared with experimental results from Abbot [6]. The mesh used with this model was relatively coarse but was specially designed to have the correct Wall Yplus values for the range of Mach numbers used in this research. The values of Wall Yplus are dependent on the resolution of the grid and the Reynolds number of the flow, and are defined only in wall-adjacent cells. The values of Wall Yplus in the wall-adjacent cells dictate how wall shear stress is calculated. According to Fluent [3] the grid should be modified so that ideally these values are smaller than +1 or greater than +30. For definition of Wall Yplus refer to appendix B. In figure 3.2 the numerical values of lift coefficient match experimental results at high Reynolds numbers ($9x10^6$, see legend in figure 3.1) and the separation angle is predicted to within one degree. This aerofoil, with the above mesh, will be used to investigate unsteady effects at low subsonic Mach numbers and to study the effect of acceleration on the angle of separation.

In figure 3.3 spark shadowgraphs of an artillery shell produced by experiment, from Van Dyke [7], are compared with density contour plots produced by Fluent at Mach 0.946 and 0.978. The meshed model is the same as the one used in this research for studying acceleration effects on axisymmetric objects. Fluent matches the shock wave pattern and the shape of the wake produced by experiment.

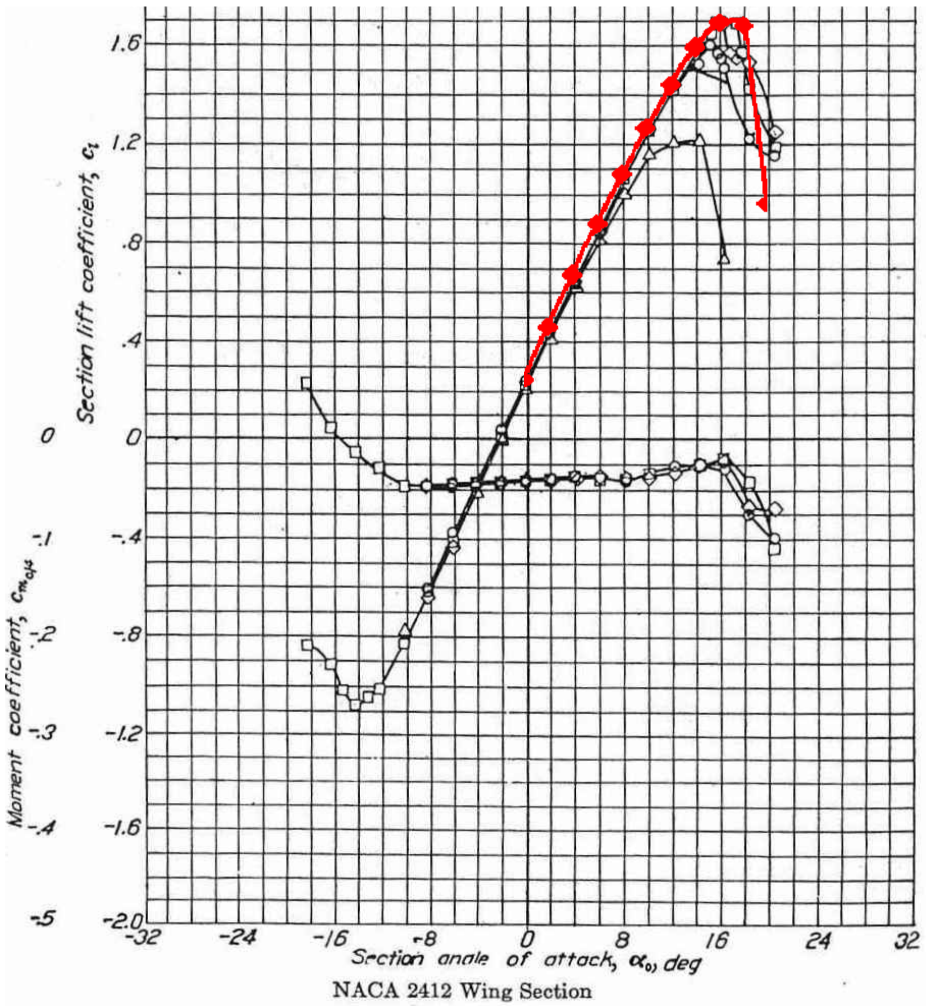

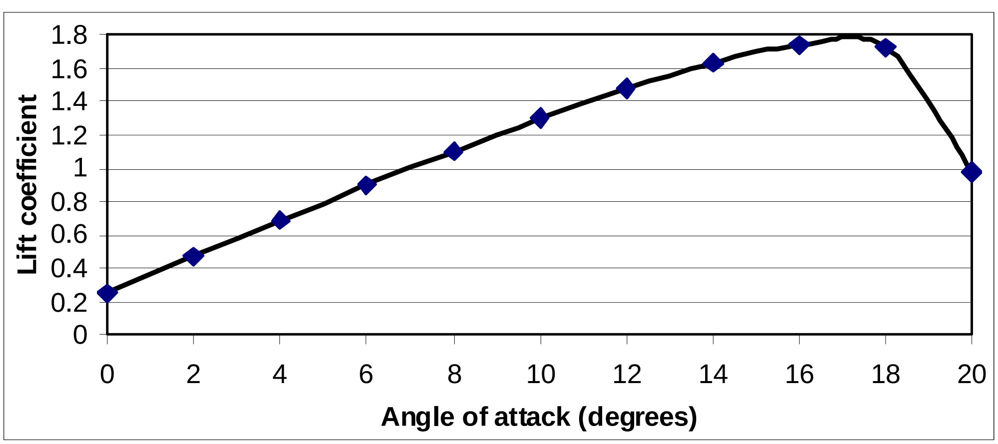

Figure 3.2: Lift coefficient versus angle of attack for NACA2412 aerofoil. The numerical results from Fluent are plotted at the bottom. At the top they are plotted in red, on the same set of axes as experimental results from Abbot [6].

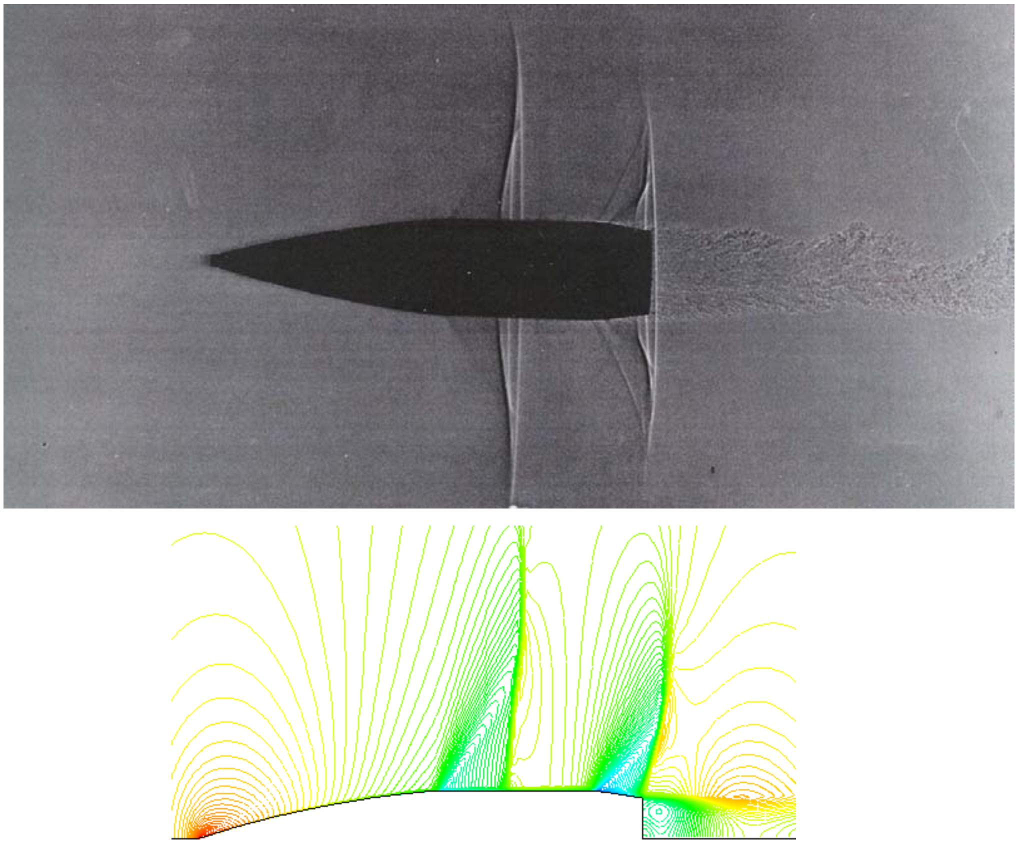

(a) Mach 0.946

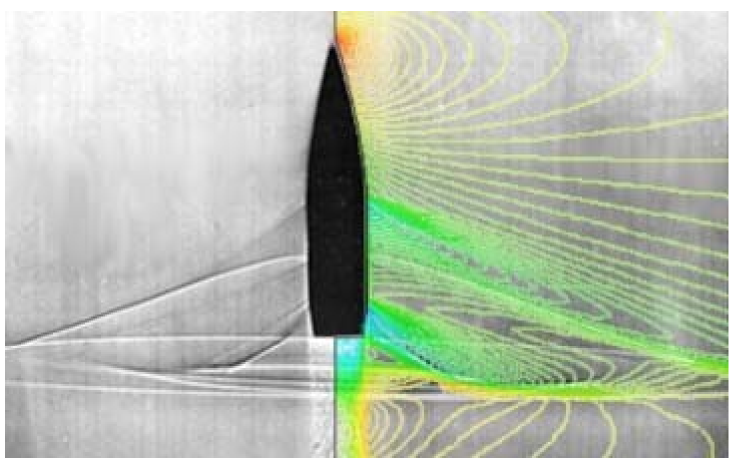

(b) Mach 0.978

Figure 3.3: Comparison of spark shadowgraph produced by experiment, from Van Dyke [7], with density contour plot produced by Fluent at Mach 0.946 and 0.978. In part (b) the two images have been rotated and superimposed for better comparison.

Figure 3.4 compares values of the drag coefficient of a large sphere, produced by Fluent, with experimental results from Hoerner [5]. A 1 m diameter sphere is used in order to ensure Reynolds numbers above transition for the entire range of Mach numbers. This meshed model is used in this investigation in a preliminary study of the effects of acceleration on sphere aerodynamics at subsonic Mach numbers. It must be noted that sphere aerodynamics is complex and a detailed study of the aerodynamic effects of acceleration on spheres is beyond the scope of this work. Here it is chosen as an example of a bluff body and the effect of acceleration on sphere drag in subsonic Mach numbers is broadly investigated. The values of steady state drag coefficient produced here correlate well with experiment.

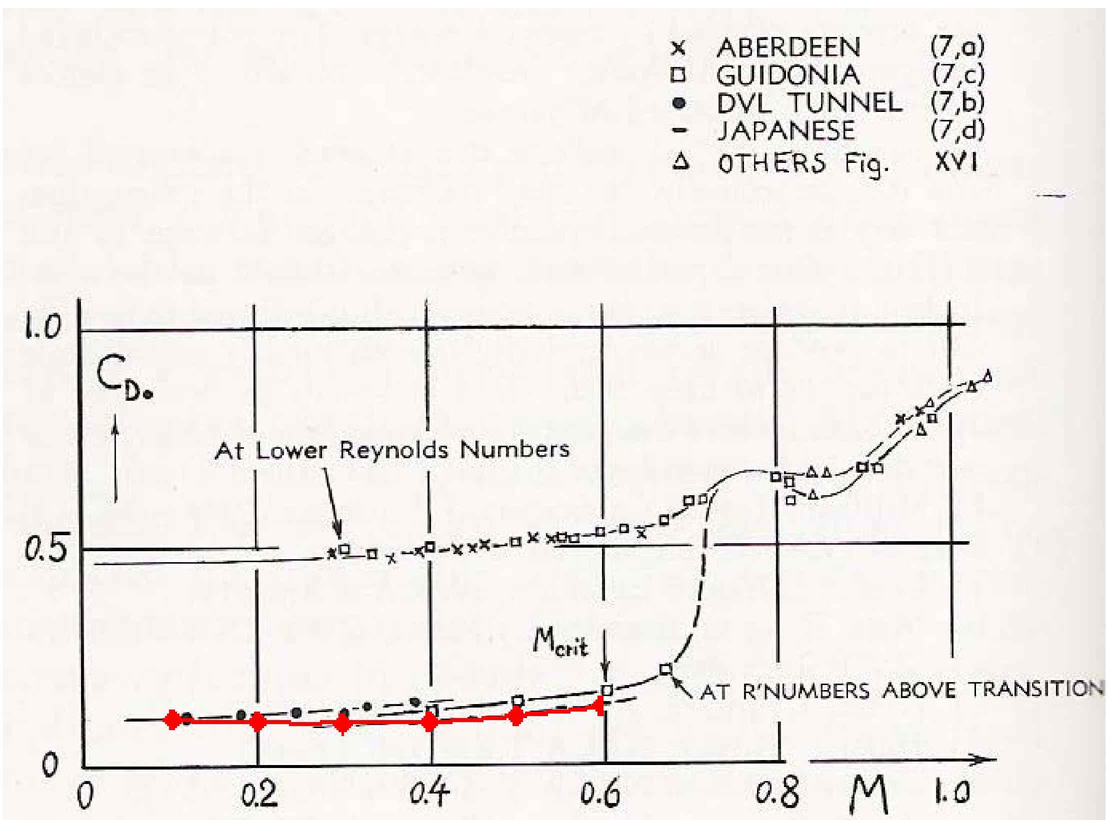

(a) Experimental results with numerical values plotted in red for comparison.

Figure 3.4: Comparison of values of a sphere drag coefficient, produced by Fluent for Reynolds numbers above transition, with experimental results from Hoerner [5].

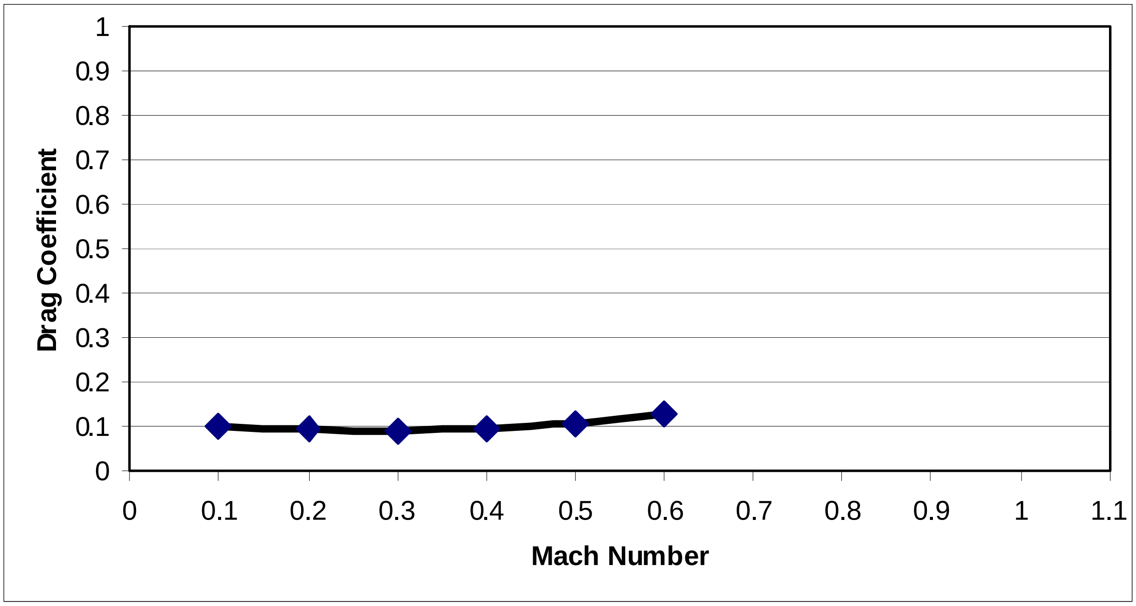

(b) Numerical values.

Figure 3.4: Continued.

3.2 Mesh convergence and mesh independence

3.2.1 Biconvex aerofoil

Two journal articles have been published, which were direct results of the research conducted for this thesis, and are listed at the beginning of this document. Both these used the biconvex aerofoil to demonstrate the aerodynamic effects of acceleration. As such this work has already been reviewed and provides a good point of departure for additional analysis. Therefore, the first aerofoil that is discussed in both the central chapters of this thesis is the biconvex aerofoil.

An important aspect of the work done for the abovementioned publications was that some of the steady and unsteady results for the biconvex aerofoil were run with finer meshes in order to ensure mesh independence. The mesh used had 80,000 hexahedral cells with 200 nodes on each face of the aerofoil. Finer meshes, with 210,000 hexahedral cells and 500 nodes and 360,000 hexahedral cells and 1,000 nodes were then examined. In the first case the shock wave position changed by 0.8% of the cord length and in the second a further 0.2%, which indicated mesh convergence. The percentage differences in lift, drag and pitching moment were similar.

As a maximum difference of 1% was observed with a much finer mesh and mesh convergence was achieved, the results were considered to be mesh independent.

3.2.2 RAE 2822 aerofoil

Validation 11 in appendix C includes a mesh independence study. Results from a quadrilateral mesh are compared with those from a hybrid mesh and they are shown to be almost identical. As these results are also validated against experiment the integrity of the meshed models is firmly established. This is especially true of the quadrilateral mesh, which is the finer of the two meshes and gives better resolution.

As the RAE 2822 is also a more practical aerofoil than the biconvex, and is suited to investigating transonic shock wave behaviour, it was decided to confirm the results obtained from the biconvex aerofoil with the RAE 2822 of validation 11. The meshed models were obtained from Fluent [3] and the second case study in chapters 4 and 5 make use of the RAE 2822 with the quadrilateral mesh. As the unsteady results from the biconvex aerofoil is confirmed by a different aerofoil, with a model that is mesh independent and validated against experiment, this provides confidence in the validity of these findings.

3.3 Significance of viscosity in investigating transonic shock wave dynamics

Although it is a known fact, that due to the effect of shock wave boundary layer interaction, the position of transonic shocks is influenced by viscosity, some authors have attempted to analyse transonic aerodynamic problems numerically by using inviscid codes [9]. The main reason for this is the perception that viscosity effects are second order and do not have a significant effect at transonic Mach numbers. However, although the viscous components of lift and drag form a small portion of the overall effect in transonic aerodynamics, shock wave boundary layer interaction can affect transonic flows significantly. This can best be demonstrated by some examples.

In figure 3.5 the static pressure versus position, at the top surface of the RAE 2822 aerofoil at Mach 0.73 and angle of attack of 2.79^0, for the viscous and inviscid cases is compared. The information for the viscous case is obtained from the validation in appendix C and matches experimental results. The inviscid code used here is Fluent inviscid and the error in the non-viscous position for the shock wave is 12% of the cord length. The viscous lift coefficient is 0.815 and the inviscid value is 1.0315, which constitutes an error of over 25%. In figure 3.6 a comparison is made between the viscous and inviscid cases for the RAE2822 aerofoil at Mach 0.85 under atmospheric conditions. The pressure contour plots and top surface pressure versus position are used to illustrate the differences. The discrepancy in the position of the shock wave is almost 40% of the cord length. As the viscous code is validated against experiment this discredits the inviscid code for analysis of transonic shock wave dynamics. From the contour plot it can also be observed that when viscosity is not taken into account the position and strength of the shock wave at the bottom surface of the aerofoil is also seriously affected.

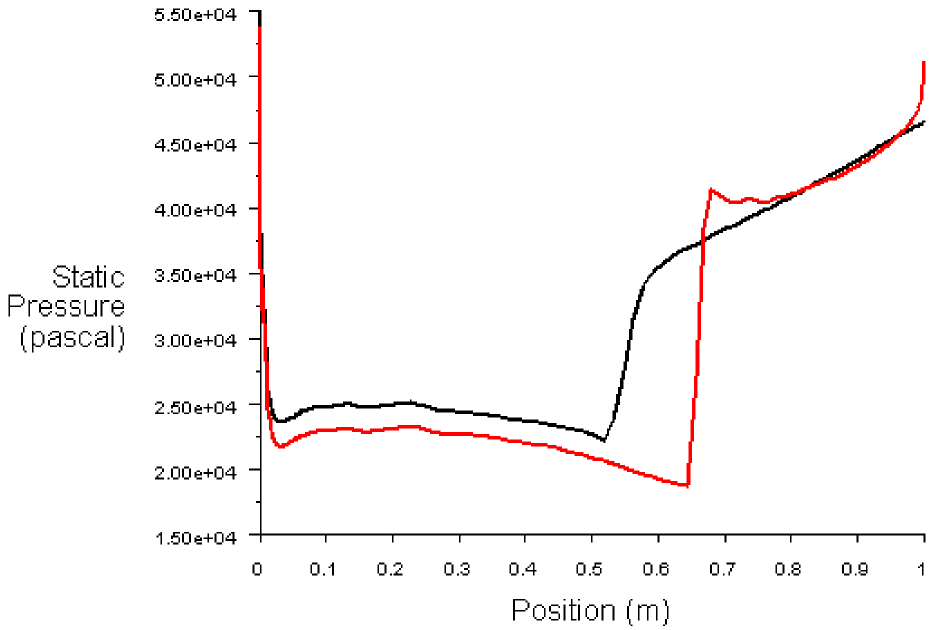

Figure 3.5: Comparison of top surface pressure versus position between the viscous (black) and inviscid (red) cases for the RAE2822 aerofoil at Mach 0.73 and 2.79^0.

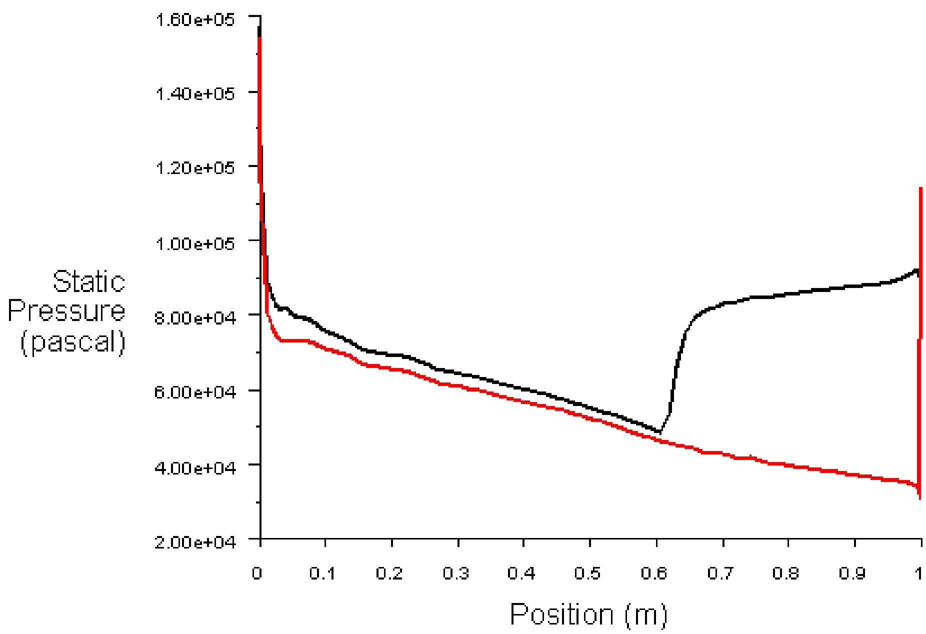

(a) Top surface pressure verses position.

Figure 3.6: Comparison of top surface pressure versus position and pressure contour plots between the viscous (black) and inviscid (red) cases, for the RAE 2822 aerofoil at Mach 0.85 and 2.79^0, under atmospheric conditions of 101325 Pa and 300K.

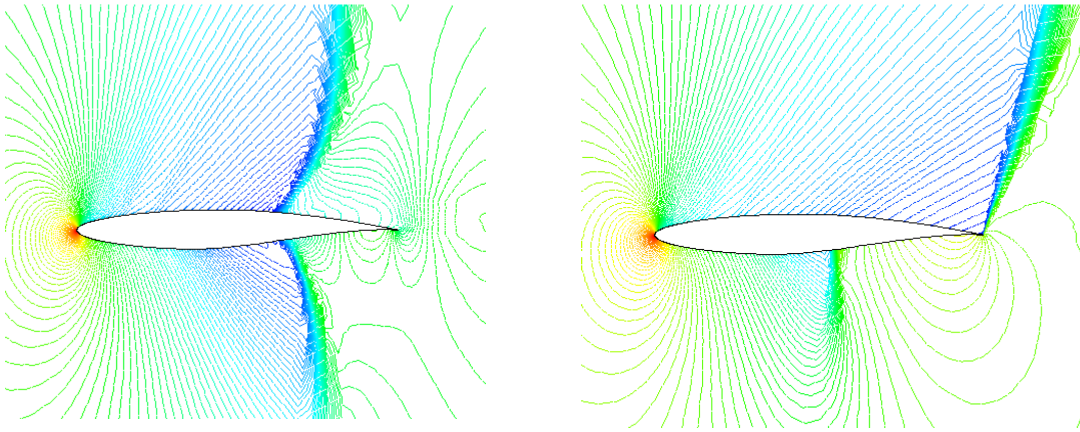

(b) The left contour plot represents the viscous case and the right the inviscid.

Figure 3.6: Continued.

The University of the Witwatersrand has an Euler based inviscid code, which was written by LT Felthun [10] and can model acceleration of objects in compressible fluids. It will be demonstrated in the next section that even at high accelerations this university in-house code correlates well with the inviscid version of Fluent. Although not shown here, these codes correlate fairly well even in the transonic range of Mach numbers, where they show a large discrepancy with the viscous results. Therefore, although Felthun's code may be suitable for subsonic and supersonic flow analysis it will also have to be considered unsuitable for investigations involving transonic shock wave dynamics. It is for such reasons that viscous models in general and the Spalart-Allmaras turbulence model in particular were used in this research.

3.4 Numerical validation of the unsteady modelling

The unsteady technique used to model the acceleration of an object in a stationary compressible fluid is discussed in chapter 2. This accelerates the fluid at the boundary of the meshed domain and the fluid in every cell inside the boundary simultaneously while keeping the object stationary. It is a technique recommended by Fluent and needs to be validated.

3.4.1 In-house code versus Fluent

A numerical validation of the above technique is achieved by comparing unsteady results from the inviscid version of Fluent with those obtained from Felthun's code [10]. As both these codes are inviscid any discrepancy resulting from viscosity effects is eliminated and any differences will reflect errors in the unsteady modelling techniques.

Felthun's code has one distinct advantage, which makes it suitable for this validation exercise. It is designed to move the object in a stationary fluid, which is a direct representation of the physical situation being modelled. A domain is created, which is large enough to enable the object to reach the desired final velocity with a given constant acceleration. Then an unsteady time-dependant simulation is conducted and the data is saved at every time step while the object is accelerated through a certain range of Mach numbers. A triangular adaptive mesh is used, which intensifies around the object especially in areas with the largest density gradient.

In the validation a diamond shaped (double wedge) aerofoil with cord length of 1m and a maximum thickness of 0.1 m is used. It is accelerated at 1041m/s^2 (106g) through Mach 0.1 to 1.6 with an angle of attack of 4 degrees. The air is at atmospheric pressure and the ambient temperature is 300 K.

In figures 3.7 to 3.9 density flood plots from the two codes are compared at Mach 1.6, 1.0 and 0.7. At each Mach number the density range is kept the same for the two codes.

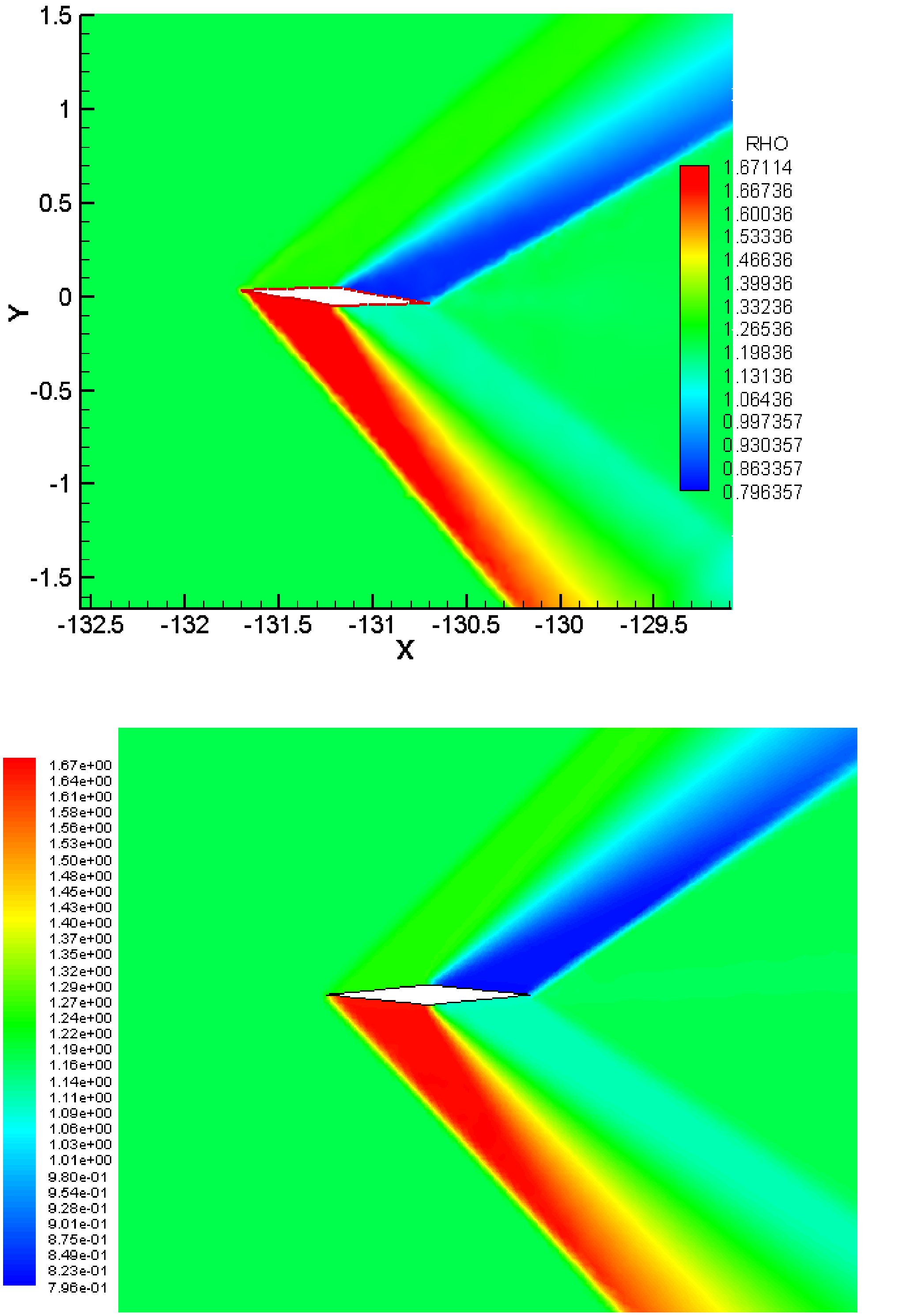

Figure 3.7: Comparison between inviscid density flood plots, at Mach 1.6 and an acceleration of 106g, from Fluent and Wits University's in-house code.

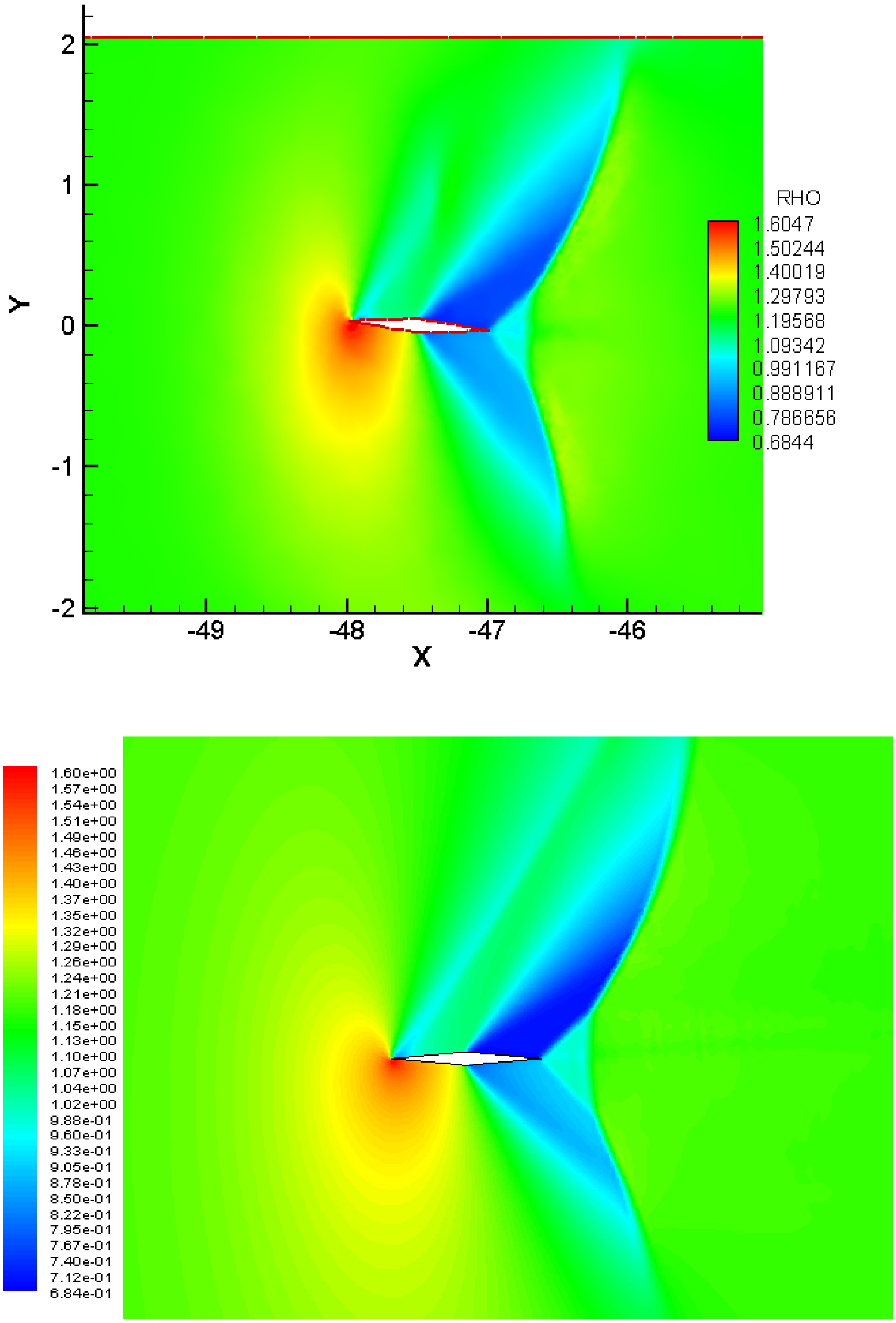

Figure 3.8: Comparison between inviscid density flood plots, at Mach 1.0 and acceleration of 106g, from Fluent and Wits University's in-house code.

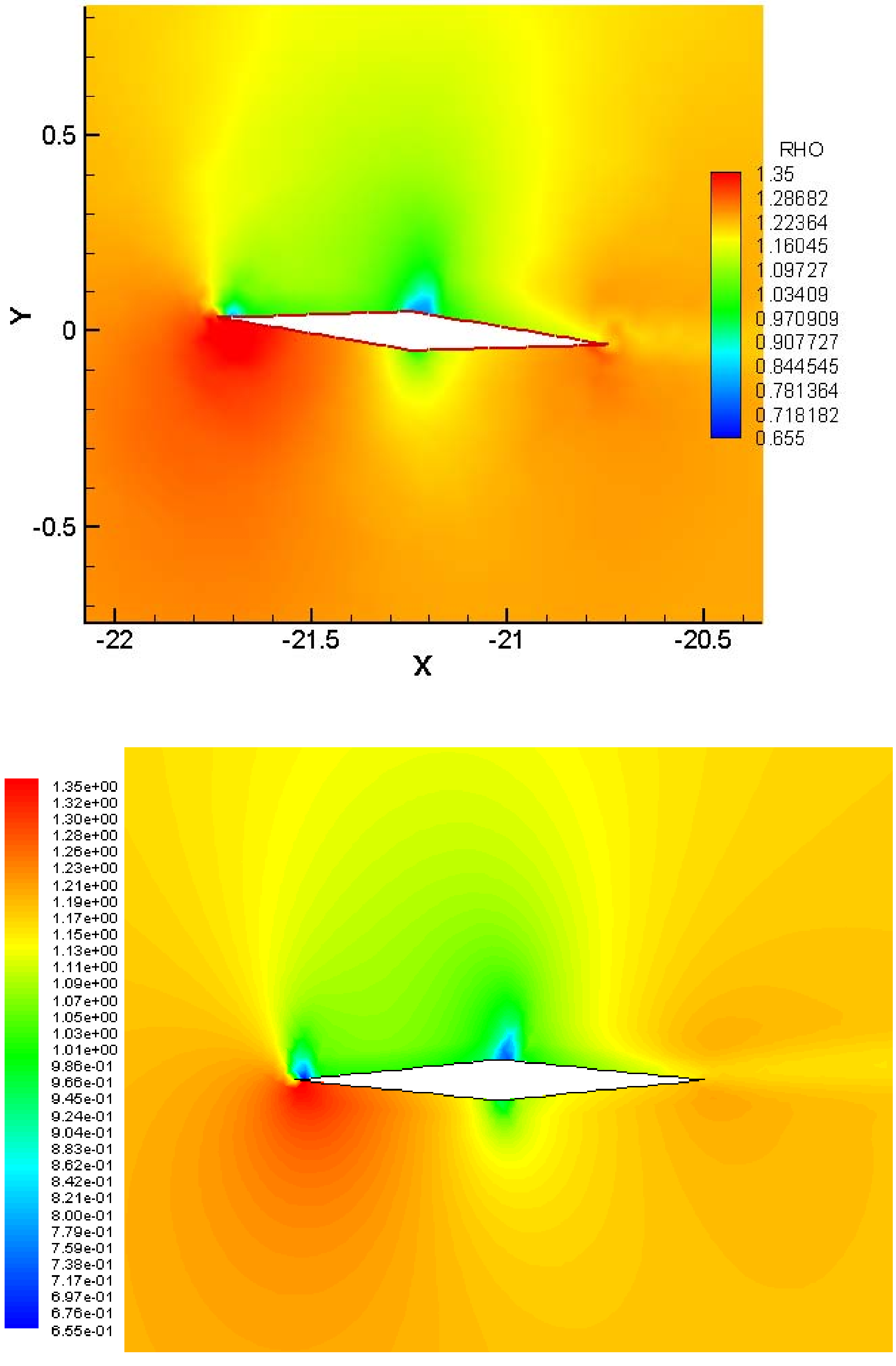

Figure 3.9: Comparison between inviscid density flood plots, at Mach 0.70 and acceleration of 106g, from Fluent and Wits University's in-house code.

Note that Felthun's code shows that the aerofoil has turned through the prescribed angle, whereas Fluent keeps the aerofoil horizontal irrespective of angle of attack, with the required flow field modelled by changing the direction at which air blows at the aerofoil. Comparison between the two codes in each case shows that in spite of the intensely high acceleration of 106g, which would normally magnify the slightest discrepancy, there is a good correlation between the two numerical models.

These codes operate on completely different principles. Felthun's code accelerates the object in a stationary fluid and the only movement of the fluid stems from the moving object, whereas Fluent achieves the same effect by keeping the object stationary and accelerating every fluid particle with equal magnitude but opposite direction to the desired acceleration. As these codes correlate well, this confirms the integrity of the technique used by Fluent.

3.4.2 Validation of unsteady shockwave dynamics

In order to numerically validate the unsteady transonic results obtained from the Spalart-Allmaras turbulence model, the Realizable κ-ε and SST κ-ω turbulence models within Fluent were used. The idea was that as these models correlated well under steady state conditions in validation 11 any discrepancy would be attributed to the unsteady modelling technique.

In figure 3.10 pressure contour plots of the Spalart–Allmaras, κ-ε and κ-ω, at Mach 0.89 and acceleration of 1041 m/s^2 (106g) are compared. The RAE 2822 aerofoil with the quadrilateral mesh of validation 11 in appendix C is used for this study. The results show that in spite of the very high acceleration of 106g and the usual sensitivity of shock waves to any errors in numerical modeling, there is a good correlation between the three cases. This confirms the integrity of the unsteady modeling technique and its suitability for studying unsteady shock wave dynamics.

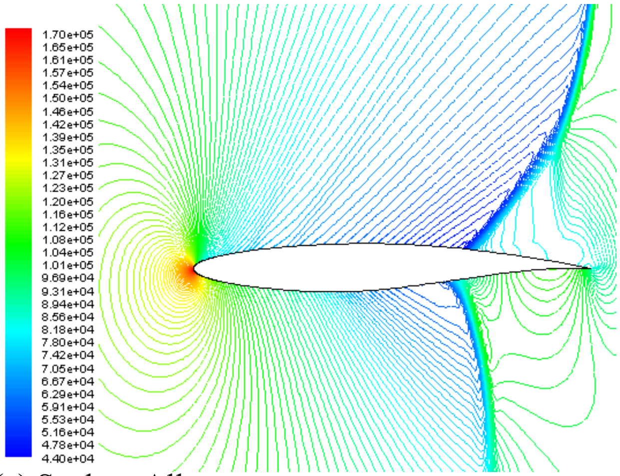

(a) Spalart–Allmaras

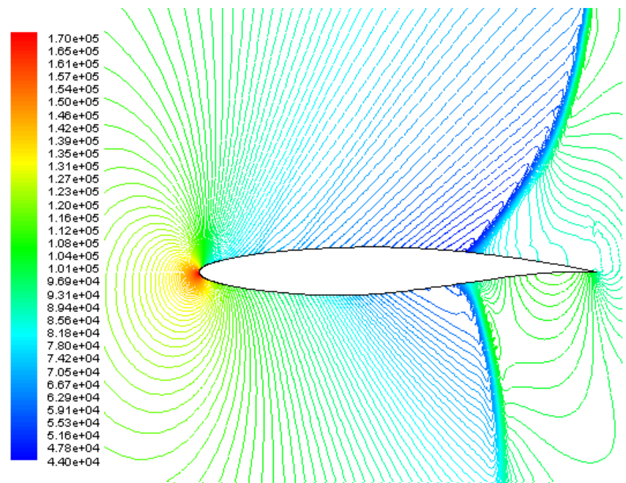

(b) κ-ε

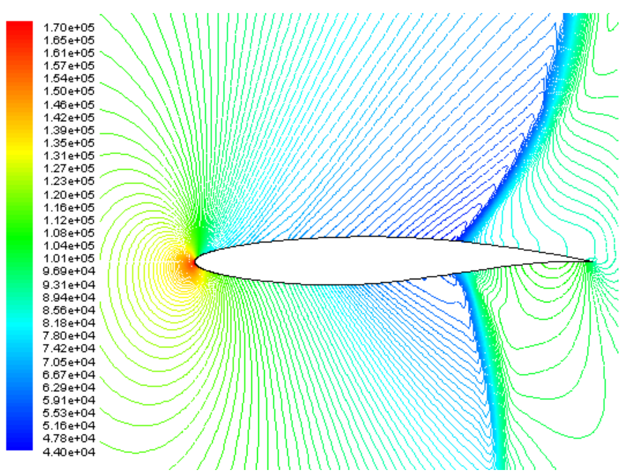

(c) κ-ω

Figure 3.10: Comparison of pressure contour plots of the Spalart–Allmaras, κ-ε and κ-ω at Mach 0.89 and acceleration of 1041 m/s^2 (106g), using a quadrilateral mesh.

In chapters 4 and 5 the RAE 2822 with the quadrilateral mesh of validation 11 in appendix C is used to confirm the results from other aerofoils. In order to ensure that the RAE 2822 unsteady results discussed in those chapters are mesh independent a study was conducted, which is summarized in Figure 3.11. Pressure contour plots of the quadrilateral mesh and the hybrid mesh at an acceleration of 1041m/s^2 (106g) and Mach 0.89 are compared and the results are found to correlate very well. This confirms mesh independence of these results under the unsteady conditions brought about by acceleration.

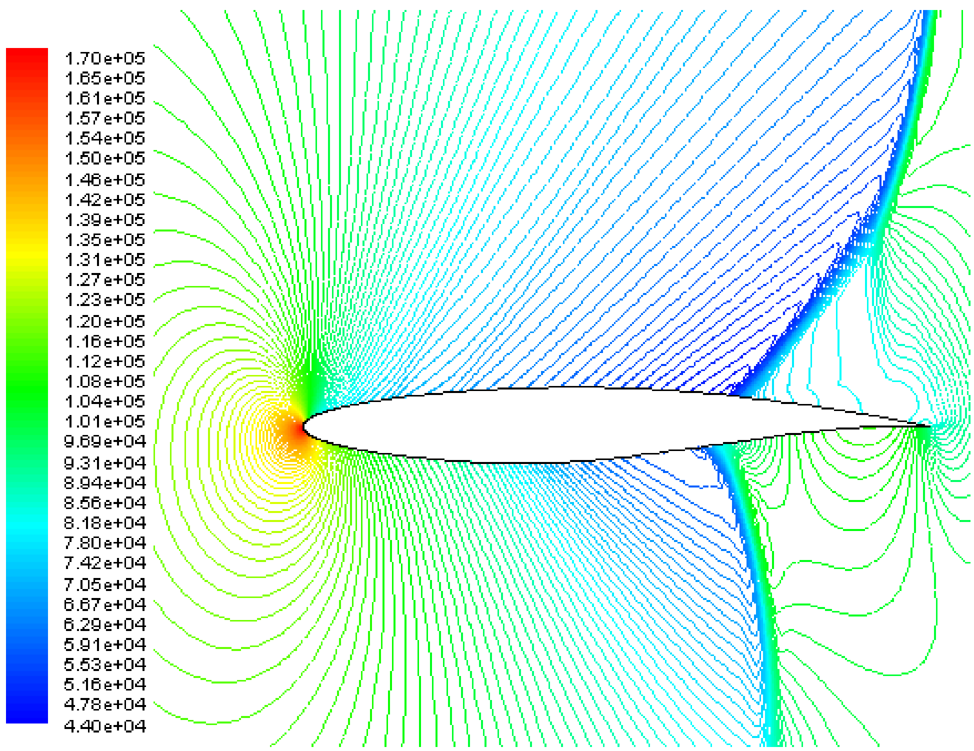

(a) Quadrilateral mesh

Figure 3.11: Mesh independence shown by comparing pressure contour plots of the quadrilateral mesh (126000 cells) and the hybrid mesh (35000 cells) at 106g and Mach 0.89.

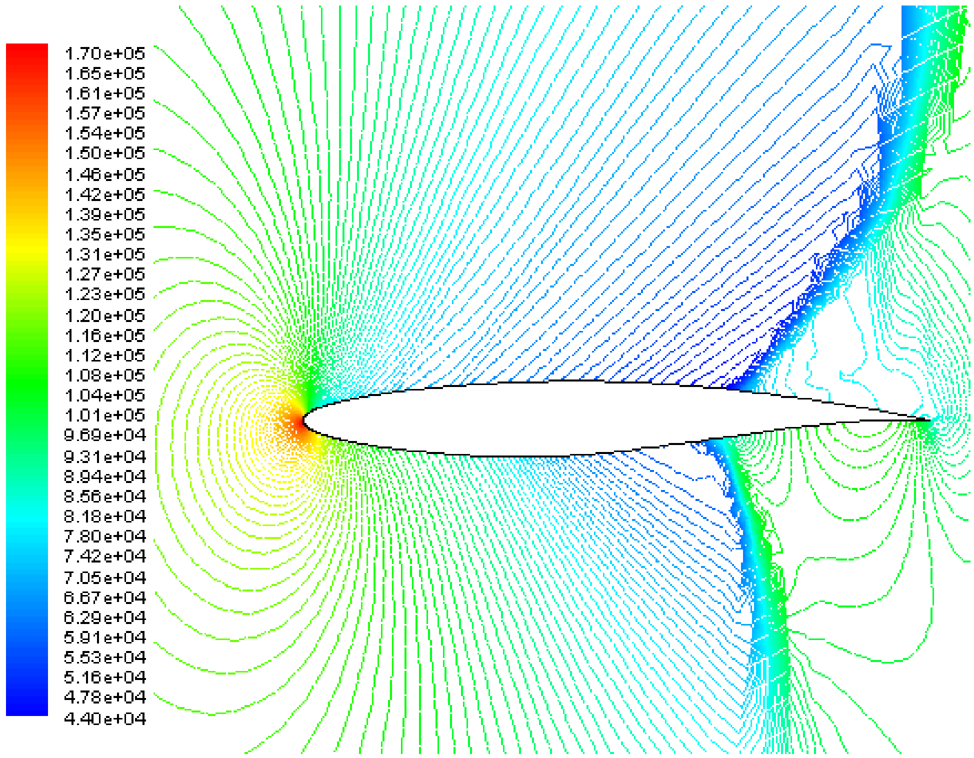

(b) Hybrid mesh

Figure 3.11: Continued

3.5 Experimental validation of unsteady results

As mentioned earlier no reference to any suitable experimental facility for validating the unsteady results of this investigation was found in literature.

In chapter 2 it is explained that, in standard wind tunnel tests either the speed of the fan or the system resistance would have to be changed gradually in order to model flow acceleration. As a result a pressure gradient is created along the length of the wind tunnel, which is unlike the physical situation being modelled. This would introduce general errors into the flow field at all Mach numbers and under transonic conditions it would affect the position of the shock wave.

It is therefore necessary to design a rig, which would accelerate the test specimen in stationary air. However, since only low velocity applications of this type of test rig were found in literature [43, 44], it became necessary to develop an in-house version of the rig.

Under the supervision of the author, two final year undergraduate students have developed preliminary designs for an experimental facility for the acceleration of a test specimen in stationary air. The design uses a magnetic rail gun, which propels the specimen forward along a 50 m track at very high accelerations. The facility is designed to accelerate the specimen to Mach 1.2 with a maximum acceleration of over 2000 m/s^2.

4. Transient aerodynamic forces

In the following two chapters the main contributions in this research are discussed. This chapter focuses on the transient aerodynamic forces resulting from acceleration and retardation. It shows that when an object is accelerated in air, the unsteady aerodynamic forces and moments experienced by the object at any instantaneous Mach number are different to those at the same Mach number under steady state conditions, when it moves at constant velocity.

In order to claim credit for some of the novelties of this research some findings were presented at conferences and two journal articles were published before the submission of the final doctoral thesis. Details of these are given at the beginning of this document. The publication in the Journal of Aerospace Engineering is of particular interest for the discussion in this chapter. It uses a biconvex aerofoil to demonstrate the aerodynamic effects of acceleration. This chapter starts with a more in depth study of that material. Then, in order to confirm and further develop those findings, the RAE 2822 aerofoil modeled by Fluent for validation 11, is used.

In validation 11 appendix C, steady state results from the quadrilateral meshed model of RAE 2822 were validated against experiment and were also found to be mesh independent. In chapter 3 the unsteady results from the same model were also validated numerically by comparing different turbulence models and were checked for mesh independence. Therefore, confirmation of the general biconvex aerofoil results by this model provides confidence in the findings of this chapter.

A study of acceleration effects at varying angles of attack is also included. Finally the effect of acceleration on axisymmetric bodies is investigated.

4.1 Subsonic and transonic acceleration of airfoils

The main two airfoils used in this investigation were a supersonic biconvex aerofoil and the RAE 2822 transonic aerofoil with the quadrilateral mesh from validation 11 of appendix C. Both had cord lengths of 1m and the biconvex had a maximum thickness of 0.1 m. Initially, particularly high accelerations 106g and −106g were chosen to enhance the differences between the steady and accelerating scenarios. However, as these accelerations may only be realistic in applications such as missile aerodynamics, accelerations lower than 9g, which occur in military aircrafts, were also looked at.

The airfoils were subjected to the following conditions:

Free-stream temperature:	300 K
Atmospheric pressure:	101 325 Pa
Accelerations:	1041 m/s^2 (106g) and 86.77 m/s^2 (8.845g)
Decelerations:	−1041 m/s^2 and −86.77 m/s^2
Angles of attack:	4 degrees for biconvex, 2.79 degrees for RAE 2822

Steady state, constant velocity, simulations were conducted at Mach numbers ranging from 0.1 to 1.6. Then, starting at Mach 0.1, the airfoils were subjected to accelerations of 1041 m/s^2 and 86.77 m/s^2 through the same range of Mach numbers. Finally, starting at Mach 1.6, they were decelerated at −1041 m/s^2 and −86.77 m/s^2 down to Mach 0.1.

Graphs of drag, lift, and pitching moment versus Mach number were plotted, and the steady and the unsteady graphs were plotted on the same set of axes. Forces and moments were not non-dimensionalized in order to avoid ambiguity in choosing an arbitrary reference velocity. Moments for the biconvex were taken at half-cord and for the RAE 2822 at a quarter-cord from the leading edge of the aerofoil.

4.1.1 Biconvex drag at high accelerations

Figures 4.1 to 4.3 show the steady and unsteady drag variation with Mach number at acceleration 1041 m/s^2 (106g) and deceleration of -1041 m/s^2 (-106g) for the biconvex aerofoil. Figure 4.1 shows the drag variation over the entire range of Mach numbers (0.1-1.6). However, over this range, the differences between the steady and the unsteady drag curves, in the subsonic region, is not clearly visible. Therefore, in Figures 4.2 and 4.3 the subsonic and transonic portions of the graph are plotted in order to improve clarity. It is clear from figure 4.2 that for subsonic Mach numbers, acceleration brings about drag forces which are higher than the steady state drag and deceleration of the aerofoil results in drag forces that are lower than the steady-state drag. However, in the transonic region of figure 4.3 this situation reverses back and forth several times and does not appear to follow any consistent pattern.

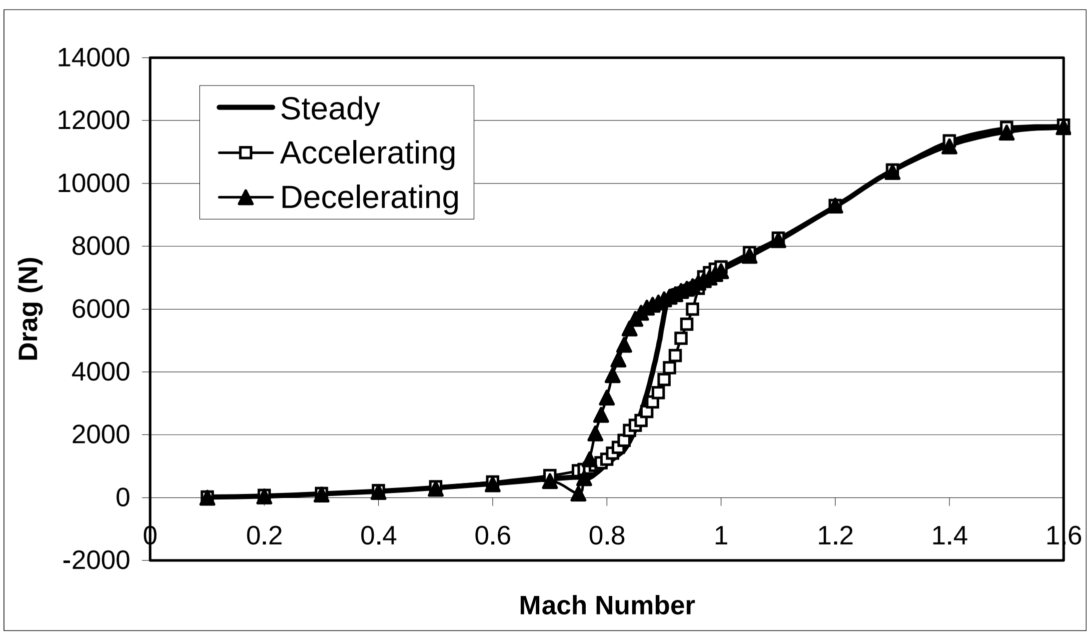

Figure 4.1: Biconvex drag at steady, +106g and –106g.

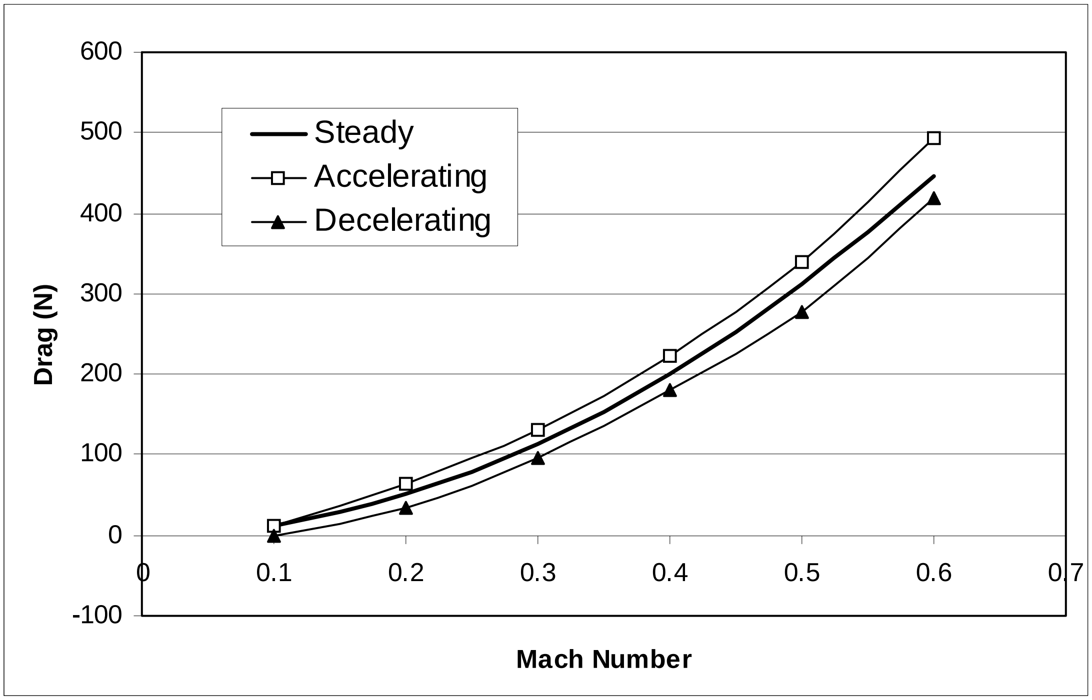

Figure 4.2: Subsonic biconvex drag at steady, +106g and –106g.

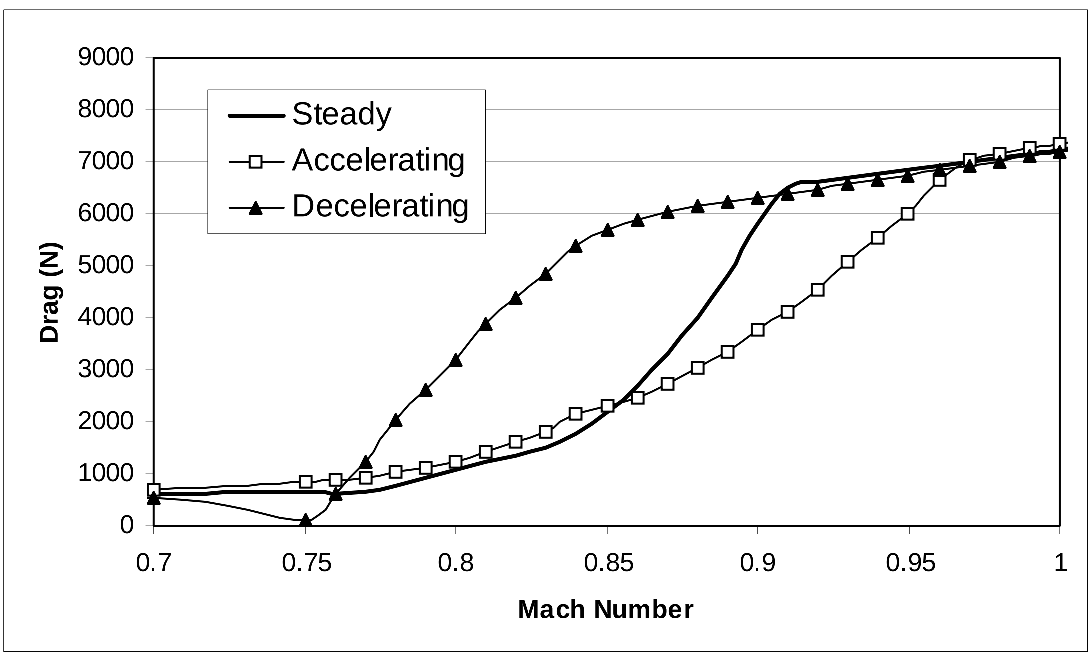

Figure 4.3: Transonic biconvex drag at steady, +106g and –106g.

4.1.2 Biconvex lift at high accelerations

Figure 4.4 shows the lift variation with Mach number for the steady and the unsteady cases over the entire range of Mach numbers (0.1-1.6) with high accelerations of 106g and –106g. In Figure 4.5 and 4.6 the subsonic and transonic portions of the lift curves are plotted for clarity. In the subsonic region acceleration results in lower lift and deceleration results in higher lift than the corresponding steady state lift values. This is opposite to the effects found when studying drag. However, in the transonic range of Mach numbers shown in figure 4.6, sudden changes in the lift forces are observed and the unsteady lift values fluctuate above and below the steady-state values. The apparently disorderly behaviour of the unsteady data was also observed with drag. However, in the case of transonic lift the acceleration curve has shifted to the right of the steady state curve and the deceleration curve has shifted to the left.

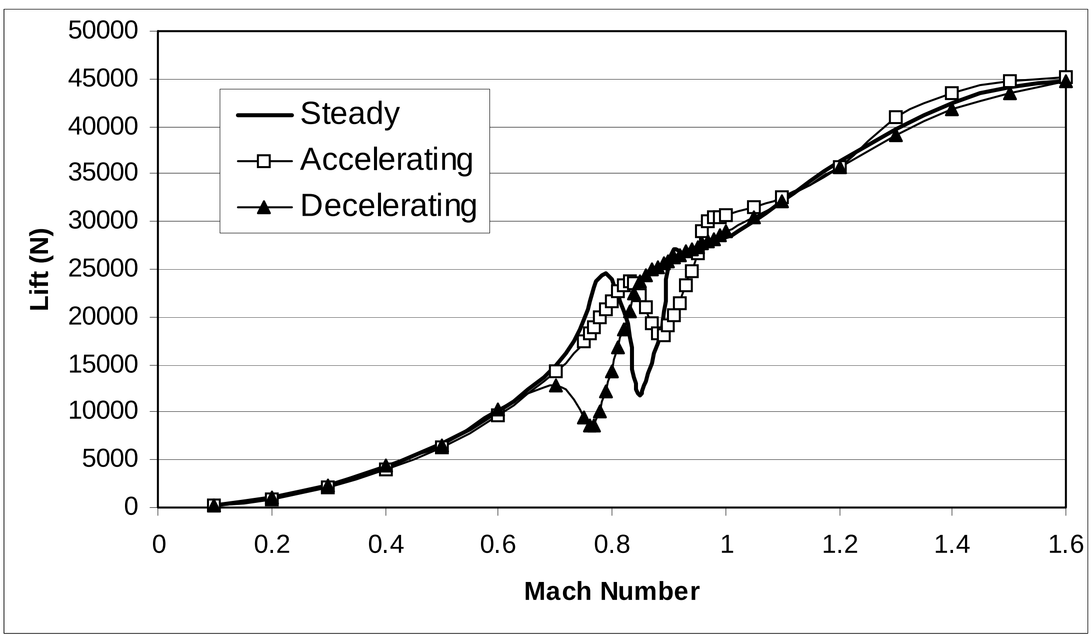

Figure 4.4: Biconvex lift at steady, +106g and –106g.

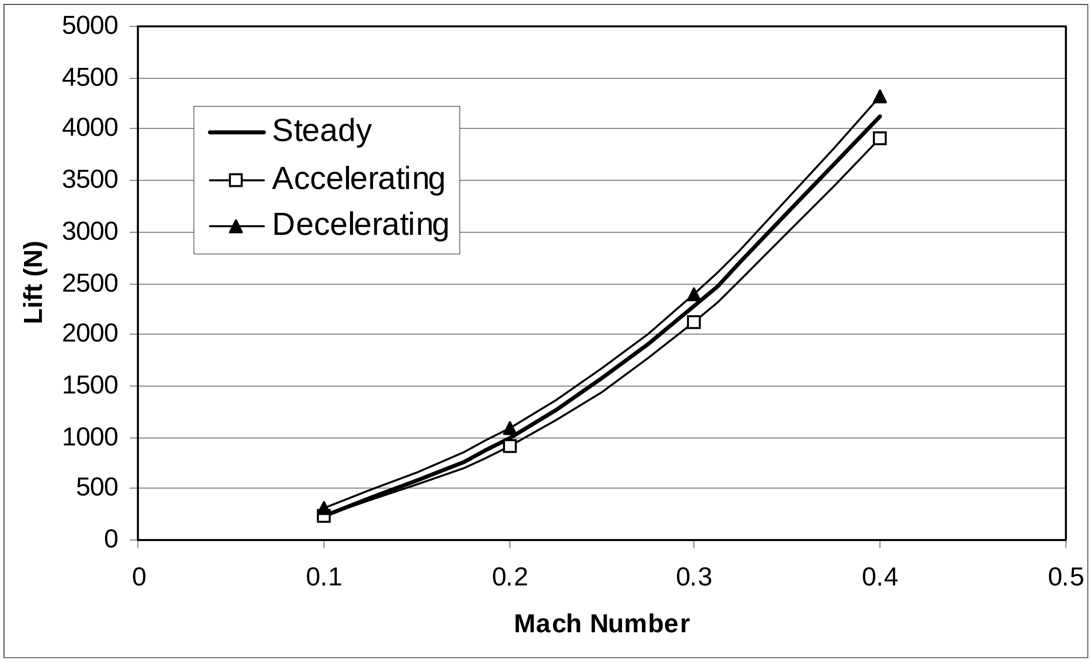

Figure 4.5: Subsonic biconvex lift at steady, +106g and –106g.

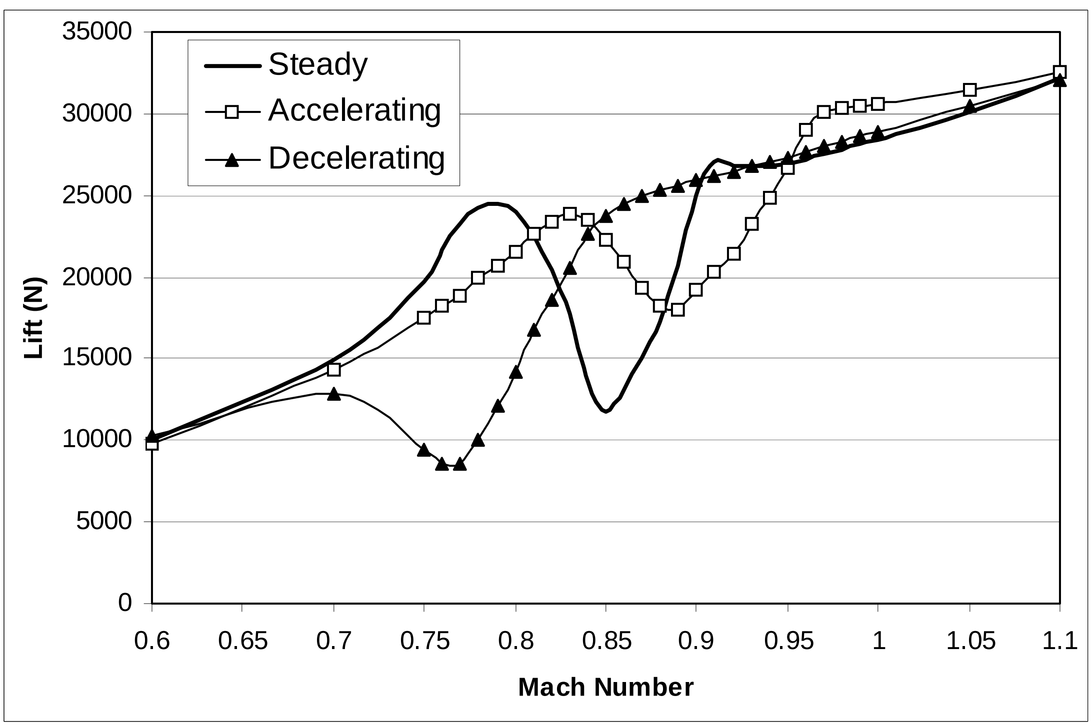

Figure 4.6: Transonic biconvex lift at steady, +106g and –106g.

4.1.3 Biconvex Moment at high accelerations

The steady and unsteady pitching moment variation versus Mach number, for high accelerations of +106g and-106g is shown in figures 4.7 to 4.9. The values over the complete range of Mach numbers (0.1-1.6) is shown in figure 4.7. The subsonic and transonic values are shown in figures 4.8 and 4.9. Although, there is a clear difference between the steady and the unsteady moment values in the subsonic range of Mach numbers, this is only specific to some airfoils and, as will be observed, is inconsistent with the RAE 2822. In the transonic region the unsteady moment fluctuates above and below the steady values, as was the case with lift and drag and the difference between the steady and unsteady pitching moments is greater in the transonic range of Mach numbers. The transonic pitching moment curves for acceleration and deceleration are much more flat than the steady state curve. However, the unsteady curves for acceleration and deceleration still shift to the right and left of the steady state values, as was observed with the transonic lift values of figure 4.6.

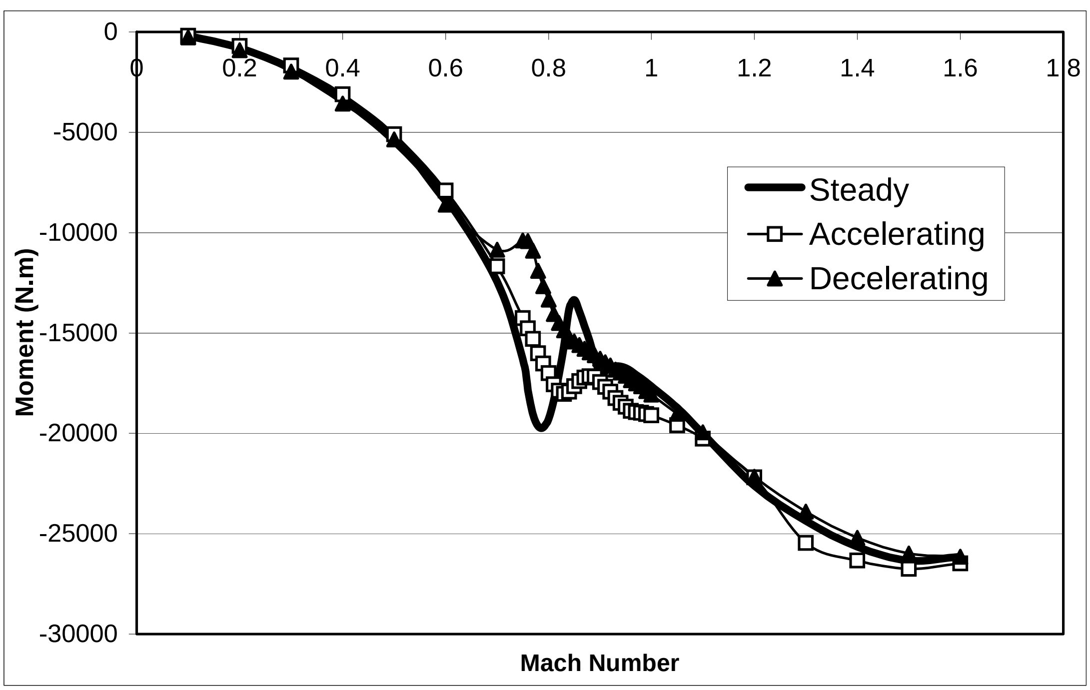

Figure 4.7: Biconvex moment at steady, +106g and –106g.

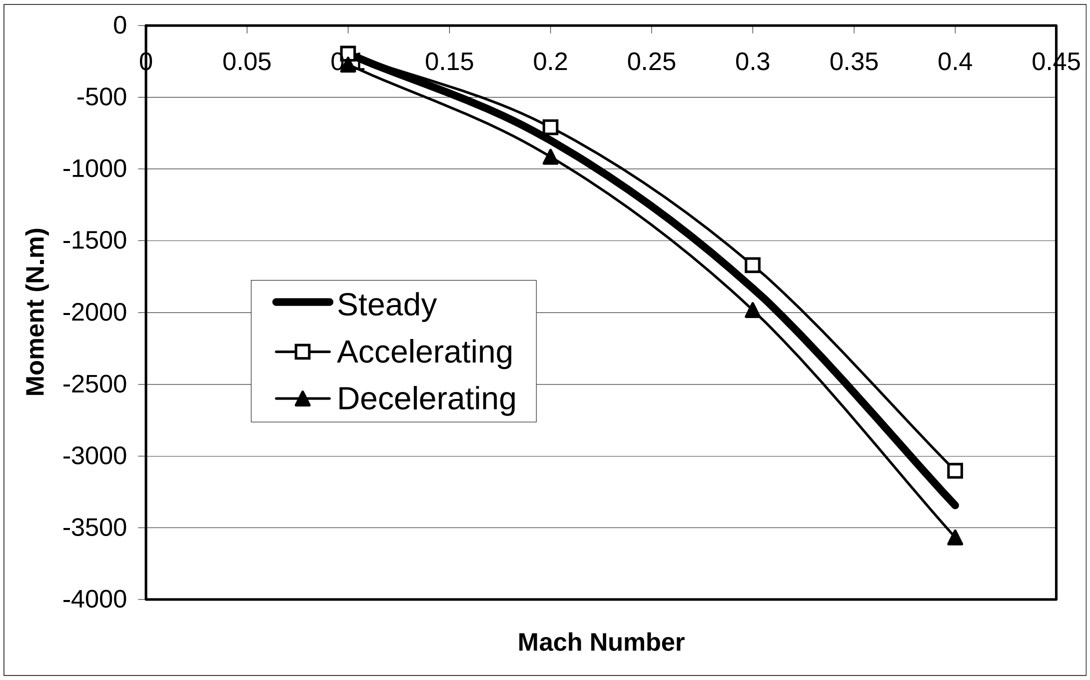

Figure 4.8: Subsonic biconvex moment at steady, +106g and –106g.

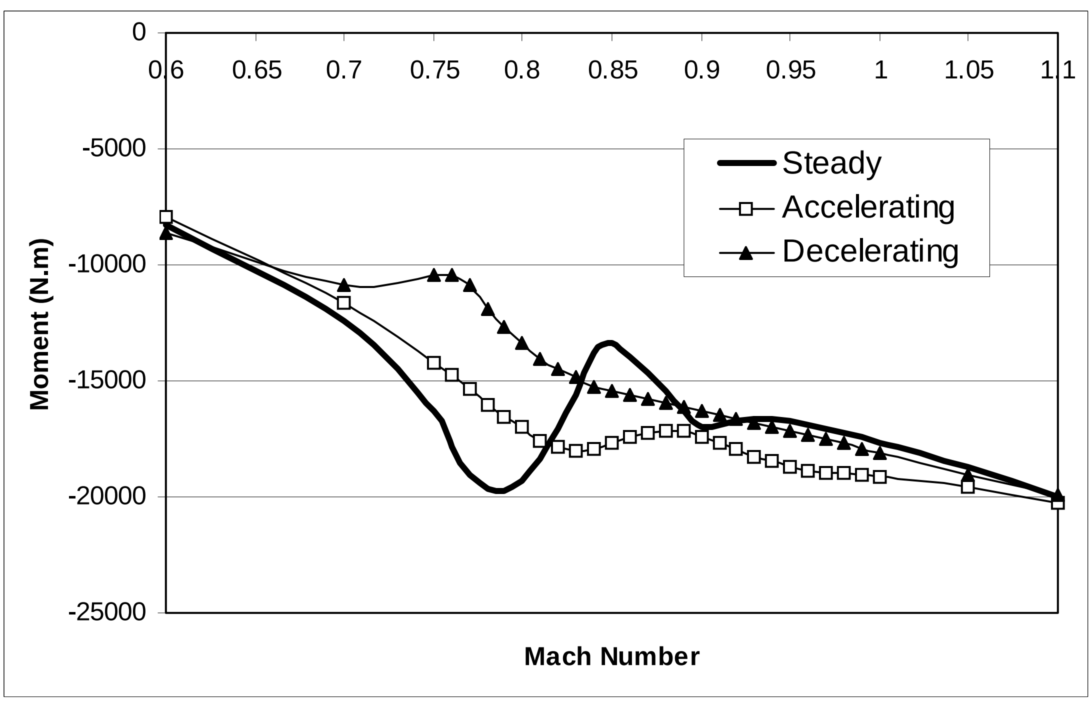

Figure 4.9: Transonic biconvex moment at steady, +106g and –106g.

4.1.4 Biconvex drag at moderate accelerations

Figures 4.10 to 4.12 show the steady and unsteady drag variation with Mach number at acceleration 86.77 m/s^2 (8.845g) and deceleration of -86.77 m/s^2 (-8.845g) for the biconvex aerofoil. Figure 4.10 shows the drag variation over the entire range of Mach numbers (0.1-1.6). In Figures 4.11 and 4.12 the subsonic and transonic portions of the graph are plotted. It is clear from figure 4.11 that for subsonic Mach numbers, acceleration brings about drag forces which are marginally higher and deceleration of the aerofoil results in drag forces that are marginally lower than the steady-state drag. Note that even at these moderate accelerations, the unsteady effects in the subsonic region, even though smaller in magnitude, were similar to what was experienced for the higher accelerations. From figure 4.12 it can be observed that, in the transonic range of Mach numbers, even with accelerations smaller than 9g, the unsteady effects are significant.

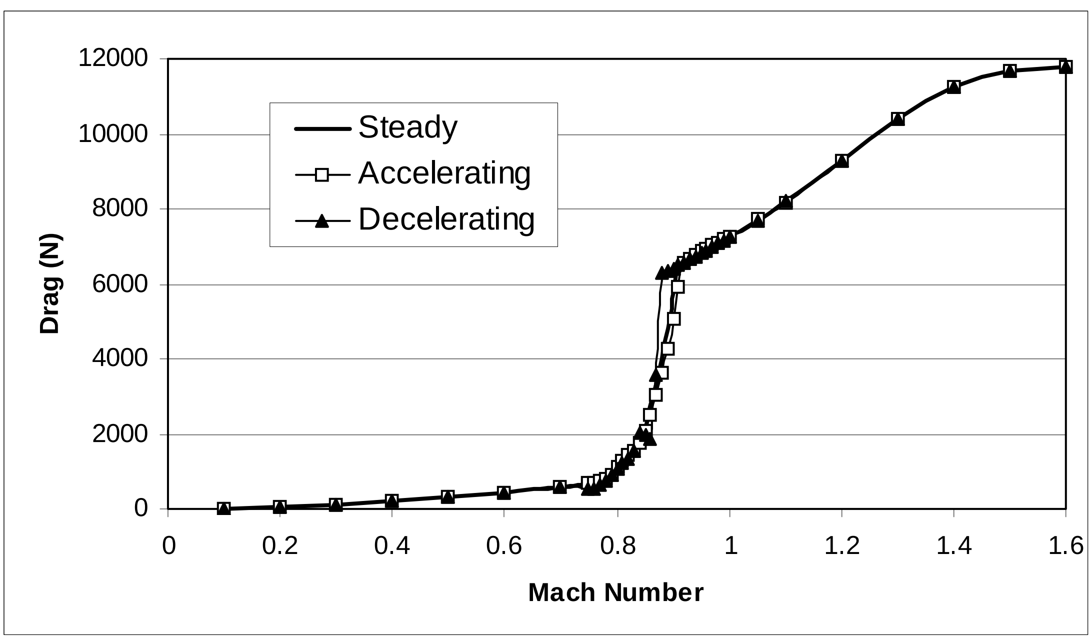

Figure 4.10: Biconvex drag at steady, +8.845g and –8.845g.

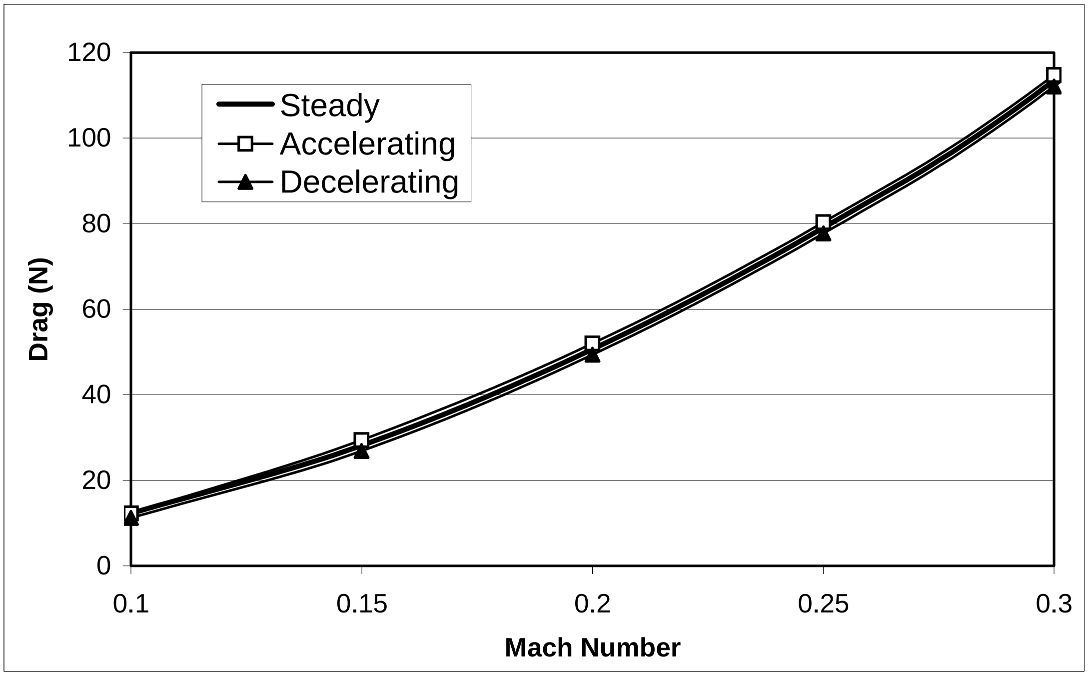

Figure 4.11: Subsonic biconvex drag at steady, +8.845g and –8.845g.

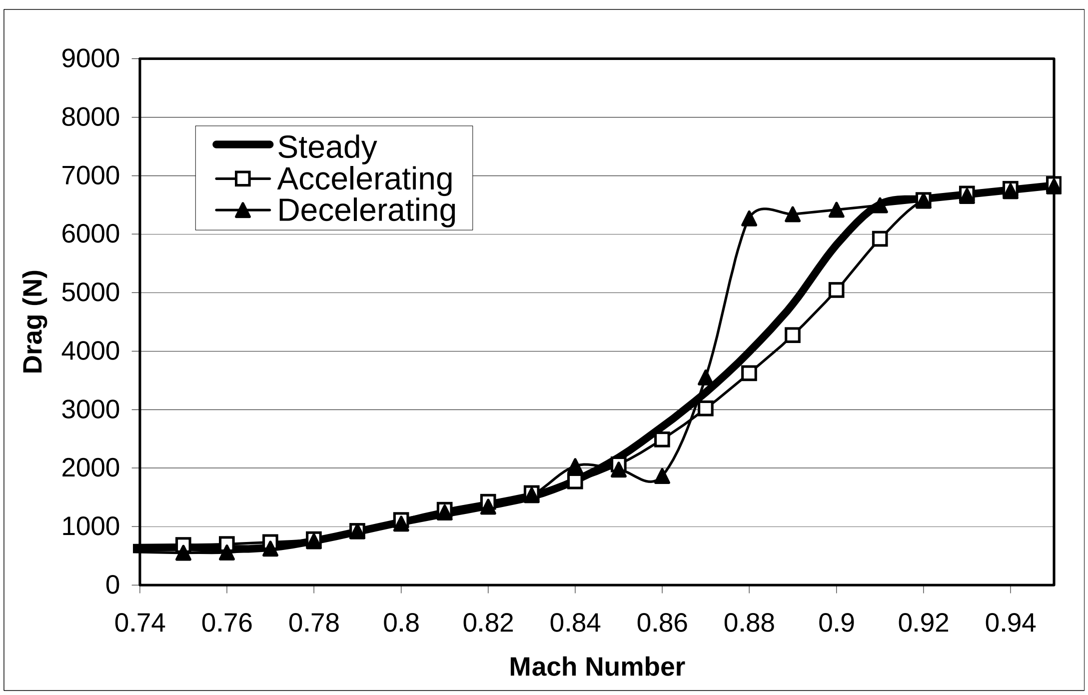

Figure 4.12: Transonic biconvex drag at steady, +8.845g and –8.845g.

4.1.5 Biconvex lift at moderate accelerations

Figure 4.13 shows the lift variation with Mach number for the steady and the unsteady cases over the entire range of Mach numbers (0.1-1.6) with accelerations of 8.845g and –8.845g. In Figure 4.14 and 4.15 the subsonic and transonic portions of the lift curves are plotted. In the subsonic region acceleration results in marginally lower lift values and deceleration results in marginally higher lift values than the corresponding steady state condition. However, in the transonic range of Mach numbers shown in figure 4.15, larger differences between the steady and unsteady conditions are apparent. The acceleration curve for transonic lift has shifted to the right of the steady state curve and the deceleration curve has shifted to the left. Clearly the effects that were observed for high accelerations are also present here on a smaller scale.

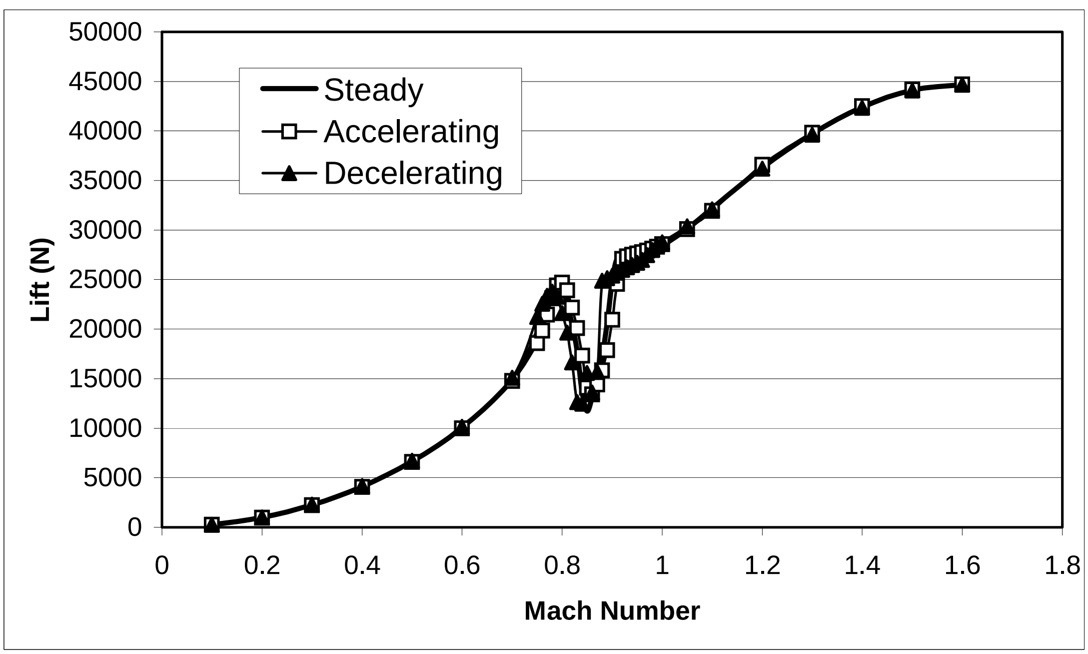

Figure 4.13: Biconvex lift at steady, +8.845g and –8.845g.

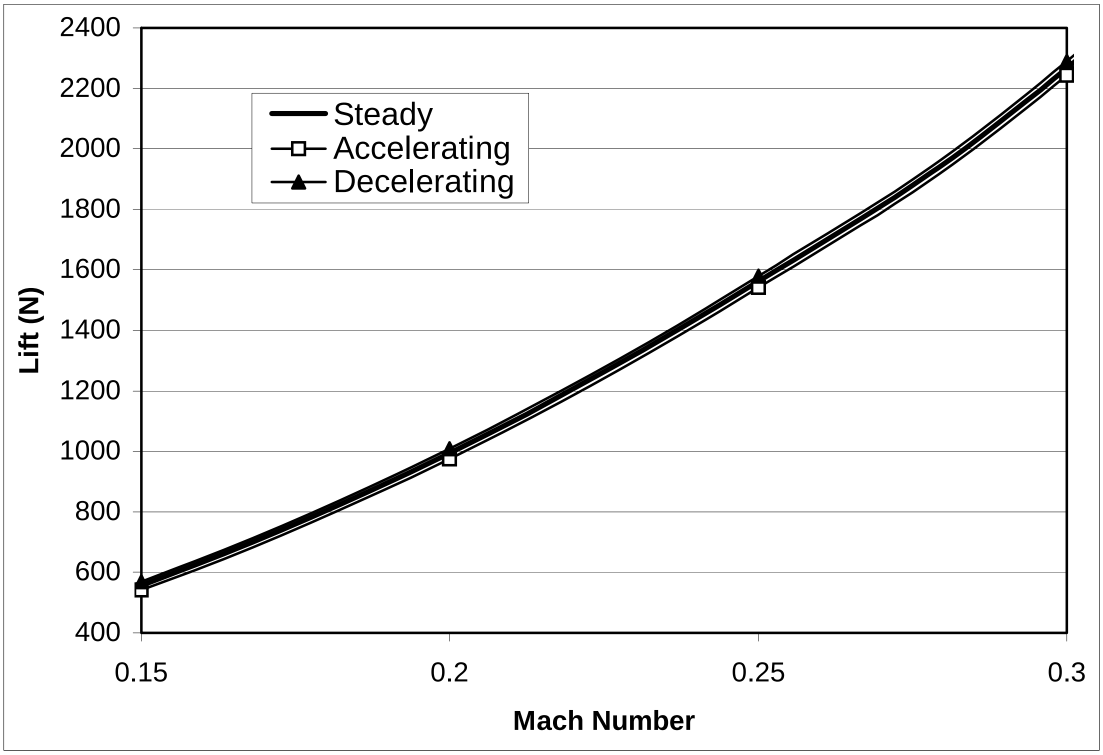

Figure 4.14: Subsonic biconvex lift at steady, +8.845g and –8.845g.

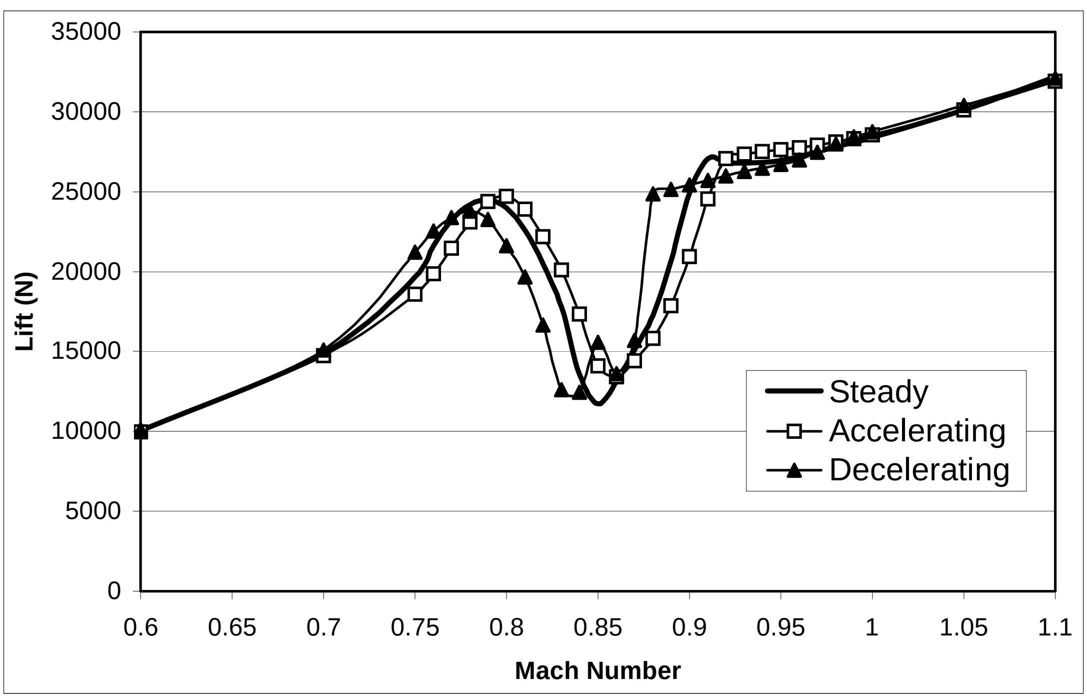

Figure 4.15: Transonic biconvex lift at steady, +8.845g and –8.845g.

4.1.6 RAE 2822 drag at high accelerations

Figures 4.16 to 4.18 show the steady and unsteady drag variation with Mach number at acceleration 1041 m/s^2 (106g) and deceleration of -1041 m/s^2 (-106g) for the RAE 2822 aerofoil. Figure 4.16 shows the drag variation over the entire range of Mach numbers (0.1-1.6). In figures 4.17 and 4.18 the subsonic and transonic portions of the graph are plotted. It is clear from figure 4.17 that for subsonic Mach numbers, acceleration of the aerofoil brings about drag forces which are higher and deceleration results in drag forces that are lower than the steady-state drag. Also note that, in comparison with the biconvex aerofoil, the difference between the steady and unsteady subsonic results is greater for RAE 2822 aerofoil. One possible explanation for this is that acceleration effects are also a function of the shape of the accelerating object. In the transonic region of figure 4.18, although the differences between the steady and unsteady forces are great, the results appear more disorderly. This is also consistent with the findings for the biconvex aerofoil.

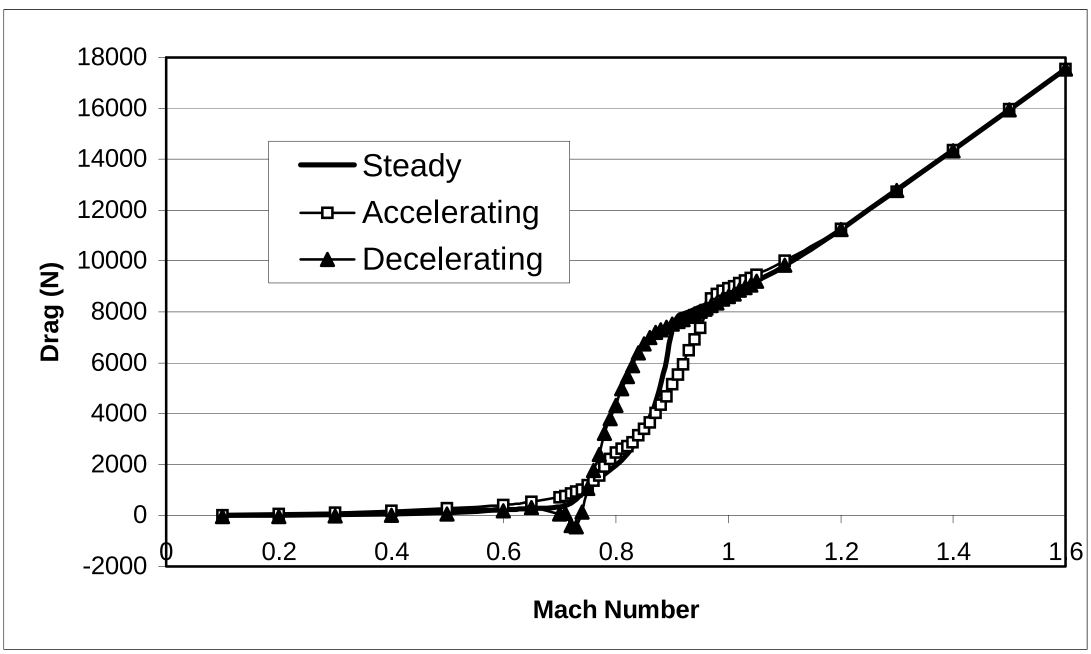

Figure 4.16: RAE 2822 drag at steady, +106g and –106g.

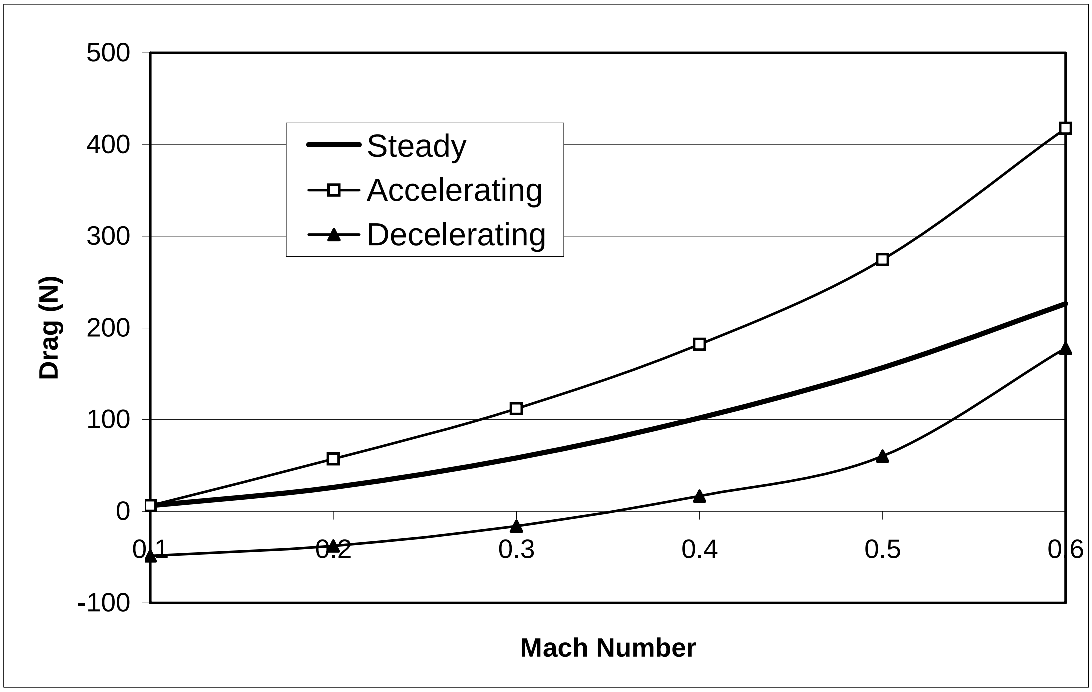

Figure 4.17: RAE 2822 subsonic drag at steady, +106g and –106g.

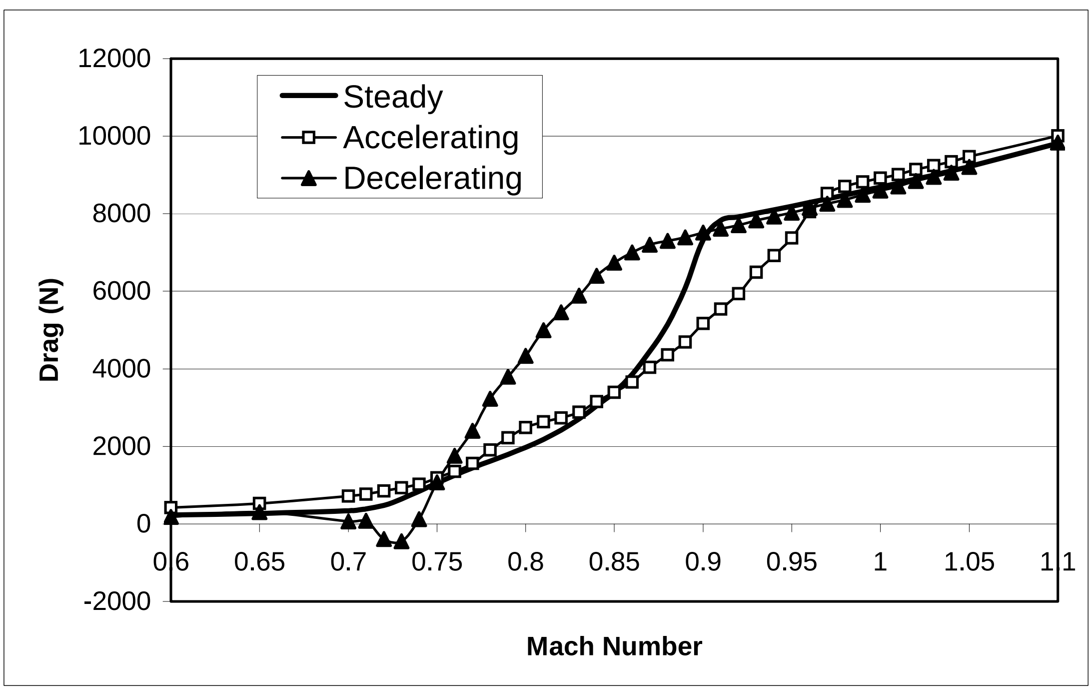

Figure 4.18: RAE 2822 transonic drag at steady, +106g and –106g.

4.1.7 RAE 2822 lift at high accelerations

Figure 4.19 shows the lift variation with Mach number for the steady and the unsteady cases over the entire range of Mach numbers (0.1-1.6) with high accelerations of 106g and –106g. In Figure 4.20 and 4.21 the subsonic and transonic portions of the lift curves are plotted. In the subsonic region acceleration results in lower lift and deceleration results in higher lift than the corresponding steady state lift values. Again these results confirm the biconvex aerofoil results but with the RAE 2822 the differences between the steady and unsteady values are more distinct. In the transonic range of Mach numbers shown in figure 4.21, sudden changes in the lift forces are observed and the unsteady lift values fluctuate above and below the steady-state values. The apparently disorderly behaviour of the unsteady data was also observed with drag. However, in the case of transonic lift the acceleration curve has shifted to the right and the deceleration curve has shifted to the left of the steady state curve. There is also a great difference in the shape of the steady and unsteady curves.

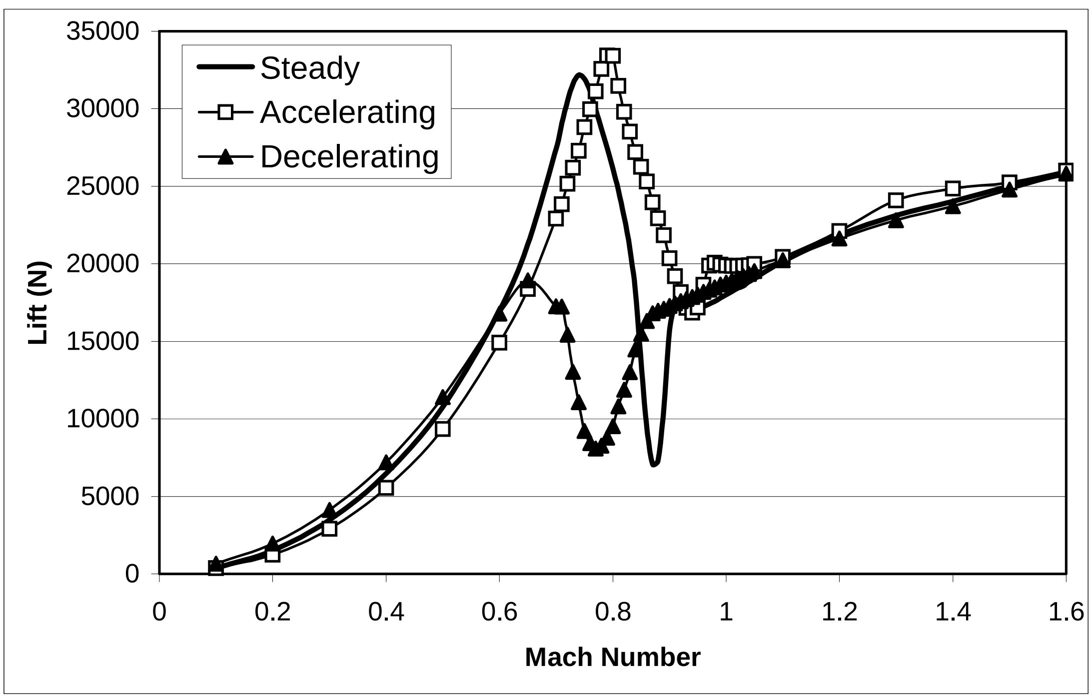

Figure 4.19: RAE 2822 lift at steady, +106g and –106g.

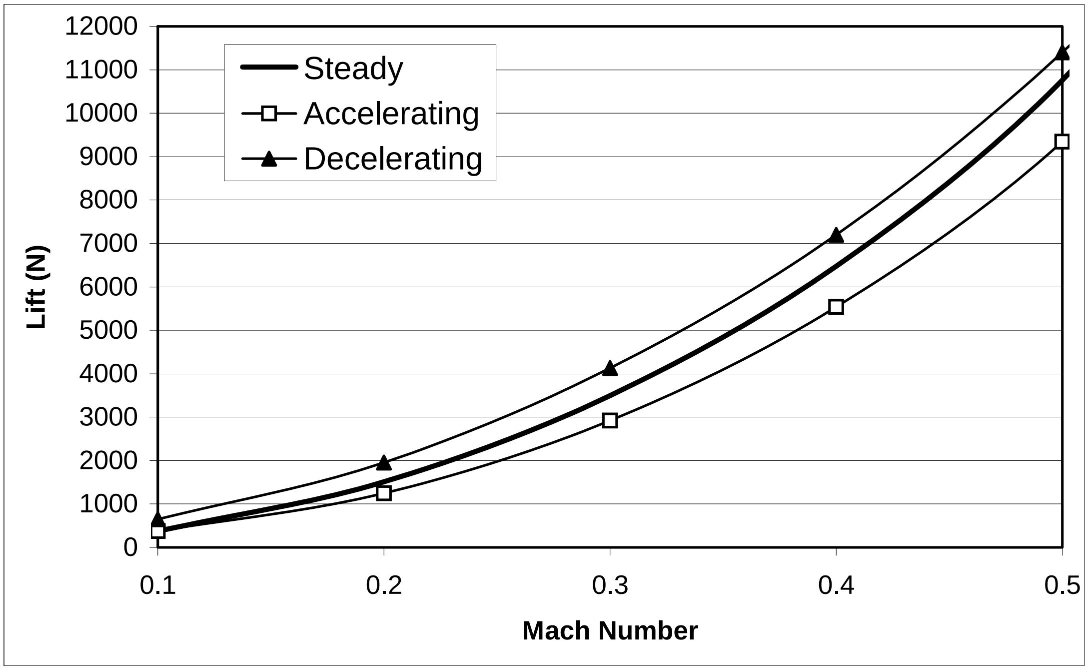

Figure 4.20: RAE 2822 subsonic lift at steady, +106g and –106g.

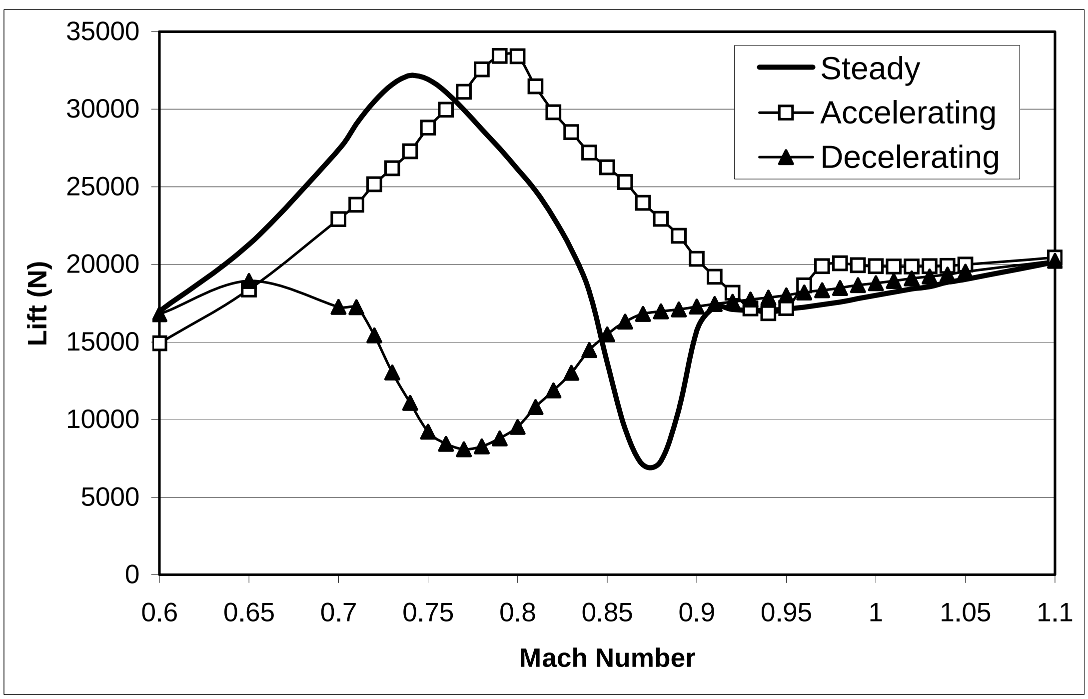

Figure 4.21: RAE 2822 transonic lift at steady, +106g and –106g.

4.1.8 RAE 2822 moment at high accelerations

The steady and unsteady pitching moment variation versus Mach number, for high accelerations of +106g and -106g is shown in figures 4.22 to 4.24. Figure 4.22 shows the values over the complete range of Mach numbers (0.1-1.6). The subsonic and transonic values are shown in figures 4.23 and 4.24. In spite of the high accelerations the subsonic steady and unsteady RAE 2822 moment curves are not easily distinguishable. This is inconsistent with the results from the biconvex aerofoil and as such no general conclusions can be drawn from these two cases for subsonic moment values. In the transonic region the moment values change significantly with changing Mach number. However, the unsteady curves for acceleration and deceleration still shift to the right and left of the steady state values but are of significantly different shapes. This provides some general consistency with the biconvex aerofoil results.

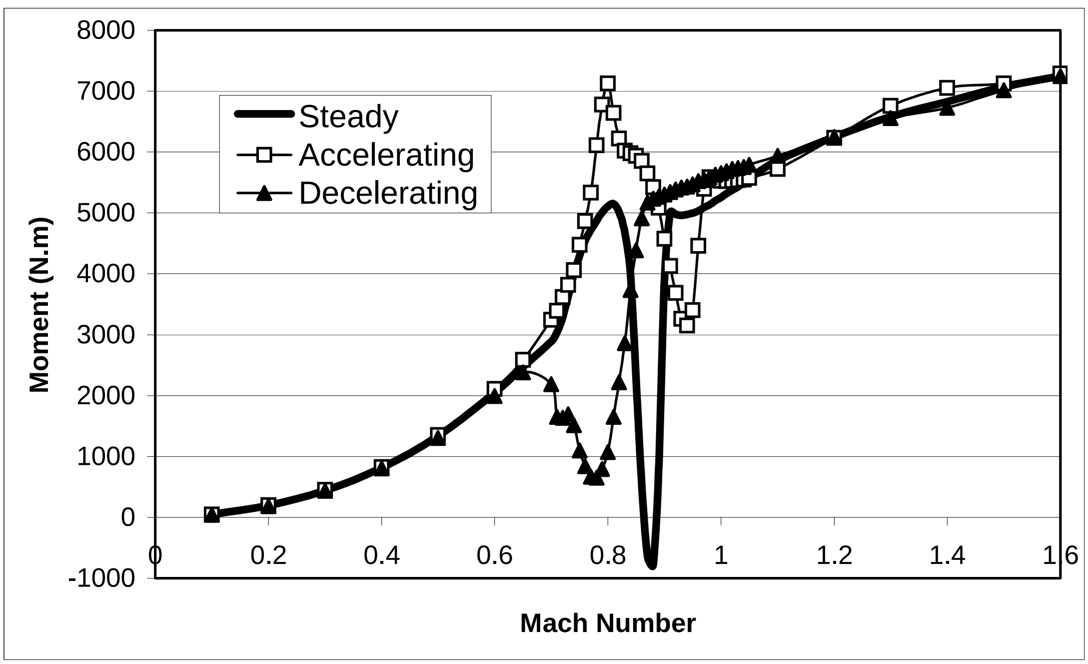

Figure 4.22: RAE 2822 pitching moment at steady, +106g and –106g.

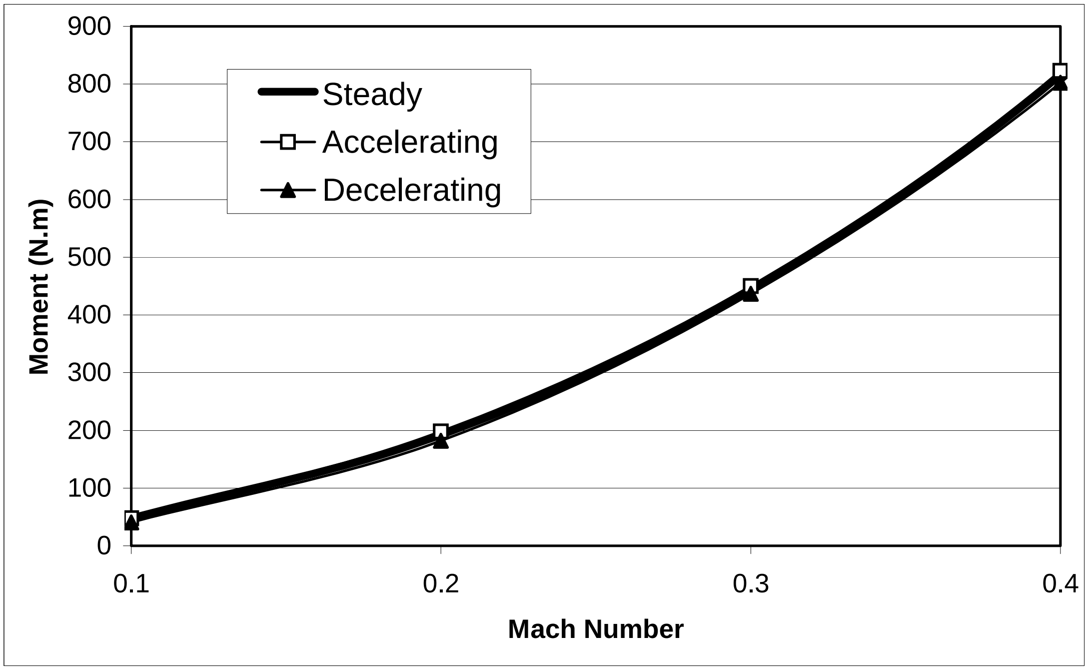

Figure 4.23: RAE 2822 subsonic pitching moment at steady, +106g and –106g.

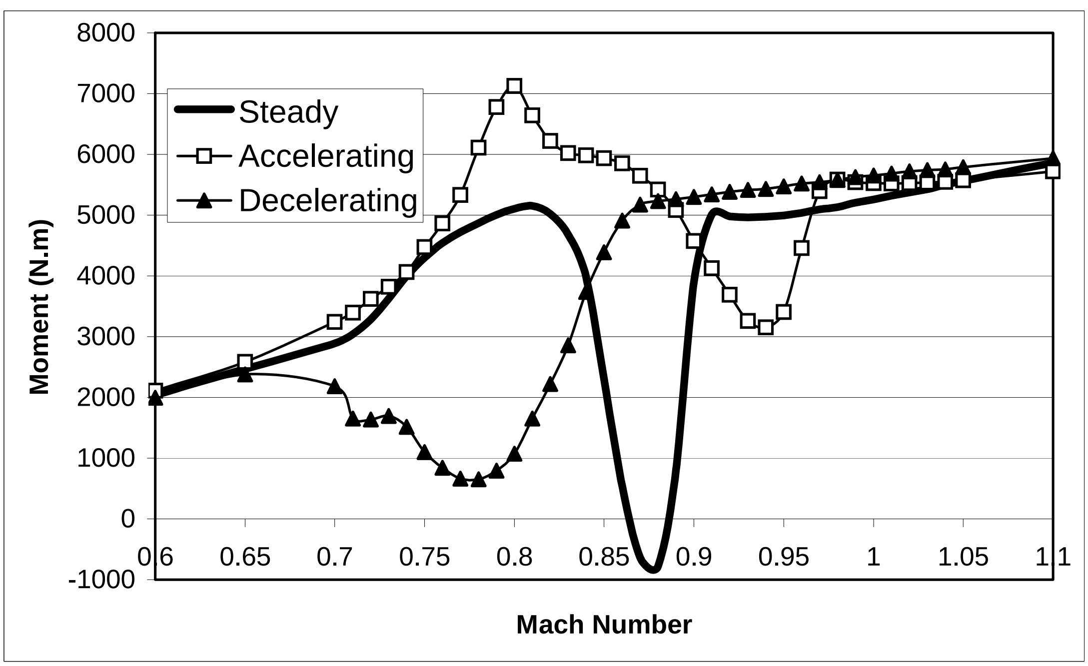

Figure 4.24: RAE 2822 transonic pitching moment at steady, +106g and –106g.

4.1.9 RAE 2822 drag at moderate accelerations

Figures 4.25 to 4.27 show the steady and unsteady drag variation with Mach number at acceleration 86.77 m/s^2 (8.845g) and deceleration of -86.77 m/s^2 (-8.845g) for the RAE 2822 aerofoil. Figure 4.25 shows the drag variation over the entire range of Mach numbers (0.1-1.6). In Figures 4.26 and 4.27 the subsonic and transonic portions of the graph are plotted. It is clear from figure 4.26 that for subsonic Mach numbers, acceleration brings about drag forces which are higher and deceleration of the aerofoil results in drag forces that are lower than the steady-state drag. Compared to the biconvex aerofoil there is a much greater distinction between the steady and unsteady subsonic drag values of the RAE 2822 aerofoil at moderate accelerations. From figure 4.27 it can also be observed that, in the transonic range of Mach numbers with moderate accelerations, the unsteady effects for this aerofoil are significant. The transonic steady and unsteady drag curves show similarity with the biconvex curves.

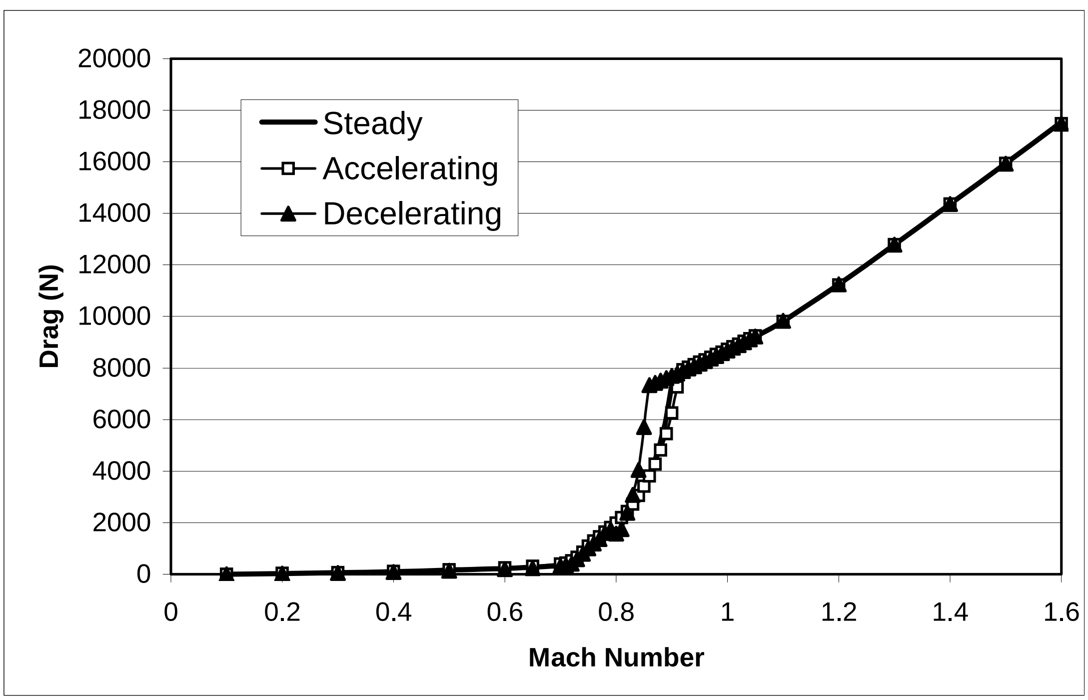

Figure 4.25: RAE 2822 drag at steady, +8.845g and –8.845g.

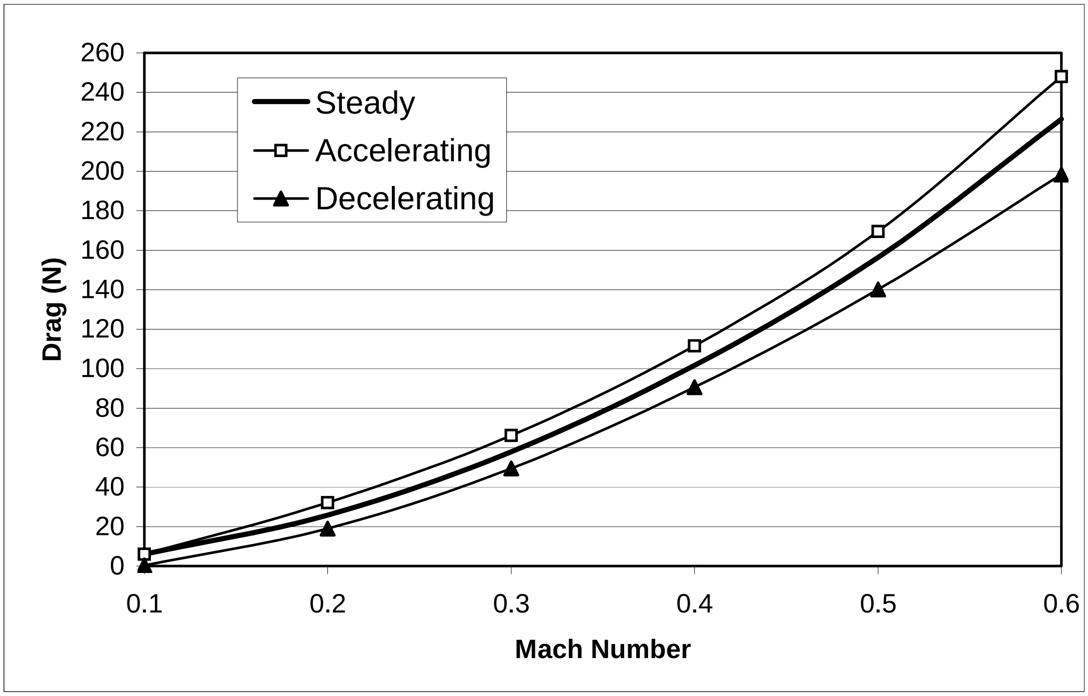

Figure 4.26: RAE 2822 subsonic drag at steady, +8.845g and –8.845g.

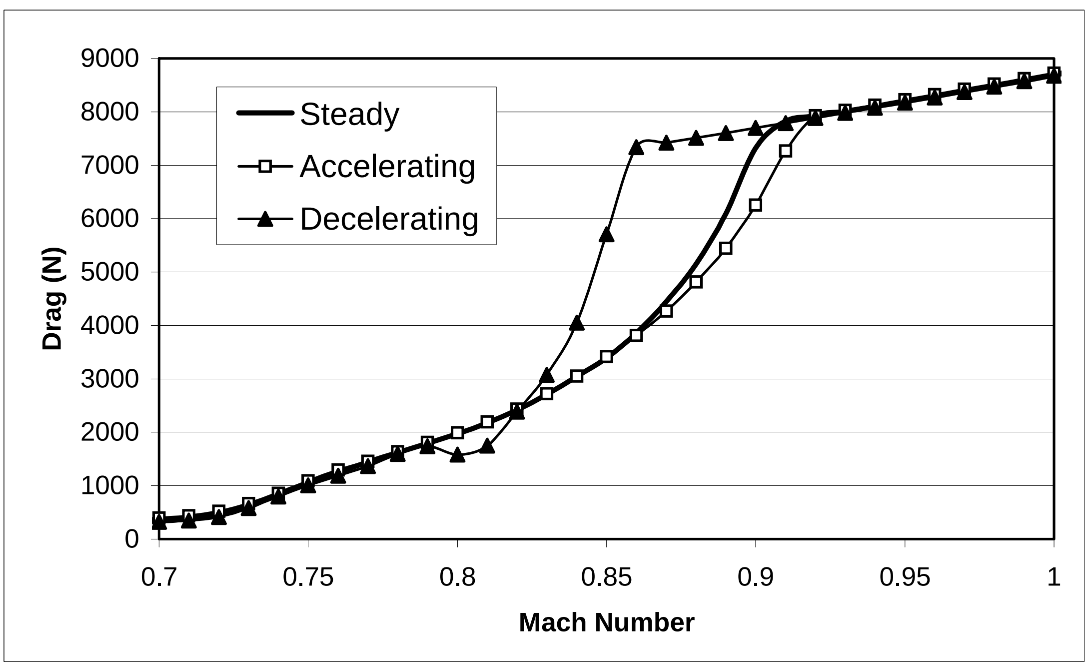

Figure 4.27: RAE 2822 transonic drag at steady, +8.845g and –8.845g.

4.1.10 RAE 2822 lift at moderate accelerations

Figure 4.28 shows the lift variation with Mach number for the steady and the unsteady cases over the entire range of Mach numbers with accelerations of 8.845g and –8.845g. In Figure 4.29 and 4.30 the subsonic and transonic portions of the lift curves are plotted. In the subsonic region acceleration results in marginally lower lift values and deceleration results in marginally higher lift values than the corresponding steady state condition. However, in the transonic range of Mach numbers shown in figure 4.30, larger differences between the steady and unsteady conditions are apparent. The acceleration curve for transonic lift has shifted to the right of the steady state curve and the deceleration curve has shifted to the left. Clearly the effects that were observed for high accelerations are also present here on a smaller scale. Comparison of the steady and unsteady lift results for the RAE 2822 and the biconvex aerofoil show similar general trends at moderate accelerations.

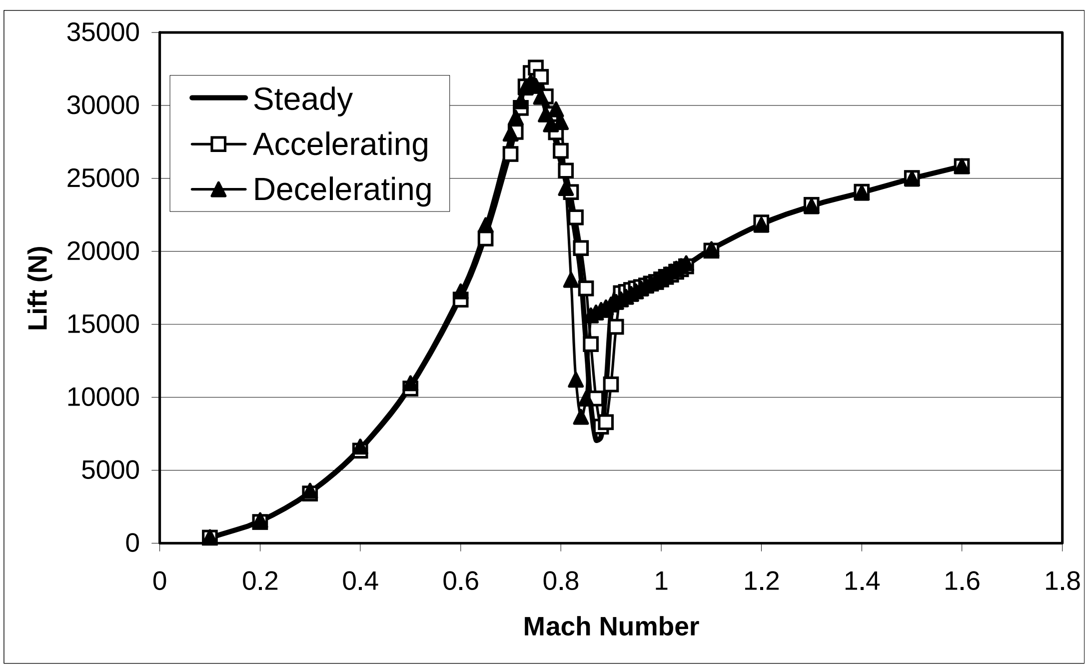

Figure 4.28: RAE 2822 lift at steady, +8.845g and –8.845g.

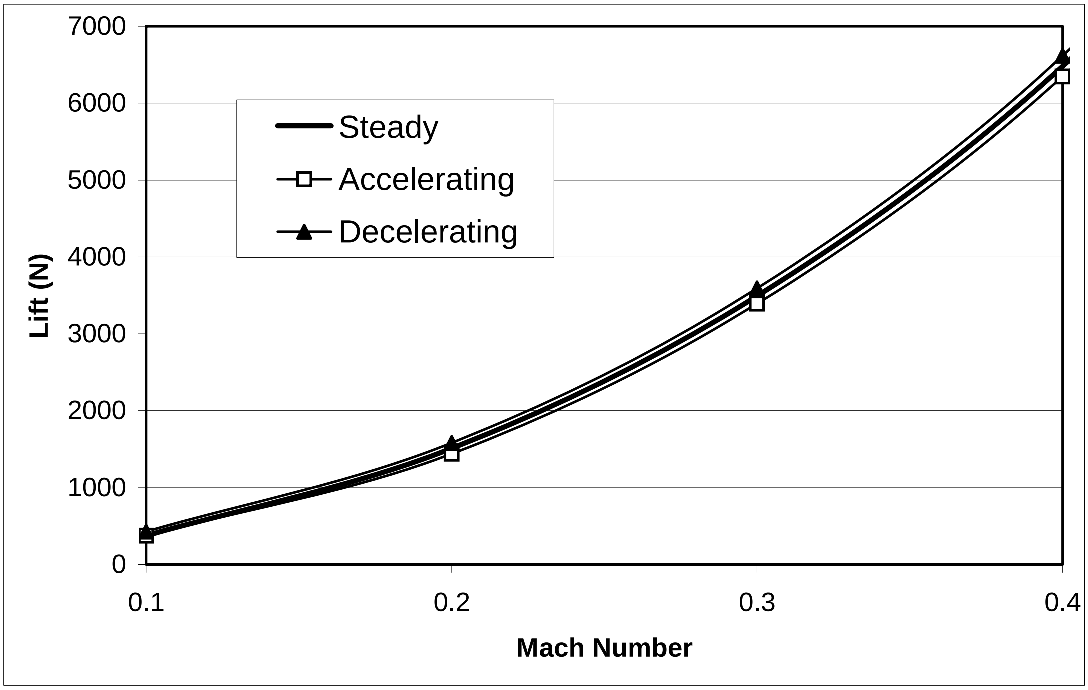

Figure 4.29: RAE 2822 subsonic lift at steady, +8.845g and –8.845g.

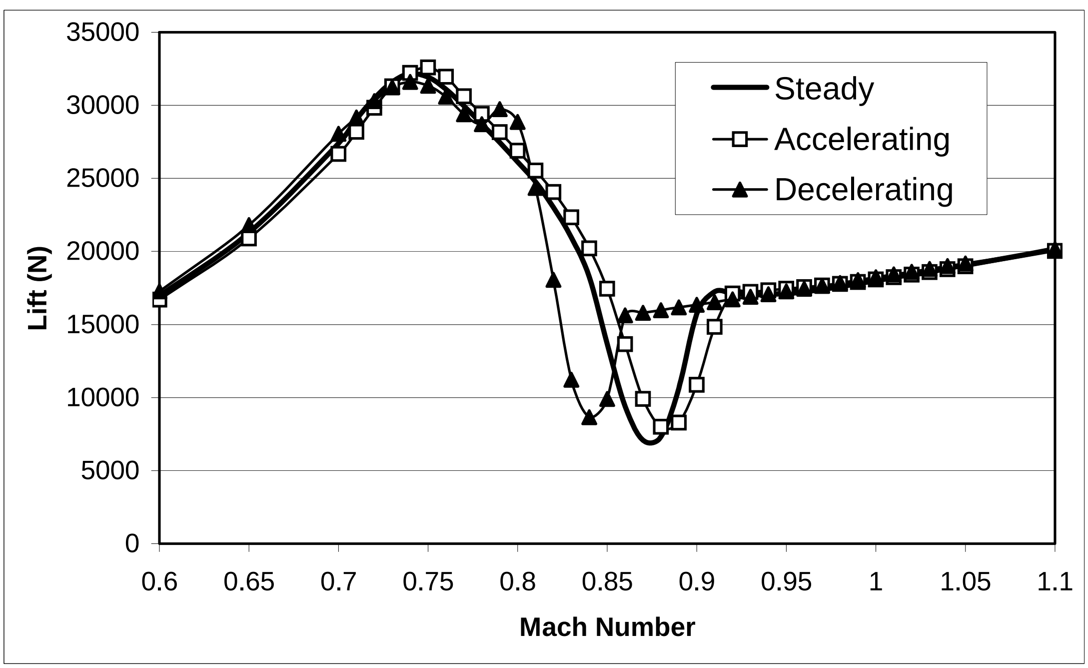

Figure 4.30: RAE 2822 transonic lift at steady, +8.845g and –8.845g.

4.1.11 Summary of results

From the investigation in this section it is evident that, for a given subsonic Mach number, unsteady acceleration effects bring about a reduction in lift and an increase in drag and retardation has the opposite effect of increasing lift and reducing drag. The transonic effects of acceleration follow a very different trend and will be discussed in detail in chapter 5. In the remaining case studies in this chapter further confirmation of the subsonic findings is presented.

4.2 Aerofoil acceleration at low subsonic Mach numbers

In this section two case studies with the NACA 2412 aerofoil are conducted. In the first the aerofoil is subjected to low Mach numbers and low accelerations in order to examine conditions encountered in motor racing. Then the effects of acceleration at different angles of attack at a given Mach number are investigated. This also provides the opportunity to look at the effects of acceleration on angle of separation.

4.2.1 Low accelerations relevant to automotive applications

In the above investigations relatively high accelerations were chosen in order to establish principles regarding accelerated motion in compressible fluids. However, there is little practical application for such high accelerations. Therefore, the purpose of this section is to look at a practical situation where the changes in aerodynamic forces, caused by acceleration, could be significant.

In Formula One motor racing the lift force generated by airfoils is used to create down force in order to improve traction and hence the handling of a car round high speed bends. In order to increase the down force the angle of attack has to be increased, which will in turn increase the drag force on the aerofoil. The final design is a trade off between drag and lift with typical angles of attack being around 15 degrees. In this example the NACA 2412 aerofoil is subjected to an acceleration of 8.677 m/s^2 (0.8845g), which falls well within the range of accelerations of a typical Formula One car. All the other conditions are maintained as with the biconvex aerofoil and the angle of attack is kept at 4 degrees. The range of Mach numbers chosen are from 0.1 to 0.2 (125 to 250 km/h). Figures 4.31 and 4.32 show the effect of acceleration on drag and lift at different Mach numbers. Figure 4.31 shows a significant % increase in drag when the accelerating scenario is compared with the steady state condition. If a similar % increase is assumed in the total drag force of the Formula One car the handling and fuel consumption could be noticeably affected. The reduction in lift (or down force) in figure 4.32 is as high as over 1% of the total lift. If a similar % reduction is assumed in the total aerodynamic down force (i.e. 1% of typically 5kN = 50N) this could drastically affect the traction and hence the handling of a car under racing conditions.

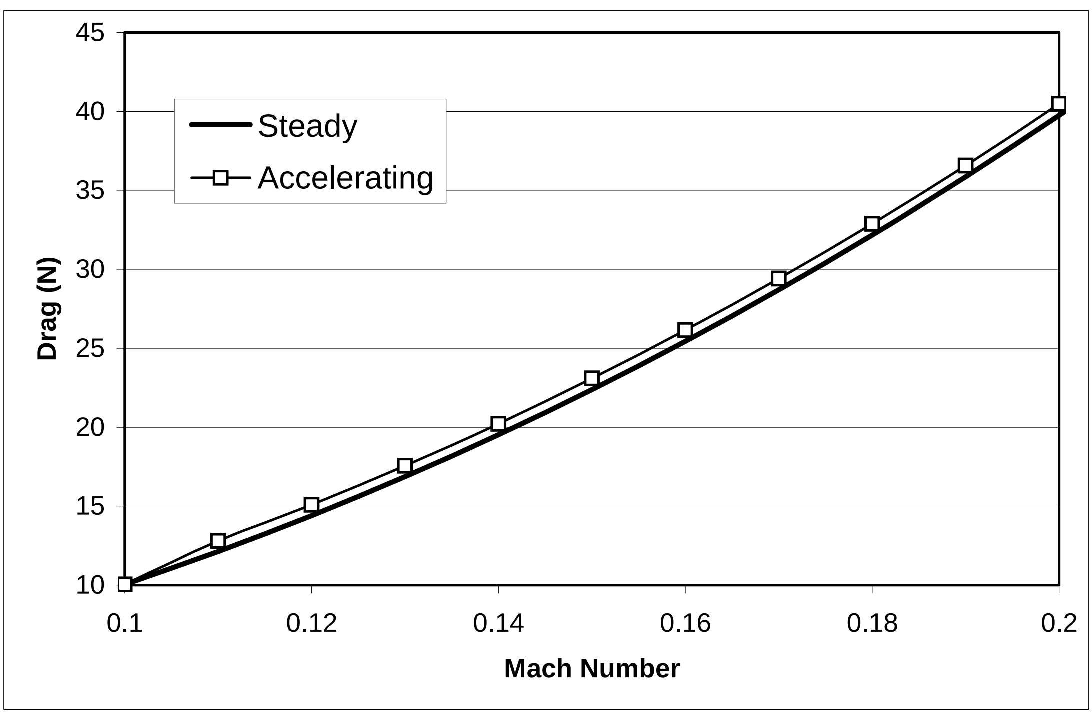

Figure 4.31: NACA2412 subsonic drag at steady and +0.8845g.

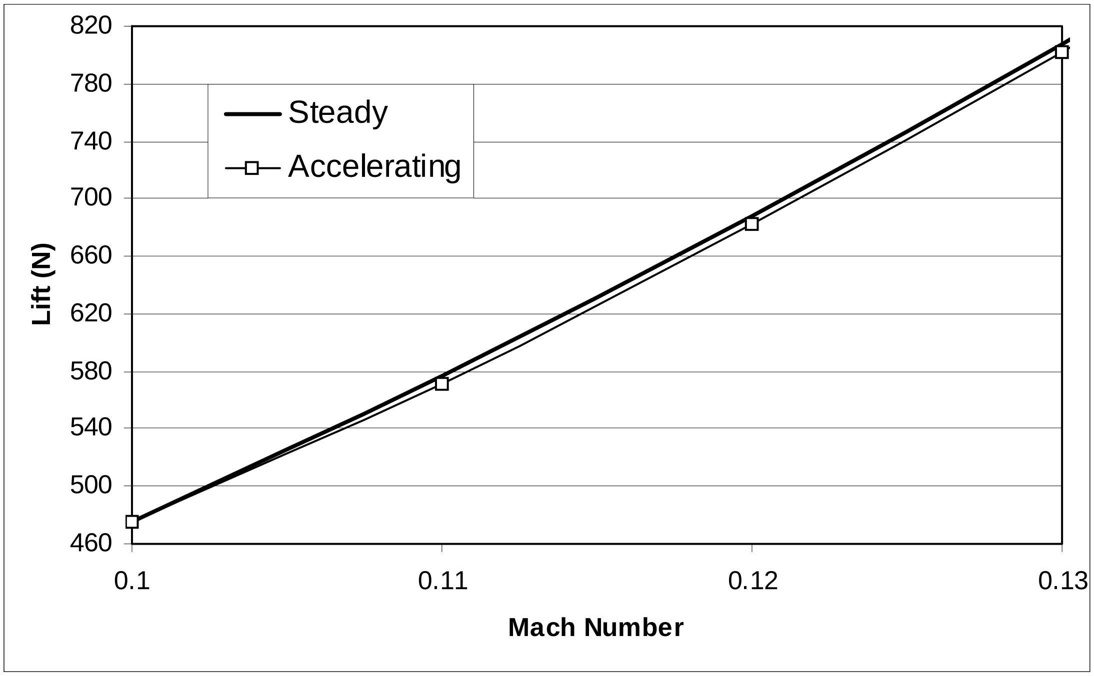

Figure 4.32: NACA2412 subsonic lift at steady and +0.8845g.

The above effects are currently being investigated in more depth. More complex modelling, taking into account the ground effect as well as the effect of accelerating the car round a bend, is required. For the present, it is clear that the aerodynamic effects caused by acceleration could have practical significance.

4.2.2 Variation in angle of attack

In this study the NACA 2412 aerofoil is used to study the subsonic effects of acceleration at various angles of attack. At each angle the steady and unsteady values of lift coefficient are compared and a graph of lift coefficient versus angle of attack is plotted on the same set of axis for the steady, accelerating and decelerating scenarios. High accelerations of 106g and -106g are chosen in order to magnify the unsteady effects. The range of Mach numbers used is 0.1 to 0.4 for acceleration and 0.4 to 0.1 for deceleration. All the other conditions are maintained as with the case of the biconvex aerofoil earlier in this chapter. Figure 4.33 shows the subsonic values of lift coefficient at steady state condition, +106g and –106g at various angles of attack at Mach 0.3 for the NACA 2412 aerofoil. In this case at angles below 12 degrees, where separation effects are not present, lift coefficient values from the steady and unsteady cases follow the same trend as was established with the biconvex and the RAE 2822 aerofoil earlier in this chapter. For example at 8 degrees the accelerating curve shows a lower value for the lift coefficient and the value of the lift coefficient from the decelerating curve is higher than the steady state value. This shows that the observed trend, with respect to steady and unsteady lift coefficients, holds true for the range of angles below the angle of separation and is not specific to one or two angles of attack. From about 12 degrees separation effects start to appear, first for the decelerating case and with higher angles of attack for the steady and finally for the accelerating scenarios. Although not presented here these results were confirmed by the NACA 0012 aerofoil with the same trend being observed at angles below the angle of separation and differences in the actual angle of separation occurring as a result of acceleration and deceleration.

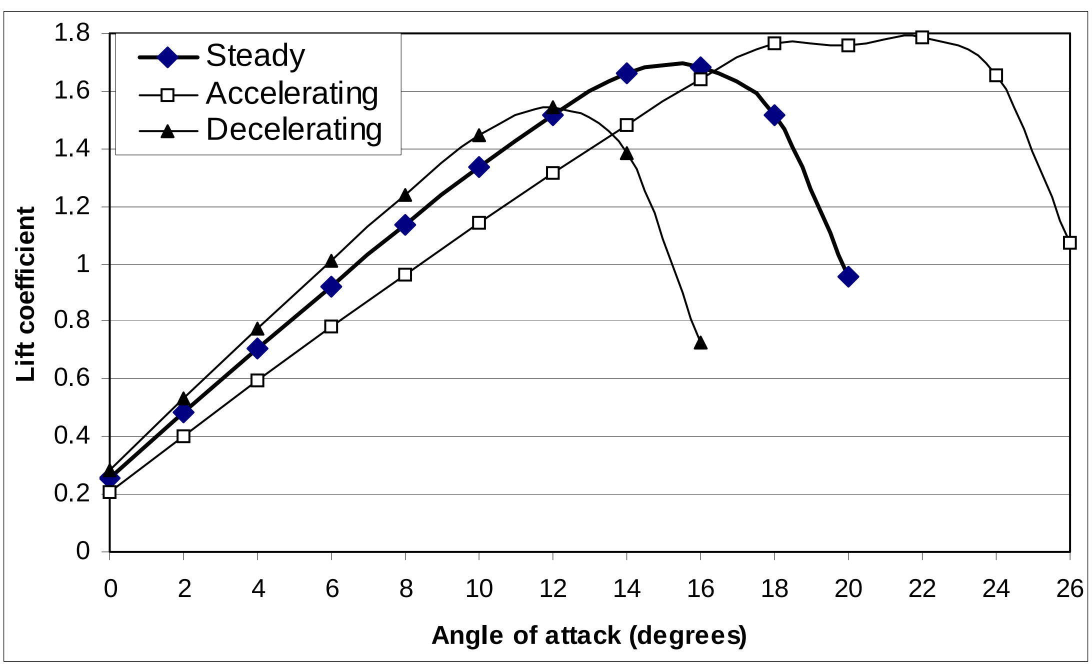

Figure 4.33: NACA 2412 subsonic lift coefficient at steady, +106g and –106g at various angles of attack. In all cases the data is captured at Mach 0.3.

In order to demonstrate that separation is actually taking place at different angles of attack in the three scenarios velocity vectors are plotted to show the direction of movement of the gas at different points in the flow field. Figures 4.34 and 4.35 compare the three cases at 16 degrees. In figure 4.34 the tail of the aerofoil for the steady and the accelerating cases is enlarged in order to improve clarity and the velocity vectors are plotted around the aerofoil for each case. It is evident that in the steady state scenario the direction of the arrows changes in the region close to the surface of the aerofoil so that their absolute velocity, in the direction of motion of the aerofoil, is higher than the aerofoil itself. This shows that separation has started to occur. However, in the accelerating case of figure 4.34 no such effect is present. In figure 4.35 the decelerating scenario at the same angle of attack is shown. Here the reversed arrows are not only present at the tail but can be seen all along the surface right to the tip of the aerofoil, which is an example of fully developed separation.

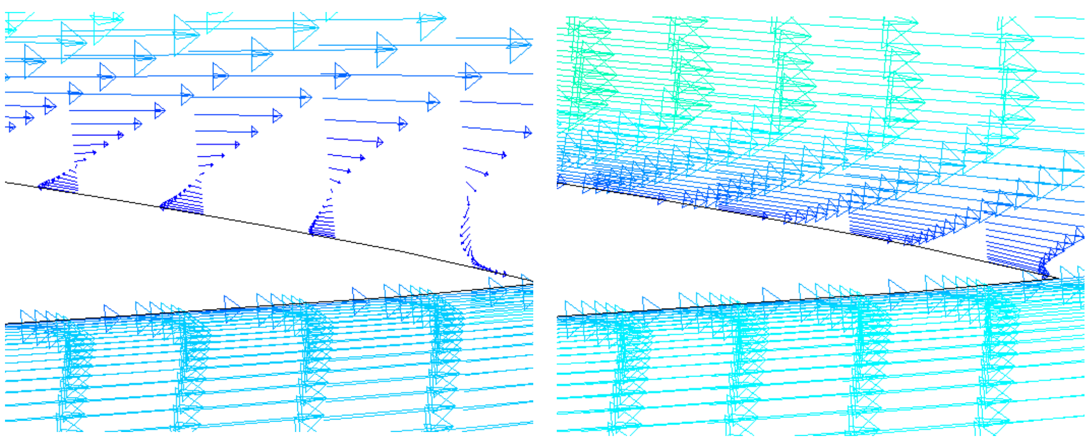

(a) Steady state (b) Acceleration of 106g

Figure 4.34: Velocity vectors at the tail of a NACA 2412 aerofoil flying at 16 degrees at Mach 0.3 (a) Under steady state condition with separation starting to occur (b) Under acceleration of 106g with no separation occurring.

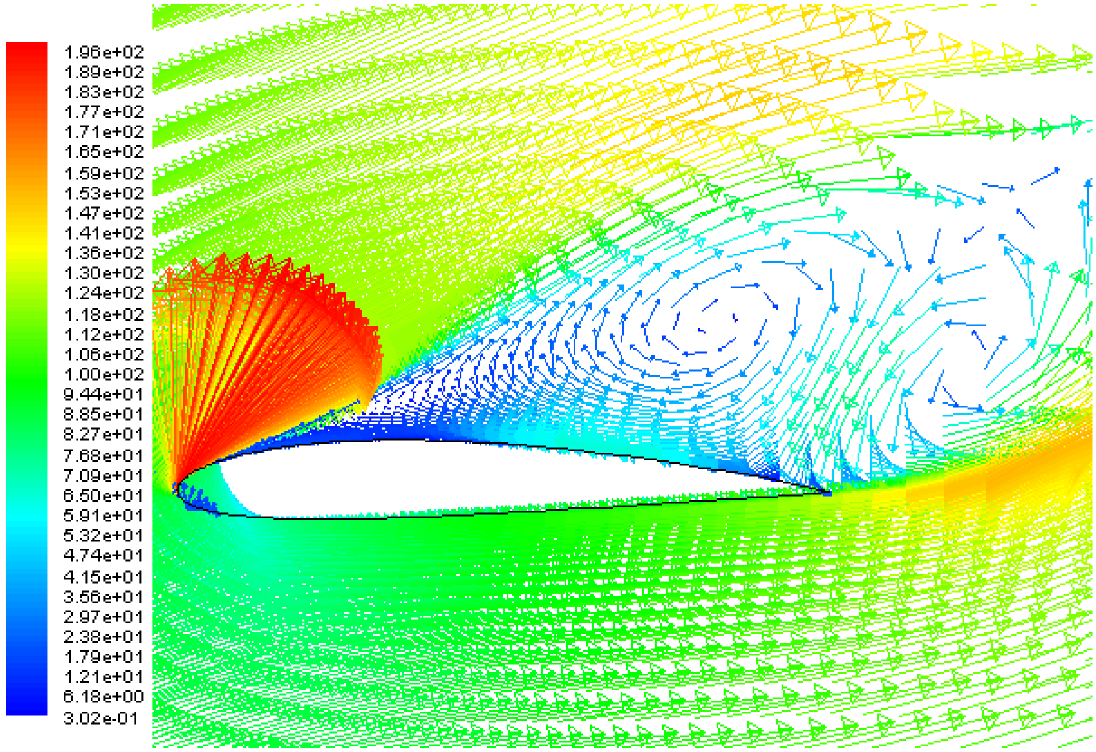

Figure 4.35: Velocity vectors for NACA 2412 aerofoil at Mach 0.3 and 16 degrees under deceleration of –106g, showing separation. Note that all vectors have been consistently enlarged to clearly show separation effects.

In figure 4.36 the velocity vector plots for an angle of attack of 20 degrees for the steady and accelerating cases are shown. From the direction of the arrows, especially along the surface of the aerofoil, it can be observed that fully developed separation has taken place for the steady state scenario. However, from the figure little evidence of separation can be seen with acceleration at this angle of attack. In fact, based on the acceleration curve of figure 4.33, separation only starts to occur after 22 degrees at this Mach number with fully developed separation occurring at 26 degrees. In figure 4.37 the velocity vector plot at an angle of attack of 26 degrees shows that fully developed separation has taken place for the accelerating case at this angle. The above discussion shows that unsteady effects in a flow field influence the angle at which separation takes place and there is a difference between this angle for the steady, the accelerating and the decelerating scenarios at the same Mach number.

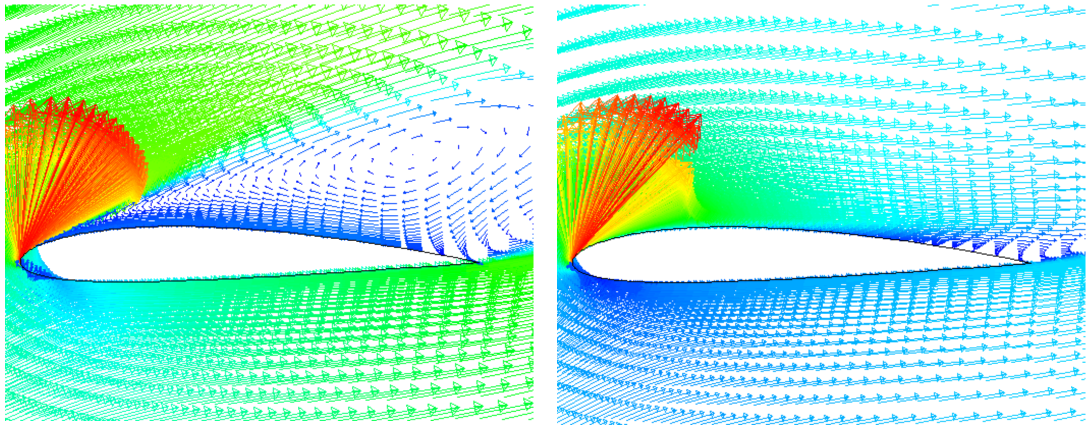

(a) Steady state (b) Acceleration of 106g

Figure 4.36: Velocity vectors for a NACA 2412 aerofoil flying at 20 degrees at Mach 0.3 (a) Under steady state condition showing separation (b) Under acceleration of 106g showing little evidence of separation.

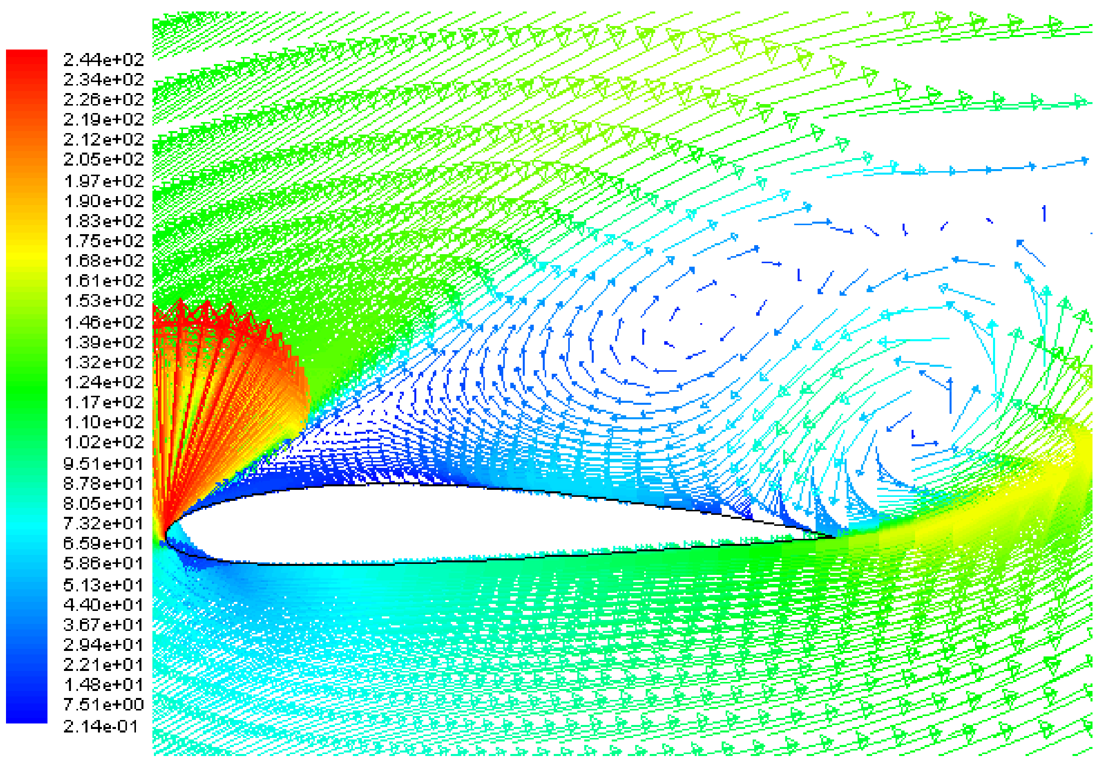

Figure 4.37: Velocity vectors for NACA 2412 aerofoil at Mach 0.3 and 26 degrees under acceleration of 106g, showing separation.

More research needs to be conducted in order to fully understand the effects that an unsteady flow field has on the angle of separation. However, at this point it can be concluded that the angle of separation can change due to unsteady effects.

4.3 Axisymmetric Bodies

This section focuses on the aerodynamic effects caused by acceleration and retardation of axisymmetric bodies in air. The objects used in this investigation were a 1 m diameter sphere and an artillery shell, taken from Van Dyke [7]. The sphere provided a good starting point for testing the effects of acceleration and retardation and gave important information regarding subsonic Mach numbers. As a great deal of steady state experimental data is available for spheres of different diameters [4, 5], mainly for low Mach numbers, this helped in the validation of some of the results. The artillery shell was useful when studying transonic flight. It also provided the opportunity to compare the effects of acceleration on different profiles. The shell was 240 mm long with a maximum diameter of 50 mm. High accelerations were chosen to enhance the differences between the steady and accelerating scenarios.

Both objects were subjected to the following conditions:

Free stream temperature:	300 K
Atmospheric pressure:	101325 Pa
Acceleration:	1041 m/s^2 (106g)
Retardation:	-1041 m/s^2
Range of Mach numbers:	0.1 to 1.6

Steady state, constant velocity, simulations were conducted for each body, at Mach numbers ranging from 0.1 to 1.6. Then, starting at Mach 0.1, each object was subjected to an acceleration of 1041 m/s^2 (106g) through the same range of Mach numbers. Finally, starting at Mach 1.6, the objects were decelerated at -1041 m/s^2

down to Mach 0.1. Graphs of drag versus Mach number were plotted, and the steady and the unsteady graphs were plotted on the same set of axes. Forces were not non-dimensionalised in order to avoid ambiguity in choosing an arbitrary reference velocity.

Figure 4.38 shows the steady and unsteady drag variations over the subsonic range of Mach numbers (0.1 to 0.6) for the sphere. In chapter 3 it was shown that the Spalart-Allmaras viscous model used here agreed with experimental data only up to Mach 0.6. Additional data and simulations are needed to validate results at higher Mach numbers. The results showed that in this range of Mach numbers acceleration resulted in an increase in drag and retardation in a reduction in drag, when compared with the steady state situation.

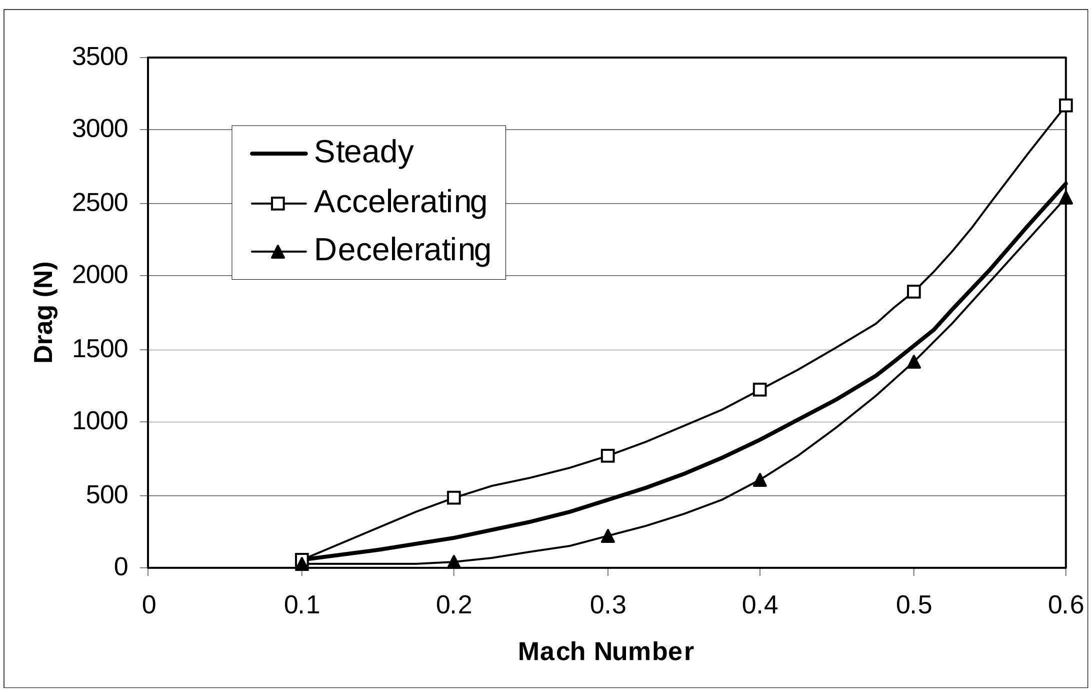

Figure 4.38: Subsonic large sphere drag at steady, +106g and –106g.

Figure 4.39 shows the results obtained for the artillery shell over the entire range of Mach numbers. In figure 4.40 the subsonic portion of the graph is enhanced in order to improve clarity. For the shell there is only a marginal difference between the steady and unsteady cases in the subsonic region, with the only significant difference observed in the transonic range of Mach numbers. Figure 4.41 expands the transonic portion of figure 4.39. Although the differences between the steady and unsteady cases in the transonic range of Mach numbers are significant they do not follow the trend in the subsonic regime. This will be discussed in more detail in chapter 5.

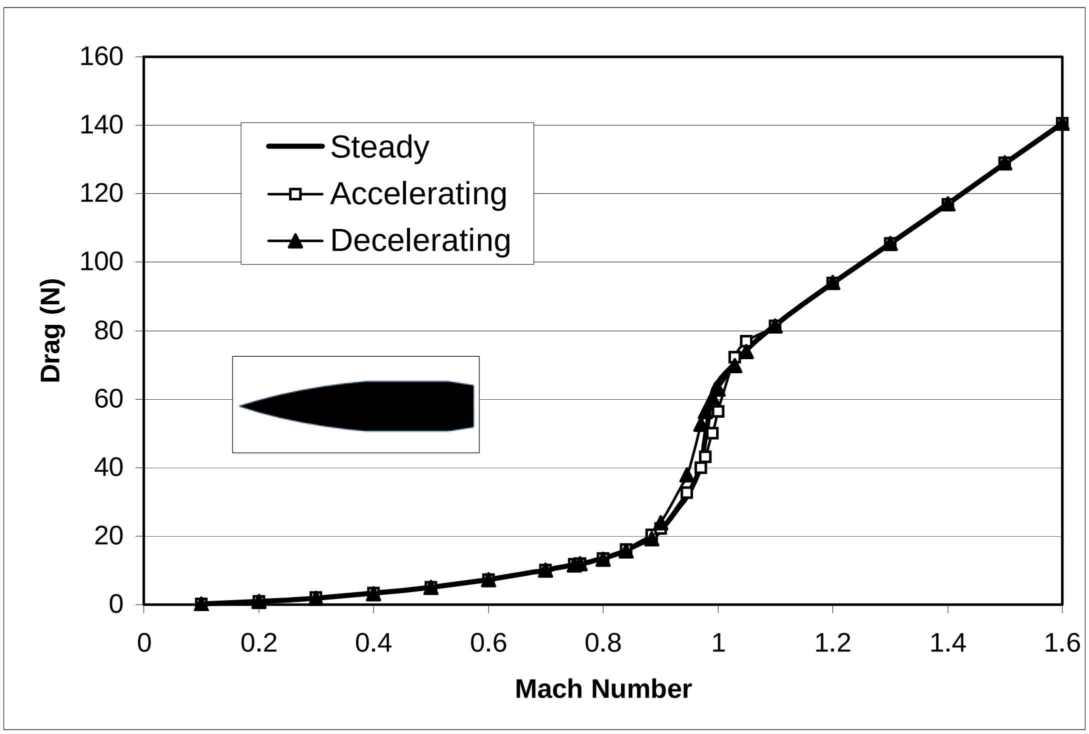

Figure 4.39: Artillery shell drag at steady, +106g and –106g.

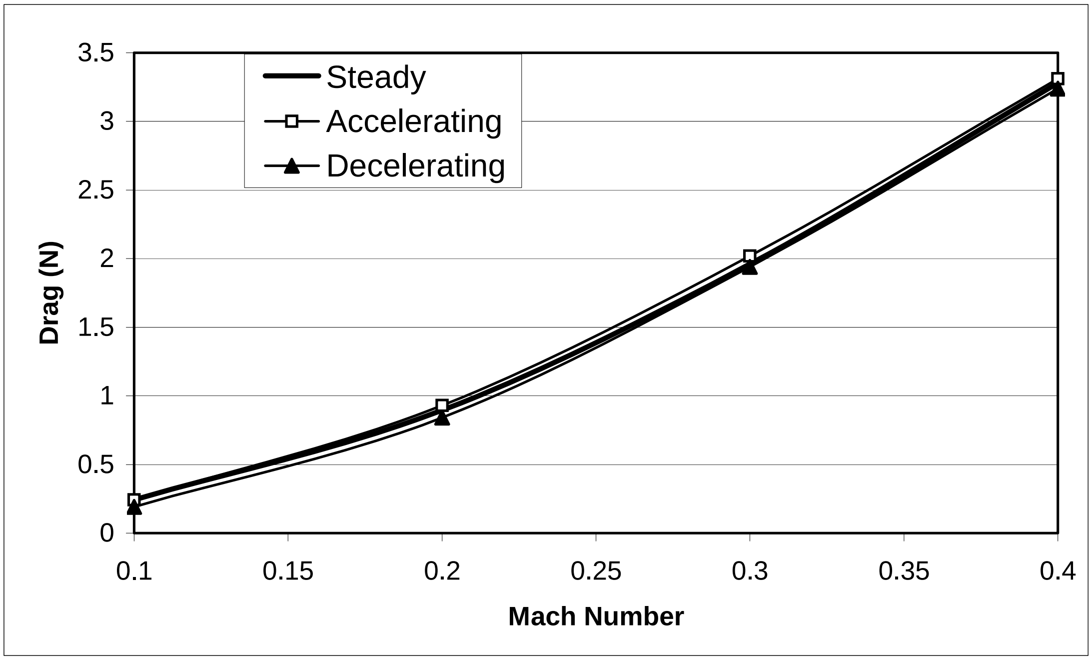

Figure 4.40: Subsonic artillery shell drag at steady, +106g and –106g.

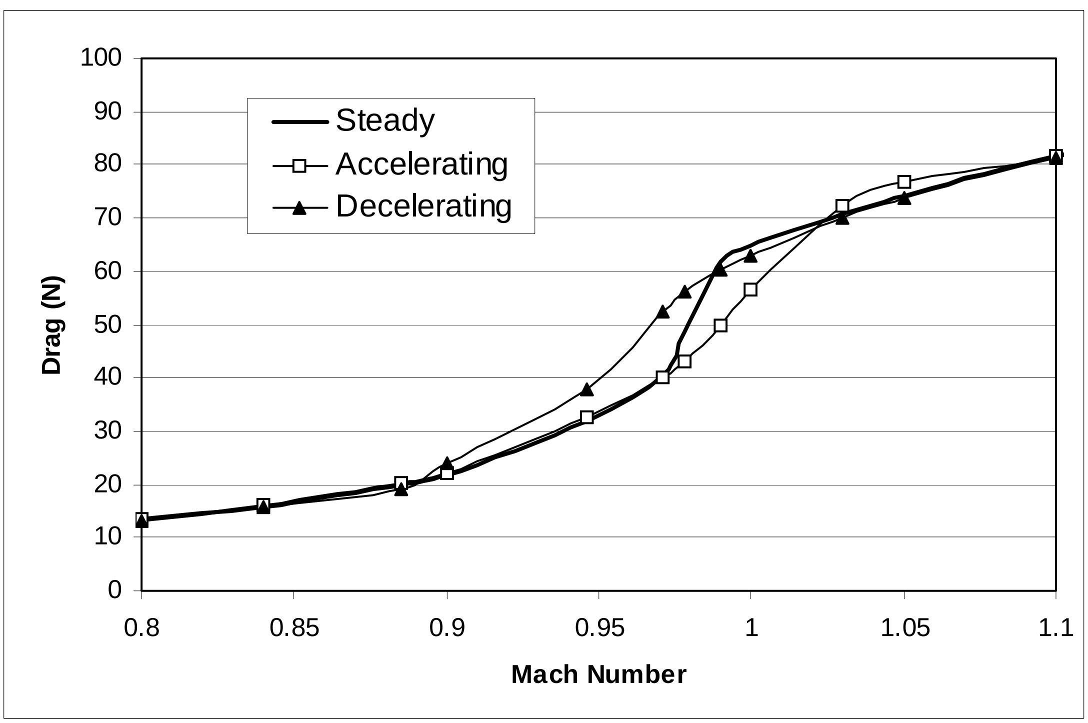

Figure 4.41: Transonic artillery shell drag at steady, +106g and –106g.

When comparing the subsonic portions of the curves for the sphere and the artillery shell it is obvious that the sphere subsonic drag is substantially changed as a result of acceleration and retardation. The subsonic results for the shell show an insignificant difference between the steady and the unsteady cases. However, even though not clearly visible, at any subsonic Mach number for the shell, acceleration does results in a slight increase and retardation in a slight reduction in drag when compared with the steady state values.   These results show that objects of different shape are not equally sensitive to the aerodynamic effects of acceleration.

It is important to note that the numerical modelling of the shell is more straightforward than the sphere because it is characterised by sharp corners at the base rather than curved surfaces on which the turbulence and boundary layer modelling is more complex. Therefore, the turbulence models used in this research are better suited for the analysis of the shell rather than the sphere, and it is the shell that is further analysed in the next chapter.

4.4 Discussion of results

When an object is accelerated in a compressible fluid, the unsteady flow field generated is not allowed sufficient time to reach equilibrium at any specific Mach number. It is therefore different to the steady state flow field at that same Mach number and is in fact influenced by its own flow field history. It has similarities to steady state flow fields corresponding to earlier conditions. As a result, the unsteady lift, drag and pitching moment at any given Mach number should also be different to the steady state values.

For example in figures 4.5 and 4.20, during acceleration, subsonic lift values were found to be lower than the corresponding steady state lift values. This can be explained by the fact that during subsonic acceleration the low pressure region on top of the aerofoil is progressively reducing in pressure with increase in aerofoil velocity. However, as there is insufficient time for equilibrium to be reached the pressure at any given velocity will not be as low as the pressure at the same velocity under steady state conditions. This will result in lower lift values during acceleration. Conversely, during subsonic retardation the pressure on top of the aerofoil is progressively increasing, but since there is insufficient time for equilibrium this pressure will not be as high as the steady state pressure at the same velocity. This will result in higher subsonic lift values during retardation.

It is not possible, however, to explain the unsteady subsonic drag results of this chapter simply by considering equilibrium effects and flow history alone. For example, during acceleration, flow history would require that the flow field reflect some of the characteristics of earlier conditions, when the Mach number was lower. As drag forces are also lower at those lower Mach numbers a similar effect would be expected under unsteady conditions. However, as shown in figures 4.2 and 4.17, the subsonic results from this chapter consistently show higher unsteady drag during acceleration, in comparison with the steady state values at the same Mach number. With deceleration the opposite effect is observed. Flow history alone would predict higher drag, but the results from this chapter consistently show lower drag values during deceleration in comparison with the steady state.

This can be explained by taking the inertia of the fluid into account. Under steady state conditions when an object moves at constant velocity through a fluid, at any specific location in the flow field with respect to the object, the flow velocity remains constant. During the acceleration of the object additional momentum is introduced into the fluid resulting in a change in the flow velocity at most points throughout the flow field. It is the resistance to this change that ultimately results in the overall increase in drag during acceleration, compared to the steady state condition. Clearly, based on the results from this chapter this component of unsteady drag outweighs the effects of flow history, which would have otherwise reduced the overall unsteady drag value in comparison with the steady state condition at the same Mach number.

During deceleration, if the flow resistance to the negative momentum introduced into the system acted in isolation, the object would experience a forward thrust. Therefore, in combination this should result in a reduction in drag, which is supported by the findings of this chapter. Again, it must be pointed out that this negative component of drag must have outweighed the effects of flow history, which would have otherwise resulted in an increase in unsteady drag compared to the steady state value at the same Mach number.

In the transonic region, as shown in figures 4.3, 4.6, 4.18 and 4.21, these effects are more pronounced but follow a very different trend. This is because, during accelerating or decelerating through transonic Mach numbers, the unsteady condition of the flow field produces different shock wave positions, on and around the surface of an object, in comparison to the steady state positions at the same Mach number. This difference in the position of the shock wave results in a more significant difference in the aerodynamic forces and moments between the steady and unsteady cases than observed outside the transonic range. In chapter 5 this subject will be dealt with in detail.

5. Shock wave dynamics

In the previous chapter it became apparent that the difference between the steady and unsteady aerodynamic forces was generally greater in the transonic range of Mach numbers. The main focus of this chapter is to investigate in more detail the unsteady aerodynamic effects of acceleration at transonic Mach numbers. This will provide explanations for some of the effects observed in chapter 4 and will also generate a new understanding of the behavior of shock waves during unsteady transonic conditions.

As mentioned previously some of the findings of this report were submitted for publication by the author and have already been published. Of particular relevance to this chapter is the publication in the Shock Wave Journal listed at the beginning of this thesis. It demonstrates the unsteady effects of transonic acceleration on shock wave dynamics. This chapter uses that material as a point of departure. Then, in order to confirm and further develop those findings the RAE 2822 aerofoil, modeled by Fluent for validation 11, and a diamond shaped aerofoil are used. At the end of this chapter a brief investigation into the aerodynamic effects of transonic acceleration on an axisymmetric body is conducted.

Confirmation of findings through the use of different case studies is an important aspect of this research. It is very likely, even in an experimental model, that certain effects observed in an investigation are specific to the particular shape of the object or other parameters in the system. In numerical models further peculiarities arising from the mesh or the specific model can produce results that have no general significance. However, by using different cases, greater confidence in the validity of the general findings is created.

5.1 Transonic shock waves on and around airfoils

The transonic results from the biconvex and the RAE 2822 airfoils obtained in the previous chapter are further investigated in this chapter. As mentioned in chapter 4, the airfoils had cord lengths of 1m and the biconvex had a maximum thickness of 0.1 m. High accelerations of 106g and –106g and moderate accelerations lower than 9g were used. The airfoils were subjected to the following conditions:

Free-stream temperature:	300 K
Atmospheric pressure:	101 325 Pa
Accelerations:	1041 m/s^2 (106g) and 86.77 m/s^2 (8.845g)
Decelerations:	–1041 m/s^2 and –86.77m/s^2
Angle of attack:	4 degrees for biconvex, 2.79 degrees for RAE 2822

Steady state constant velocity simulations were conducted at Mach numbers ranging from 0.1 to 1.6. Then, starting at Mach 0.1, the airfoils were subjected to accelerations of 1041 m/s^2 (106g) and 86.77 m/s^2 (8.845g) through the same range of Mach numbers. Finally, starting at Mach 1.6, they are decelerated at –1041 m/s^2 and –86.77 m/s^2 down to Mach 0.1. However the transonic portion of the data was selected for the investigation in this chapter.

Pressure flood plots, density contour plots and graphs of pressure versus position were used in conjunction with the already acquired transonic results from chapter 4 to explain the nature of the aerodynamic forces and to obtain a better understanding of the unsteady transonic flow fields generated during acceleration. Forces and moments were not non-dimensionalized in order to avoid ambiguity in choosing an arbitrary reference velocity.

5.1.1 Dynamics of shockwaves on biconvex aerofoil surfaces

Figures 5.1, 5.2 and 5.3 show the transonic portion of the drag, lift and pitching moment curves for the biconvex aerofoil under high acceleration of 106g and deceleration of -106g and at constant velocity. The subsonic portions of these curves are not shown, as these were handled in chapter 4. There, it was shown that for subsonic Mach numbers acceleration produced an increase in drag and a reduction in lift and retardation a reduction in drag and an increase in lift. However, no such general trend is observed here in the transonic region, as the unsteady lift and drag values fluctuate above and below the steady state values and the differences are more significant in this region. The unsteady lift and drag curves also shift to the right and left of the steady state curve, shifting to the right with acceleration and to the left with deceleration.

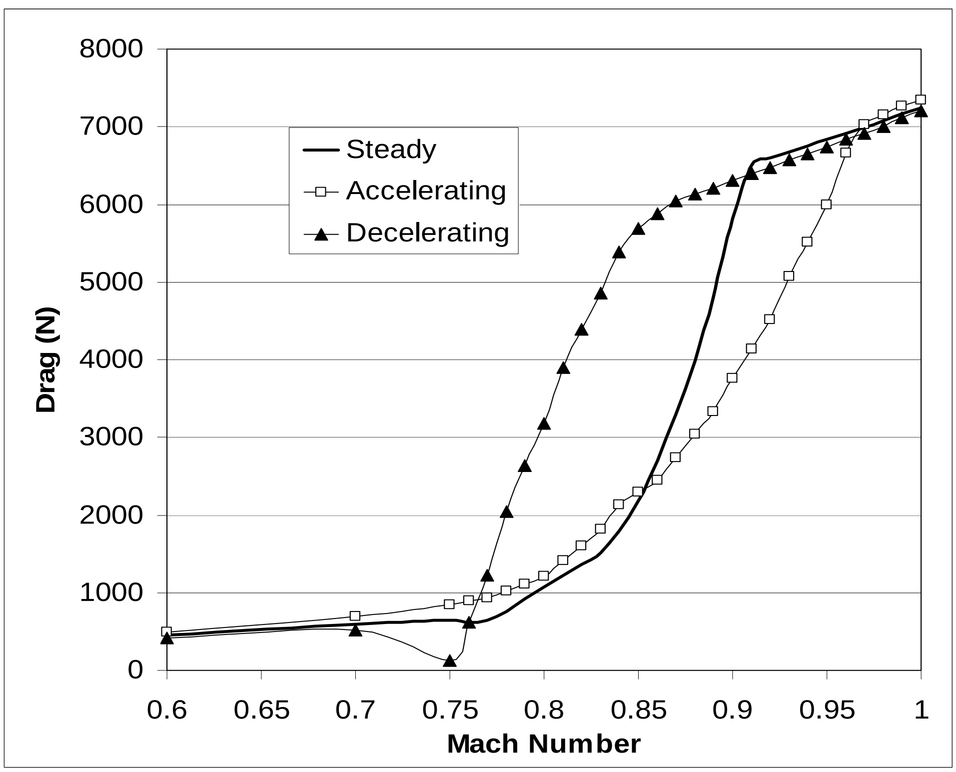

Figure 5.1: Biconvex transonic drag at steady, +106g and –106g.

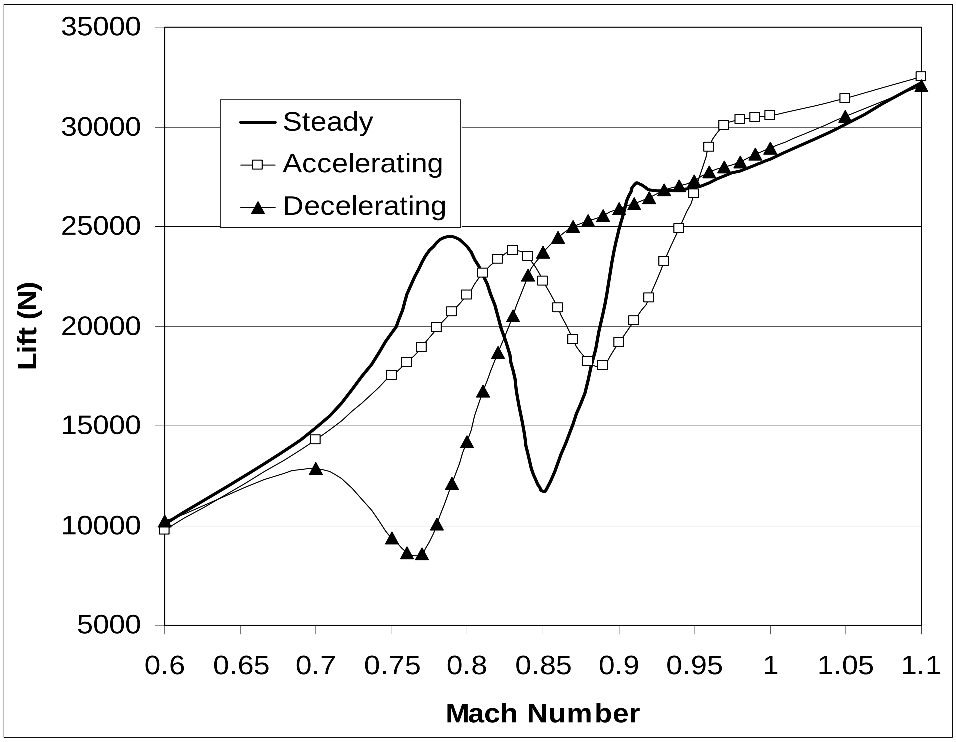

Figure 5.2: Biconvex transonic lift at steady, +106g and –106g.

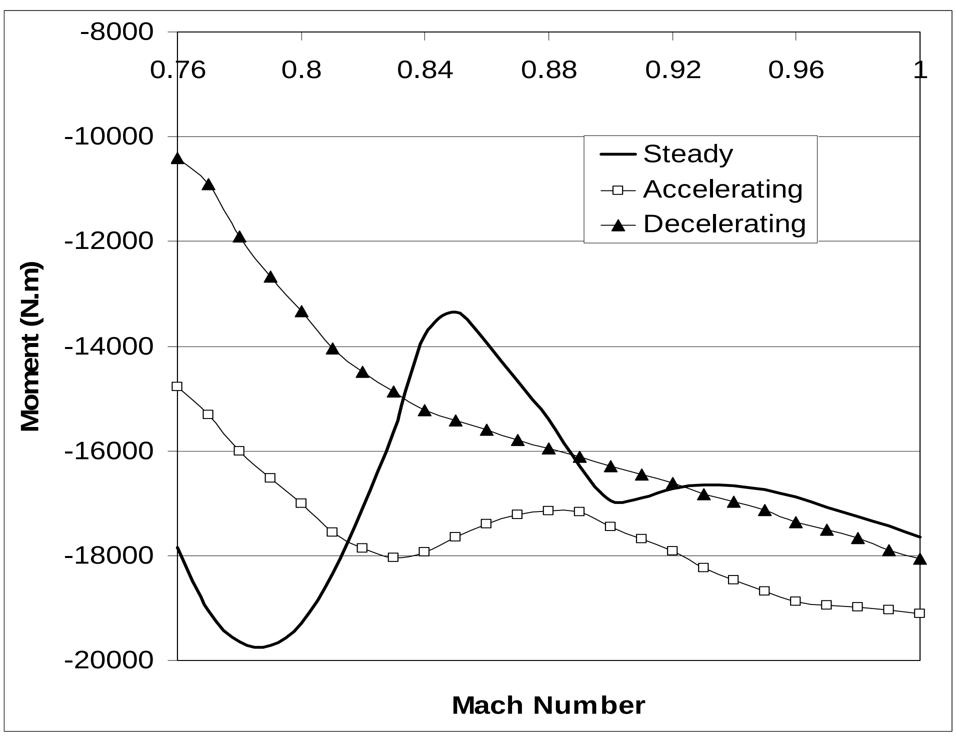

Figure 5.3: Biconvex transonic pitching moment at steady, 106g and –106g.

Figures 5.4 and 5.5 represent the moderate acceleration cases. The steady and unsteady drag and lift variations with transonic Mach numbers are shown for the biconvex aerofoil. Acceleration = 86.77 m/s^2 (8.845g) and deceleration = -86.77 m/s^2 for the unsteady cases. It can be observed that, in the transonic range of Mach numbers, even with accelerations slightly less than 9g, the unsteady effects are still significant.

In order to explain the differences between the steady and unsteady cases in the transonic range of Mach numbers, the flow field around the aerofoil needs to be taken into consideration. Of particular importance is the variation in the position of the shock wave on the surfaces of the aerofoil. In figures 5.6 to 5.9 pressure flood plots and graphs of pressure versus position are used to show variations in shock wave position on the surfaces of the biconvex aerofoil, for the steady and unsteady cases, at different Mach numbers.

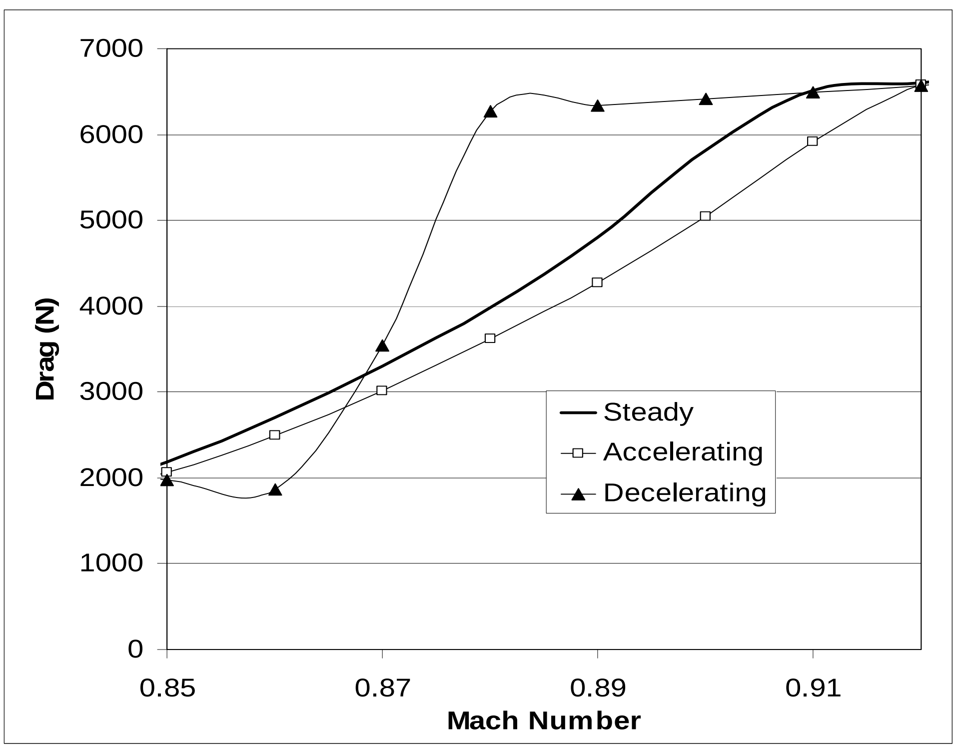

Figure 5.4: Biconvex transonic drag at steady, +8.845g and –8.845g.

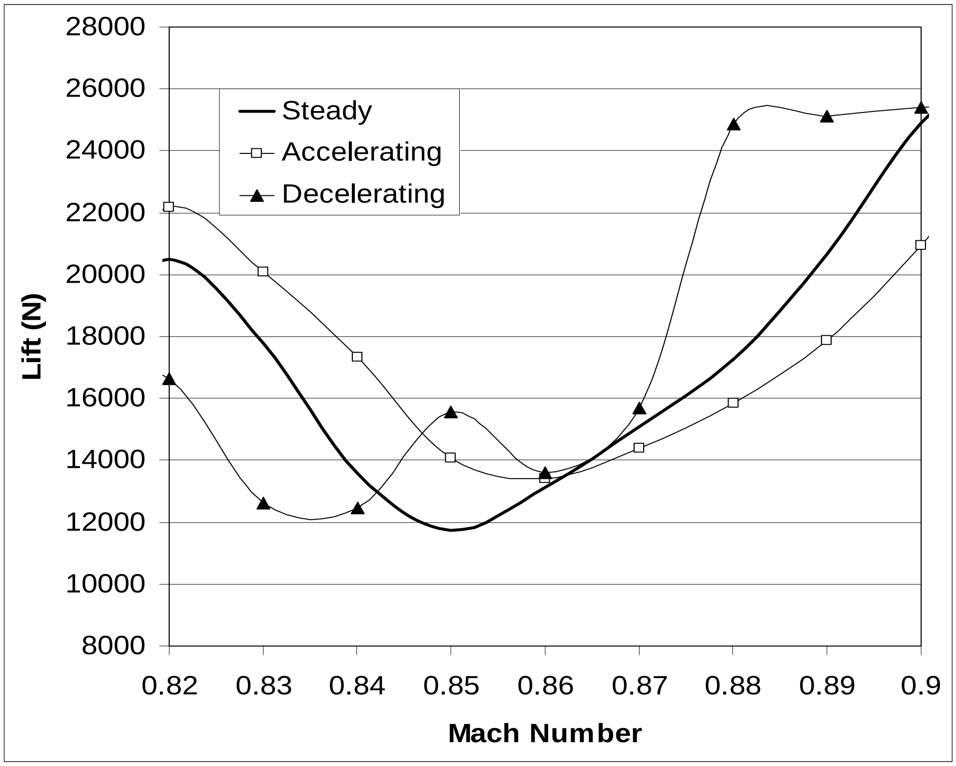

Figure 5.5: Biconvex transonic lift at steady, +8.845g and –8.845g.

Figure 5.6 shows the variation in the shock wave position at Mach 0.89. Acceleration = 1041 m/s^2 (106g) and deceleration = -1041 m/s^2 for the unsteady cases. In figure 5.6 (a) the pressure flood plots for the 3 cases are shown. When the steady state flow field on the left is compared with the accelerating scenario shown in the middle, the shock wave on the upper surface of the aerofoil has moved to the left in the accelerating case even though at that instant the Mach number is the same in both cases. This can be confirmed by looking at the graphs of pressure versus position shown in figures 5.6 (b) and 5.6 (c).

It is important to note that there is a high-pressure region behind the shock wave, which usually reduces lift and drag and can also affect the pitching moment on the aerofoil. In the accelerating scenario, the shock wave moves to the left towards the leading edge of the aerofoil. This results in an increase in the size of the high-pressure region behind the shock wave, which in turn should result in a reduction in lift and drag when compared with the steady state situation. In figures 5.1 and 5.2 a confirmation of the above explanation can be observed, where at Mach 0.89 both the accelerating lift and drag are lower than steady state values. Conversely, in the decelerating scenario on the right of figure 5.6 (a), confirmed by the graph of pressure versus position in 5.6 (d), where the shock wave has moved completely to the right, wiping out the high-pressure region behind the shock on the upper surface of the aerofoil, lift and drag are expected to rise significantly. This can be observed in figures 5.1 and 5.2, where the decelerating lift and drag values, at Mach 0.89, are substantially higher than the steady state values.

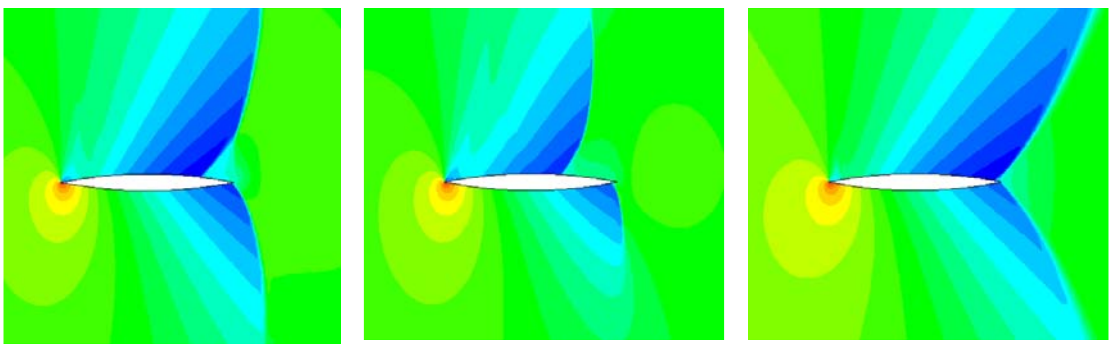

(a) From left to right flood plots of steady state, 106g and –106g.

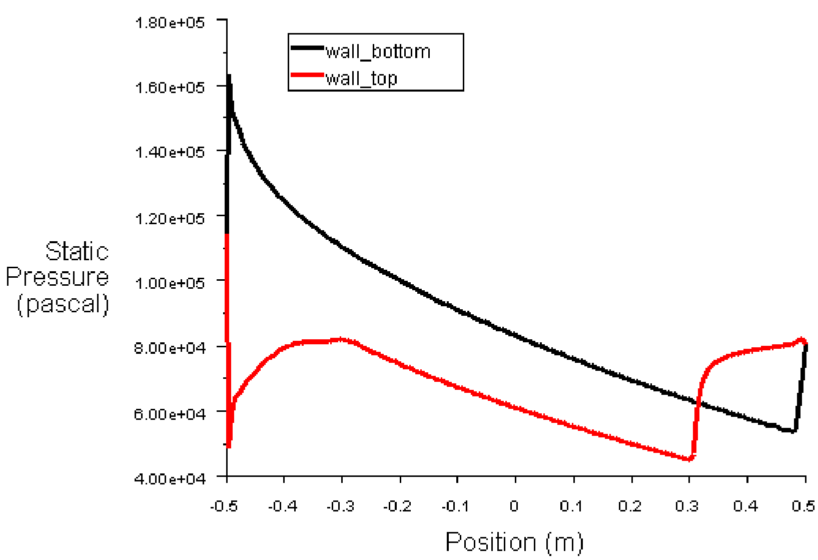

(b) Steady state pressure versus position.

Figure 5.6: Biconvex shock waves at steady state, 106g and -106g at Mach 0.89.

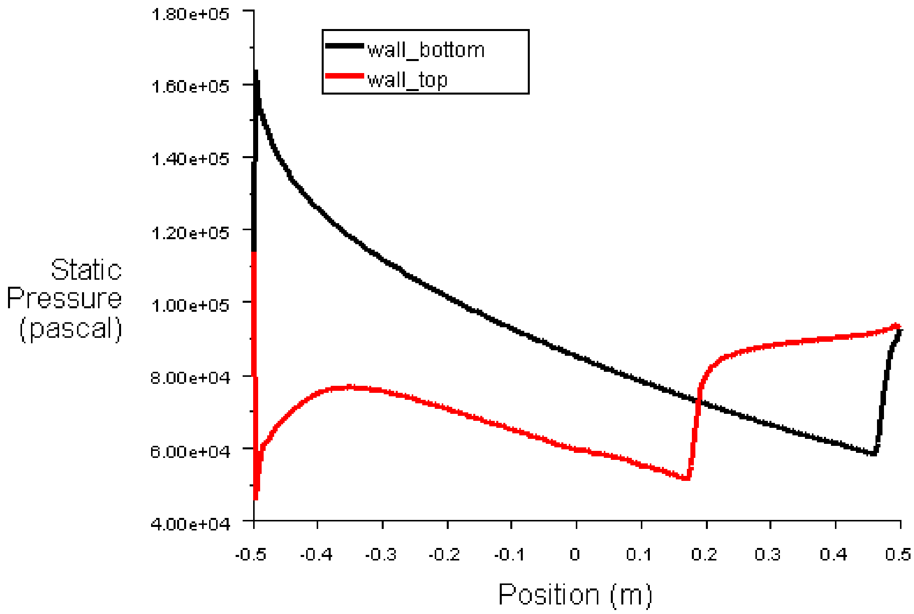

(c) Accelerating pressure versus position.

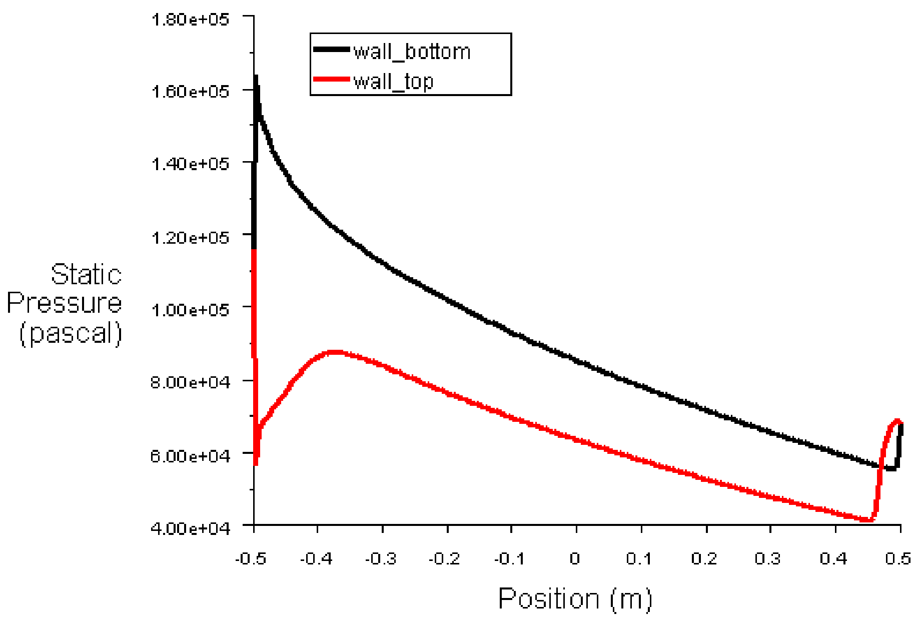

(d) Decelerating pressure versus position.

Figure 5.6: Continued

In figure 5.7 at Mach 0.86, the accelerating and steady state conditions show similar shock position and low-pressure regions on the upper surface of the aerofoil. However, at the lower surface the low-pressure region for the accelerating case is smaller. As a result, a higher lift value is expected. The drag should be lower as the low-pressure region is situated towards the trailing edge of the aerofoil and a reduction in its size should reduce air resistance against forward motion. In the decelerating scenario, where the shock wave has moved completely to the right, wiping out the high-pressure region behind the shock on the upper surface, lift and drag are expected to be higher than the steady state situation. Confirmation of the above explanation can be observed at Mach 0.86 in figures 5.1 and 5.2.

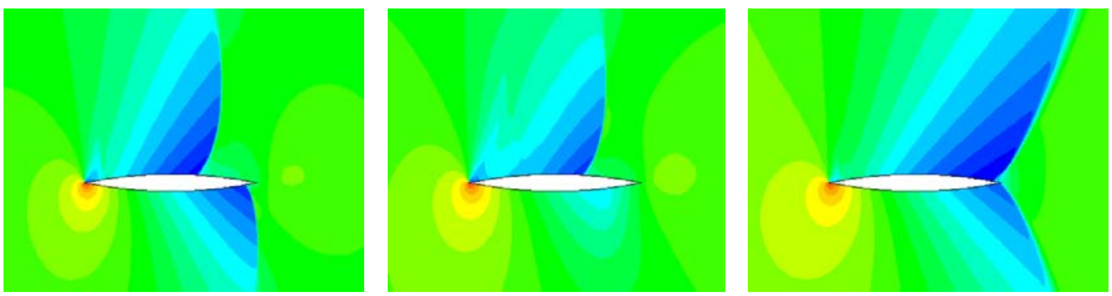

(a) From left to right flood plots of steady state, 106g and –106g.

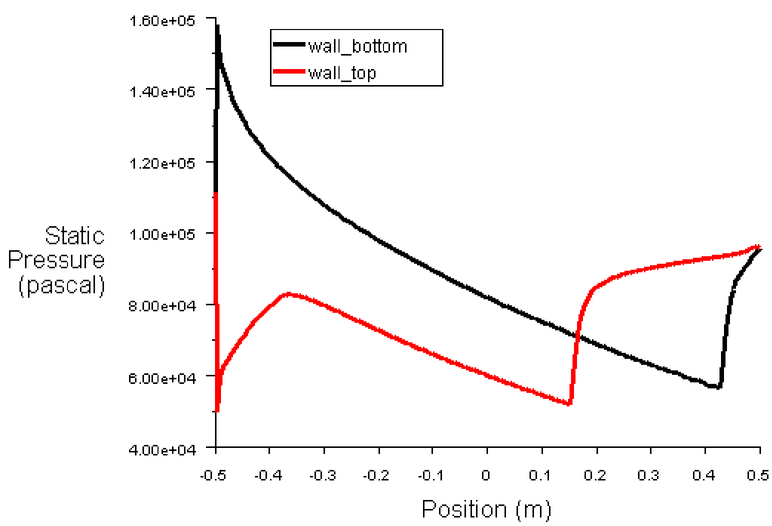

(b) Steady state pressure versus position.

Figure 5.7: Biconvex shock waves at steady state, 106g and -106g at Mach 0.86.

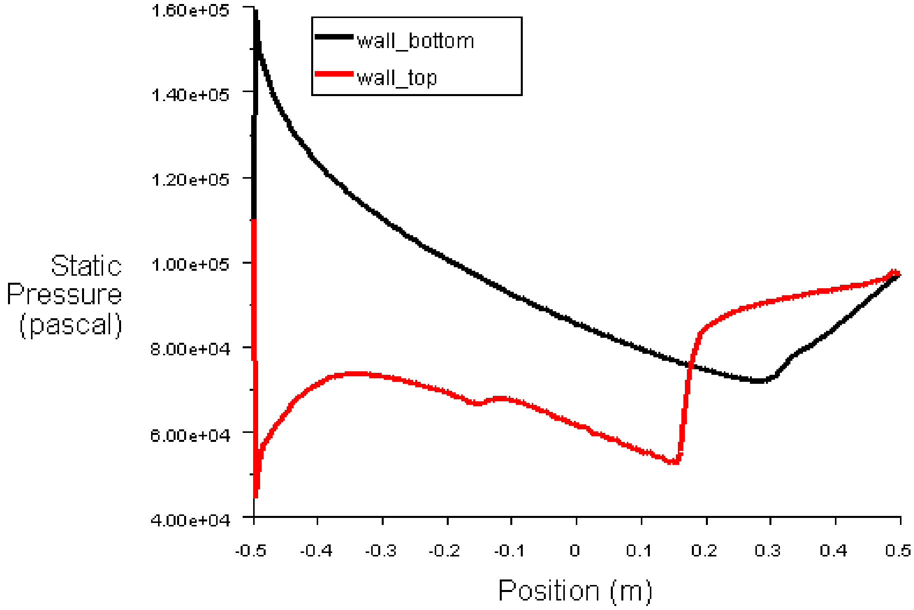

(c) Accelerating pressure versus position

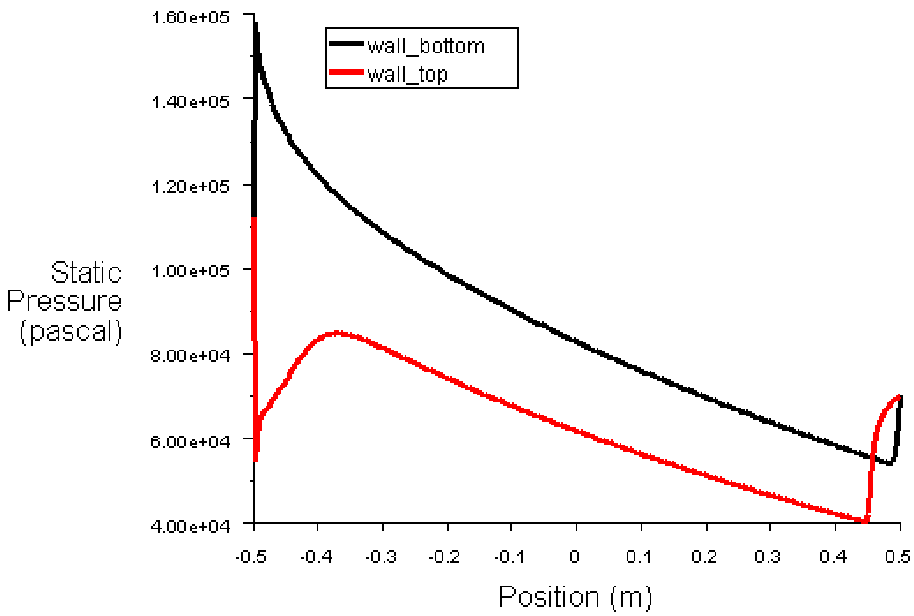

(d) Decelerating pressure versus position.

Figure 5.7: Continued.

Similar arguments can be used to explain the differences in aerodynamic forces at Mach 0.79 using figure 5.8. However, of particular interest is the fact that although the flow field around the steady state and accelerating scenarios are quite similar, the flow field around the decelerating case shown on the right of figure 5.8 (a) is very different. An explanation for this is given at the end of this chapter in section 5.4. The difference between the steady and unsteady moments is not always obvious by inspection of the flow field and can only be accurately determined through computation as was done in figure 5.3. The oscillation in pressure coefficient in figure 5.8 (b) and later in figure 5.9 needs to be the subject of further investigation.

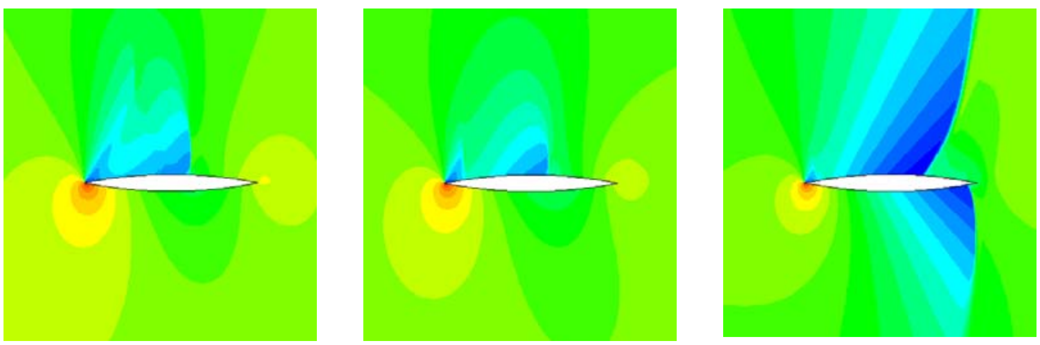

(a) From left to right flood plots of steady state, 106g and –106g.

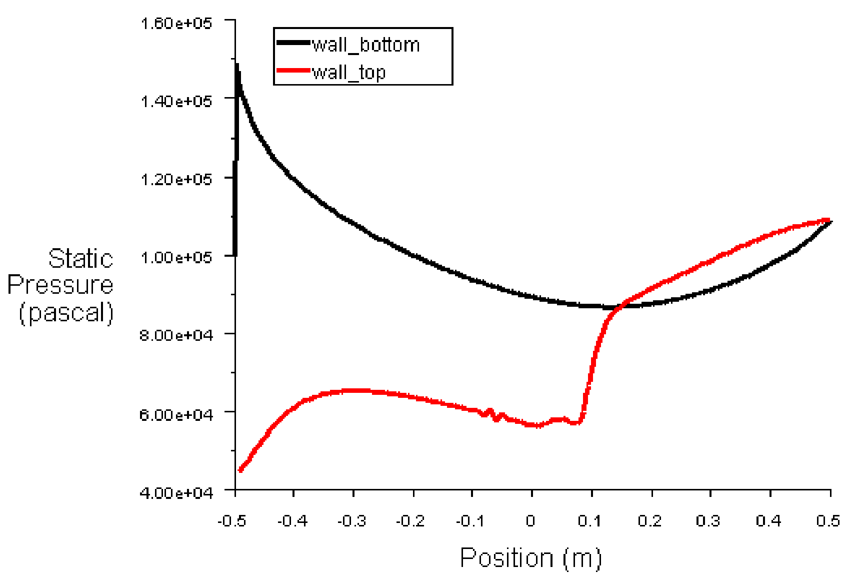

(b) Steady state pressure versus position.

Figure 5.8: Biconvex shock waves at steady state, 106g and -106g at Mach 0.79.

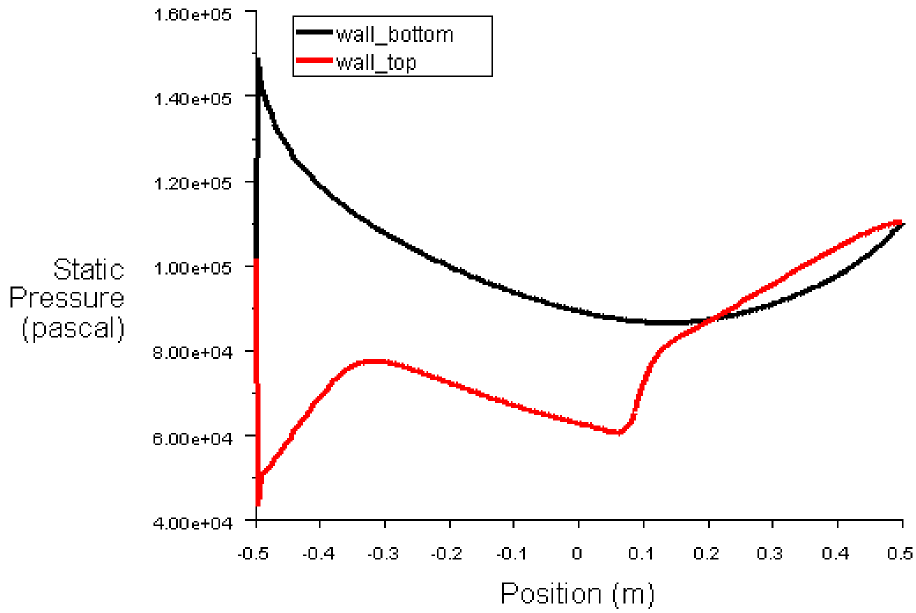

(c) Accelerating pressure versus position.

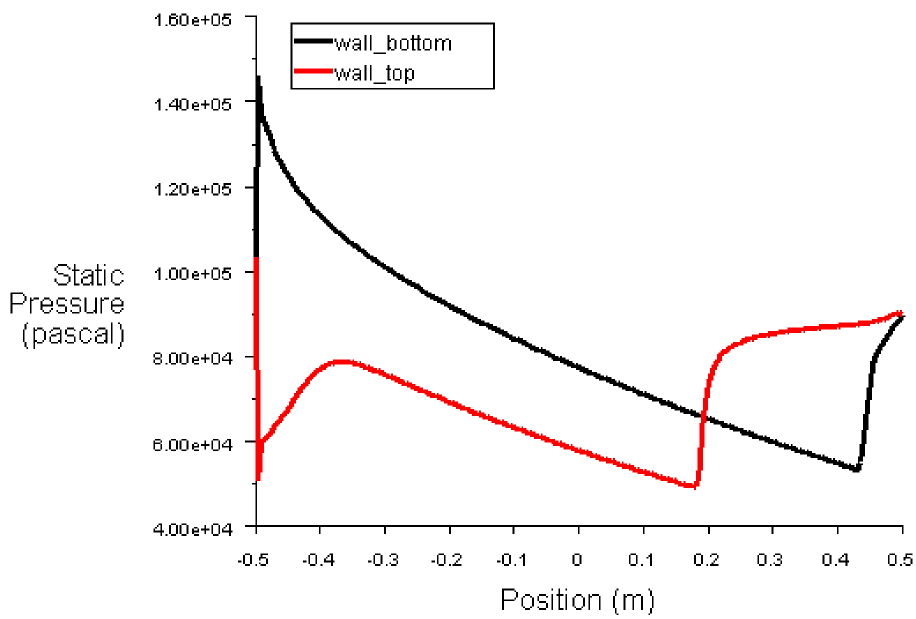

(d) Decelerating pressure versus position.

Figure 5.8: Continued.

Figure 5.9 compares the steady state scenario with lower accelerations of 86.77m/s^2 (8.845g) and −86.77m/s^2 at Mach 0.89. The accelerating shock has moved slightly to the left of the steady state but the decelerating shock wave has made a significant move to the right, close to the trailing edge of the aerofoil. This shows that even with accelerations or retardations slightly lower than 9g the movement of the shock wave can be significant. In figures 5.4 and 5.5 the transonic drag and lift curves for the lower accelerations are shown. As before, explanations could be given to relate the position of the shock waves in figure 5.9 to the differences in aerodynamic forces in figures 5.4 and 5.5 at Mach 0.89.

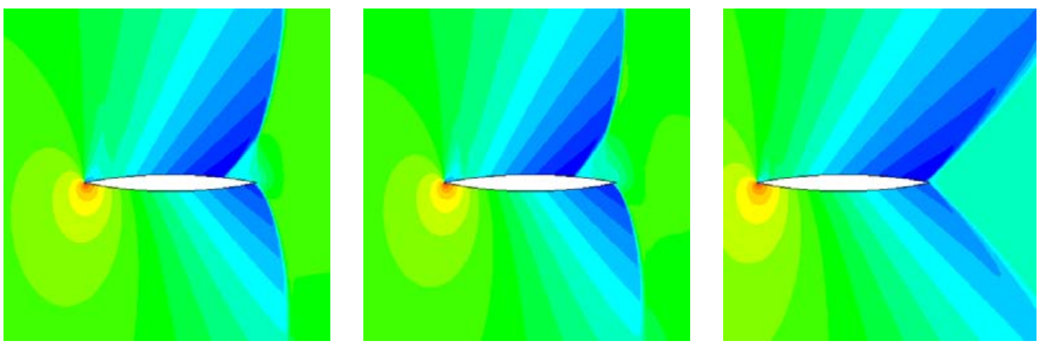

(a) From left to right plots of steady state, 8.845g and –8.845g.

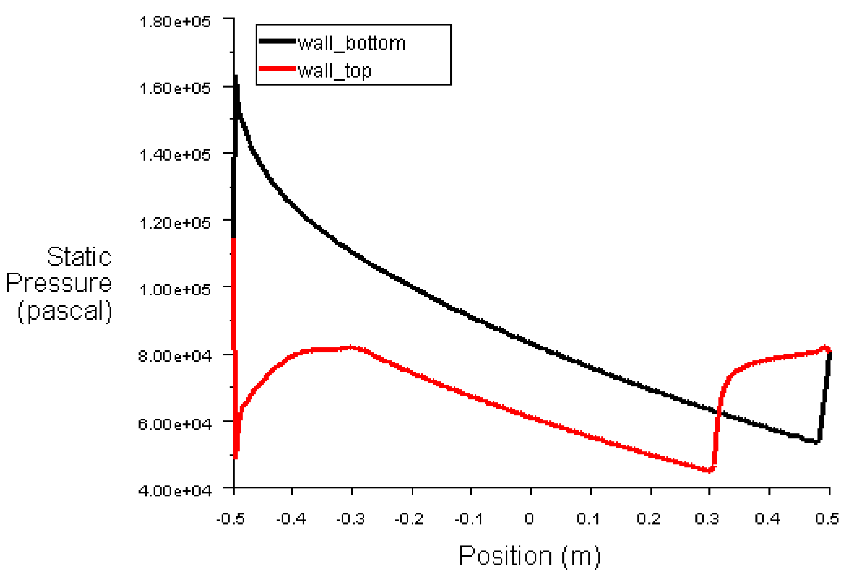

(b) Steady state pressure versus position.

Figure 5.9: Biconvex shock waves at steady state, 8.845g and –8.845g at Mach 0.89.

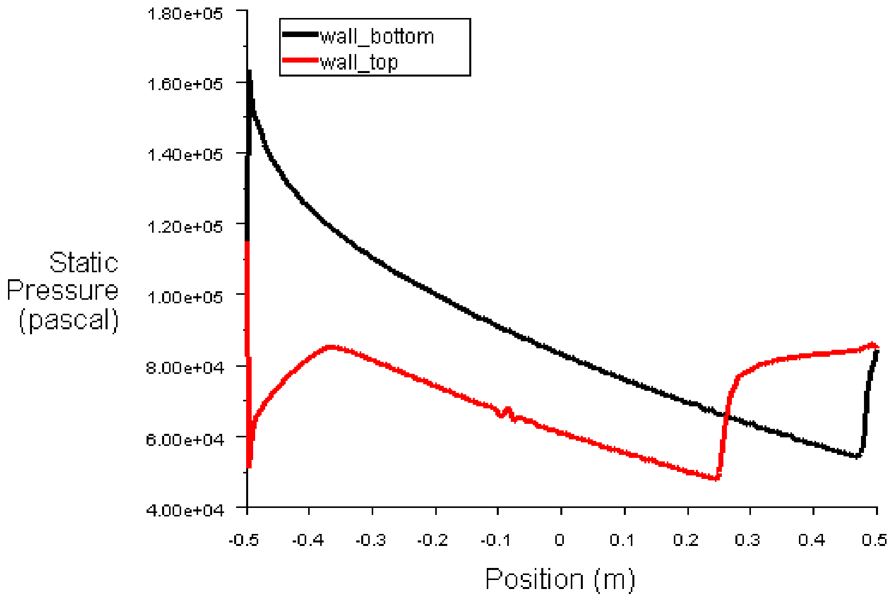

(c) Accelerating pressure versus position.

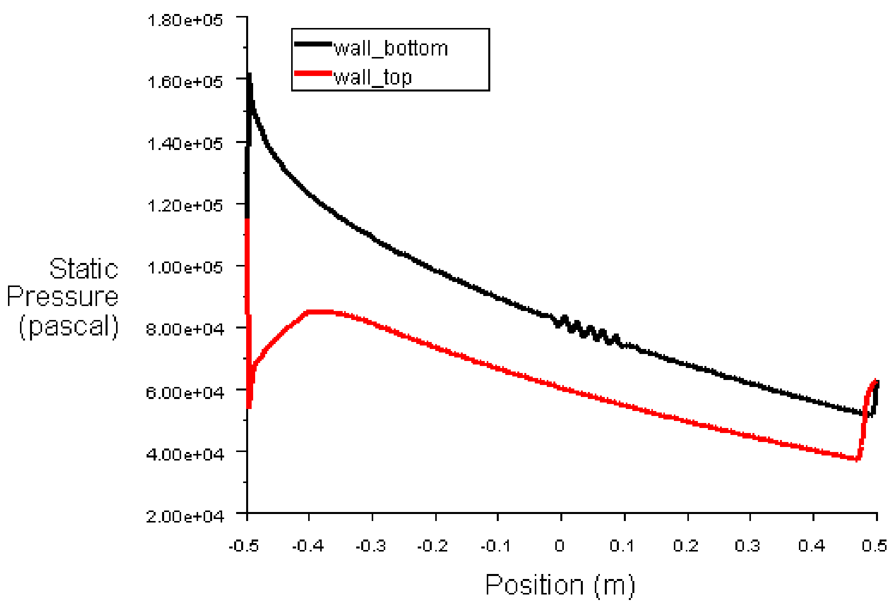

(d) Decelerating pressure versus position.

Figure 5.9: continued

At some steady state transonic Mach numbers, a compression wave follows in the wake of the aerofoil. This is a well-known phenomenon in steady state transonic aerodynamics and was, for example, documented by Becker [8] from case histories that took place before 1950. However, the behaviour of this wave during acceleration and deceleration is of interest here.

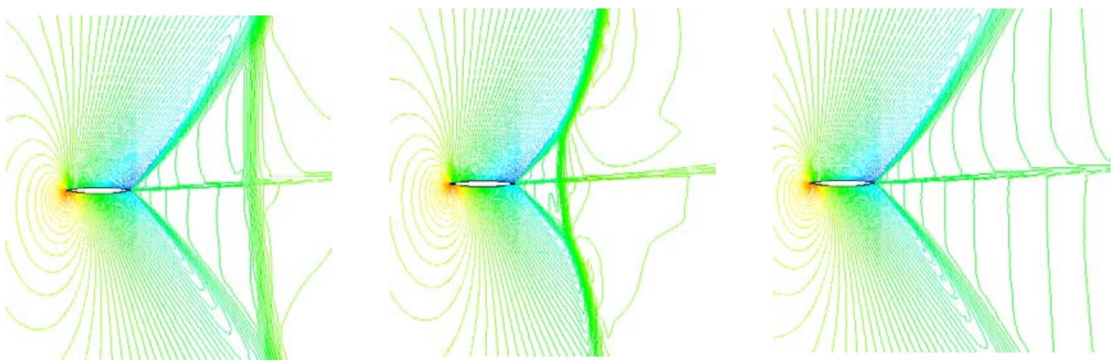

Figure 5.10: Density contour plots showing variation in the position of a trailing compression wave behind the biconvex aerofoil, for the steady and unsteady cases, at Mach 0.95. On the left constant velocity is shown, in the middle acceleration and on the right deceleration. Acceleration = 86.77 m/s^2 (8.845g) and deceleration = -86.77 m/s^2 for the unsteady cases.

It was found, from the numerical studies performed for this research that the trailing compression wave moved closer to or away from the trailing edge of the aerofoil during acceleration or retardation at the same instantaneous Mach number. Figure 5.10 shows the density contour plots for the biconvex aerofoil at Mach 0.95 for the steady and unsteady cases, with acceleration of 86.77m/s^2 (8.845 g) and deceleration of −86.77m/s^2 for the unsteady cases. On the left constant velocity is shown, in the middle acceleration and on the right deceleration. Comparison between the different cases shows that during acceleration the compression wave moves closer to the trailing edge and strengthens. Conversely, during deceleration the compression wave moves away and falls behind the trailing edge reducing in intensity. In figure 5.11, a better view of the compression wave during deceleration is shown, by zooming out of the diagram in figure 5.10.

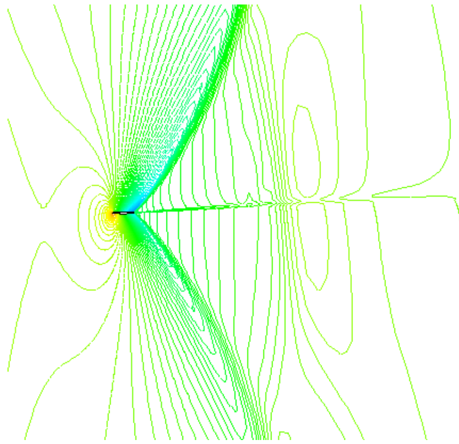

Figure 5.11: The trailing wave behind the biconvex aerofoil, at Mach 0.95 and deceleration of -86.77 m/s^2, captured here by zooming out of the diagram on the right of figure 10.

The development of the trailing compression wave is investigated in figures 5.12 and 5.13. In figure 5.12 a viscous turbulent model (Spalart–Allmaras) and in figure 5.13 an inviscid model is used. Initially, by considering the viscous model, it appears as though the lambda-foot at Mach 0.89 shown on the left of figure 5.12 evolves to generate the trailing compression wave at higher Mach numbers.

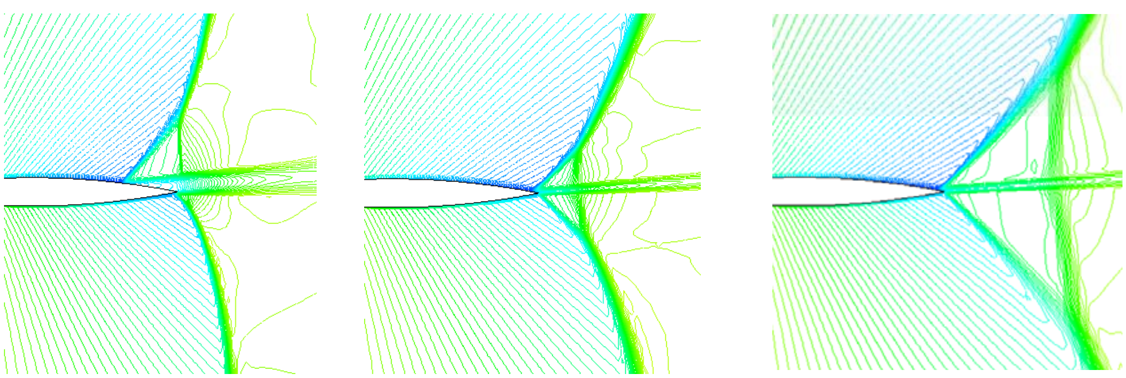

Figure 5.12: Using the Spalart-Allmaras (viscous) turbulence model the steady state density contour plots are examined, from left to right, at Mach 0.89, 0.91 and 0.92 respectively, showing the evolution of the trailing wave.

However, the inviscid case in figure 5.13 shows no lambda foot at Mach 0.89. In fact no lambda foot appears at any Mach number in the inviscid case as this phenomenon is viscosity related and is brought about by shock wave boundary layer interaction [49]. Even so, when using the inviscid model, the trailing wave still develops as the Mach number is increased. This shows that the development of the trailing compression wave is purely pressure related, born from the interaction of the two concave tail shock stream lines in the wake of the aerofoil, and inviscid numerical models should be able to predict the actual position of this wave.

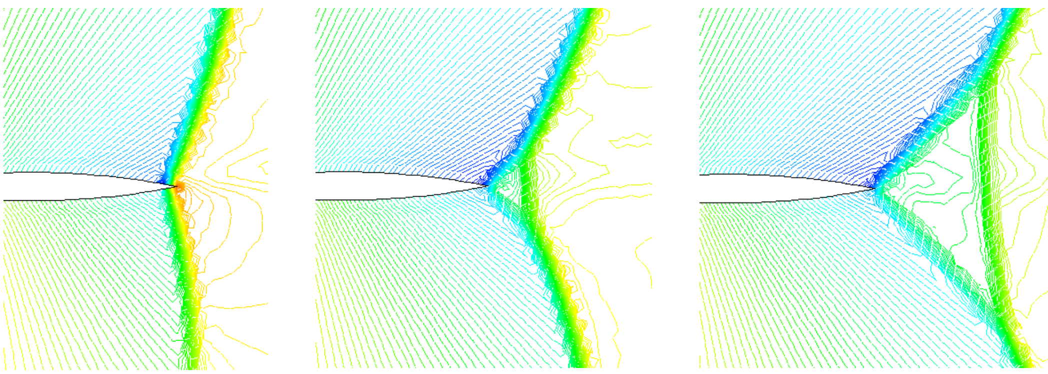

Figure 5.13: The evolution of the trailing wave, using Fluent's inviscid model. From left to right the steady state density contour plots are examined at Mach 0.89, 0.91 and 0.92 respectively.

Under steady state conditions, a bow shock appears in front of the aerofoil at supersonic aerofoil Mach numbers. This effect is absent in steady state at sonic and subsonic Mach numbers, as shown in figure 5.14. Similarly, although not shown here, it was found that during acceleration of the aerofoil from subsonic to supersonic Mach numbers the bow shock was absent at subsonic and sonic aerofoil velocities and only appeared when the aerofoil reached supersonic velocities relative to free stream conditions. However, during deceleration (-8.845g) of the aerofoil from supersonic to the subsonic Mach numbers, as shown in figure 5.15, there is an increase in the stand-off distance between the bow shock and the leading edge of the aerofoil. The bow shock is still present at sonic and subsonic Mach numbers, moving further ahead as the aerofoil Mach number is reduced by deceleration.

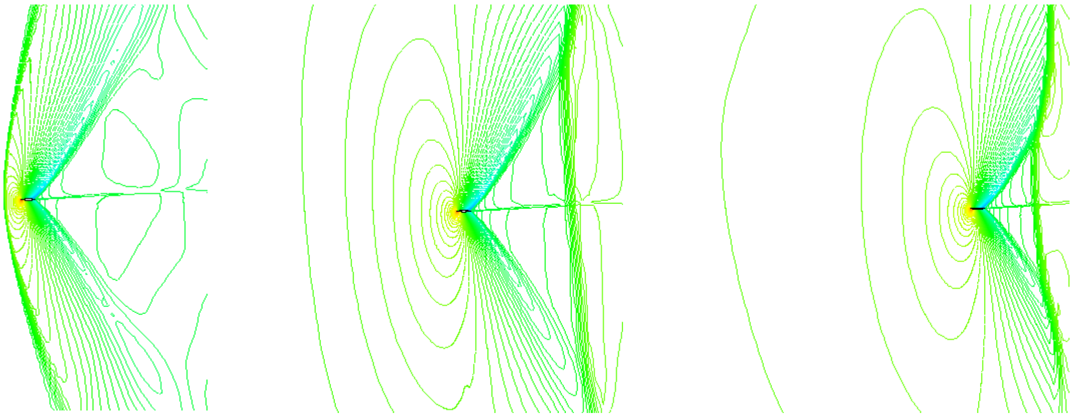

Figure 5.14: From left to right, steady state density contour plots at Mach 1.1, 1.0 and 0.97, showing that under steady state conditions the bow shock only exists at Mach numbers upside from 1.

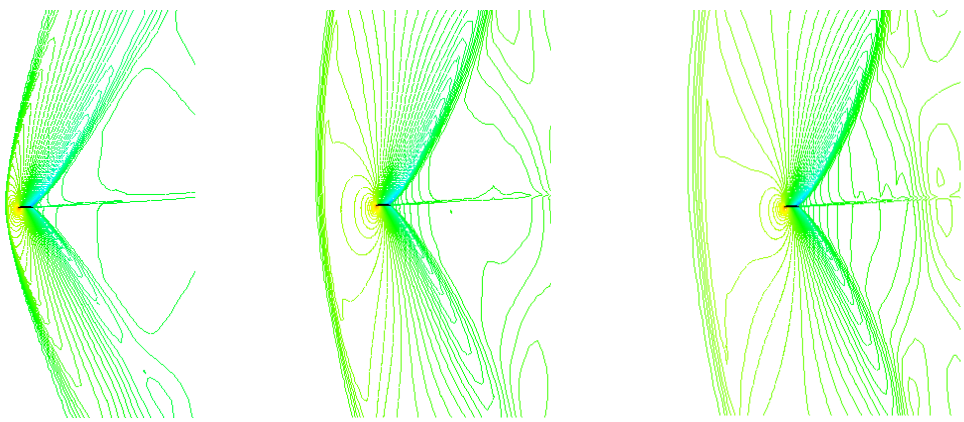

Figure 5.15: The variation in the position of the bow shock during deceleration from supersonic to subsonic Mach numbers. From left to right density contour plots at Mach 1.1, 1.0 and 0.97 are shown for a deceleration of -86.77 m/s^2 (-8.845g)

Figures 5.16 and 5.17 show the movement of the bow shock at a much higher deceleration (−106g). At higher decelerations the reduction in Mach number occurs much faster leaving little time for the flow field to react to the changing Mach number. This will in turn limit the bow shock movement with reduction in Mach number in comparison with the lower decelerating case of figure 5.15. As a result, as shown in figure 5.17, the bow shock is still visible well into the subsonic region at Mach 0.60. These effects are due to flow history and will be explained in section 5.4.

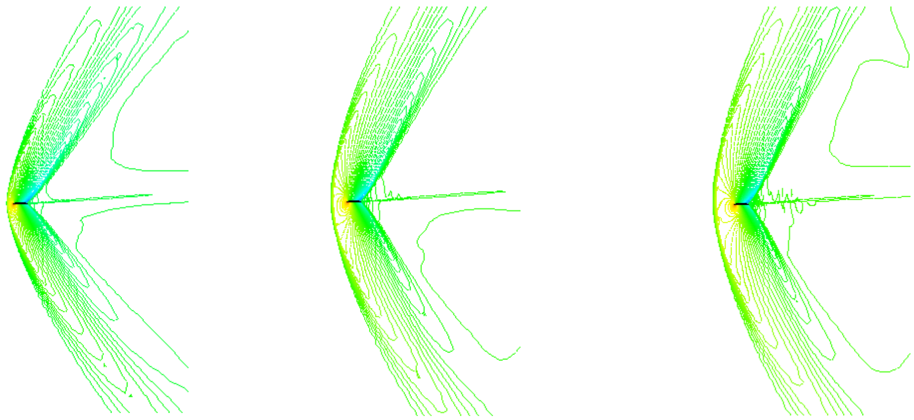

Figure 5.16: The variation in the position of the bow shock during deceleration from supersonic to subsonic Mach numbers. From left to right density contour plots at Mach 1.1, 1.0 and 0.97 are shown for a deceleration of -1041 m/s^2 (-106g).

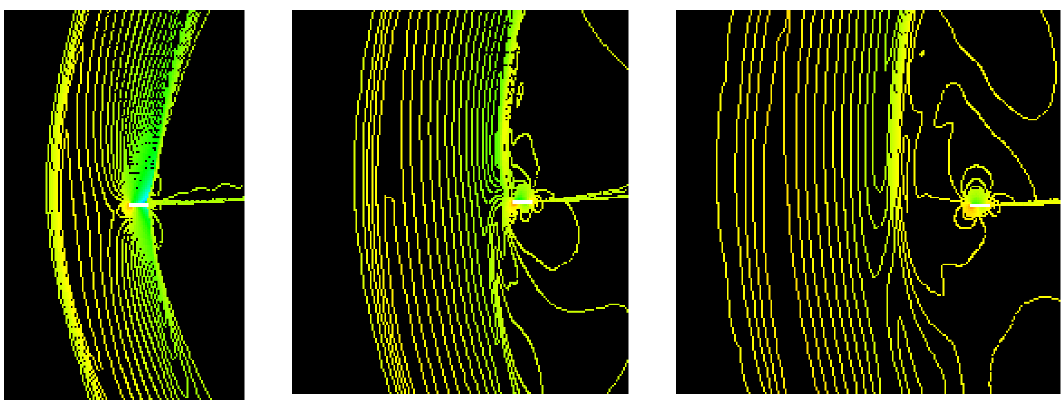

Figure 5.17: The variation in the bow shock position during deceleration of -1041 m/s^2 (-106g) for lower subsonic Mach numbers. From left to right density contour plots at Mach 0.82, 0.70 and 0.60 are shown. Also note the movement of the tail shock to the front of the aerofoil.

Study of the tail shock under high deceleration gives rise to another interesting observation, which is shown in figure 5.17. With deceleration the tail shock widens in angle, becoming more obtuse. At high decelerations it also moves forward over the surface of the aerofoil eventually ending up in front of the aerofoil. This is shown on the right-hand side of figure 5.17, when the aerofoil is decelerating at −106g at Mach

0.60. As discussed in section 5.4 this effect is also the result of flow history and is completely absent under steady state conditions and during acceleration. In figure 5.18 the diagram in the middle of figure 5.17, representing deceleration at Mach 0.7 is enlarged and compared with the steady state condition at the same Mach number. This shows that the tail shock, which has moved to the front of the aerofoil under deceleration at Mach 0.7, is completely absent under steady state conditions at the same Mach number.

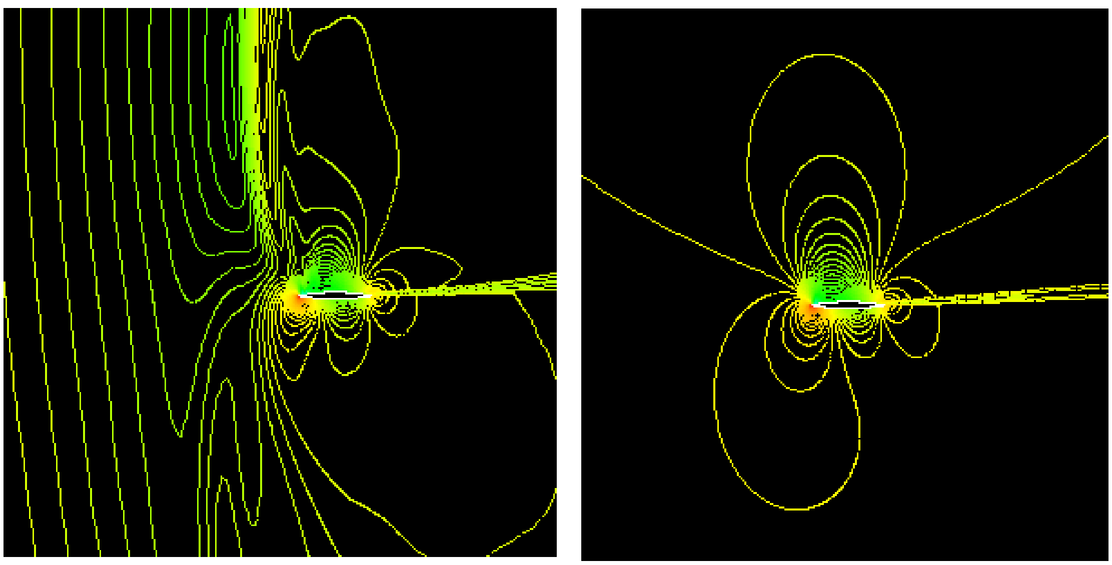

Figure 5.18: Unsteady density contour plot (deceleration = -1041 m/s^2) at Mach 0.7 and the steady state plot at the same Mach number are compared, showing that the tail shock is completely absent in the steady state condition.

5.1.2 Dynamics of shockwaves on RAE 2822 aerofoil surfaces

This section provides an opportunity to conduct a study of steady and unsteady shock wave dynamics using a more practical aerofoil. As mentioned before, the RAE 2822 aerofoil, meshed by Fluent and tested against experimental data, is used to confirm the general findings from the biconvex aerofoil case study.

Figures 5.19, 5.20 and 5.21 show the transonic portion of the drag, lift and pitching moment curves for the RAE 2822 aerofoil under high acceleration of 1041 m/s^2 (106g) and deceleration of -1041 m/s^2 and at constant velocity. As with the biconvex aerofoil, the unsteady transonic lift and drag values fluctuate above and below the steady state values and the differences are more significant than experienced in the subsonic region. The unsteady lift and drag curves also shift to the right and left of the steady state curve generally shifting to the right with acceleration and to the left with deceleration, as was previously observed.

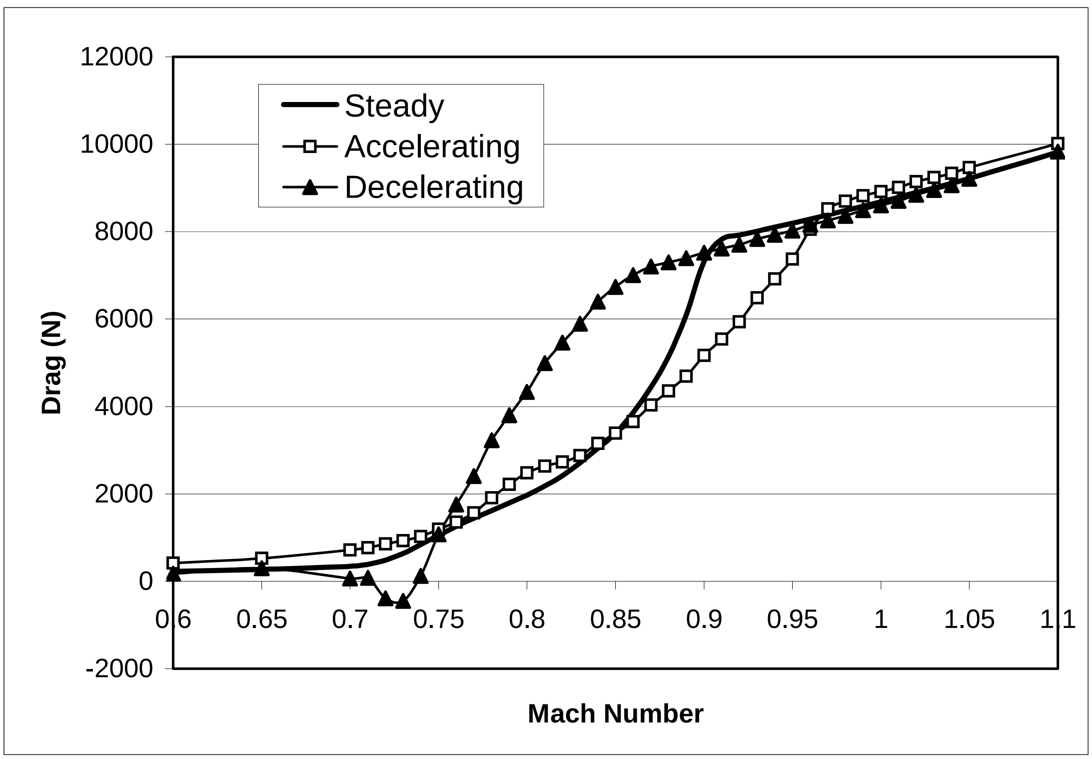

Figure 5.19: RAE 2822 transonic drag at steady, +106g and –106g.

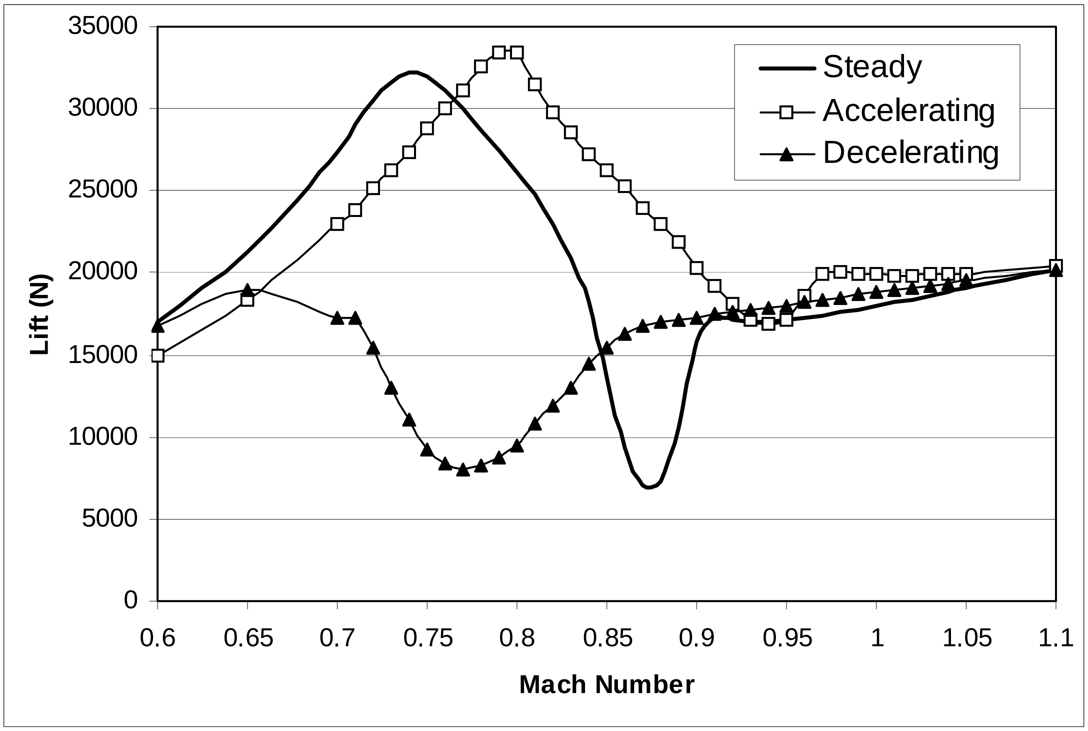

Figure 5.20: RAE 2822 transonic lift at steady, +106g and –106g.

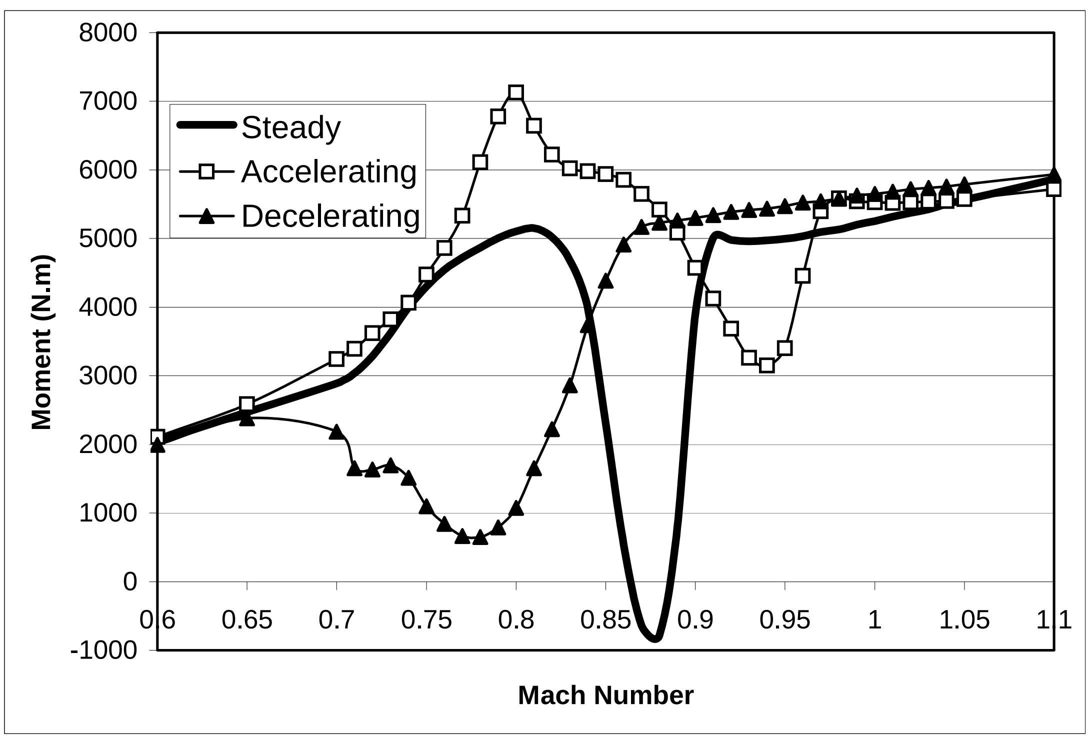

Figure 5.21: RAE 2822 transonic pitching moment at steady, +106g and –106g.

In figures 5.22 and 5.23 the steady and unsteady drag and lift variations with transonic Mach numbers are shown for the RAE 2822 aerofoil at an acceleration of 86.77 m/s^2 (8.845g) and deceleration of -86.77 m/s^2. The differences between the steady and unsteady transonic cases are explained by studying the shock wave positions, as was done for the biconvex aerofoil. In figures 5.24 to 5.27 pressure flood plots and graphs of pressure versus position are used to show variations in shock wave position on the surfaces of the RAE 2822 aerofoil, for the steady and unsteady cases, at different Mach numbers. It is evident that even with accelerations slightly less than 9g, there is considerable difference between the steady and the unsteady cases in the transonic region.

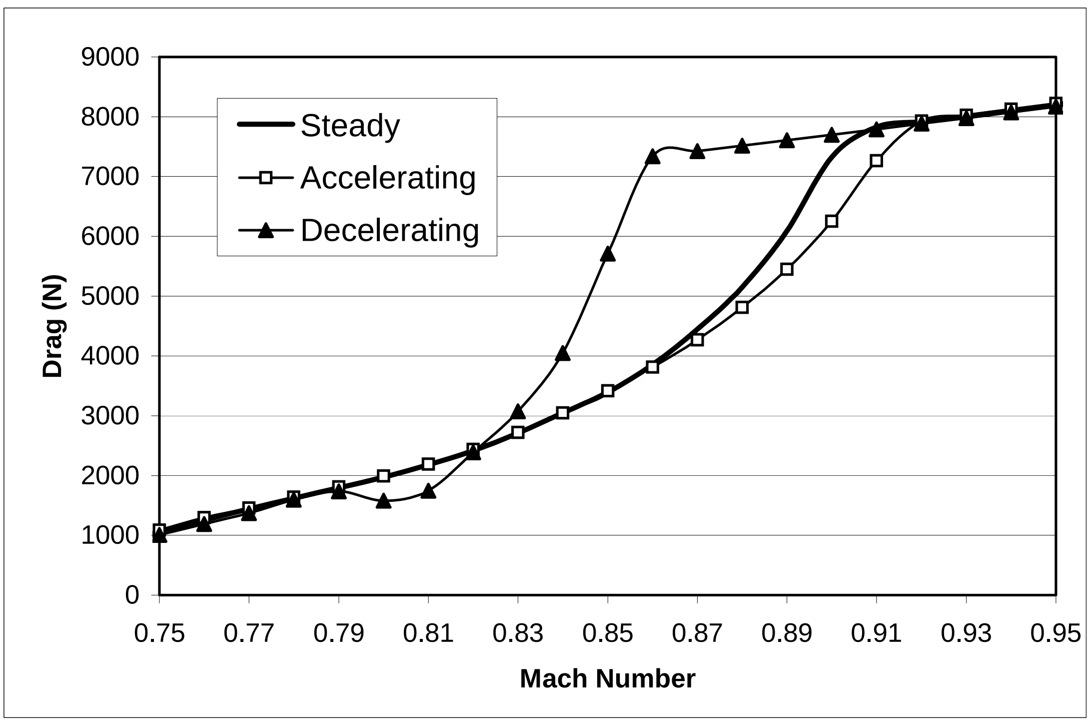

Figure 5.22: RAE 2822 transonic drag at steady, +8.845g and –8.845g.

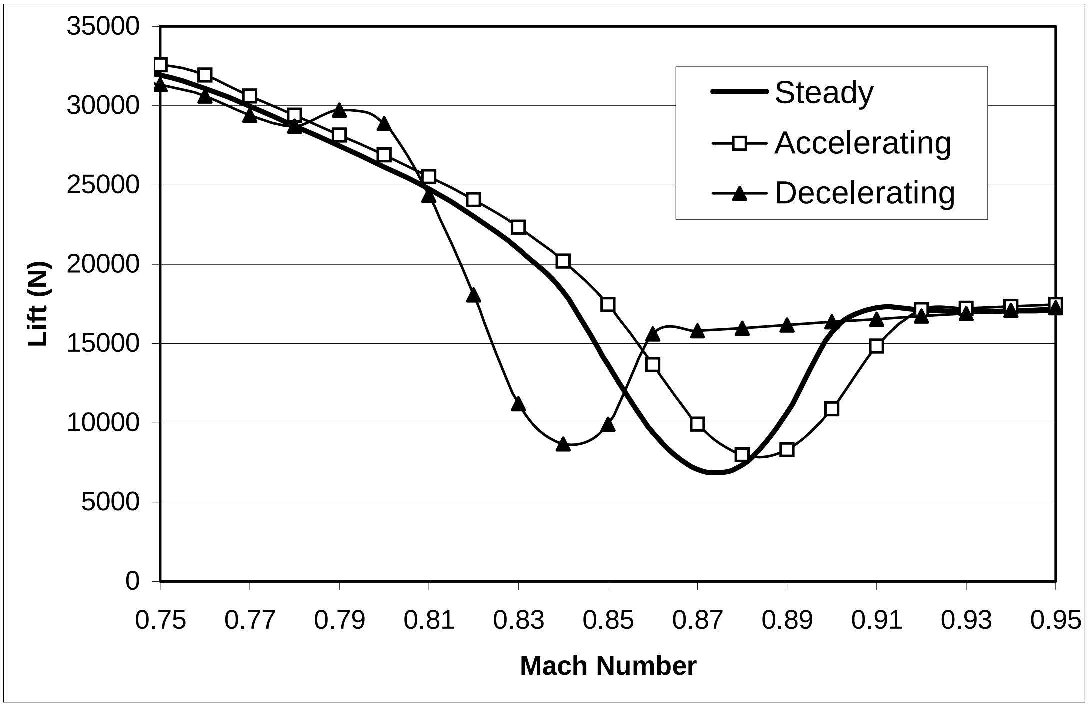

Figure 5.23: RAE 2822 transonic lift at steady, +8.845g and –8.845g.

In figure 5.24 the variation in the shock wave position at Mach 0.89 at steady state, 106g and -106g is shown. In the accelerating case, the shock wave on the upper surface of the aerofoil has moved to the left towards the leading edge, when compared to the steady state scenario. This results in an increase in the size of the high-pressure region behind the shock wave, which in isolation would result in a reduction in lift and drag when compared to the steady state situation. However, in this case significant shock movement at the lower surface of the aerofoil affects the overall result. In the accelerating case this shock wave has also moved to the right, creating a larger high-pressure region than the one generated by the movement of the shock wave at the top of the aerofoil. This, together with the fact that the size of the low-pressure region at the lower surface of the aerofoil has reduced substantially compared to the steady state scenario, should result in a higher overall lift value during acceleration. Conversely, when considering drag during acceleration, the large high-pressure region at the lower surface towards the trailing edge of the aerofoil, only serves to reinforce the effects at the upper surface. Therefore, a reduction in the overall drag would still be expected. In figures 5.19 and 5.20 a confirmation of the above explanation can be observed, where at Mach 0.89 the accelerating drag is lower than steady state but the lift value during acceleration is higher. In the decelerating scenario, compared to the steady state, the shock wave on the upper surface has moved to the trailing edge with no significant changes taking place at the lower surface of the aerofoil. Based on the explanation given for the biconvex aerofoil in a similar situation the unsteady lift and drag are expected to be higher than the steady state condition, which is confirmed by figures 5.19 and 5.20.

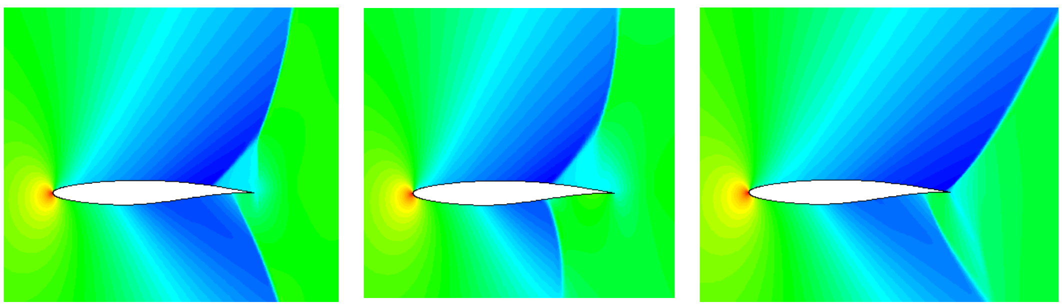

(a) From left to right, flood plots of steady state, 106g and -106g.

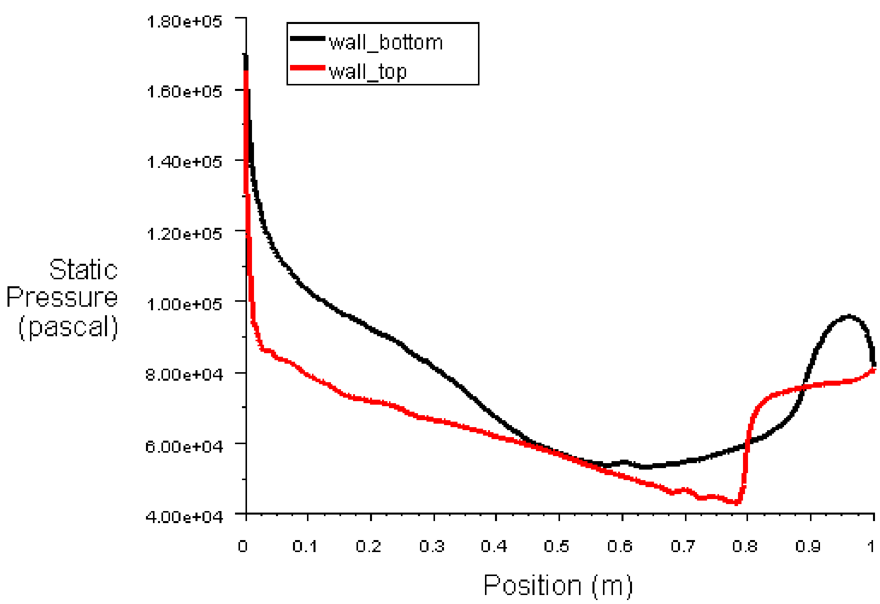

(b) Steady state pressure versus position.

Figure 5.24: RAE 2822 shock waves at steady state, 106g and -106g at Mach 0.89.

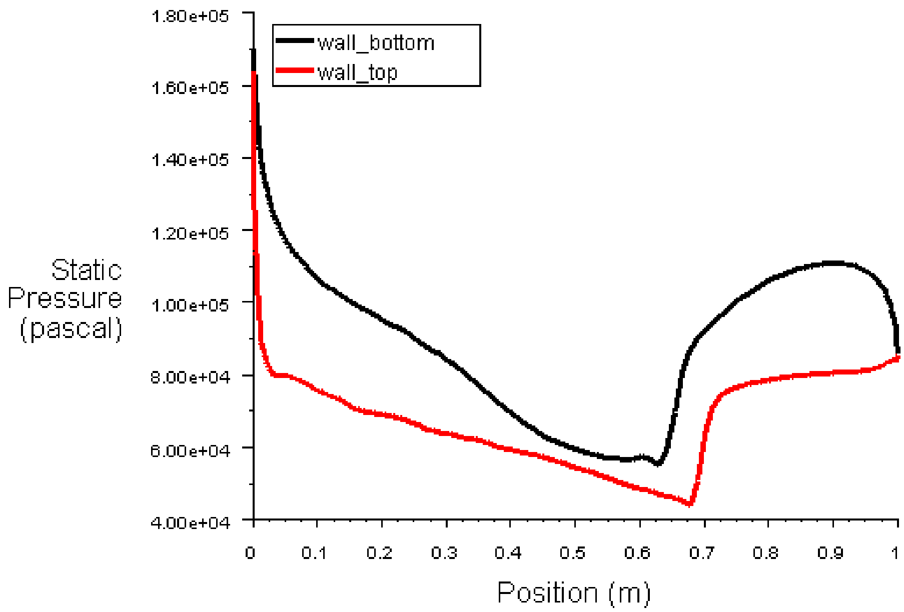

(c) Accelerating pressure versus position.

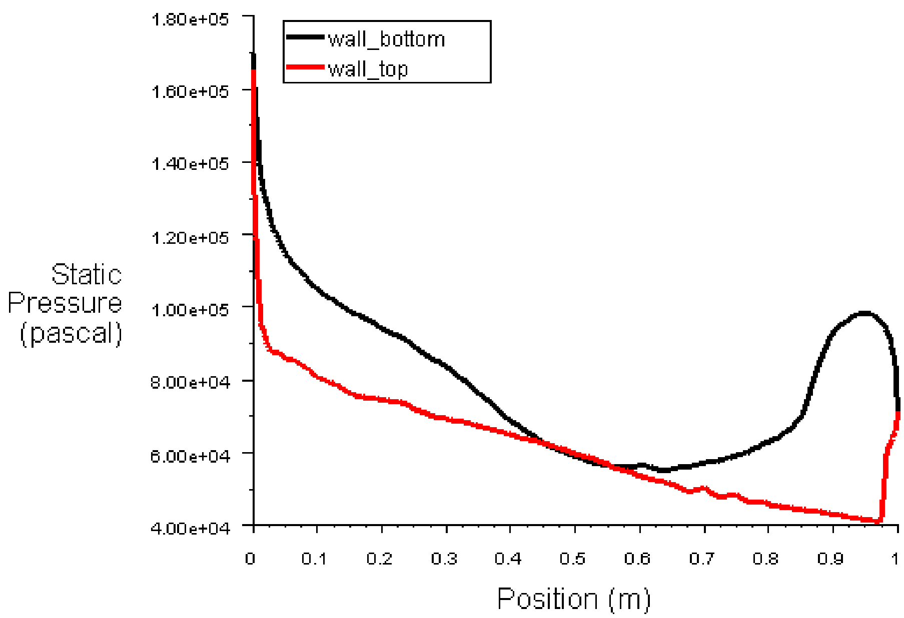

(d) Decelerating pressure versus position.

Figure 5.24: Continued.

In figure 5.25 at Mach 0.80, the shock for the accelerating condition has moved closer to the trailing edge than the steady state condition resulting in a smaller high pressure region behind the shock. As the high-pressure region near the trailing edge helps in the lowering of drag, a reduction in its size will increase drag. The lift should also increase as any reduction in the size of the high-pressure region on the upper surface should increase lift. The lift is also increased by the general increase in pressure at the lower surface of the aerofoil. Confirmation of the above explanation can be observed at Mach 0.80 in figures 5.19 and 5.20. An explanation for the significant difference observed in the decelerating scenario is given in section 5.4.

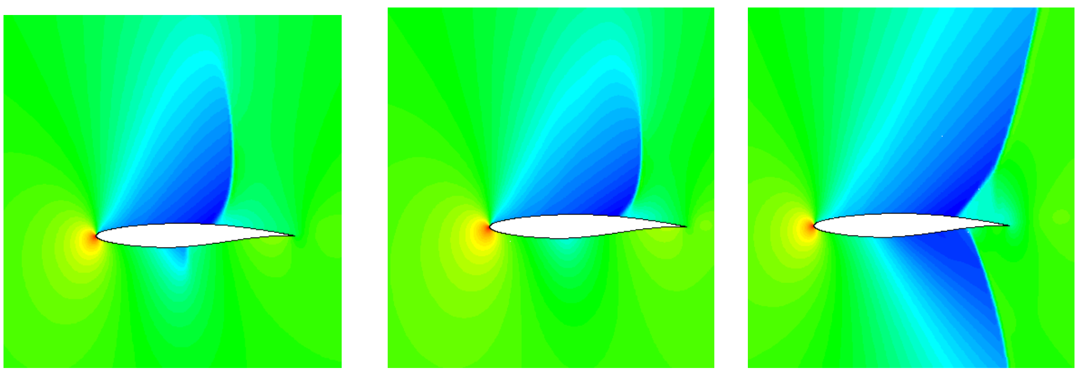

(a) From left to right, flood plots of steady state, 106g and -106g.

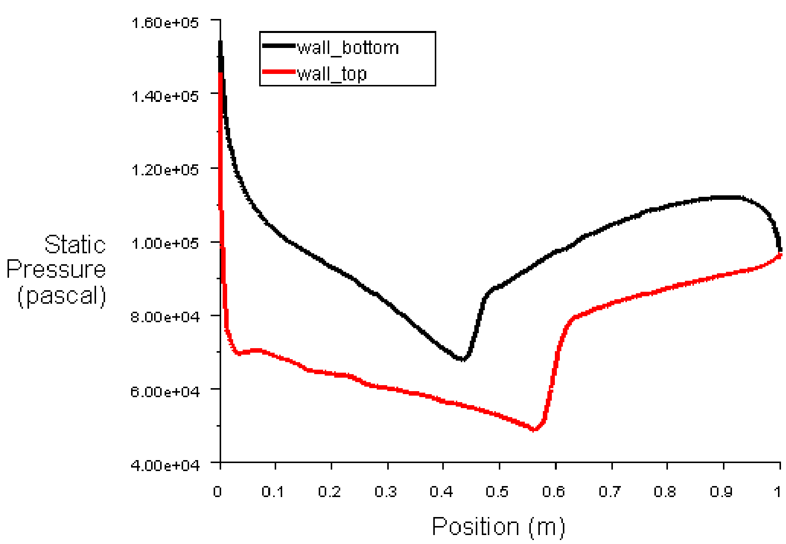

(b) Steady state pressure versus position.

Figure 5.25: RAE 2822 shock waves at steady state, 106g and -106g at Mach 0.80.

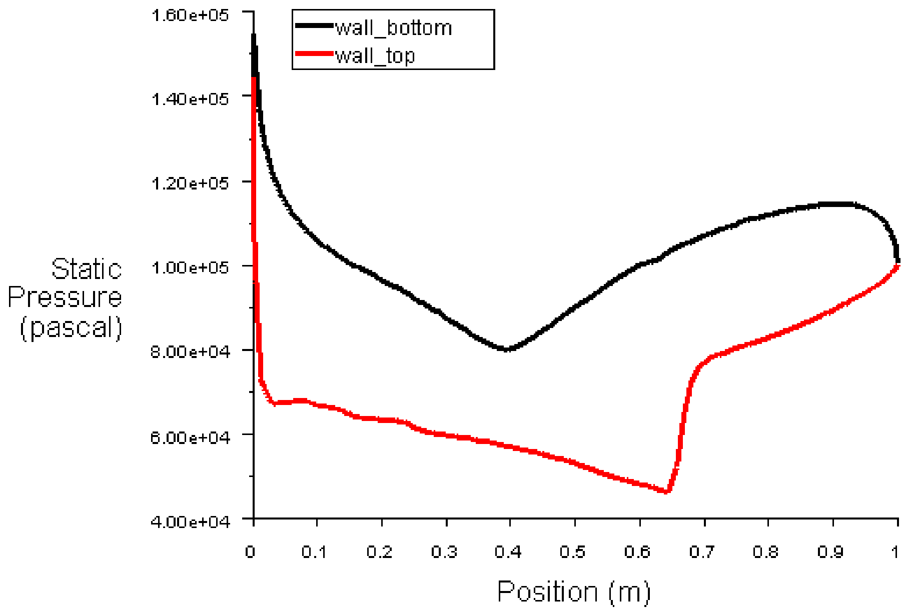

(c) Accelerating pressure versus position.

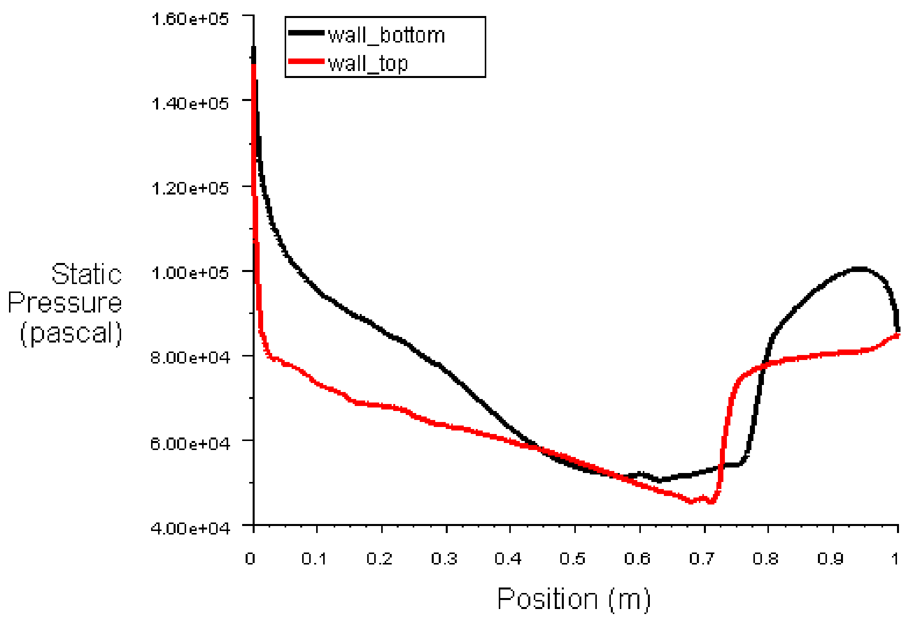

(d) Decelerating pressure versus position.

Figure 5.25: Continued

Figure 5.26 shows the variation in the position of the shock wave on the surface of the aerofoil, for the steady and unsteady cases at Mach 0.73. High accelerations of 1041 m/s^2 (106g) and -1041 m/s^2 are used. The steady state condition is similar to the one used by Fluent, in validation 11. It is interesting to observe the effects of acceleration and deceleration even at this relatively low transonic Mach number. As with the biconvex aerofoil the difference between the steady and unsteady moments is not always obvious by inspection of the flow field and can only be accurately determined through computation as in figure 5.21. This shows great differences in pitching moment between the transonic steady and unsteady conditions.

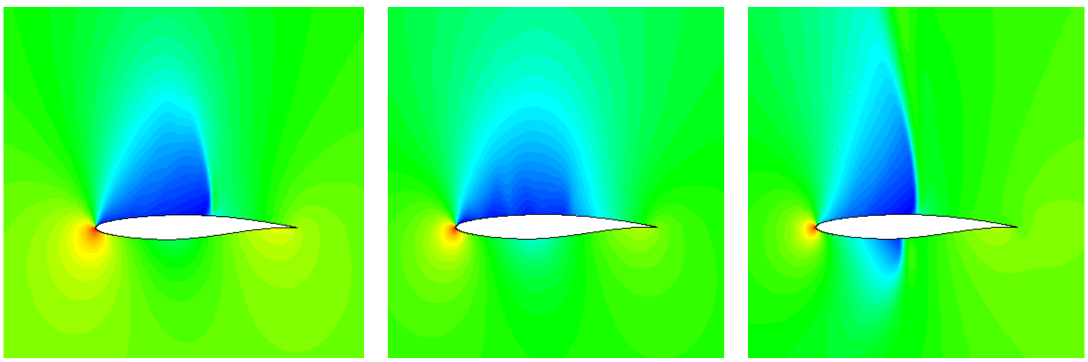

(a) From left to right, flood plots of steady state, 106g and -106g.

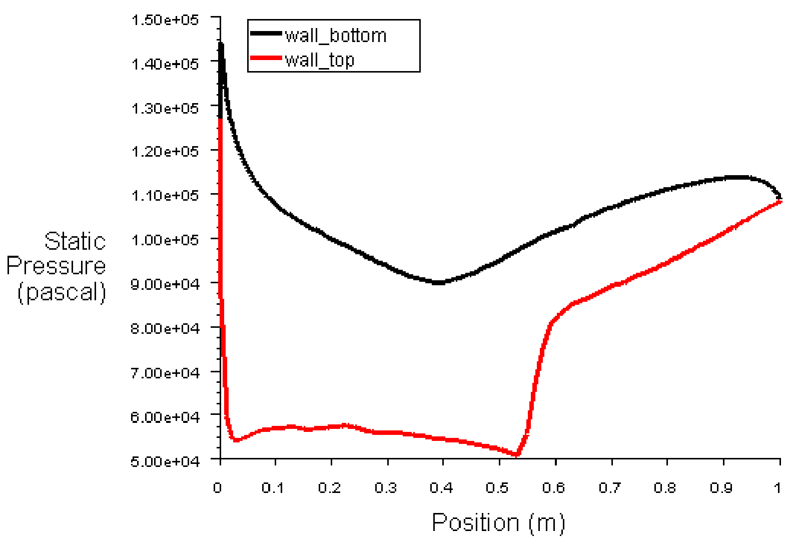

(b) Steady state pressure versus position.

Figure 5.26: RAE 2822 shock waves at steady state, 106g and -106g at Mach 0.73.

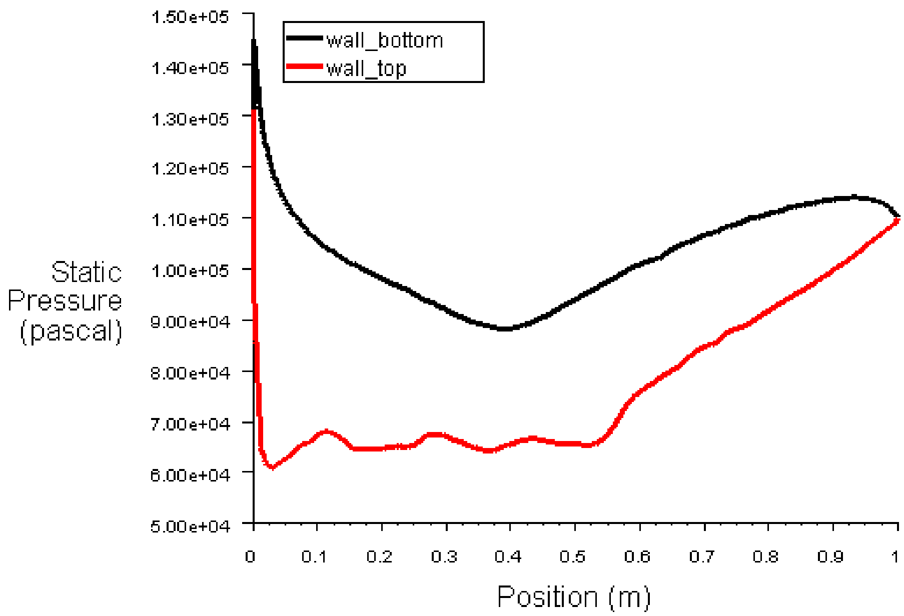

(c) Accelerating pressure versus position.

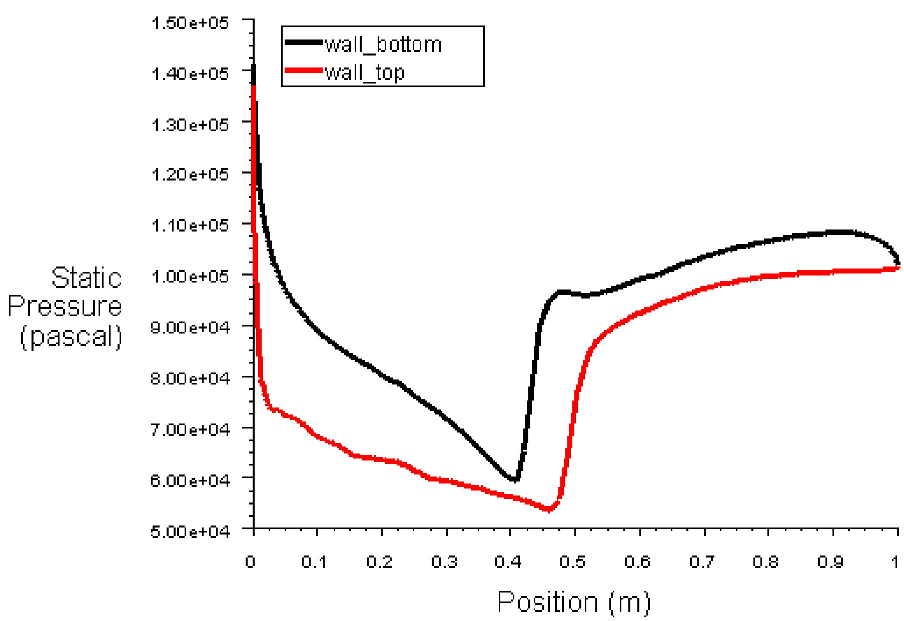

(d) Decelerating pressure versus position.

Figure 5.26: Continued.

In figure 5.27 the steady state is compared with moderate acceleration cases of 86.77m/s^2 (8.845g) and −86.77m/s^2 at Mach 0.80. The accelerating shock has moved slightly to the left of the steady state but the decelerating shock wave has moved right to the trailing edge of the aerofoil. In figures 5.22 and 5.23 the transonic drag and lift curves for the lower accelerations are shown. These show that, as with the biconvex aerofoil, even with lower accelerations or retardations the movement of the shock wave and its effect on aerodynamic forces can be significant. As before, the flow fields and the position of the shock waves could be used to explain the differences in aerodynamic forces.

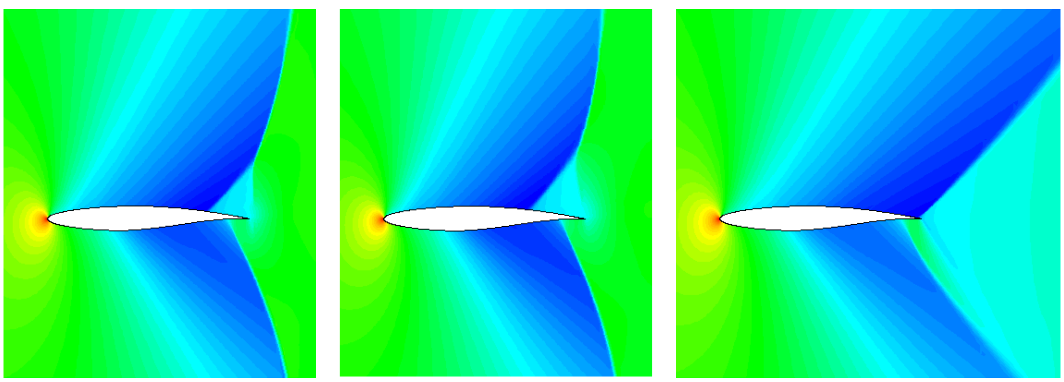

(a) From left to right, plots of steady state, 8.845g and -8.845g.

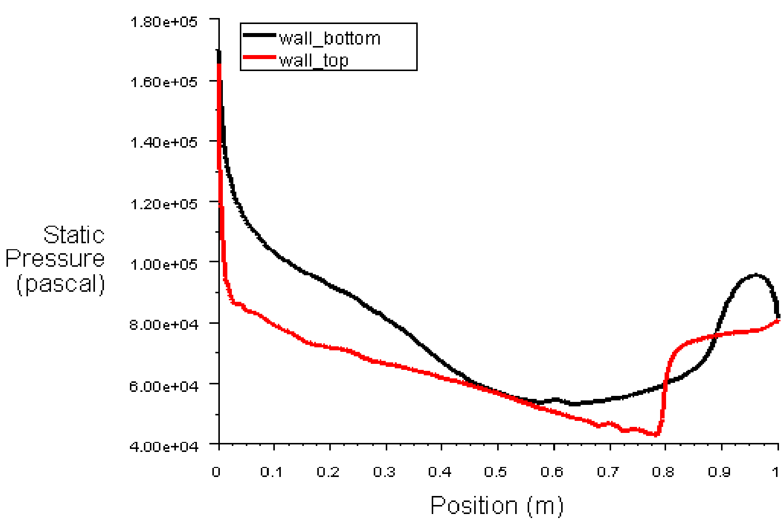

(b) Steady state pressure versus position.

Figure 5.27: RAE 2822 shock waves at steady, 8.845g and -8.845g at Mach 0.80.

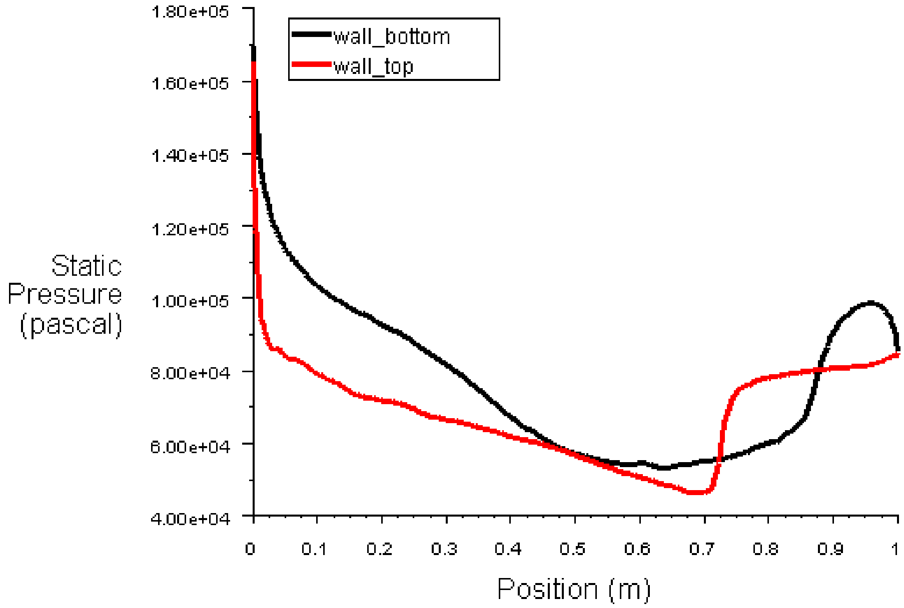

(c) Accelerating pressure versus position.

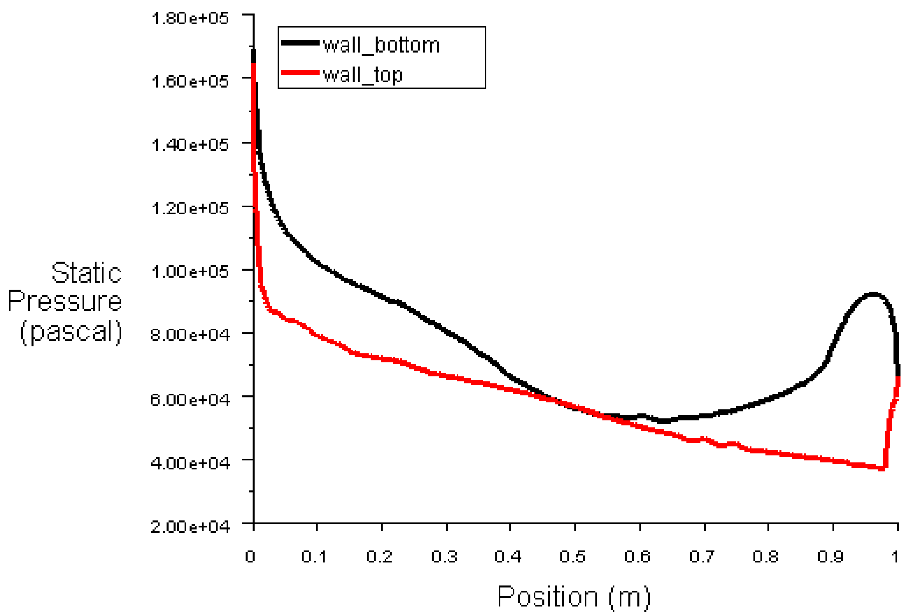

(d) Decelerating pressure versus position.

Figure 5.27: Continued.

As already mentioned, it is a well-established fact that at some steady state transonic Mach numbers a compression wave follows in the wake of an aerofoil. It was found with the RAE 2822, similar to the case with the biconvex aerofoil, that the trailing compression wave moved closer to or away from the trailing edge during acceleration or retardation at a given instantaneous Mach number. Figure 5.28 shows the density contour plots for the RAE 2822 aerofoil at Mach 0.92 for the steady and unsteady cases, with acceleration of 86.77m/s^2 (8.845 g) and deceleration of −86.77m/s^2. On the left constant velocity is shown, in the middle acceleration and on the right deceleration. Comparison between the different cases shows that during acceleration the compression wave moves closer to the trailing edge and strengthens. Conversely, during deceleration the compression wave moves away and falls behind the trailing edge reducing in intensity.

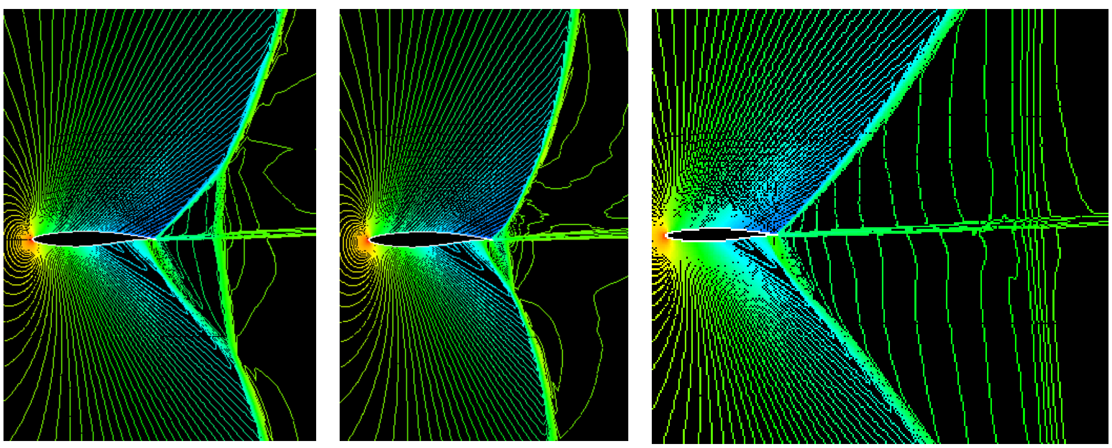

Figure 5.28: Density contour plots showing variation in the position of a trailing compression wave behind the RAE2822 aerofoil, for the steady and unsteady cases, at Mach 0.92. On the left the constant velocity case is shown, in the middle acceleration and on the right deceleration. Acceleration = 86.77 m/s^2 (8.845g) and deceleration = -86.77 m/s^2 for the unsteady cases.

As with the biconvex case, under steady state conditions a bow shock appears in front of the RAE 2822 aerofoil at supersonic aerofoil Mach numbers. This effect is absent at sonic and subsonic steady state conditions, as shown in figure 5.29. However, during the deceleration of the aerofoil at –86.77m/s^2 (-8.845 g) from supersonic to the subsonic Mach numbers, there is an increase in the stand-off distance between the bow shock and the leading edge of the aerofoil. The bow shock is still present at sonic and subsonic Mach numbers, moving further ahead as the aerofoil Mach number is reduced by deceleration. These effects are shown in figure 5.30.

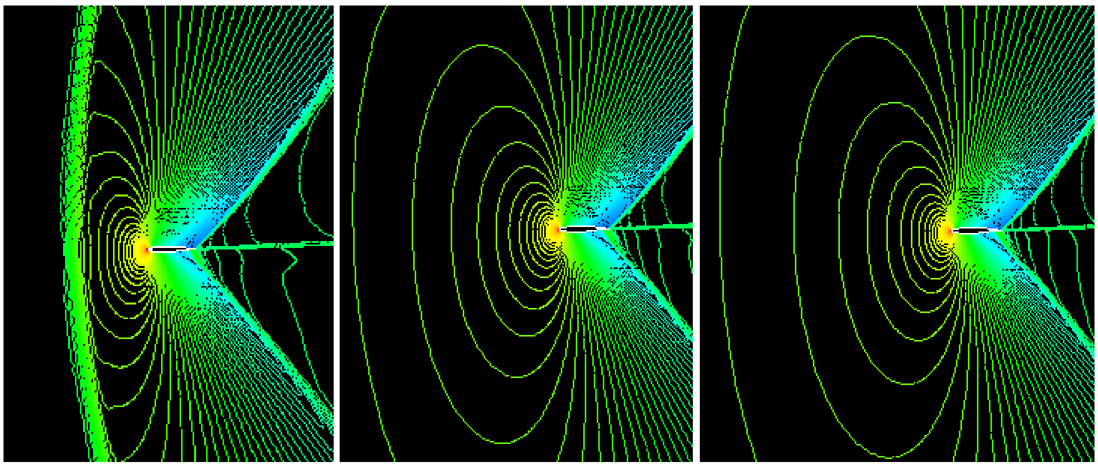

Figure 5.29: From left to right, steady state density contour plots showing the bow shock at Mach 1.1 and its disappearance at Mach 1.0 and 0.98. This shows that under steady state conditions the bow shock only exists at Mach numbers greater than 1.

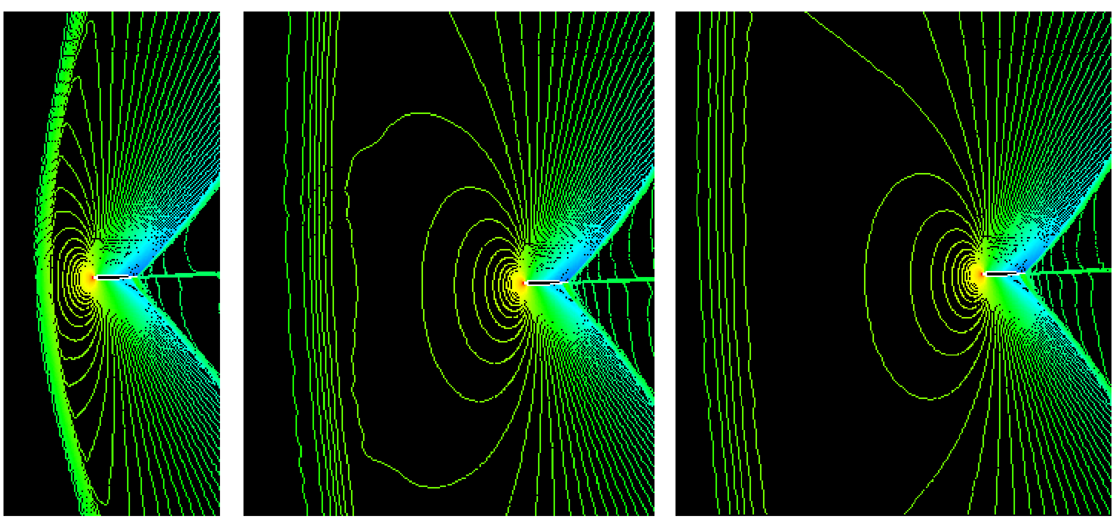

Figure 5.30: The variation in the position of the bow shock during deceleration from supersonic to subsonic Mach numbers. From left to right density contour plots at Mach 1.1, 1.0 and 0.98 are shown for a deceleration of $-86.77\ m/s^2$.

Figure 5.31 shows the movement of the bow shock at a considerably greater aerofoil deceleration of –1041 m/s^2 (−106g). At such decelerations, as the reduction in aerofoil Mach number occurs much faster, little time is available for the flow field to react. This will in turn limit the bow shock movement in comparison with the lower decelerating case of figure 5.30. As a result, as shown in figure 5.31, the bow shock is still fairly close to the leading edge at Mach 0.61, which is well into the subsonic range.

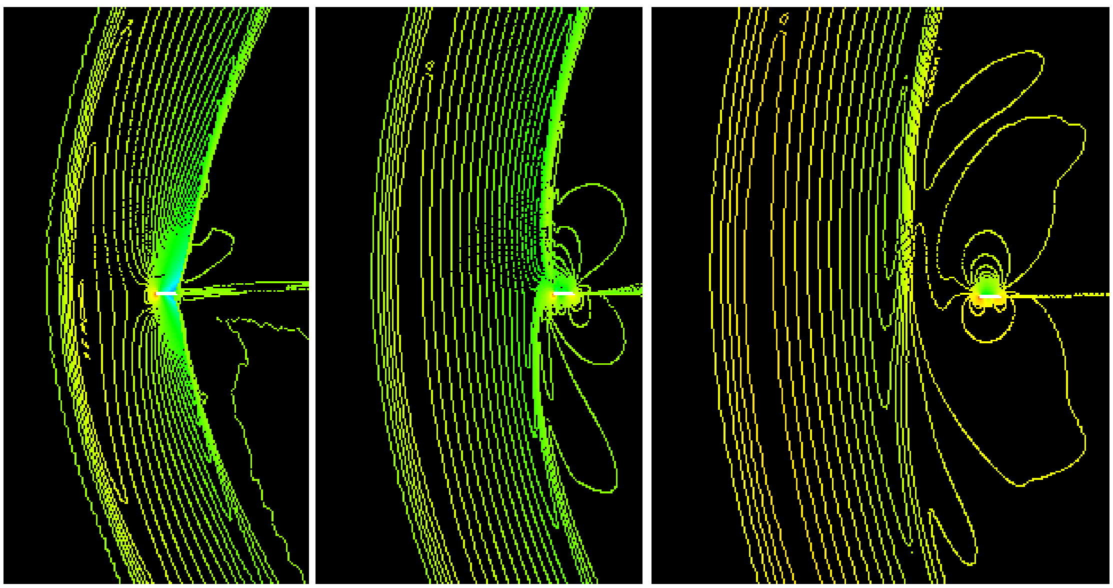

Figure 5.31: The variation in the position of the bow shock during deceleration of –1041 m/s^2. From left to right density contour plots at Mach 0.82, 0.70 and 0.61 are shown. Also note the movement of the tail shock to the front of the aerofoil.

As with the biconvex aerofoil, the tail shock under high deceleration produces some fascinating results shown in figure 5.31. Initially it widens in angle, becoming more obtuse. It also moves forward over the surface of the aerofoil eventually ending up in front of the aerofoil. This is shown on the right-hand side of figure 5.31 when the aerofoil is decelerating at −106g at Mach 0.61. In figure 5.32 the complex shock wave pattern with the bow shock in front followed by the tail shock is captured for lower Mach numbers at –106g. It is interesting to note that the shock waves are still fairly strong at Mach 0.3 with the tail shock having moved a substantial distance ahead of the aerofoil.

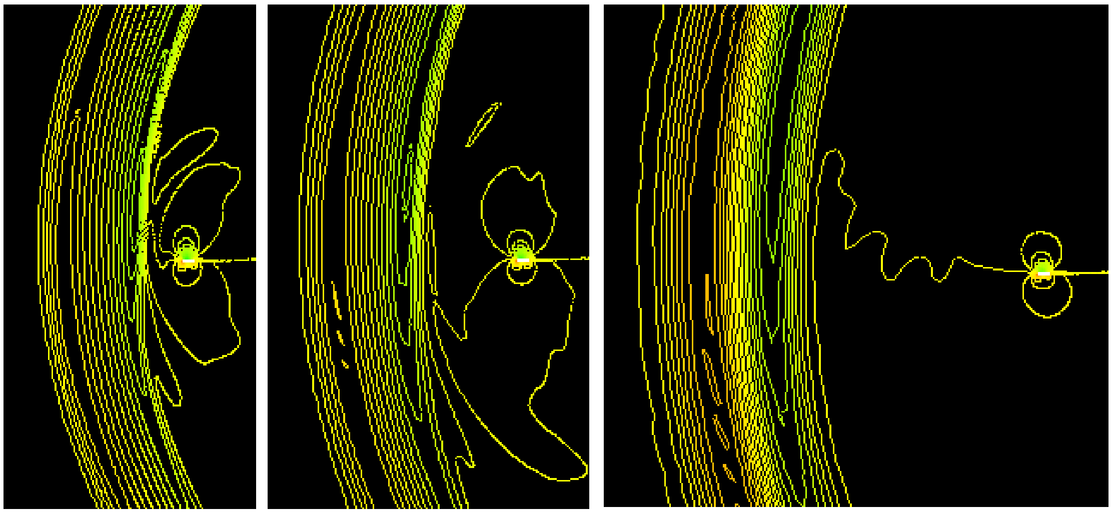

Figure 5.32: Further variation in the position of the bow shock and tail shock at lower subsonic Mach numbers with deceleration of –1041 m/s^2. From left to right density contour plots at Mach 0.61, 0.50 and 0.30 are shown respectively.

Although not shown here, at lower decelerations of less than –9g, the tail shock did not behave in the same manner. In fact it dissipated before it could reach the front of the aerofoil. The results observed here are only possible, when the deceleration is so high that the flow field has no time to react to the changes in aerofoil Mach number.

5.2 Diamond shaped aerofoil transonic aerodynamics

In this section a diamond shaped (double wedged) aerofoil is subjected to high accelerations in order to study the effect of the kink or abrupt bend, which is on the upper and lower surfaces of this aerofoil, on the steady and unsteady shock wave dynamics. For example, it would be of interest if this would have a significant effect on the variation in shock wave position when compared to other airfoils.

The diamond shaped aerofoil chosen here has a cord length of 1m and a maximum thickness of 0.1 m. High accelerations of 106g and –106g were used. The airfoil was subjected to the following conditions:

Free-stream temperature:	300 K
Atmospheric pressure:	101 325 Pa
Acceleration:	1041 m/s^2 (106g)
Deceleration:	–1041 m/s^2
Angle of attack:	4 degrees

Steady state, constant velocity, simulations were conducted at Mach numbers ranging from 0.1 to 1.6. Then, starting at Mach 0.1, the airfoil was subjected to an acceleration of 1041 m/s^2 (106g) through the same range of Mach numbers. Finally, starting at Mach 1.6, it was decelerated at –1041 m/s^2 down to Mach 0.1. The transonic portion of the data was selected for this investigation.

Variations of steady and unsteady lift and drag versus Mach number as well as pressure flood plots, density contour plots and graphs of pressure versus position are used to obtain a better understanding of the unsteady transonic flow fields generated during acceleration and to explain the nature of the unsteady aerodynamic forces. Forces and moments were not non-dimensionalized in order to avoid ambiguity in choosing an arbitrary reference velocity.

Figures 5.33 and 5.34 show the transonic portion of the drag and lift curves for the diamond shaped aerofoil under acceleration of 106g and deceleration of -106g and at constant velocity. The subsonic portions of these curves, although not shown here, confirmed the general findings from chapter 4. In other words, acceleration produced an increase in drag and a reduction in lift and retardation a reduction in drag and an increase in lift. However, as with the biconvex aerofoil, in the transonic region the unsteady lift and drag values fluctuate above and below the steady state values. The unsteady lift curve also shifts to the right and left of the steady state curve, shifting generally to the right with acceleration and to the left with deceleration. The movement of the drag curve is less distinct but follows a similar general trend.

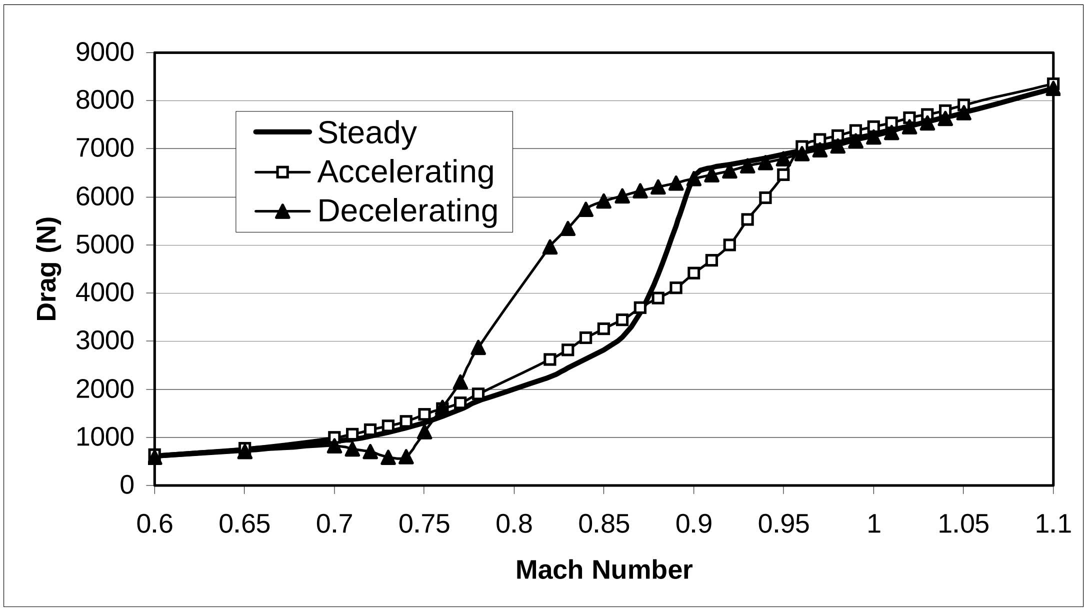

Figure 5.33: Steady and unsteady transonic drag versus Mach number for a diamond shaped aerofoil. Acceleration = 1041 m/s^2 (106g) and deceleration = -1041 m/s^2.

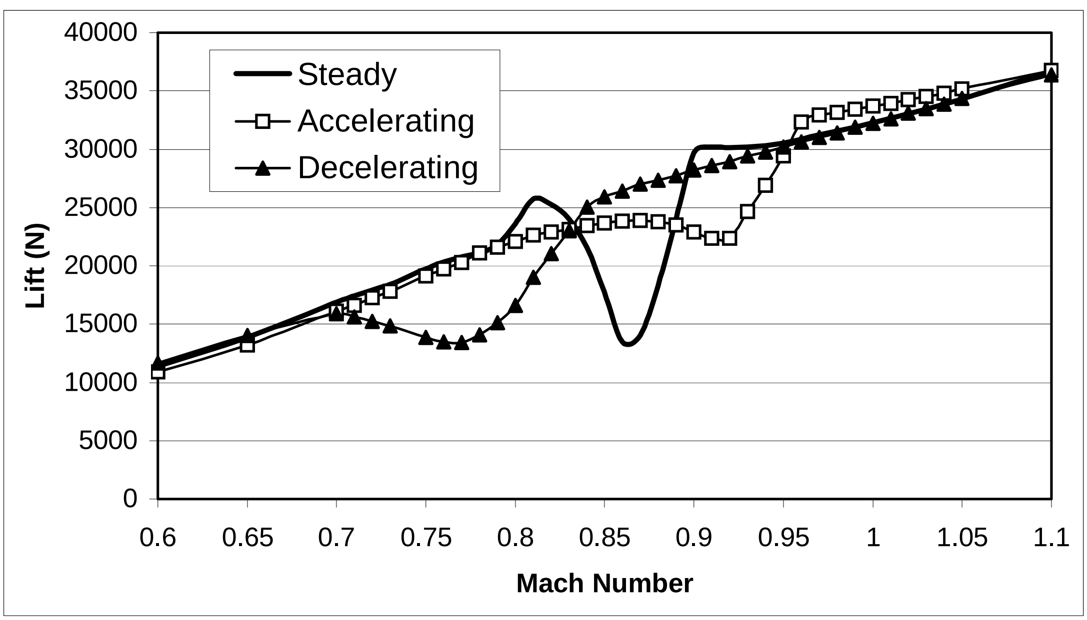

Figure 5.34: Steady and unsteady transonic lift versus Mach number for a diamond shaped aerofoil. Acceleration = 1041 m/s^2 (106g) and deceleration = -1041 m/s^2.

Figure 5.35 shows the variation in the shock wave position at Mach 0.85. In figure 5.35 (a) the pressure flood plots for the 3 cases are shown. When the steady state flow field on the left is compared to the accelerating scenario shown in the middle, the shock wave on the upper surface of the aerofoil has moved to the right, the shock wave at the lower surface has moved to the left and the low pressure region at the tip of the aerofoil has reduced in size for the accelerating case. It is therefore expected that lift should be higher with the accelerating scenario as the shock movements would both increase the overall lift value and the reduction in the size of the low pressure region at the tip of the aerofoil would have a less significant impact on the overall lift. This can be confirmed by examining the lift curves of figure 5.34. As already mentioned, the size of the high-pressure region behind the shock wave on either surface, would inversely affect drag. Therefore, in the accelerating case, the shock movement to the right at the top surface should increase drag and the movement to the left at the bottom surface should reduce drag. This makes it difficult to predict the overall result by inspection and computation is required to determine the final steady and accelerating drag values as per figure 5.33. Conversely, in the decelerating scenario on the right of figure 5.35 (a), confirmed by the graph of pressure versus position in 5.35 (d), where the shock waves at the upper and lower surfaces of the aerofoil have moved completely to the right, wiping out the high-pressure region behind the shock, drag is expected to rise significantly. This can be observed in figure 5.33, where the decelerating drag value at Mach 0.85 is substantially higher than the steady state value. Decelerating lift must be substantially higher than the steady state as the low-pressure region at the top, for deceleration, is far stronger than the one on the lower surface of the aerofoil, whereas the opposite effect is observed under steady state condition. The slightly stronger steady state low-pressure region at the tip of the aerofoil is not sufficient to reverse this effect. This prediction is also confirmed by the lift curves in figure 5.34 at Mach 0.85.

The above analysis shows that, for the diamond shaped aerofoil, the shock wave position is affected by acceleration and deceleration and similar correlations that existed between the shock wave positions and aerodynamic forces for the biconvex and RAE 2822 airfoils also exist here. However, from the graphs of pressure versus position it is apparent that the low pressure regions on both surfaces of the diamond shaped aerofoil did not develop progressively, as observed in other airfoils, but instead an abrupt expansion wave was formed at the kink on both surfaces. The low-pressure region then ended, as with most airfoils, through a shock wave formed further towards the trailing edge. It is the position of this shock wave that was affected by the unsteady flow fields. The expansion wave formed at the kink did not change its position.

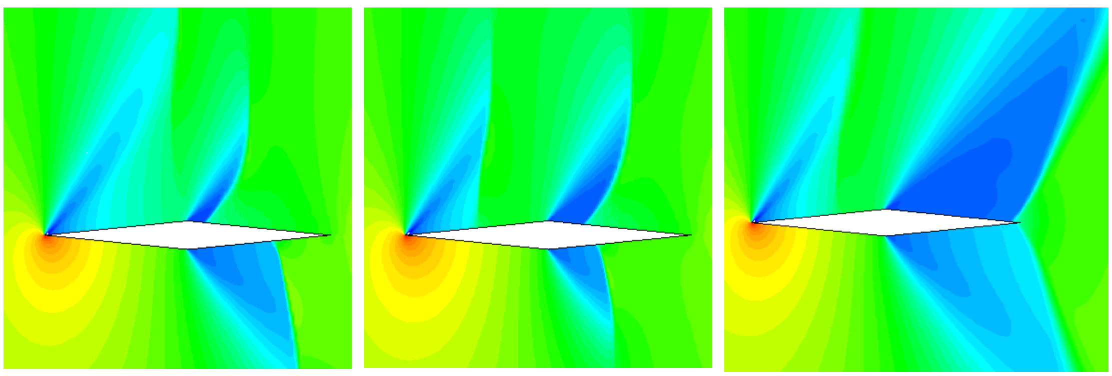

(a) From left to right, flood plots of steady state, 106g and -106g.

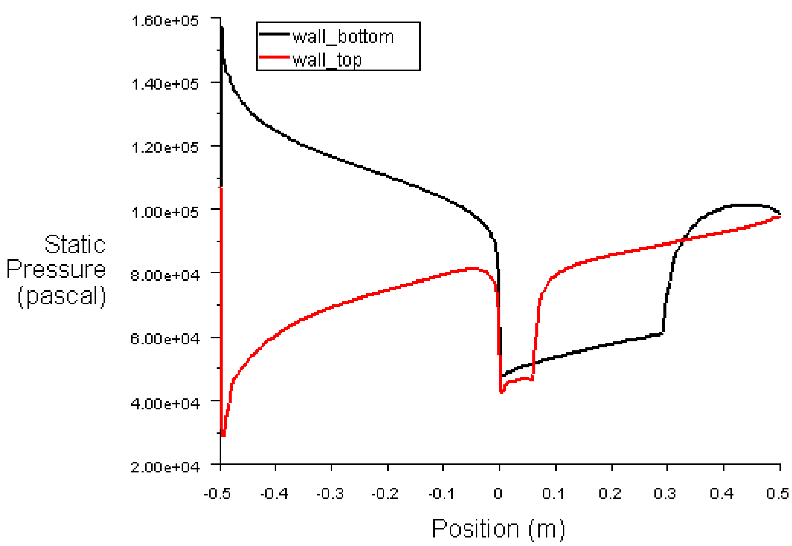

(b) Steady state pressure versus position.

Figure 5.35: Diamond aerofoil shock waves at steady, 106g and -106g at Mach 0.85.

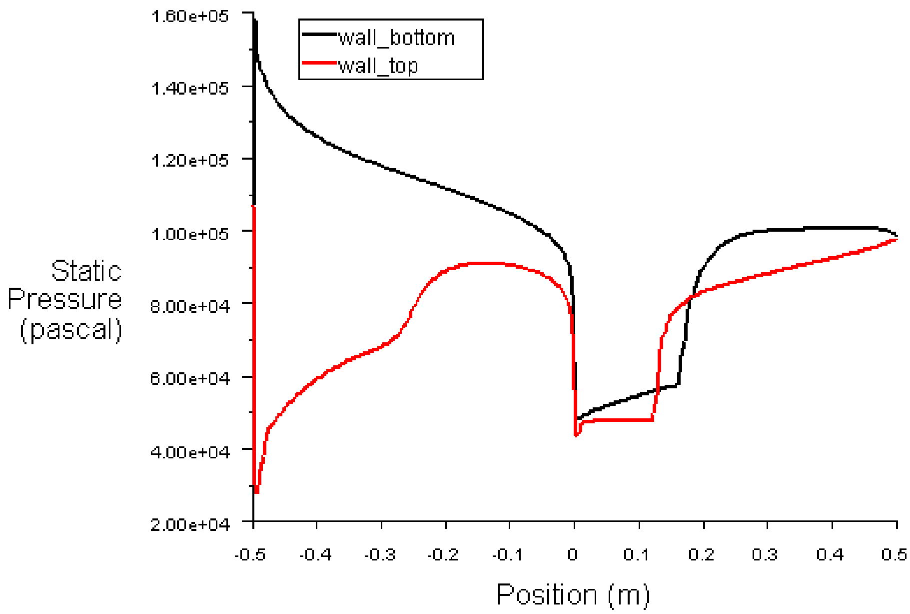

(c) Accelerating pressure versus position.

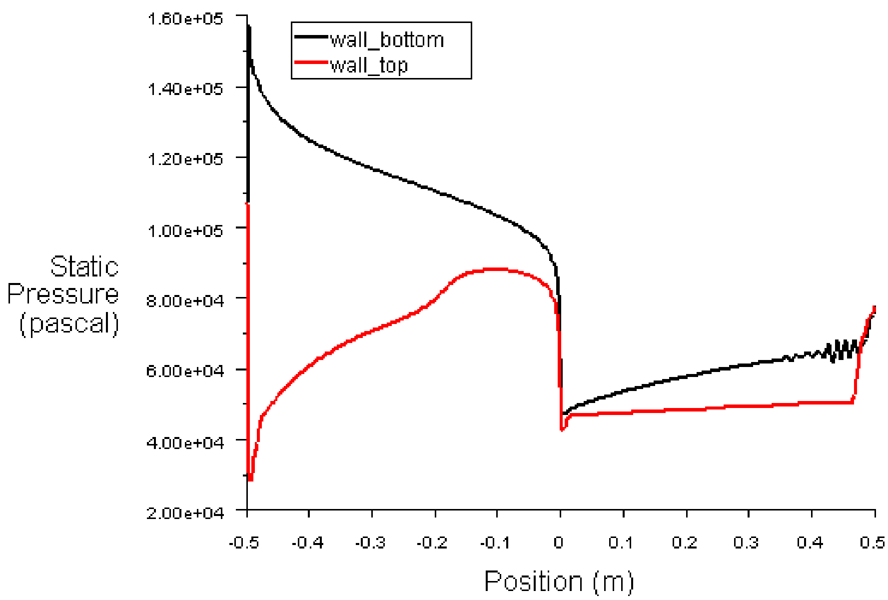

(d) Decelerating pressure versus position.

Figure 5.35: Continued.

In figure 5.36, pressure contour plots are used to examine the variation in the position of the shock wave on the surfaces of the diamond shaped aerofoil, for the steady and unsteady cases, at Mach 0.76 and accelerations of 106g and –106g. The steady and accelerating cases have similar flow fields, but the decelerating scenario is significantly different. This can be attributed to the movement of the tail shock at high decelerations also encountered with other airfoils. At this point the tail shock has moved forward and reached the centre of the aerofoil due to the high deceleration.

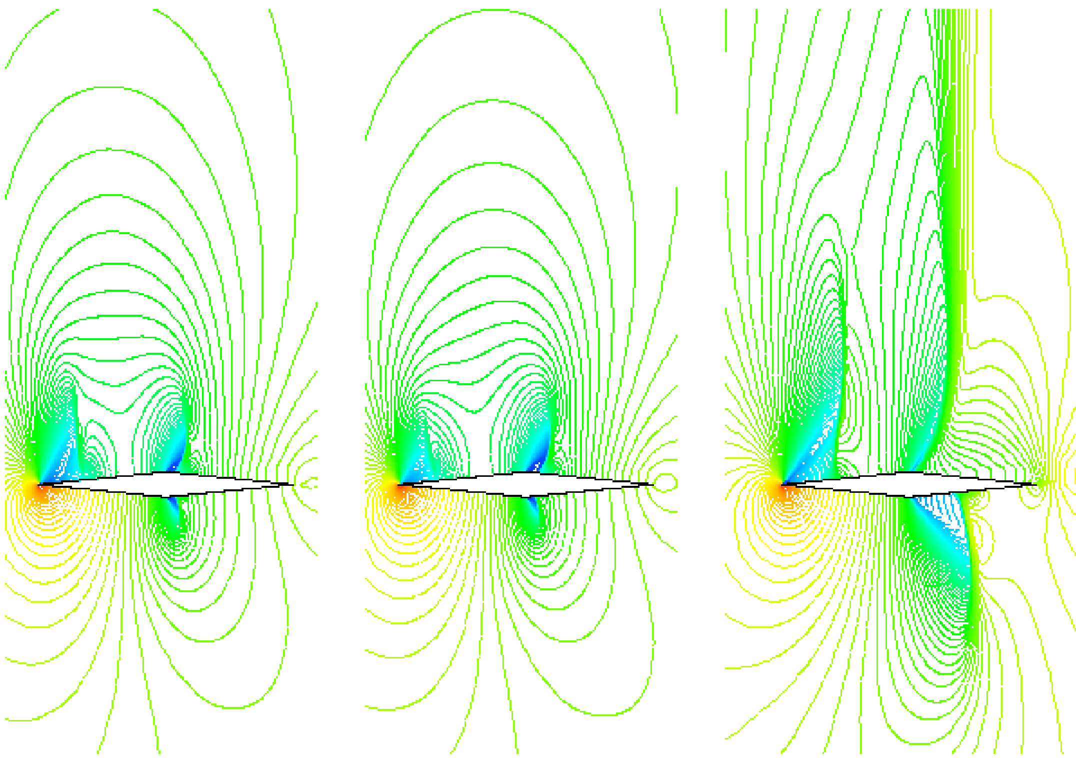

Figure 5.36: The variation in the position of the shock wave on the surface of the diamond shaped aerofoil, for the steady and unsteady cases, at Mach 0.76. On the left constant velocity is shown, in the middle acceleration and on the right deceleration. Acceleration = 1041 m/s^2 (106g) and deceleration = -1041 m/s^2. Note that the tail shock has moved to the centre of the aerofoil due to the high deceleration.

In figures 5.37 and 5.38 the movement of the tail shock from the rear to the front of the aerofoil is examined. In figure 5.38 a more detailed study of the flow field is undertaken in order to highlight some important effects. For example, it is interesting to note that the moving tail shock almost completely wipes out the low-pressure regions on both sides of the aerofoil. Even the expansion waves at the kinks almost disappear. Explanations for these effects will be given in section 5.4.

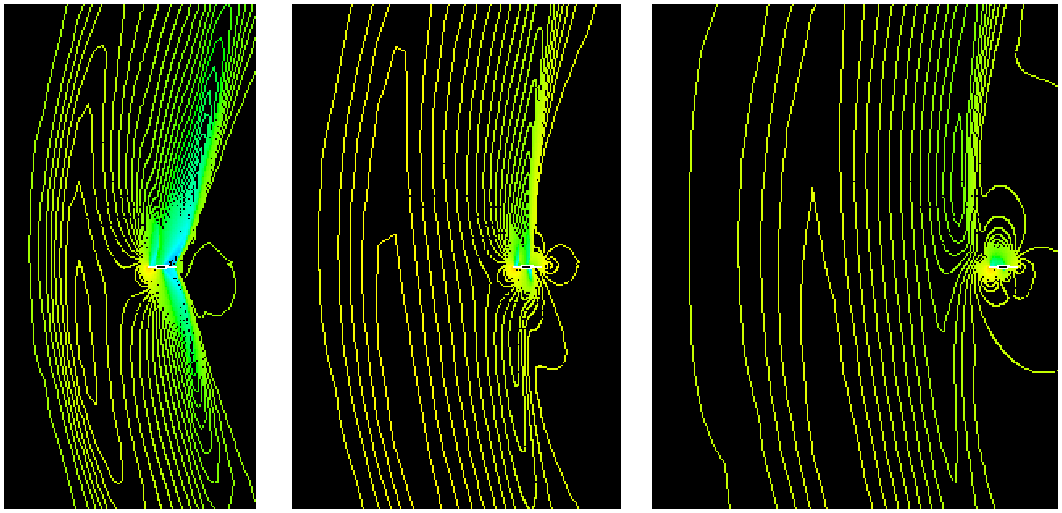

Figure 5.37: Variation in the position of the bow shock and tail shock at subsonic Mach numbers with deceleration of –1041 m/s^2. From left to right pressure contour plots at Mach 0.85, 0.76 and 0.70 are shown respectively.

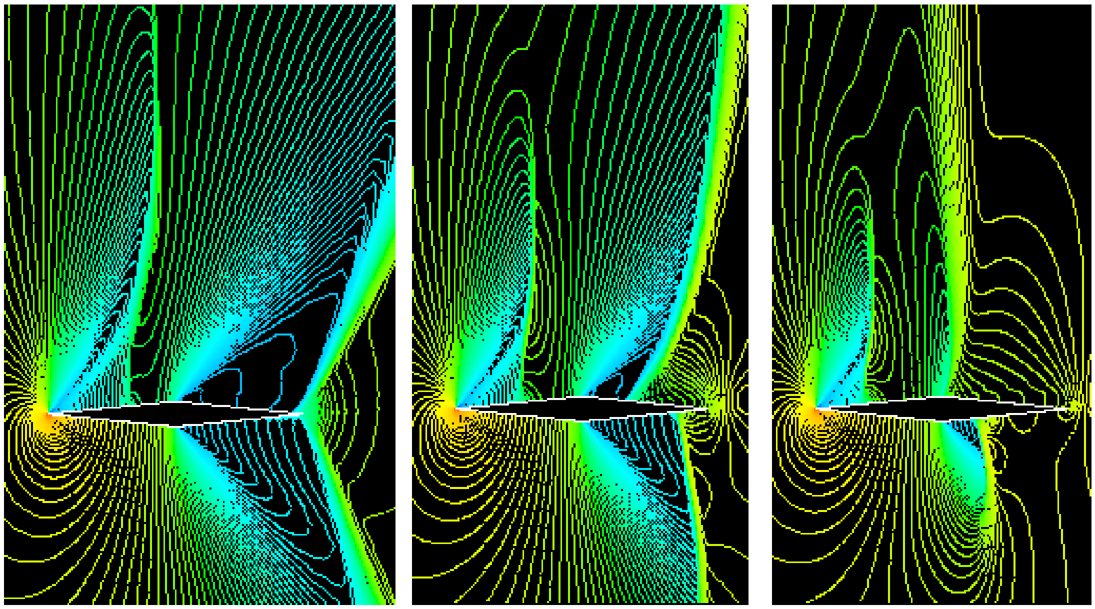

(a) From left to right Mach 0.85, 0.79 and 0.75 are shown respectively.

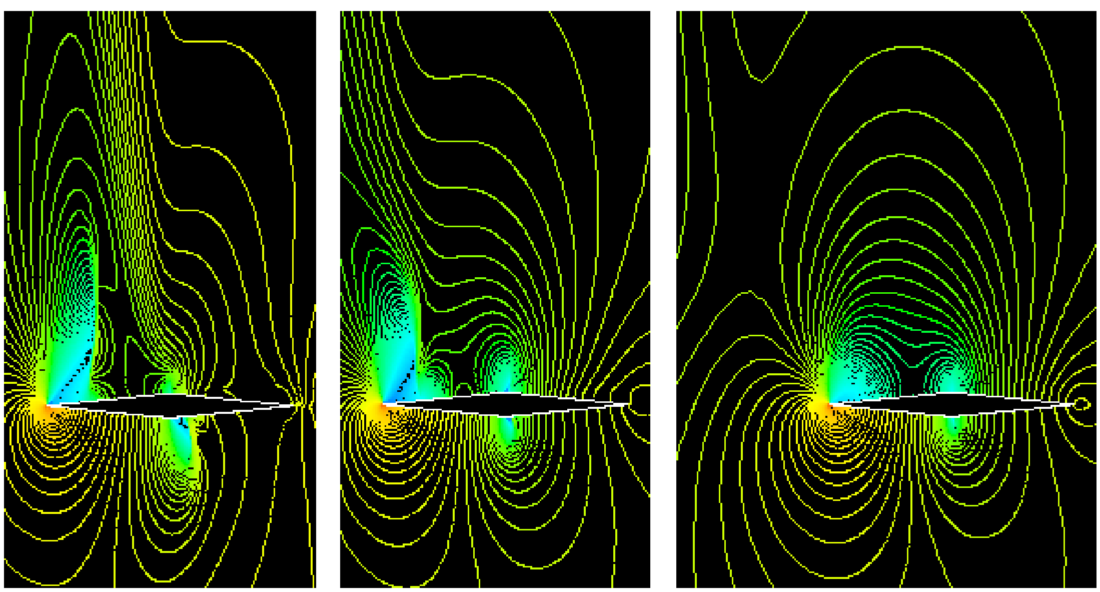

(b) From left to right Mach 0.74, 0.72 and 0.70 are shown respectively.

Figure 5.38: Pressure contour plots showing the variation in the position of the tail shocks on both surfaces of the aerofoil with a deceleration of -1041 m/s^2 at subsonic Mach numbers. Note how the forward movement of the tail shocks, brought about by deceleration, almost wipes out the low-pressure regions on both surfaces of the aerofoil.

5.3 Axisymmetric Bodies

In chapter 4 the aerodynamic effects caused by acceleration and retardation of axisymmetric bodies were discussed. One of the objects used was an artillery shell taken from the images from Van Dyke [7]. The artillery shell is useful when studying transonic flight, as the experimentally obtained flow fields at transonic Mach numbers can be generated numerically with the turbulence models used in this research. Therefore, it is used in this section to examine transonic shockwave behaviour. The shell is 240 mm long with a maximum diameter of 50 mm. High accelerations were chosen to enhance the differences between the steady and accelerating scenarios. The shell was subjected to the following conditions:

Free stream temperature:	300 K
Atmospheric pressure:	101325 Pa
Acceleration:	1041 m/s^2 (106g)
Retardation:	-1041 m/s^2

Steady state, constant velocity, simulations were conducted, at Mach numbers ranging from 0.1 to 1.6. Then, starting at Mach 0.1, the shell was subjected to an acceleration of 1041 m/s^2 (106g) through the same range of Mach numbers. Finally, starting at Mach 1.6, it was decelerated at –1041 m/s^2 down to Mach 0.1. Forces were not non-dimensionalised in order to avoid ambiguity in choosing an arbitrary reference velocity. The transonic portion of the data was selected for the investigation in this section.

Figure 5.39 shows the steady and unsteady drag variation with transonic Mach number for the artillery shell. Although the differences between the steady and unsteady cases in the transonic range of Mach numbers are significant they follow a different trend to the one experienced in the subsonic regime. However, it has already been shown, throughout the course of this chapter, that shock wave related behaviour is predominantly responsible for such large differences in the transonic region. In this case an interesting extension to this concept comes into effect.

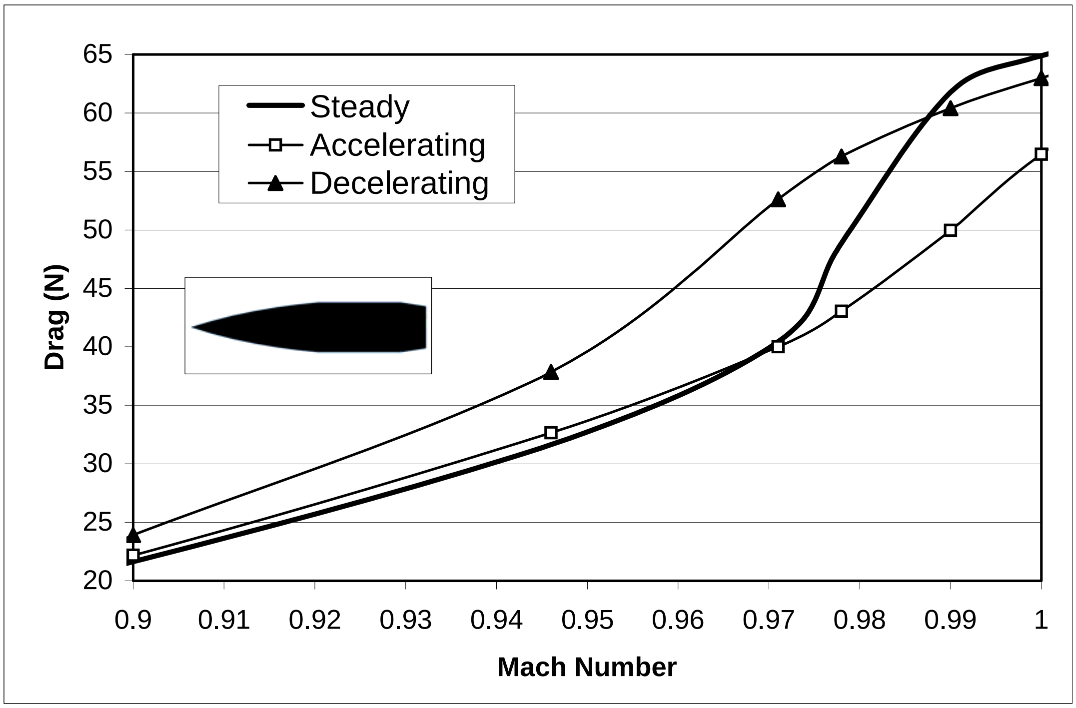

Figure 5.39: Steady and unsteady drag variation with transonic Mach number for an artillery shell. Acceleration = 1041 m/s^2 and deceleration = -1041 m/s^2.

In figure 5.40 graphs of pressure versus position, for the artillery shell at Mach 0.978, are compared on the same set of axes. Black represents the steady state, red represents the accelerating and green the decelerating scenarios. As the steady and unsteady curves match very closely, it is difficult to explain the large differences in drag at this Mach number purely by considering aerodynamically induced pressure on the surface of the shell. In fact, based on surface pressure alone, it could be argued that the decelerating scenario, shown in figure 5.40 in green, should have an overall drag value lower or equal to the steady state. This is because the higher pressure at the trailing edge during deceleration should results in a lower drag value compared to the steady state, and the slightly higher pressure towards the tip, which would usually increase drag, is too small to outweigh the effect of the higher pressure on the trailing edge. Although not shown, differences in viscous drag were also found to be negligible and were within 0.2% of the overall drag for the three cases. Even so, as shown in figure 5.39, the decelerating drag at Mach 0.978 is almost 20% higher than the steady state value.

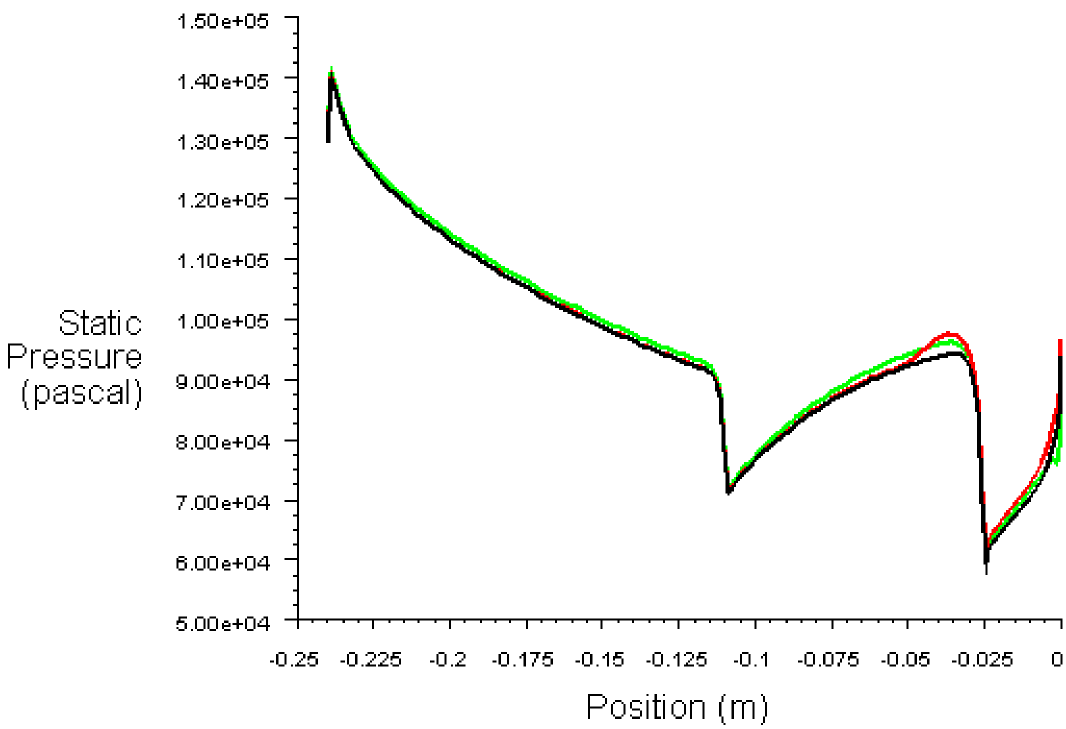

Figure 5.40: Pressure versus position at Mach 0.978. Black represents the steady state, red represents the accelerating and green the decelerating scenarios.

An explanation for this can be given by taking wave drag into consideration. Figure 5.41 compares the pressure contour plots for the artillery shell at Mach 0.978. The decelerating scenario has by far the biggest shock wave. This wave must move a much larger amount of air in its forward motion and the shell will consequently experience the largest drag during deceleration.

In the accelerating scenario the shell experiences a lower drag force than in the steady state, as shown in figure 5.39 at Mach 0.978. Although, this can be partly attributed to lower wave drag, due to the smaller shock wave during acceleration shown in figure 5.41, it can also be attributed to the higher surface pressure at the trailing edge of the shell in comparison with the steady state condition shown in figure 5.40. Either of these effects would result in a lower drag force during acceleration when acting in isolation. Here, the combined effect is experienced.

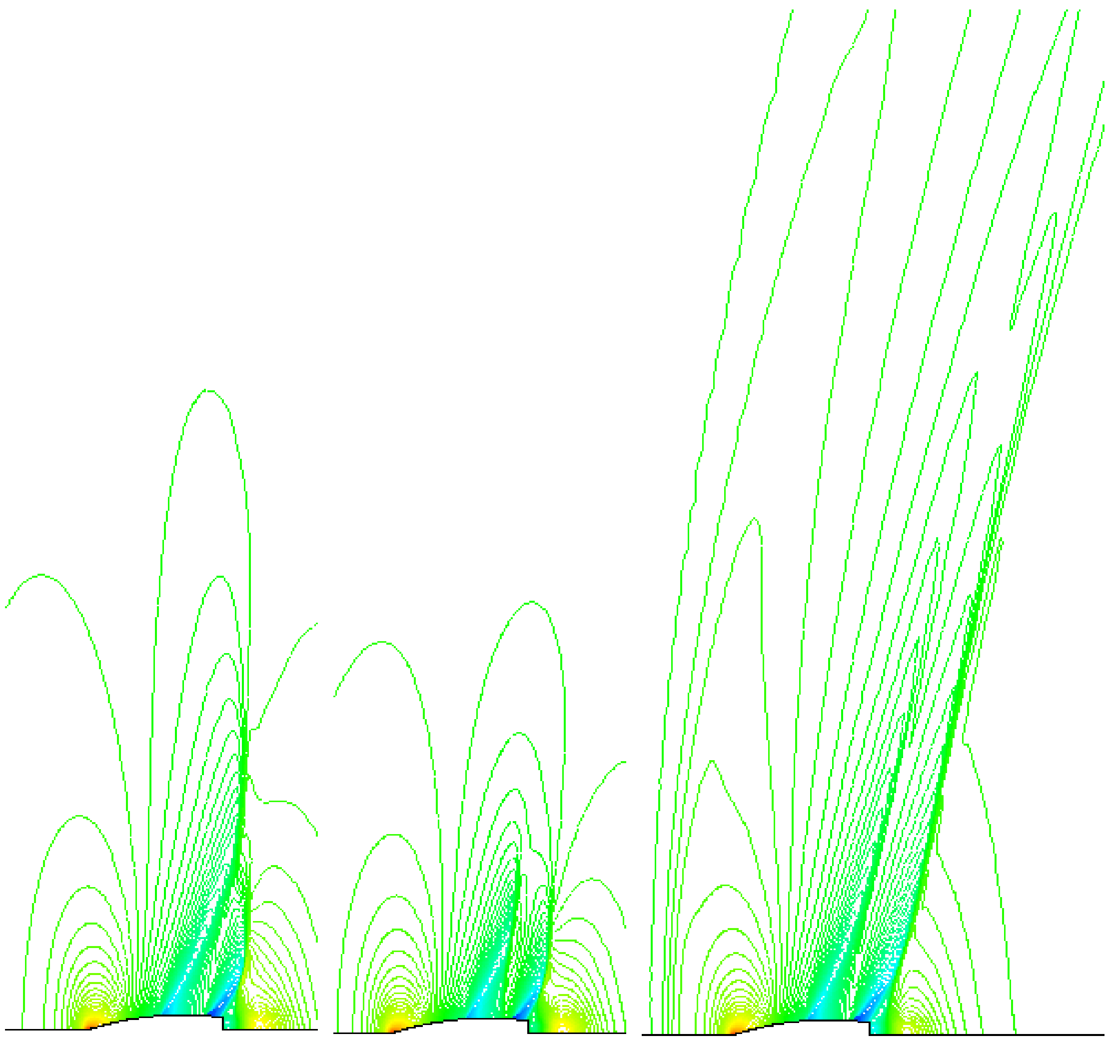

(a) Steady (b) Accelerating (c) Decelerating

Figure 5.41: Pressure contour plots for the artillery shell at Mach 0.978. The constant velocity, accelerating and decelerating case are shown. Acceleration = 1041 m/s^2 and deceleration = -1041 m/s^2. Note that there is a relation between size of the shock waves and the drag force shown in figure 5.39.

5.4 Discussion

As discussed in the previous chapter, when an object is accelerated in a compressible fluid, the unsteady flow field generated is not allowed sufficient time to reach equilibrium at any specific Mach number. It is therefore different to the steady state flow field at that same Mach number and is in fact influenced by its own flow field history. It has similarities to steady state flow fields corresponding to earlier conditions. As a result, the unsteady lift, drag and pitching moment at any given Mach number should also be different to the steady state values. During acceleration, subsonic lift values were found to be lower than the corresponding steady state lift values at the same Mach number. This was explained in the previous chapter by arguing that the unsteady flow field, during subsonic acceleration, has insufficient time to reach equilibrium and will reflect some of the characteristics of earlier conditions, when the Mach number was lower. Hence the lower lift values during subsonic acceleration. Conversely, during subsonic retardation, lift values higher than the steady state values at the same Mach number are experienced.

Similar arguments can explain the differences between the steady and unsteady aerodynamic curves in the transonic region. This is done by taking into account the position of the shock waves on the surfaces of the aerofoil. For example, as shown in figures 5.6 and 5.7, when accelerating or decelerating through transonic Mach numbers the unsteady condition of the flow field, which is influenced by flow history, will produce different positions for the shock waves to the steady state position at the same Mach number. This difference in the position of the shock waves usually outweighs all other factors when determining aerodynamic forces and moments and will result in a more significant difference between the steady and unsteady cases than observed outside the transonic range.

An interesting situation arises at Mach numbers on the edge of the transonic region. For example, for the biconvex aerofoil in figures 5.8 at Mach 0.79 and for the RAE 2822 in figure 5.25 at Mach 0.80, the flow fields for the steady and unsteady cases are shown. As already explained, based on flow history, unsteady flow fields are similar to the steady state flow fields of earlier conditions. Therefore, the accelerating flow fields are similar to steady state subsonic flow fields at lower Mach numbers. This explains the similarity between the steady and accelerating scenario, as flow fields do not vary significantly with changing subsonic Mach numbers. However, the decelerating flow fields would be similar to steady state flow fields at higher Mach numbers, which fall well into the transonic region. The great difference between the steady and decelerating cases, with shock waves on both surfaces of the aerofoil for the decelerating case, confirms this.

In the case of trailing compression waves, it is obvious from figures 5.12 and 5.13, that in the steady state condition the wave moves further away from the trailing edge of the aerofoil with increasing Mach number. As there is insufficient time for equilibrium during acceleration or retardation, the flow field at any instant resembles the steady state flow field of earlier conditions. For example during acceleration the position of the trailing wave would be similar to the steady state position at lower Mach numbers and would therefore be closer to the aerofoil. Conversely, during retardation the position of the trailing wave would be similar to the steady state position at higher Mach numbers and would therefore be further behind the trailing edge of the aerofoil. This explains the behavior of the trailing wave in figures 5.10 and 5.28.

Under steady state conditions as shown in figure 5.14, and during acceleration, a bow shock appeared only at supersonic Mach numbers. However, figures 5.15 to 5.17 show that during deceleration the bow shock is also present at subsonic Mach numbers. This can be explained by noting that any unsteady flow field is influenced by its history. Therefore, when an aerofoil decelerates from supersonic to subsonic

Mach numbers the bow shock, which was formed during supersonic flight, would still be present and would travel at supersonic velocity. As a result it would detach and move ahead of the front edge of the aerofoil, which at this point moves at subsonic velocity.

The tail shock behavior under steady state conditions is such that if the Mach number were reduced in steady state from supersonic to subsonic values, the tail shock would move forward over the surface of the aerofoil reducing in intensity and would eventually disappear before reaching the front of the aerofoil. At high decelerations, from supersonic to subsonic Mach numbers, the tail shock moves from the rear to the front of the aerofoil without much loss in intensity and eventually detaches from the leading edge and moves ahead of the aerofoil as shown in figures 5.17, 5.31 and 5.32. This can be attributed to the fact that the initial velocity of the tail shock is supersonic and as it moves at a higher velocity than the fast decelerating aerofoil, it ends up in front of the aerofoil. On its way from the rear to the front of the aerofoil the tail shock, which is a compression wave, almost wipes out the low-pressure regions on both surfaces of the aerofoil. This is illustrated with the diamond shaped aerofoil in figure 5.38 but was also observed in other airfoils.

In section 5.3 it was suggested that the higher drag force on the artillery shell during deceleration was mainly due to wave drag. This was because the decelerating shock wave was far larger than the shock under steady state or during acceleration at the same Mach number. This can be explained by considering the flight history of the object. It was decelerated from supersonic velocities and as there was insufficient time for the flow field to reach equilibrium it still exhibited supersonic characteristics. As the shock waves are far larger during supersonic flight, these characteristics were present in the decelerating scenario. It is also interesting to note that a bow shock is present in the decelerating case in figure 5.41, which is further proof that the flow field was exhibiting supersonic characteristics.

6. Concluding remarks

In this work the aerodynamics effects generated by objects moving through air at constant velocity at specific Mach numbers were compared to the effects resulting from the acceleration and deceleration of those objects through the same Mach numbers. In other words, in each case, the steady state condition was compared to the unsteady scenarios at a given Mach number. Two-dimensional and axisymmetric models were used for this application with Fluent as the CFD software. The study focused on airfoils and axisymmetric bodies. What follows is a statement of some of the main conclusions.

6.1 Conclusions

The unsteady flow field at a given instantaneous Mach number, resulting from the acceleration or deceleration of an aerofoil, is different to the steady state flow field at that same Mach number. This is because unsteady flow fields are time dependent and are influenced by their history.

In airfoils, in the subsonic range of Mach numbers, acceleration produced a reduction and retardation an increase in lift compared to steady state values. This was explained by recognizing that under transient conditions the flow field does not have sufficient time to reach equilibrium and reflects the characteristics of earlier conditions. During acceleration those earlier conditions represent times when the Mach number and hence the lift was lower. The same argument explains the higher lift values during deceleration.

In the subsonic region, acceleration of airfoils and axisymmetric bodies produced an increase in drag and the retardation a reduction in drag. This effect was explained by considering that, unlike lift, unsteady drag is not only influenced by its flow history but also by the inertia of the fluid through which the object is accelerated. Based on the numerical results the inertia effects are dominant in the determination of subsonic drag. However, in the transonic range of Mach numbers where flow history influences the position of shock waves it usually outweighs the inertia effects.

It was found that acceleration and deceleration had moderate effects on the aerodynamic forces in the subsonic range of Mach numbers. In the transonic region these effects were more pronounced but appear random. This is because, during accelerating or decelerating through transonic Mach numbers, the unsteady condition of the flow field produced different shock wave positions on and around the surface of the object, compared to the steady state positions at the same Mach number. This difference in the position of the shock wave resulted in a more significant difference in the aerodynamic forces and moments between the steady and unsteady cases than observed outside the transonic range.

Study of the flow field in the wake of aerofoils showed significant differences between the steady and unsteady cases at the same instantaneous Mach number. The changes in the position of a trailing wave, which were brought about by acceleration and retardation, were of particular interest. Under steady state condition the trailing wave moved further behind the trailing edge with increasing Mach number. As there was insufficient time for equilibrium during acceleration or retardation, the flow field at any instant resembled the steady state flow field corresponding to an earlier condition. For example during acceleration the position of the trailing wave would be similar to the steady state position at lower Mach numbers and was therefore closer to the aerofoil. Conversely, during retardation the position of the trailing wave would be similar to the steady state position at higher Mach numbers and was therefore further behind the trailing edge of the aerofoil.

During deceleration of aerofoils from supersonic to subsonic Mach numbers there was an increase in the stand-off distance between the bow shock and the leading edge of the aerofoil with the bow shock still present at subsonic Mach numbers and moving increasingly ahead of the aerofoil. At constant velocity or during acceleration from subsonic velocities no bow shock was observed when the aerofoil moved at subsonic or sonic Mach numbers. This was explained by noting that any unsteady flow field is influenced by its history. Therefore, when an aerofoil decelerates from supersonic to subsonic Mach numbers the bow shock, which was formed during supersonic flight, would still be present and would travel at supersonic velocity. As a result it would detach and move ahead of the front edge of the aerofoil, which at this point moves at subsonic velocity.

At high aerofoil decelerations from supersonic to subsonic Mach numbers, the tail shock moved to the front and eventually overtook the aerofoil. This can be attributed to the fact that the initial velocity of the tail shock was supersonic and as it moved at a higher velocity than the fast decelerating aerofoil, it ended up in front of the aerofoil.

Study of the transonic effects of acceleration and retardation on axisymmetric bodies showed that just short of sonic velocity the higher drag force on the artillery shell during deceleration was mainly due to wave drag. This was because the decelerating shock wave was far larger than the shock under steady state or during acceleration at the same Mach number. Again the flight history of the object was used to explain the existence of the large shock wave during deceleration. The artillery shell was decelerated from supersonic velocities and as there was insufficient time for the flow field to reach equilibrium it still exhibited supersonic characteristics. Since the shock waves are far larger during supersonic flight, these characteristics were present in the decelerating scenario. The larger shock wave must move a much larger amount of air in its forward motion and the shell will consequently experience the largest drag during deceleration.

6.2 Recommendations for future work

A number of projects have already been initiated by the author, which would form a continuation to the work presented here. Where possible, aspects of some of these have been assigned to final year undergraduate students as their final year project. Two of these are mentioned below.

The first is the development of an experimental facility to measure the aerodynamic effects of accelerating an object in stationary air. It is necessary to develop an in-house version of such a rig, as wind tunnel models are unsuitable for this purpose and the only existing test rigs found in literature that move the object, are designed for low velocity applications. Under the supervision of the author, two final year undergraduate students have developed preliminary designs for an experimental facility for the acceleration of a test specimen in stationary air. The design uses a magnetic rail gun, which propels the specimen forward along a 50 m track at very high accelerations. The facility is designed to accelerate the specimen to Mach 1.2 with a maximum acceleration of over 2000 m/s^2. It is the development of such a design into an experimental facility that is essential for the experimental validation of the unsteady numerical results in this research and is an important continuation to this work.

The second is the study of the effects of transonic acceleration on spheres. Using the Spalart-Allmaras turbulence model preliminary studies of this type were conducted by the author. These were not presented here, as more sophisticated modeling techniques are required to fully capture sphere aerodynamics. However, from the existing data, it is apparent that large spheres, with Reynolds numbers above transition, are far more sensitive to the aerodynamic effects of acceleration than smaller spheres that have subcritical Reynolds numbers in transonic Mach numbers.

REFERENCES

[1] G M Lilley, R Westley, A H Yates and J R Busing. Some aspects of noise from supersonic aircraft. *College of Aeronautics,* Report 71:396-414, March 1953.

[2] P H Oosthuizen and W E Carscallen. Compressible Fluid Flow. *McGraw Hill,* U.S.A., 1997.

[3] Fluent Inc. *Fluent 6.3 User and Tutorial Guides.* New Hampshire, U.S.A., 2007.

[4] R B Morrison and M J Ingle. Design Data for Aeronautics and Astronautics. *Wiley*, U.S.A., 1962.

[5] S F Hoerner. Fluid Dynamic Drag, theoretical, experimental and statistical information. *Published by the Author,* U.S.A., 1965.

[6] I H Abbott and A E Von Doenhoff. Theory of wing sections including a summary of airfoil data. *Dover Publications, Inc.,* New York, 1959.

[7] M. Van Dyke. *An Album of Fluid Motion*. The Parabolic Press, 1982.

[8] J W Becker. The high-speed frontier, case histories of four NACA programs, 1920-1950. *NASA SP-445,* Washington DC, U.S.A., 1980.

[9] H Jiang and P A Forsyth. Robust linear and nonlinear strategies for solution of the transonic Euler equations. *Computers & Fluids,* 24, 7: 753-770, 1995.

[10] L T Felthun and B W Skews. Dynamic shock wave reflection. *AIAA Journal*, 42, 8: 1633-1639, 2004.

[11] F Lien and G Kalitzin. Computations of transonic flow with the v^2-f turbulence model. *International journal of Heat and Fluid Flow*, 22:53-61, 2001.

[12] M Hafez and E Wahba. Multigrid acceleration for transonic aerodynamic flow simulations based on a hierarchical formulation. *International Journal for Numerical Methods in Fluids*, 47:517-541, 2005.

[13] M Hafez, A Shatalov and E Wahba. Numerical simulations of incompressible aerodynamic flows using viscous/inviscid interaction procedures. *Computer Methods in Applied Mechanics and Engineering*, 195:3110-3127, 2006.

[14] D A Gottfried and S Fleeter. Unsteady cascade aerodynamics in the time domain. *Journal of Propulsion and Power*, 18, 3: 519-527, May-June 2002.

[15] B B Prananta, M H L Hounjet and R J Zwaan. Two-dimensional transonic aeroelastic analysis using thin-layer Navier-Stokes methods. *Journal of Fluids and Structures*, 12:655-676, 1998.

[16] P R Spalart and S R Allmaras. A one-equation turbulence model for aerodynamic flows. *AIAA-92-0439, 30th Aerospace Sciences Meeting & Exhibit*, Reno, NV, January 1992.

[17] B Becker, M Reyer and M Swoboda. Steady and unsteady numerical investigation of transitional shock-boundary-layer-interactions on a fan blade. *Aerospace Science and Technology*, 11:507-517, 2007.

[18] W K Sekar and B Laschka. Calculation of the transonic dip of airfoils using viscous-inviscid aerodynamic interaction method. *Aerospace Science and Technology,* 9:661-671, 2005.

[19] J Ballmann, J Boucke and C Braun. Aeroelastic sensitivity in the transonic Regime. *IUTAM Symposium Transsonicum IV,* Goettingen, Germany, 2-6 September 2002, 65-70. Kluwer Academic Publishers, Dordrecht, The Netherlands, 2003.

[20] D J Mavriplis and D W Levy. Transonic drag prediction using an unstructured multigrid solver. *Journal of Aircraft,* 42, 4: 887-893, July-August 2005.

[21] J M Délery. The different facets of an old but always present concern: shockwave/boundary layer interaction. *IUTAM Symposium Transsonicum IV,* Goettingen, Germany, 2-6 September 2002, 91-98. Kluwer Academic Publishers, Dordrecht, The Netherlands, 2003.

[22] M Swoboda and W Nitsche. Shock boundary-layer interaction on transonic airfoils for laminar and turbulent flow. *Journal of Aircraft,* 33, 1: 100-108, January-February 1996.

[23] L E Ericsson. Dynamic airfoil flow separation and reattachment. *Journal of Aircraft,* 32, 6: 1191-1197, November-December 1995.

[24] M Hafez and E Wahba. Simulations of viscous transonic flows over lifting airfoils and wings. *Computers & Fluids,* 36:39-52, 2007.

[25] M Tsubokura, T Kobayashi, N Oshima, K Kitoh, H Zhang, K onishi and T Tominaga. High performance computation of unsteady flow around a formula car using large scale les on earth simulator. *12th International Symposium on*

[26] M R Ahmed and S D Sharma. An investigation on the aerodynamics of a symmetrical airfoil in ground effect. *Experimental Thermal and Fluid Science*, 29:633-647, 2005.

[27] R B Tahir, S Molder and E V Timofeev. Unsteady starting of high Mach number air inlets – A CFD study. *39th AIAA/ASME/SAE/ASEE Joint propulsion Conference and Exhibit*, Huntsville, Alabama, July 2003.

[28] Y Ikushima, S Kuroda and M Ohji. Use of a strain gauge accelerometer in the aerodynamic study of a spherical body at free fall. *Fluid Dynamics Research*, 9:143-153, 1992.

[29] R Y S Lai and C P Fan. Drag on a sphere accelerating rectilinearly in a elastico-viscous fluid. *Int.J.Engng Sci*, 16: 303-311, 1978.

[30] Y Tsuji, N Kato and T Tanaka. Experiments on the unsteady drag and wake of a sphere at high Reynolds numbers. *Int. J. Multiphase Flow*, 17, 3: 343-354, 1991.

[31] I M A Gledhill, K Forsberg, P Eliasson, J Baloyi and J Nordström. Investigations of acceleration effects on missile aerodynamics using computational fluid dynamics. *Aerospace Science and Technology*, 13:197-203, 2009.

[32] W C Selerowicz and A P Szumowski. Airfoil flow instabilities induced by background flow oscillations. *Experiments in Fluids*, 32:441-446, 2002.

[33] R M Fernie and H Babinsky. Unsteady shock motion on a NACA0012 aerofoil at low reduced frequencies. *American Institute of Aeronautics and Astronautics Paper*, 2004-49.

[34] P Freymuth, W Bank and M Palmer. Visualization of accelerating flow around an airfoil at high angles of attack. *Z. Flugwiss, Weltraumforsch, (Journal of light sciences and space research),* 7:392-400, 1983.

[35] P Freymuth, M Palmer and W Bank. Visualization of accelerating flow around an airfoil at angles of attack of 0^0 to 30^0. *Proceedings of the Eighth Symposium on Turbulence,* University of Missouri, USA, 135-144, 1983.

[36] F Finaish, M Palmer and P Freymuth. A parametric analysis of vortex patterns visualized behind airfoils in accelerated flow. *Reprints of the Ninth Symposium on Turbulence*, University of Missouri, USA, 10-1 to 10-10, 1984.

[37] P Freymuth, W Bank and M Palmer. Reynolds number dependence of vortex patterns in accelerated flow around airfoils. *Experiments in Fluids,* 3:109-112, 1985.

[38] P Freymuth, F Finaish and W Bank. The wing tip vortex system in a starting flow. *Z. Flugwiss, Weltraumforsch, (Journal of light sciences and space research),* 10:116-118, 1986.

[39] P Monnet , M Coutanceau, O Daube and T A Phuoc Loc. The use of visualization as a guide in the numerical determination of the flow around an abruptly accelerated elliptic cylinder or aerofoil. *Proceedings of the Third International Symposium on Flow Visualization*, University of Michigan, Michigan USA, 363-368, 1983.

[40] R H Ellsworth and T J Mueller. Airfoil boundary layer measurements at low Re in an accelerating flow from a nonzero velocity. *Experiments in Fluids*, 11: 368-374, 1991.

[41] T K Sengupta, T T Lim, S V Sajjan, S Ganesh and J Soria. Accelerated flow past a symmetric aerofoil: experiments and computations. *Journal of Fluid Mechanics*, 591: 255-288, 2007.

[42] G T Minkkinen, T A Wilson and G S Beavers. An experiment on the lift of an accelerated airfoil. *AIAA Journal Technical Notes*, 14, 5: 687-689, May 1976.

[43] R S Sawyer and J P Sullivan. Lift response of a rectangular wing undergoing a step change in forward speed. *AIAA Journal Technical Notes*, 28, 7: 1306-1307, July 1990.

[44] R S Sawyer and J P Sullivan. Lift development of delta wings undergoing constant acceleration from rest. *Journal of Aircraft*, 28, 11: 735-740, November 1991.

[45] J E Marquart and F E Eastep. Numerical representation of pitching and nonpitching airfoils undergoing linear acceleration. *Journal of Aircraft*, 35, 5: 761-768, September-October 1998.

[46] H Hamdani and M Sun. Aerodynamic forces and flow structures of an airfoil in some unsteady motions at small Reynolds number. *Acta Mechanica*, 145:173-187, 2000.

[47] Y K Lee, S Raghunathan, H D Kim and T Setoguchi. Unsteady aerodynamic characteristics of an aerofoil at a gradual speed change. *43rd AIAA Aerospace Sciences Meeting and Exhibit*, Reno, Nevada, January 2005.

[48] T J Barber E Leonardie and R D Archer. Appropriate CFD boundary conditions for the prediction of ground effect aerodynamics. *The Aeronautical Journal,* 545-547, 1999.

[49] J M Delery. Shock Wave/Boundary Layer Interactions. Hand Book of Shock Waves, volume 2. *Academic Press,* 2001.

APPENDIX A: User Defined Functions

A.1 Modelling acceleration by accelerating fluid at far field

As described in chapter 2 the user-defined functions developed for this investigation are designed to model accelerating objects in compressible fluids. Initially attempts were made to develop models by accelerating the fluid at far field. However, although such models gave reasonable results at very low velocities and accelerations, high velocities and accelerations resulted in fairly steep pressure and velocity gradients across the flow field, which was not at all representative of the physical case being modelled. The following is an example of a user-defined function where only the fluid at far field is accelerated. The programming language used is C.

```
/* User-Defined Function for unsteady flow Mach number */
/* Author: H. Roohani */

#include "udf.h"
DEFINE_PROFILE(unsteady_Mach, thread, position)
{
 float t, Mach;
 face_t f;
 t = RP_Get_Real("flow-time");
 Mach = (0.1+0.3*t);
 begin_f_loop(f, thread)
 {
  F_PROFILE(f, thread, position) = Mach;
 }
 end_f_loop(f, thread)
}
```

The initial velocity is defined in terms of the far-field Mach number at 101.325 kPa and 300 K (i.e. 347.0877 m/s). Therefore, in this case the initial velocity is Mach 0.1 (i.e. 34.70877 m/s). For convenience acceleration is defined as the rate of change of Mach number. Therefore, an acceleration of 104.126 m/s^2 translates to a change in Mach number of 0.3 per second. This results in the representation of velocity at time t as Mach = 0.1 + 0.3t, shown in the above program.

A.2 Modelling acceleration by using source terms

In order to address the problems encountered at higher velocities and accelerations the above technique is modified by adding momentum and energy source terms to the user defined function. As shown in chapter 2, the source term equations simplify to the following:

Momentum Source $= \rho dv/dt$ ***[N/m3]***

Energy Source $= \rho v dv/dt$ ***[W/m3]***

It is clear that at constant acceleration the momentum source term becomes a constant and can be put directly into the Fluent source term panel. The energy source term would remain a variable and must therefore be included as part of the user defined function. The following is an example of a user-defined function designed for a constant acceleration case.

```
/* User-Defined Function for unsteady flow Mach number */
/* Author: H. Roohani */

#include "udf.h"
DEFINE_SOURCE(uns_Energy,c,t,dS,eqn)
{
```

```
real source;
float time, Energy;

time = RP_Get_Real("flow-time");
Energy = 1.176674*347.0877*(0.1+0.25*time)*0.25*347.0877;
source = Energy;
dS = 0;
return source;
}
DEFINE_PROFILE(unsteady_Mach, thread, position)
{
float t, Mach;
face_t f;
t = RP_Get_Real("flow-time");
Mach = (0.1+0.25*t);
begin_f_loop(f, thread)
{
 F_PROFILE(f, thread, position) = Mach;
}
end_f_loop(f, thread)
}
```

As with the previous case, velocity and acceleration are defined in terms of the far-field Mach number, and if necessary converted to SI units. Therefore, the acceleration in this case is equivalent to a change in Mach number of 0.25 per second, which is 86.77 m/s^2 (8.845g). The density for air at 101.325 kPa and 300 K is 1.176674 kg/m^3, which is the value used above. For other accelerations, the 0.25 term in the user defined function must be changed to other appropriate coefficients, which would need to be a negative value for any decelerating motion. For different initial velocities the 0.1 term must be altered.

For variable acceleration, the momentum source term must be written into the user defined function, and the Mach number and energy terms must be altered in order to model the acceleration.

APPENDIX B: Additional technical information

In this chapter supplementary technical information is provided. This includes information about the mesh and numerical modelling used in each case study as well as background theoretical information relating to all cases.

B.1 The biconvex aerofoil

The mesh for this aerofoil is shown in figure B.1. It has a total of 80000 hexahedral cells with 200 nodes at each surface of the aerofoil. The Domain is 40m by 40m with the 1m cord length aerofoil placed at its centre. A mesh convergence study was performed in order to arrive at this mesh resolution. This is explained in chapter 3.

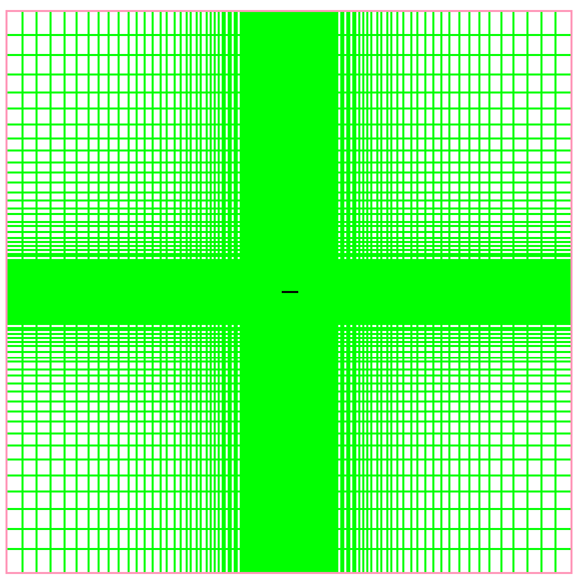

(a) The entire domain.

Figure B.1: Details of the mesh used for the biconvex aerofoil.

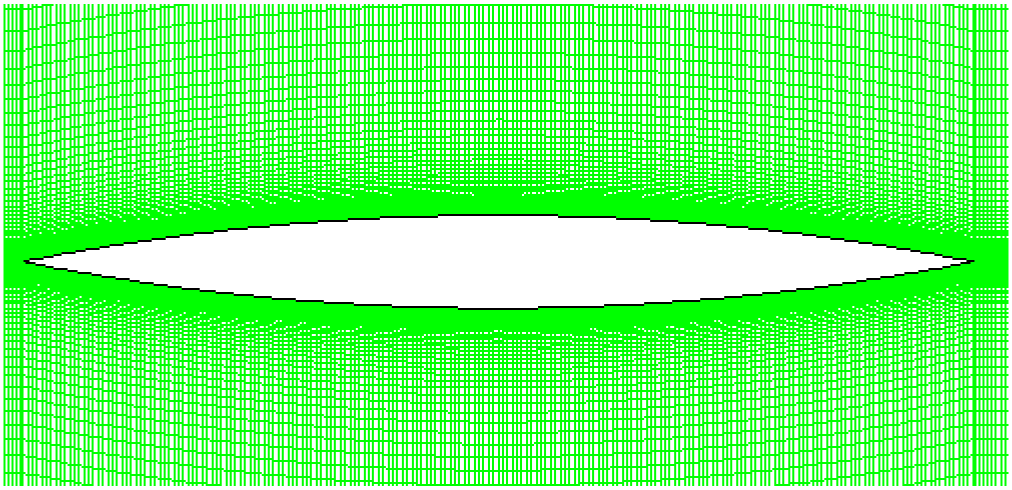

(b) Mesh around the aerofoil.

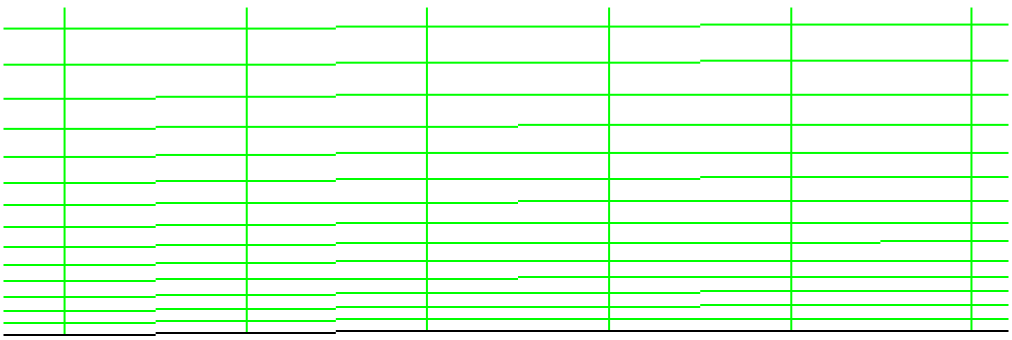

(c) Mesh at the boundary.

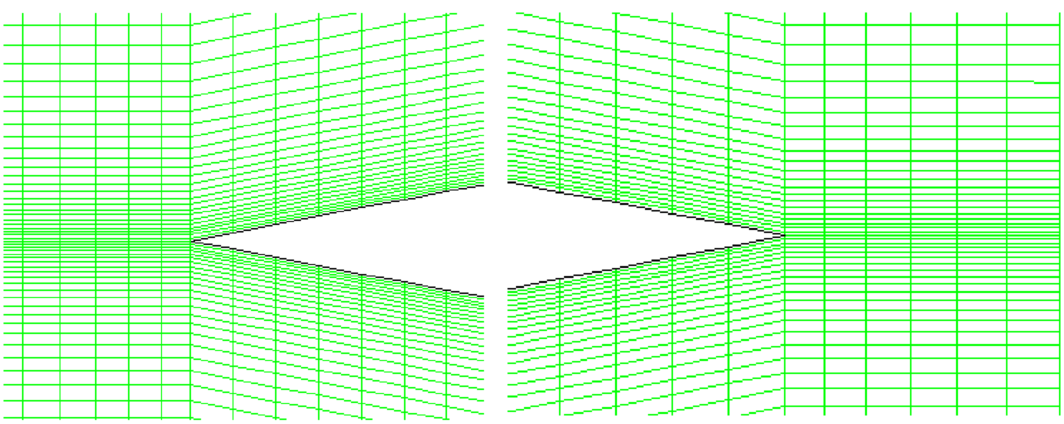

(d) Mesh at the leading edge (left) and trailing edge (right).

Figure B.1: Continued.

No mesh adaption was used here or indeed in any of the other cases, as the purpose of this study was to capture the shocks on the surface or in the close vicinity of the object and the mesh in those areas was designed to be sufficiently fine.

B.2 The RAE 2822 aerofoil

The meshed domain used for the RAE 2822 aerofoil is shown in figure B.2. It has a maximum length of 143m and a maximum width of approximately 128m with the 1m cord aerofoil placed 56m to the right of the circular boundary. The meshed domain has a total of 126900 hexahedral cells with 210 nodes at each surface of the aerofoil. This mesh was supplied by Fluent© and is the main one used in appendix C (validation11). It was therefore used to produce results which matched experiment and were mesh independent. The large Domain and the relatively fine mesh away from the aerofoil makes it useful for studying shock wave dynamics around the aerofoil.

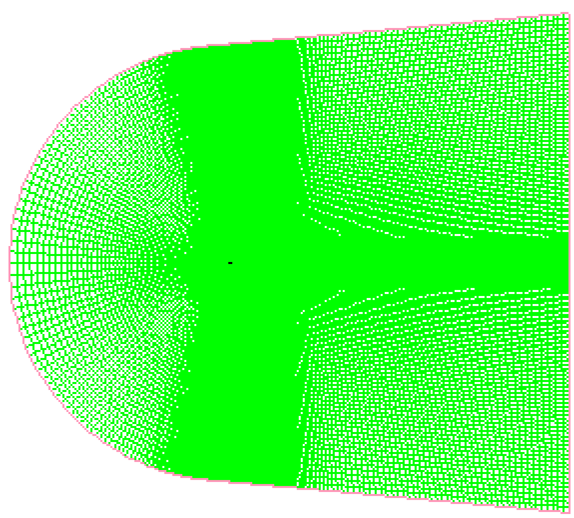

(a) The entire domain

Figure B.2: Details of the mesh used for the RAE 2822 aerofoil.

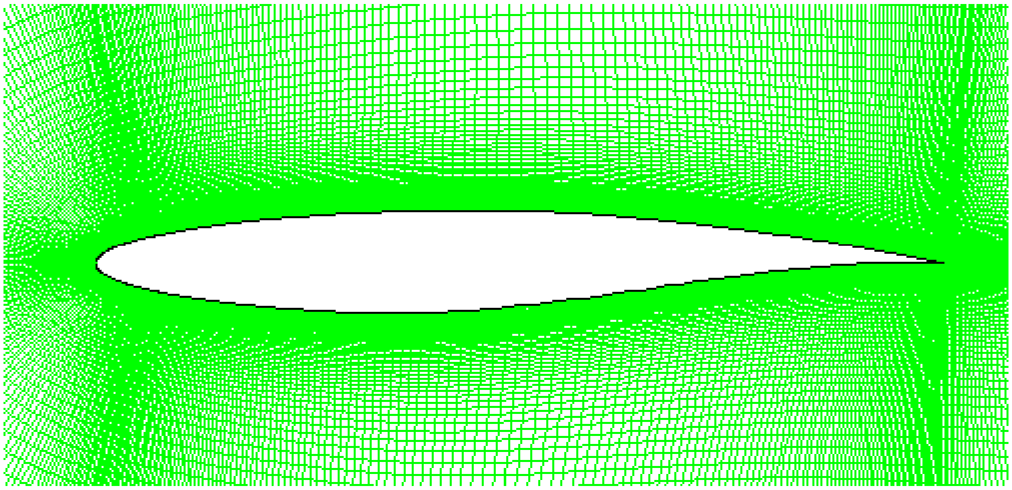

(b) Mesh around the aerofoil.

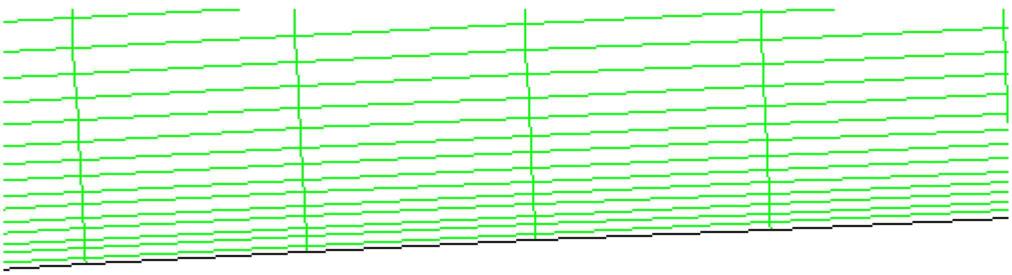

(c) Mesh at the boundary.

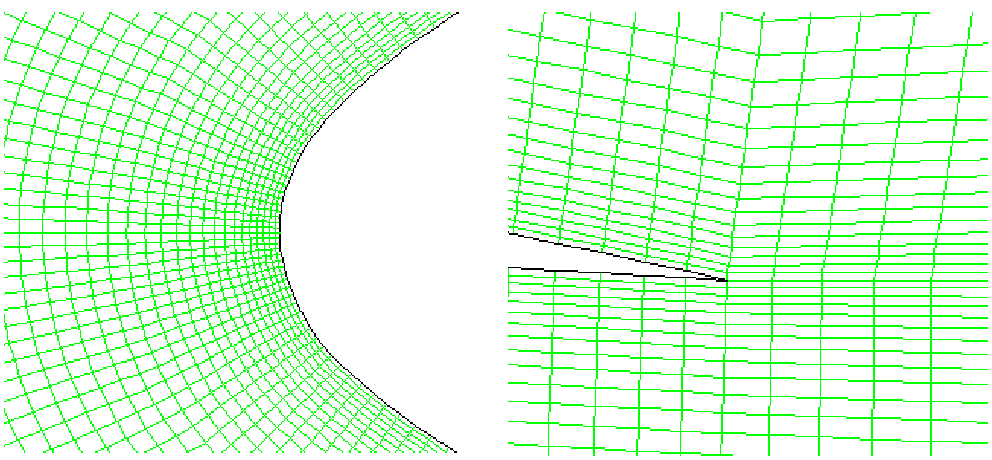

(d) Mesh at the leading edge (left) and trailing edge (right).

Figure B.2: Continued.

B.3 The NACA 2412 aerofoil

In this research the NACA 2412 aerofoil was used exclusively for subsonic studies, ranging between Mach 0.1 and 0.4, where no shock capturing was required. As described in chapter 3 a relatively coarse mesh was chosen for this aerofoil because of wall Yplus considerations where the mesh was shown to be better suited for the range of Mach numbers in question than finer meshes. In figure 3.2 of chapter 3 numerical values of lift coefficients obtained by using this mesh were compared with experimental results and a fairly good correlation was obtained. This further confirmed that the mesh was suitable for the range of Mach numbers for which it was used. In figure B.3 below the mesh is shown. It has a total of 10000 hexahedral cells with 70 nodes at each surface of the aerofoil. The Domain is 20m long and has a maximum width of 20m. The 1m cord aerofoil is placed approximately at the centre of the mesh.

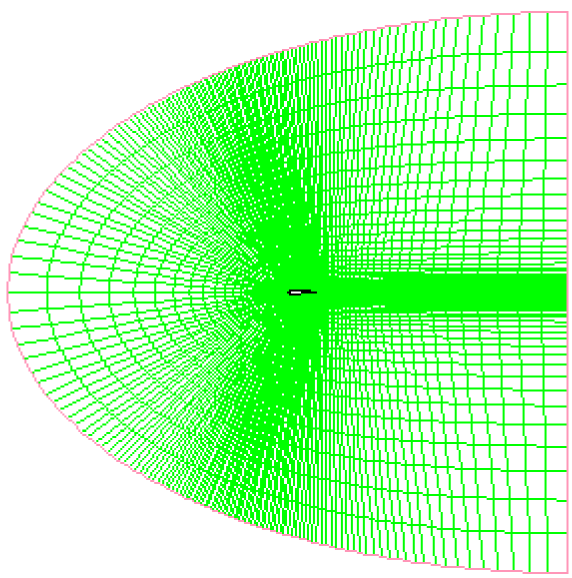

(a) The entire domain

Figure B.3: Details of the mesh used for the NACA 2412 aerofoil.

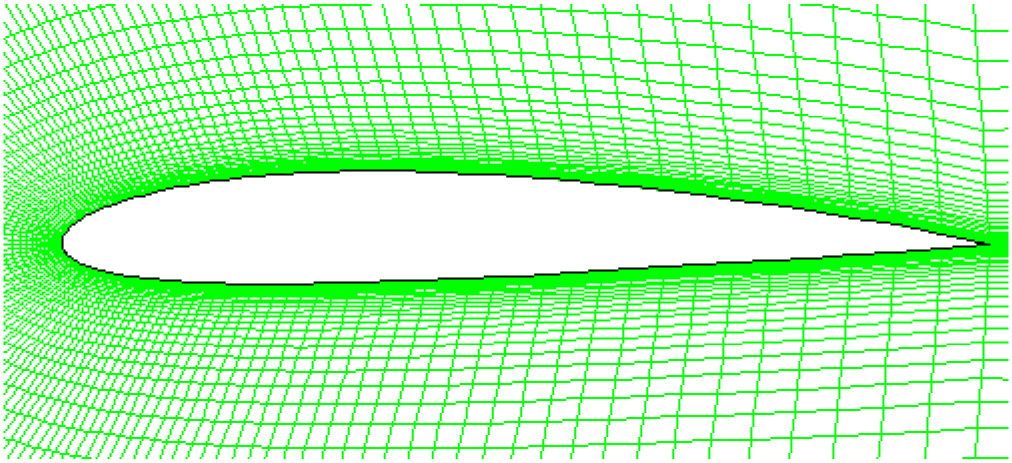

(b) Mesh around the aerofoil.

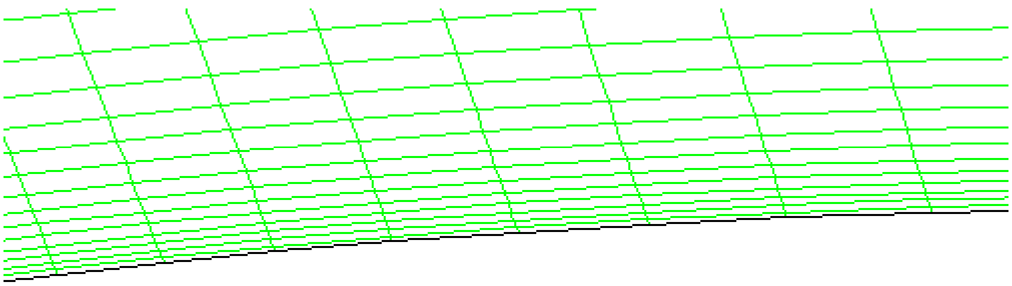

(c) Mesh at the boundary.

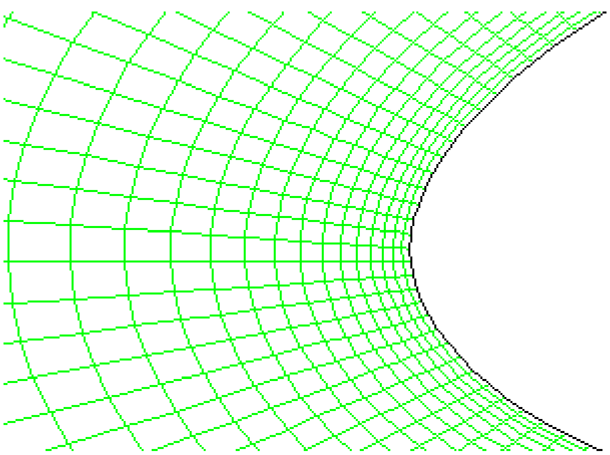

(d) Mesh at the leading edge.

Figure B.3: Continued.

B.4 The diamond shaped aerofoil

The main reason for this case study was to analyse the shockwave dynamics close to the surface of the diamond shaped aerofoil and to investigate the effect of the kink, which is the discontinuity present on both surfaces of this aerofoil, on the unsteady flow behaviour. It was for this reason that the mesh close to the boundary was designed to be the finest of all the cases investigated but the mesh resolution away from the aerofoil was allowed to be relatively coarse.

The meshed domain has a total of 40000 hexahedral cells with 300 nodes on each surface of the aerofoil. The Domain is 40m by 40m with the 1m cord length aerofoil placed at its centre. Details of the mesh are shown in figure B.4 below.

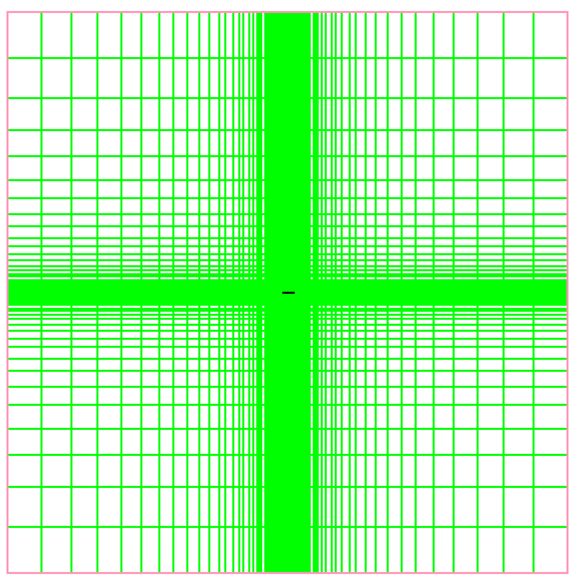

(a) The entire domain

Figure B.4: Details of the mesh used for the diamond shaped aerofoil.

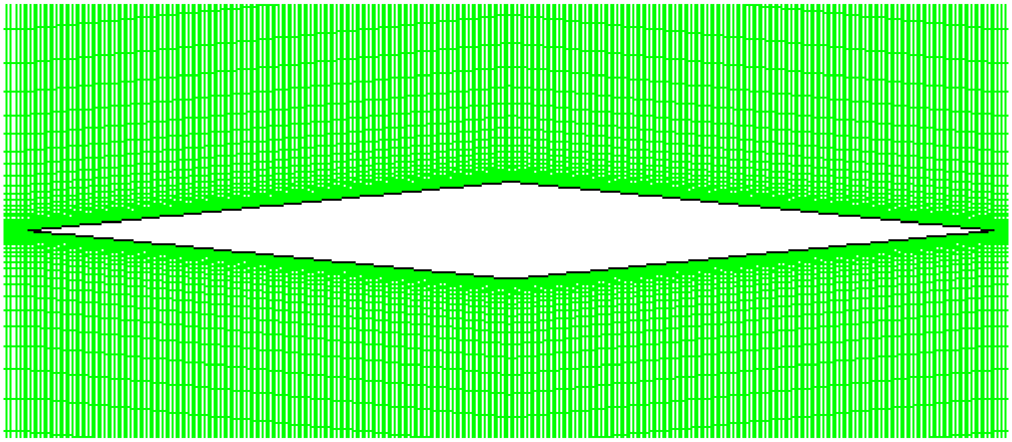

(b) Mesh around the aerofoil.

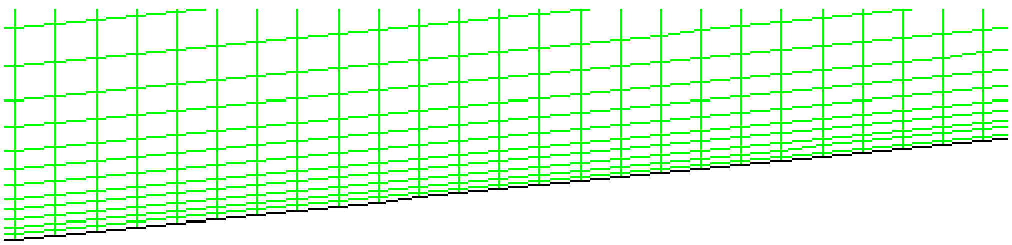

(c) Mesh at the boundary.

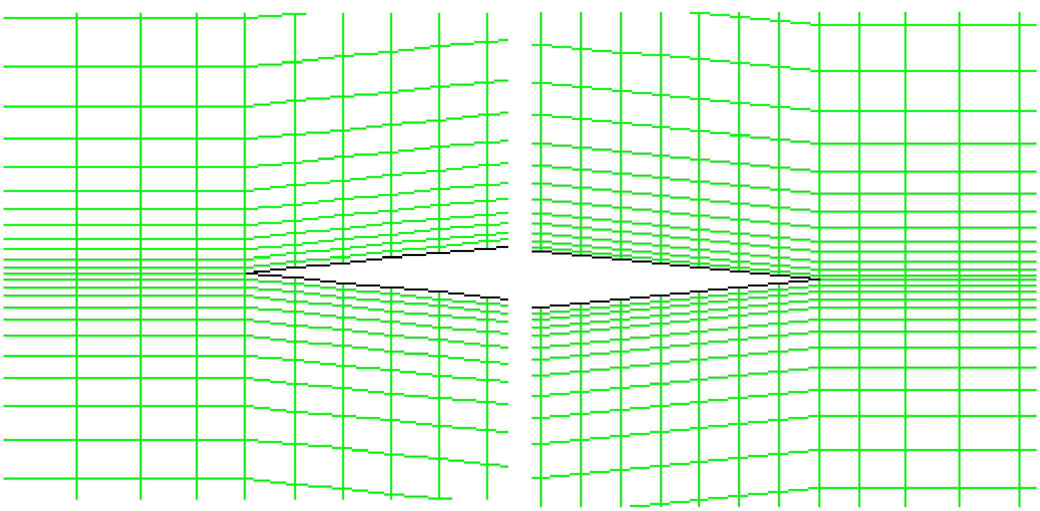

(d) Mesh at the leading edge (left) and trailing edge (right).

Figure B.4: Continued.

B.5 The sphere

In figure B.5 a semicircular axisymmetric mesh used for modelling the sphere is shown. The axial line of symmetry is drawn horizontally in yellow at the bottom of the meshed domain. In order to visualize the three dimensional domain modelled, the displayed mesh must be seen as a cross section of that domain at any angle of rotation about the axis of symmetry. The displayed axisymmetric mesh has 30 000 hexahedral cells with 200 nodes on the surface of the displayed portion of the sphere. The sphere has a diameter of 1m and the radius of the meshed semicircular domain is 20m.

For proper analysis of sphere aerodynamics a much finer three dimensional mesh is required. Also Large Eddy Simulation (LES) or Direct Numerical Simulation (DNS) would be necessary if flow details such as eddies are to be captured. However, in this investigation a broad study mainly focusing on sphere drag at subsonic Mach numbers is undertaken and the good correlation with experimental results shown in chapter 3 confirms that the mesh is adequate for this application.

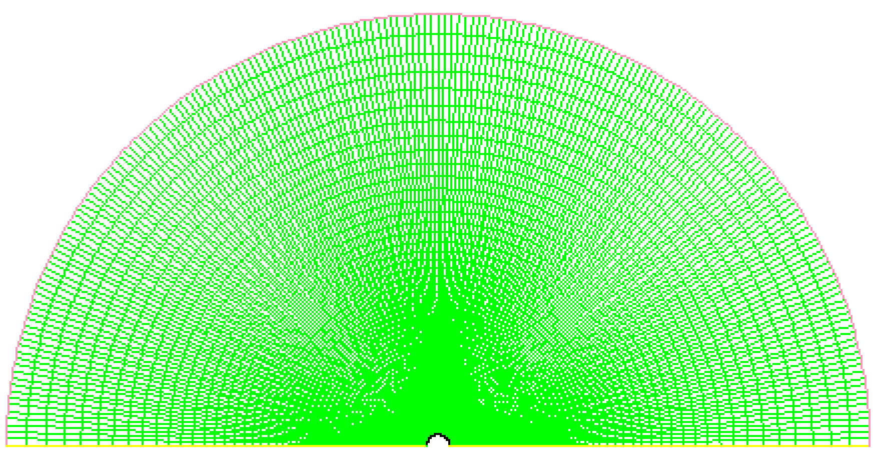

(a) The entire domain

Figure B.5: Details of the mesh used for the sphere.

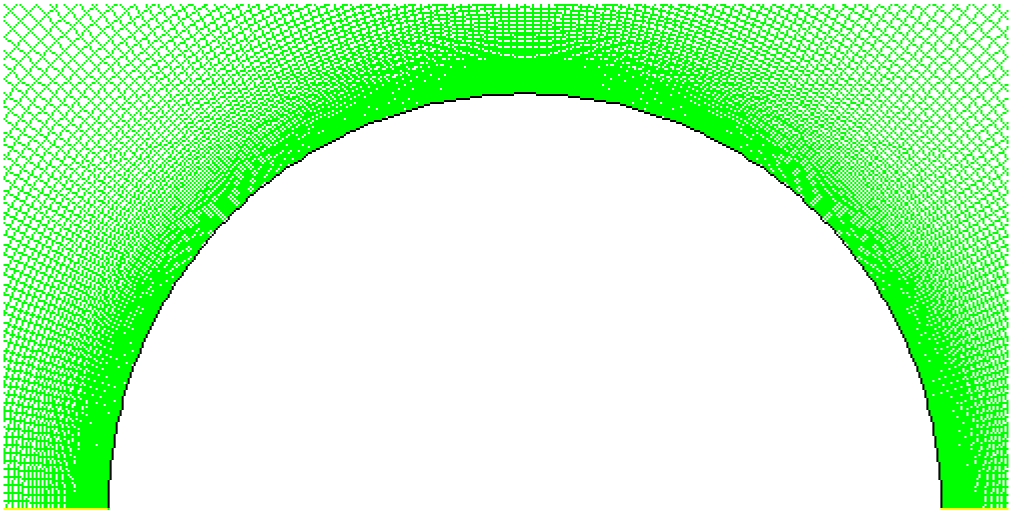

(b) Mesh around the sphere.

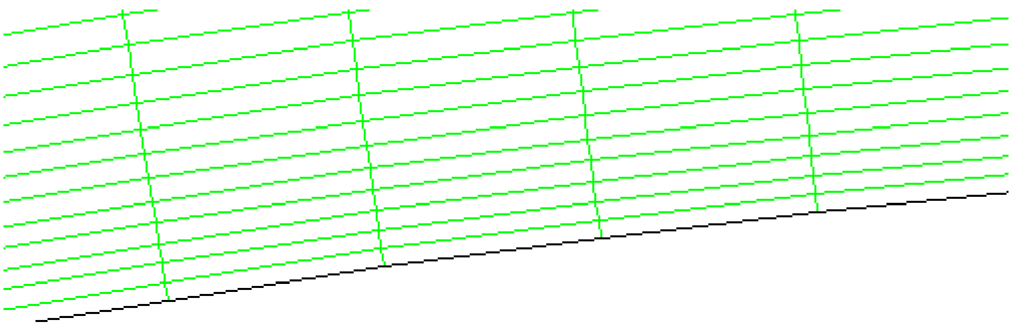

(c) Mesh at the boundary.

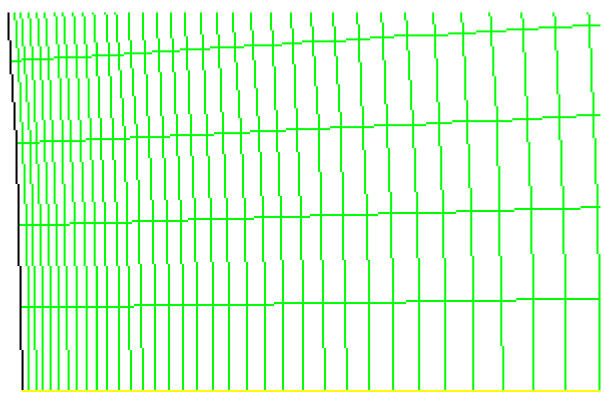

.
(d) Mesh in the wake of the sphere.

Figure B.5: Continued

B.6 The artillery shell

The mesh used for the artillery shell is shown in figure B.6 below. The meshed domain is 20m long and has a radius of 10m about the axial line of symmetry, which is shown in yellow. The 240mm long shell, which has a maximum diameter of 50mm, is placed symmetrically at the centre of the meshed domain. The displayed axisymmetric mesh has a total of 48700 hexahedral cells with 245 nodes at the surface of the displayed portion of the shell.

Although the experimental information available in literature only allowed a qualitative comparison with the numerical data obtained from this mesh, the turbulence models used are more suitable for analysing the aerodynamics of the shell rather than the sphere. This is because the numerical modelling of the shell is more straightforward as it is characterised by sharp corners at the base rather than curved surfaces on which the turbulence and boundary layer modelling is more complex.

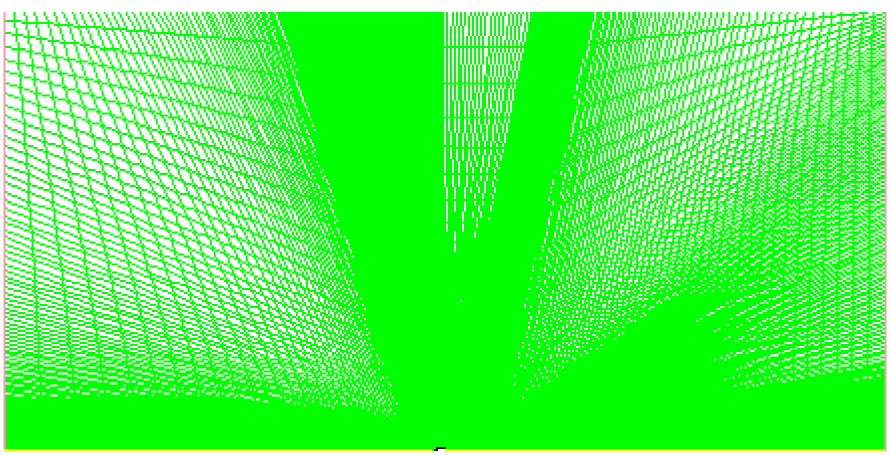

(a) The entire domain

Figure B.6: Details of the mesh used for the artillery shell.

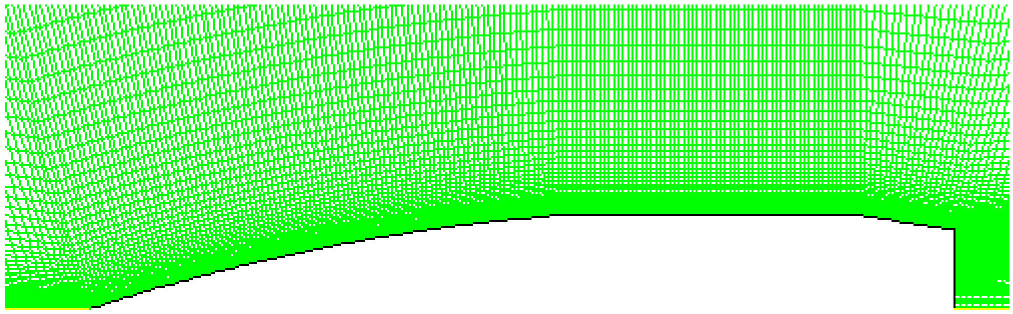

(b) Mesh around the shell.

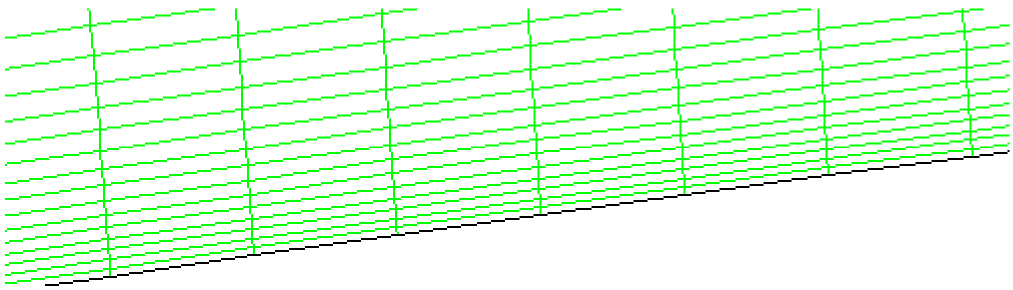

(c) Mesh at the boundary.

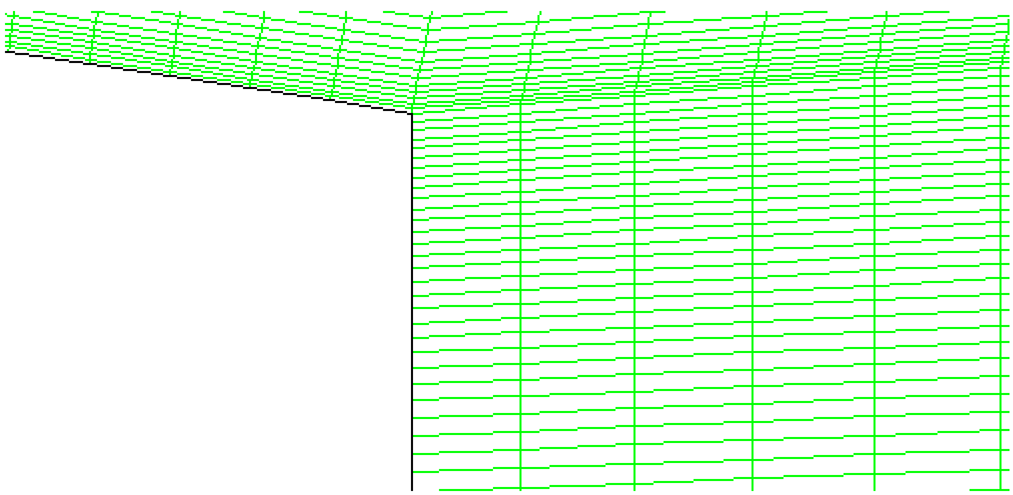

(d) Mesh in the wake of the shell.

Figure B.6: Continued.

B.7 Further details of CFD simulations

Details of all the different meshes used in this research are given above and information on the boundary conditions is given in the previous chapters as each case is presented. In this section other relevant information relating to time steps and convergence criteria are discussed.

B.7.1 Application of time steps in unsteady Modelling

For acceleration of 106g (1041 m/s^2) or -106g time steps of 0.001 seconds were used. Therefore, in order to accelerate an object from Mach 0.1 to 1.6 or from Mach 1.6 to 0.1 a total of 500 time steps were required. On the other hand, for accelerations of 8.845g (86.77 m/s^2) and -8.845g, a time step size of 0.01 seconds was found to be appropriate. In these cases 600 time steps were required to accelerate the object from Mach 0.1 to 1.6 or vice versa. Similarly, in the lower acceleration case of the Formula 1 scenario of section 4.2.1, time steps of 0.01 seconds were used. In this case 400 time steps were required in order to accelerate the object from Mach 0.1 (125 km/h) to Mach 0.2 (250 km/h). In this research Mach number is defined as the velocity of sound at atmospheric pressure of 101325 Pa and ambient temperature of 300 K, which is 347.0877 m/s.

In all the above cases the empty domain verification technique illustrated in figure 2.12 of chapter 2 was used to ensure that the time step sizes used were adequately small to give reliable results. In the case of the Formula 1 scenario the values of unsteady lift and drag were also tested for convergence with reduction in the size of time steps. This was done by comparing unsteady values of lift and drag at the same flow time, obtained by using time steps of 0.1s, 0.01s and 0.001s. It turned out that any reduction in the size of time steps beyond 0.01s resulted only in insignificant changes in unsteady lift or drag, which confirmed convergence.

B.7.2 Convergence criteria in numerical simulations

As Fluent is the main CFD software used in this research, the standard convergence criteria in numerical simulations are the ones defined by Fluent and are built into the Fluent source code [3]. These involve the solution of continuity, momentum and energy equations as well as transport equations, which depends on the choice of turbulence model used. In Fluent an equation can be checked for convergence in four different ways. These are the absolute option, the relative option, the relative and absolute combined as well as the option where no convergence checking is done. An explanation to these is given in the Fluent User's Guide [3].

In this research the absolute convergence criterion was used in conjunction with lift, drag and moment curves. In absolute convergence checking the residual of an equation at an iteration is compared with a user-specified value. If the residual is less than the user-specified value, that equation is deemed to have converged. In order to ensure convergence the user-specified residual values were chosen to be significantly lower than the default values from Fluent. For example the default user-specified value for the turbulence model transport equations was 10^{-3}. This value was lowered to 10^{-7} in all simulations. In steady state simulations lift, drag, and pitching moment were also monitored for convergence by ensuring that they had reached a constant value. This was particularly a useful method of testing convergence when the residuals were not reducing to values below the user-specified value.

In unsteady simulations specifying the number of iterations per time step was found to be a useful way of addressing the problem of non-reducing residual. In Fluent the default number of iterations per time step is 20 but in order to ensure convergence as many as 300 iterations per time step were used. This ensured that the flow field and the aerodynamic forces converged at any time step.

B.7.3 Shock capturing

The in-house code written by L.T. Felthun is designed to move an object in a stationary fluid. It captures shock through the use of mesh refinement in areas were there is a high pressure gradient, whether the object is accelerating or moving at constant velocity.

In Fluent mesh refinement schemes are available. However, as the purpose of this study was to capture the shocks on the surface or in the close vicinity of the object and the mesh in those areas was designed to be sufficiently fine, no mesh refinement was used in simulations using Fluent.

B.8 Fundamental equations solved in the simulations

As mentioned above in the simulations conducted in this research Fluent solved the continuity, momentum and energy equations as well as transport equations, which depended on the choice of turbulence model. The form of these equations used by Fluent is given in the Fluent User's Guide [3] or the Theory Guide. However, as an example the momentum equation for viscous flow, generally referred to as the Navier-Stokes equation, is given below:

$$\frac{\partial}{\partial t}(\rho\vec{v})+\nabla\cdot(\rho\vec{v}\vec{v})=-\nabla p+\nabla\cdot\left(\bar{\bar{\tau}}\right)+\rho\vec{g}+\vec{F}$$

$\rho\vec{g}$ and $\vec{F}$ are the gravitational and external body forces respectively. The symbol $\left(\bar{\bar{\tau}}\right)$ is the stress tensor and p represents static pressure. $\vec{F}$ also contains model-dependent source terms such as porous-media and user-defined sources.

It is important to note that all the equations solved by Fluent have a component which allows user defined source terms to be included. This was essential in modelling accelerating objects in stationary compressible fluids as described in chapter 2.

B.9 The Wall Yplus Parameter in turbulence modelling

The Wall Yplus is a non-dimensional parameter defined by the equation

$$y^+ = \rho\, u_\tau\, y_P \,/\, \mu$$

where $u_\tau = (\tau_w \,/\, \rho_w)^{1/2}$ is the friction velocity, with shear stress τ_w and fluid density ρ_w evaluated at the wall. y_P is the distance from point $\boldsymbol{P}$ to the wall, ρ is the fluid density and μ is the fluid viscosity at point $\boldsymbol{P}$. The point $\boldsymbol{P}$ is the centre point of any cell adjacent to the wall.

As already mentioned in chapter 3 the mesh near the wall should be designed to ensure that values of the wall Yplus are either less than 1 or greater than 30. Values between 1 and 30 do not yield reliable results. More details about wall Yplus can be obtained from Fluent user guide [3] or the theory guide.

APPENDIX C: Validation Case from Fluent

A validation case supplied by Fluent© is included here, where steady state results obtained by using Fluent are compared with experimental data. The comparison shows very good correlation between computation and experiment and validates the Fluent code for steady state external aerodynamic computations. The pressure-far-field boundary condition technique described in chapter 2 is used here.

It is important to note that the validation examines aerodynamic forces and shock wave position, which form the main focus of this study.

Validation 11. Transonic Flow Over an RAE 2822 Airfoil

11.1 Purpose

The purpose of this validation is to compare the predictions of FLUENT with the experimental data of Cook et al. [1] for flow over an RAE 2822 airfoil. The quantities examined are:

1. Static pressure coefficient, C_p.
2. Lift and drag coefficients.
3. Shock position on the airfoil.

11.2 Problem Description

The problem under consideration involves flow over an RAE 2822 airfoil at a free-stream Mach number of 0.73. The angle of attack is 3.19 degrees, which corresponds to case 9 in the experimental data of Cook et al. [1]. Since the calculations were done in free-stream conditions, the angle of attack has been modified to account for the wind-tunnel wall effects. An angle of attack equal to 2.79 degrees was used in the calculations, as suggested by Coakley [2].

The geometry of the RAE 2822 airfoil is shown in Figure 11.2.1. It is a thick airfoil with a chord length, c, of 1.00 m and a maximum thickness, d, of 0.121 m. The domain extends $55c$ from the airfoil, so that the presence of the airfoil is not felt at the outer boundary.

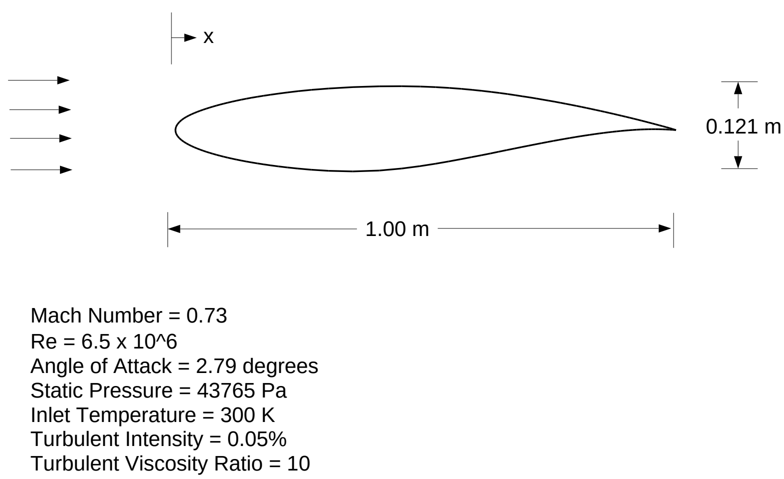

Figure 11.2.1: Geometry of the RAE 2822 Airfoil

11.3 References

1. Cook, P.H., McDonald, M.A., and Firmin, M.C.P., *AEROFOIL RAE 2822 Pressure Distribution and Boundary Layer and Wake Measurements*, AGARD Advisory Report No. 138, 1979.

2. Thomas J. Coakley., Numerical Simulation of Viscous Transonic Airfoil Flows, AIAA 25th Aerospace Sciences Meeting, 1987.

11.4 Results

A comparison of FLUENT's predictions of the static pressure coefficient C_p with experimental data has been done for a hybrid and a quadrilateral mesh. In general, FLUENT's predictions agree well with the experimental data.

The shock location over the airfoil is quantified as the location where the top surface pressure coefficient increases rapidly. Table 11.4.1 compares the numerical predictions of the shock location, the lift coefficients, and the drag coefficients with the experimental values.

Table 11.4.1: Comparison of the Predictions of Lift and Drag Coefficients, and Shock Location

Mesh	**Model**	**Lift (C_L)**	**Drag (C_D)**	**Shock (x/c)**
	Experiment	0.803	0.0168	0.52
Hybrid	Realizable k-ϵ	0.825	0.0181	0.52
	SST k-ω	0.781	0.0164	0.50
	Spalart-Allmaras	0.815	0.0171	0.52
Quadrilateral	Realizable k-ϵ	0.828	0.0181	0.52
	SST k-ω	0.782	0.0163	0.50
	Spalart-Allmaras	0.817	0.0170	0.52

From Table 11.4.1, the predicted shock locations and lift coefficients are predicted within 4% of the experimental results, and the drag coefficients are predicted within 8% of the experimental results for all six runs.

11.4.1 Validation-Specific Information

Solver:	FLUENT 2ddp
Version:	6.3.19
Solution Files:	1. `rae_hybrid_rke_nb.cas`, `rae_hybrid_rke_nb.dat`
	2. `rae_hybrid_sst_nb.cas`, `rae_hybrid_sst_nb.dat`
	3. `rae_hybrid_sa_nb.cas`, `rae_hybrid_sa_nb.dat`
	4. `rae_quad_rke.cas`, `rae_quad_rke.dat`
	5. `rae_quad_sst.cas`, `rae_quad_sst.dat`
	6. `rae_quad_sa.cas`, `rae_quad_sa.dat`

These solution files are available from the Fluent Inc. User Services Center as described in the Introduction.

11.4.2 Plot Data

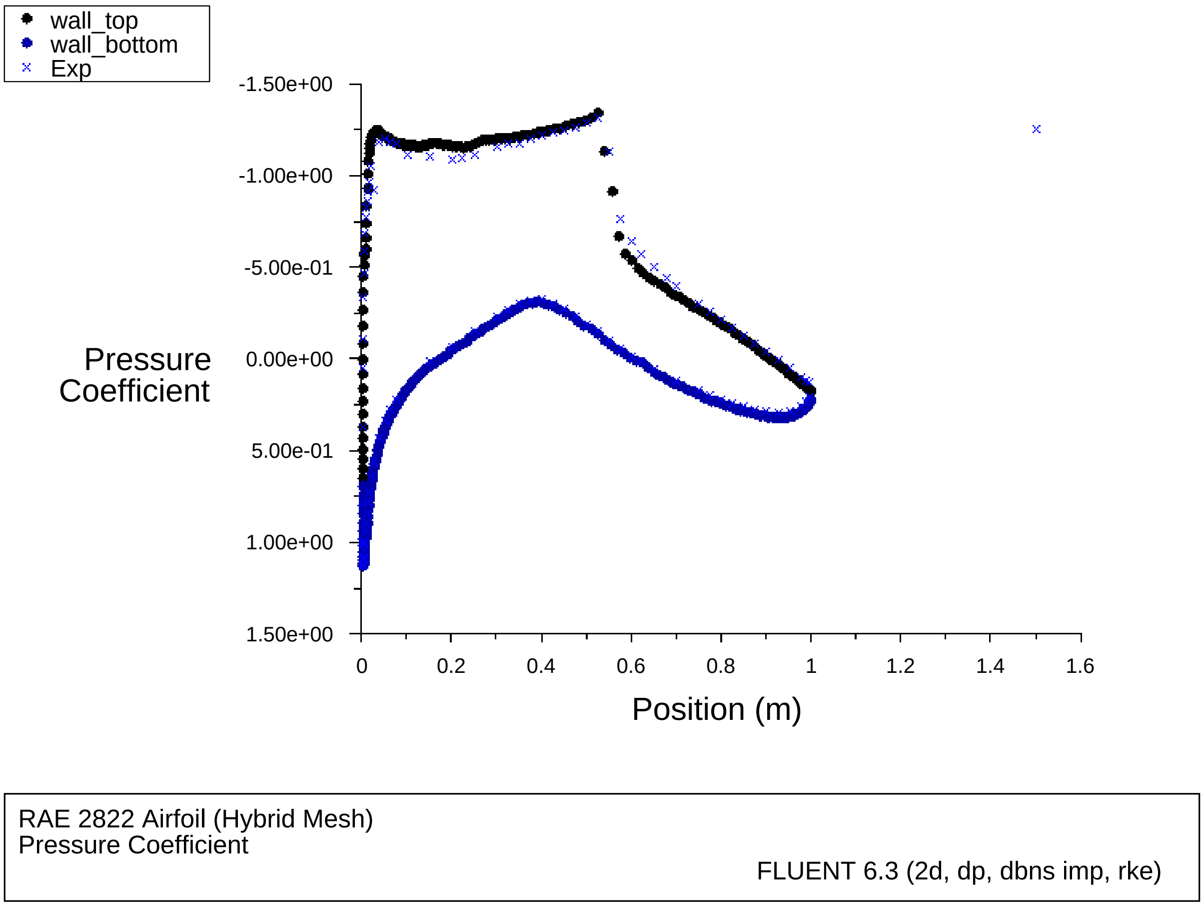

Figure 11.4.1: Comparison of FLUENT's Predictions of the Static Pressure Coefficient C_p With the Experimental Data for the Hybrid Mesh, Realizable k-ϵ Case

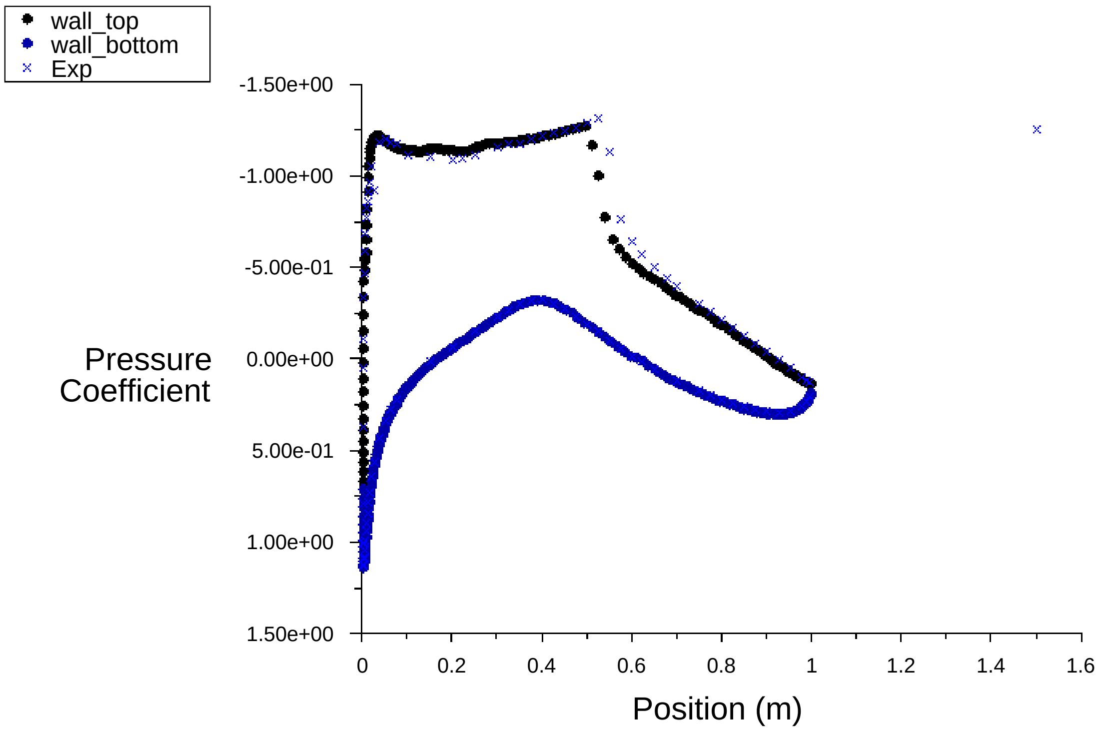

RAE 2822 Airfoil (Hybrid Mesh)
Pressure Coefficient
FLUENT 6.3 (2d, dp, dbns imp, sstkw)

Figure 11.4.2: Comparison of FLUENT's Predictions of the Static Pressure Coefficient C_p With the Experimental Data for the Hybrid Mesh, SST k-ω Case

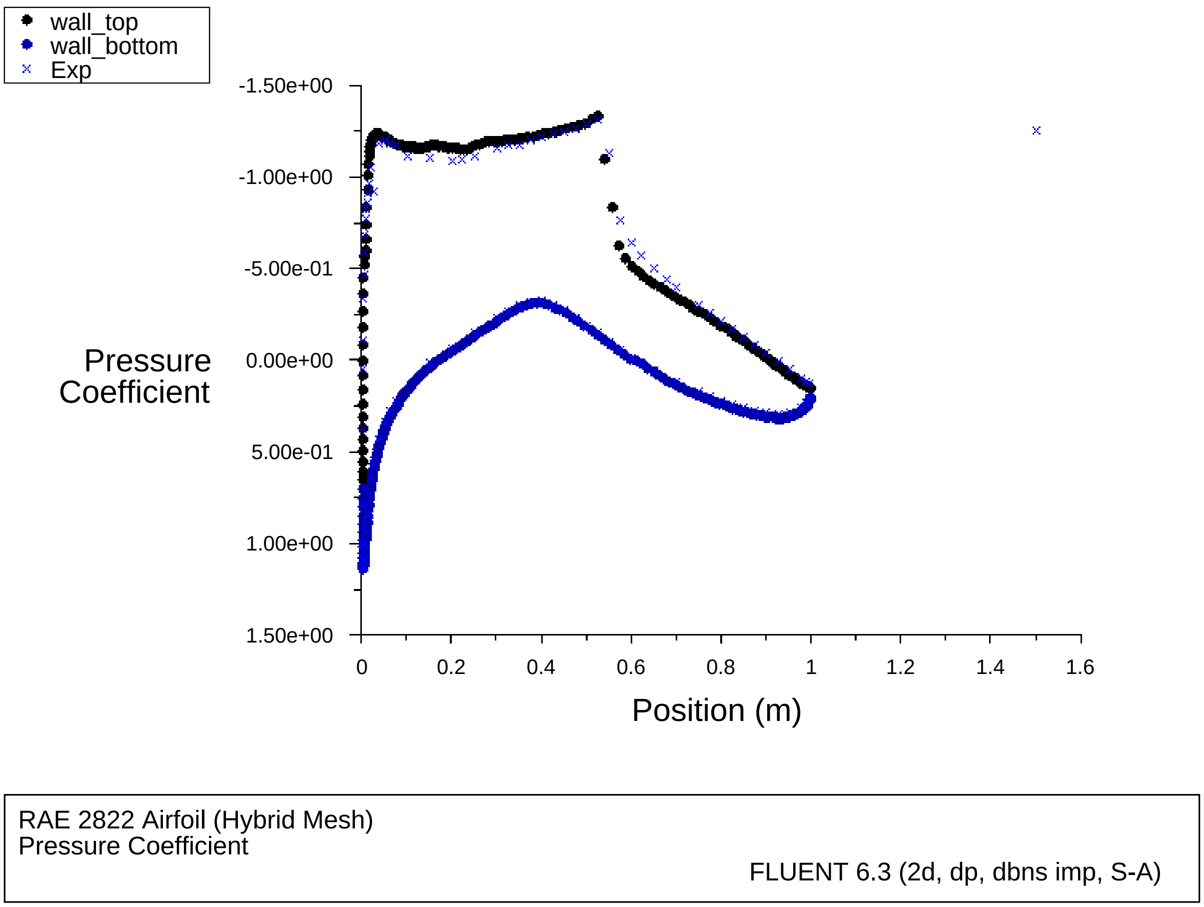

Figure 11.4.3: Comparison of FLUENT's Predictions of the Static Pressure Coefficient C_p With the Experimental Data for the Hybrid Mesh, Spalart-Allmaras Case

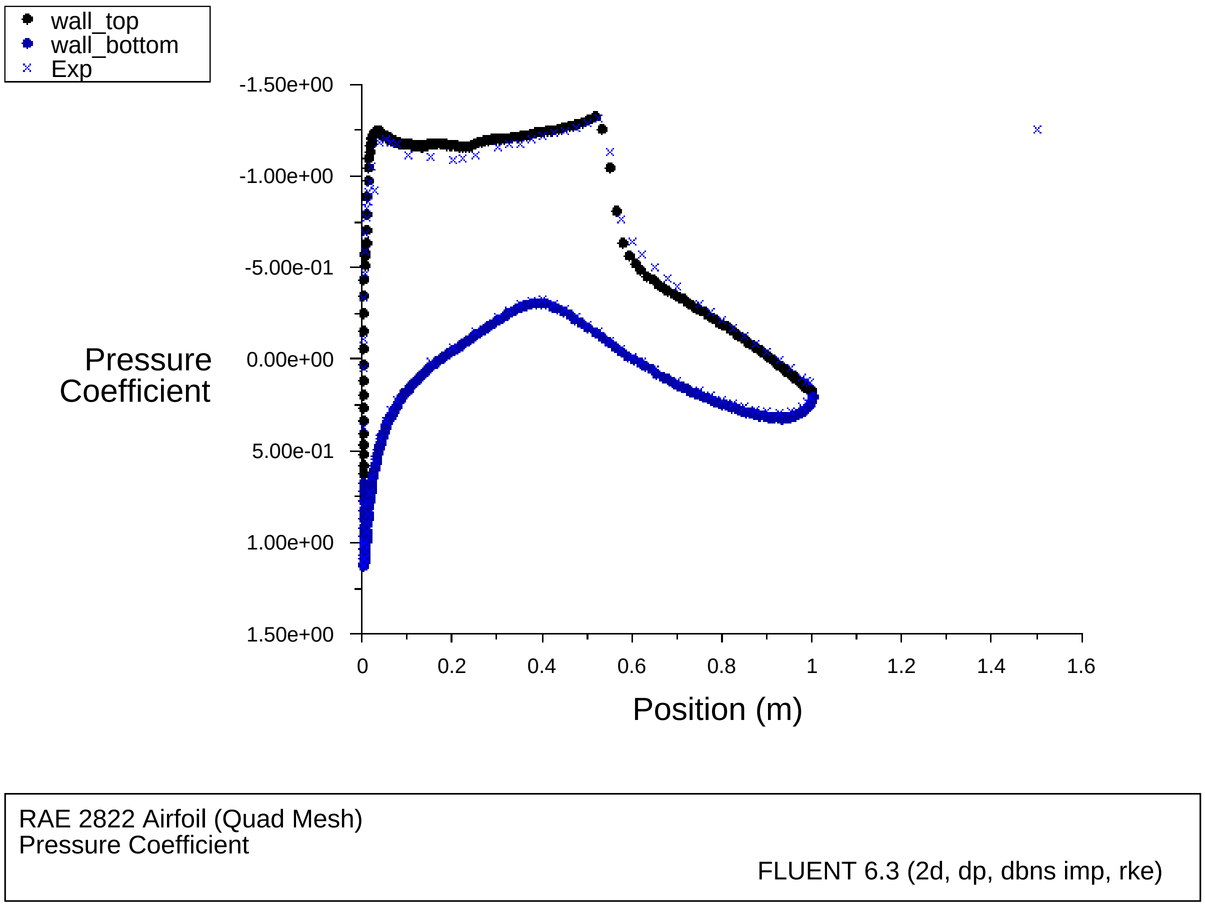

Figure 11.4.4: Comparison of FLUENT's Predictions of the Static Pressure Coefficient C_p With the Experimental Data for the Quadrilateral Mesh, Realizable k-ϵ Case

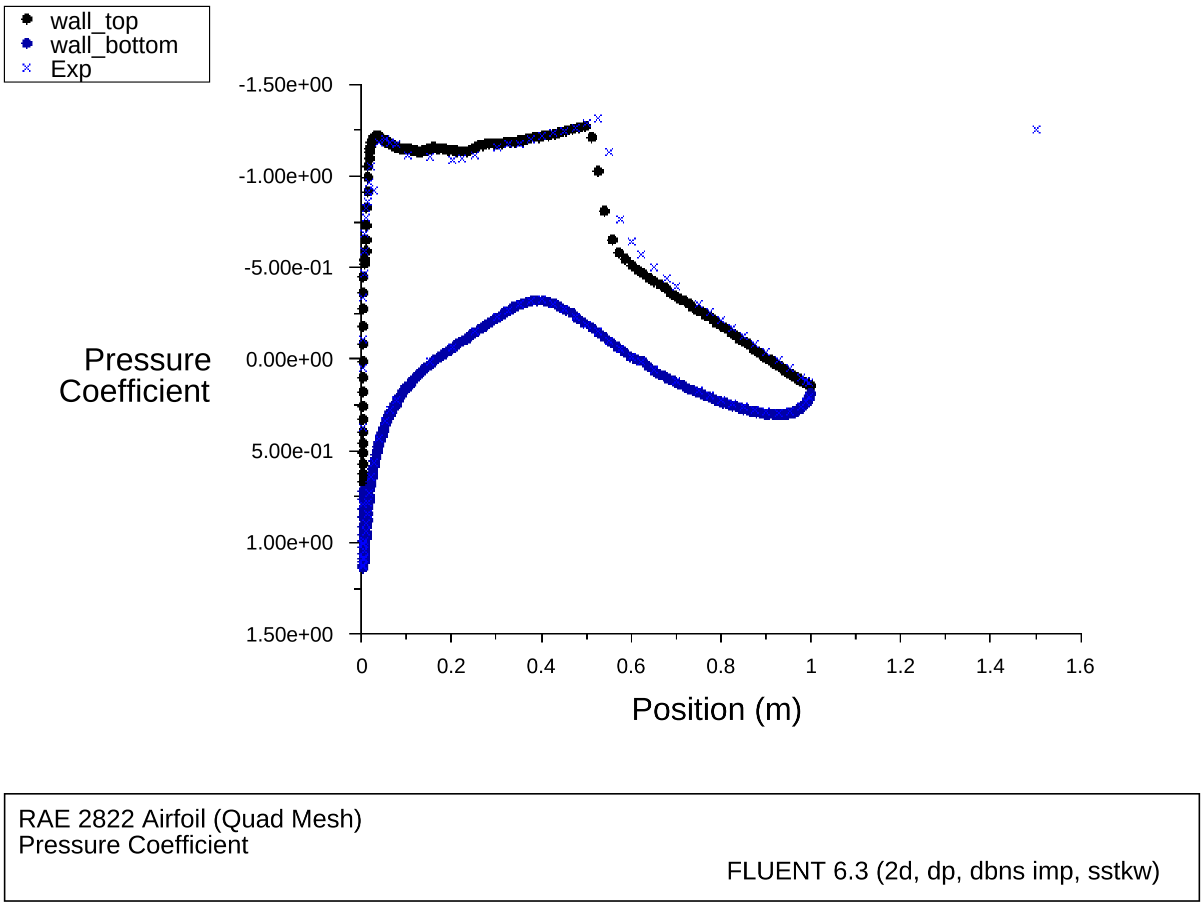

Figure 11.4.5: Comparison of FLUENT's Predictions of the Static Pressure Coefficient C_p With the Experimental Data for the Quadrilateral Mesh, SST k-ω Case

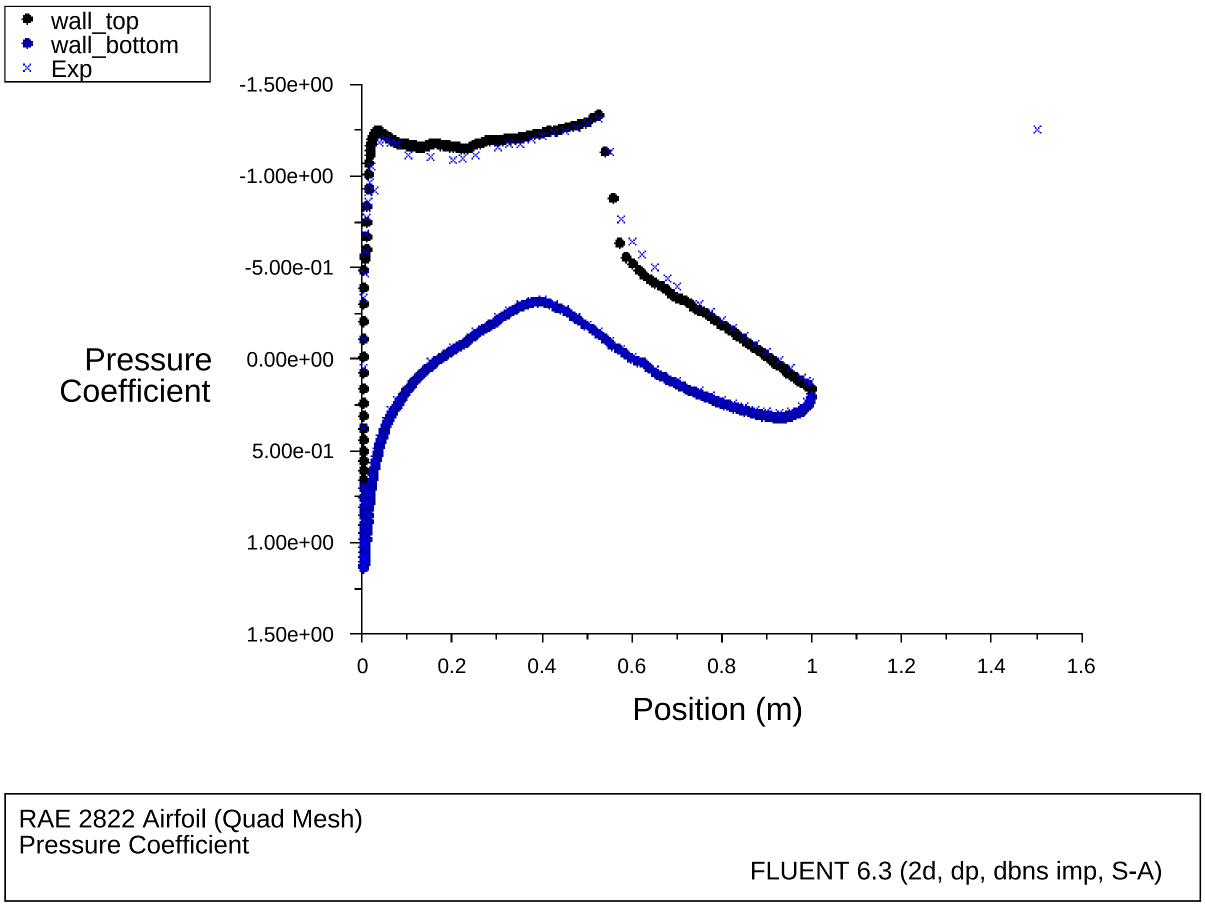

Figure 11.4.6: Comparison of FLUENT's Predictions of the Static Pressure Coefficient (C_p) With the Experimental Data for the Quadrilateral Mesh, Spalart-Allmaras Case